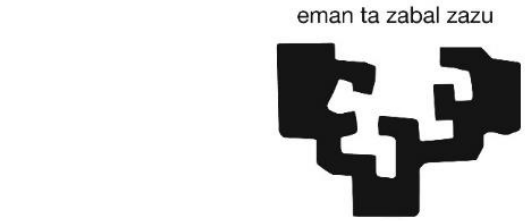

Phase-Stabilization In $FAPbI_3$-Based Perovskite Solar Cells Via Powder Engineering And Additivisation Strategies

Dissertation by

Muhammed Haris, Palattuparambil Usman

In Partial Fulfilment of the Requirements
For the Degree of Doctor of Philosophy

Supervised by
Prof. Dr. Shahzada Ahmad
Dr. Samrana Kazim

Tutor/Coordinator
Prof. Luis Maria Lezama Diago

University of the Basque Country
Leioa, Spain

September 2023

eman ta zabal zazu

Universidad del País Vasco

Euskal Herriko Unibertsitatea

Phase-Stabilization In $FAPbI_3$-Based Perovskite Solar Cells Via Powder Engineering And Additivisation Strategies

Muhammed Haris, Palattuparambil Usman

This research works for the degree of Doctor of Philosophy by the University of Basque Country, Leioa, Spain [Universidad del País Vasco/Euskal Herriko Unibertsitatea (UPV/EHU)] has been carried out at the Basque Centre for Materials, Applications and Nanostructures (BCMaterials) and the Department of Organic and Inorganic Chemistry, the Faculty of Science and Technology of the UPV/EHU.

BCMATERIALS

BASQUE CENTER FOR MATERIALS, APPLICATIONS & NANOSTRUCTURES

ehugroup

DEDICATIONS

I dedicate this thesis to my parents, my grand-parents, my siblings, my wife, and all my family members for their continued love, support and encouragement. To every person who has accompanied me on this scientific journey.

TABLE OF CONTENTS

ACKNOWLEDGEMENTS

In the name of Allah, profound gratitude and love to the Almighty for leading me to the easy completion of this doctoral studies. The achievements showcased in this dissertation owe their success to the invaluable assistance and unwavering support from a group of exceptional scientists with whom I had the privilege to collaborate throughout my four-year Ph.D journey. I am deeply grateful for their guidance and camaraderie throughout this rewarding academic endeavour.

To start with, I would like to express my gratitude to my research supervisor, prof. Shahzada Ahmad for his thoughtful mentorship, his help, care and support. I am deeply indebted to him for granting me the freedom to independently design and develop new ideas. His support and encouragement have been instrumental in fostering my creativity and allowing me to explore innovative concepts with confidence. I am truly thankful my Co-supervisor Dr. Samrana Kazim for opening the doors of this fascinating dissertation. She has guided me throughout the journey with insightful discussions. I appreciate both Shahzada and Samrana for arranging the needed facilities and funding whenever required. I extend gratitude to my tutor and Ph.D coordinator Prof. Luis Lezama for being kind throughout the journey.

I am very grateful to Prof. Aldo Di Carlo and his group for supporting me at CHOSE, Rome for my Ph.D secondment programme. It is my pleasure to appreciate all my collaborators including Prof. Michael Gratzel, Prof. Mohammad Khaja Nazeeruddin, Prof. Dario Bassani, Prof. Roy Vellaisamy, Prof. Eliseo Ruiz, Prof. Aysegul Uygun, Prof. Melepurath Deepa and their entire team for their valuable suggestions and ideas.

I would like to take this opportunity to thank my beloved group members including Dr. Manual Salado, Dr. Peng Huang, Dr. Meenakshi Pegu, Dr. David Payno, Dr. Naveen Harindu, Dr. Yassin, James Martin, Mahdi Gassara and all visiting students for your kind suggestions and help. I also thank Dr. Roberto Fernandez, Dr. Javier Del Campo, Dr. Txema Porro and Dr. Eduardo Fernandez for their assistance. I appreciate all the administrative staff, technical staff and facility staff of both BCMaterials and UPV/EHU for maintaining a positive and easy approachable environment. I appreciate European Union H2020 Programme under the ERC grant 726360 for the financial support of my

research works. I also thank the VIPERLAB action for providing financial assistance for my overseas visit and stay at CHOSE, Rome.

At this moment, I remember all my teachers and friends from childhood including, Prof. Janardan kundu, Prof. Sujith A, Mrs. Bincy Francis, Prof. Davika Rani, Mrs.Krishnambika, Mr. Poly, Mr.Peter, Mrs.Cini, Mrs.Lincy, Dr. Shibin, Mr. Munavvar, Mr.Fayis, Mr.Shine, Mr.Eldhose, Mr. Abdul Azeez, Dr. Ali Koonari, and Dr. Salim KM, who supported me at every stage of my life.

Finaly, I want to express my profound gratitude to my parents, my grandparents, my sister (Thahasin), my brothers(Faris and Shefeek), my wife (Shefeekha), my nephew (Aahil), my family members and my people from Paruthipra, Kerala, India. Their unwavering support and encouragement have been the bedrock of my journey, enabling me to face and overcome numerous challenges along the way. Their belief in my abilities and constant encouragement have given me the strength to push beyond my limits and strive for excellence.

Muhammed Haris P. U.
Leioa
September 2023

ABSTRACT

The steep rise in greenhouse gas emissions and increasing global energy demand ignited the innovation and implementation of clean and green energy resources such as *solar energy*. Among the *photovoltaics* (PV) technologies introduced over the last century, the new-born metal halide perovskite based PV thin films established themselves as a potential contender for commercial PV technologies owing to their excellent optoelectronic, cost-competitive, ease of fabrication, and solution processibility properties. The champion single-junction *perovskite solar cell* (PSC) measured an outstanding *power conversion efficiency* (PCE) of over 26% within just 15 years of research at a laboratory scale. Despite their rapid success story, the current state-of-art PSC, with *formamidinium lead triiodide* ($FAPbI_3$) as a light absorber, faces some challenges which prevent them from commercialising the product. Although the $FAPbI_3$ possess an advantageous lower-bandgap and higher Shockley-Queisser theoretical efficiency of up to 32.3%, their room-temperature polymorphism and existence of thermodynamically stable non-photoactive phase prohibit their implantation in commercial PVs. This dissertation describes innovative approaches adapted to stabilize and to understand the structure-stability-performance correlations in the photoactive $FAPbI_3$ based PSCs.

We first developed a room-temperature processible, cost-competitive powder engineering protocol for *cesium* (Cs) amalgamated $FAPbI_3$ (δ-$Cs_{0.1}FA_{0.9}PbI_3$), where the Cs insertion reduced the fabrication temperature from 150 ºC to 80 ºC. Owing to the higher crystallinity and enhanced light absorption, the champion PSC fabricated from δ-$Cs_{0.1}FA_{0.9}PbI_3$ powder delivered an improved PCE of over 17% with reduced hysteresis in comparison with the δ-$FAPbI_3$ counterpart. We then extended the powder engineering protocol to develop black α-$FAPbI_3$ powder via annealing of δ-$FAPbI_3$ powder and systematically compared the two powder methods with the conventional route. Through an in-depth structural and optoelectronic analysis, we demonstrated that the microstrain, representing structural disorder, and Urbach energy, indicating electronic disorder, were reduced drastically in the order of α-$FAPbI_3$ < δ-$FAPbI_3$ < conventional route. The reduced microstrain improved the phase stabilization and reduced Urbach energy boosted the V_{OC}. In short, the developed powder engineering strategies demonstrated enhanced phase stability for $FAPbI_3$ under ambient storage and thermal aging for a longer time along with the device reliability. However, considering the real-life implantation of PSCs,

their water uptake capability is crucial and the hydrogen migration tracking via conventional imaging or mass spectroscopy tools is challenging. In this scenario, we demonstrated proton diffusion to probe the indirect hydrogen migration using a custom-built-modified transmission infrared spectroscopy, which allowed the direct monitoring of the deterioration of the perovskite layer by moisture. We found the moisture/water blocking ability of the perovskite layer is in the order of $Cs_{0.1}FA_{0.9}PbI_3$ > $FAPbI_3$ > $MAPbI_3$. Additionally, we quantified the water-blocking ability of $Cs_{0.1}FA_{0.9}PbI_3$ as 5 times higher than that of $FAPbI_3$.

In addition to the powder methods, we further employed various additivisation strategies to enhance the stability and performance of $FAPbI_3$-based PSCs. Firstly, we employed two ultra-hydrophobic ionic liquids as the additives in $FAPbI_3$ devices and the PCE showed a boost from 16% to 18%. The emerged semi-ionic F-Pb interaction resulted in surface passivation and stabilisation. Despite the various strategies including composition engineering, interface engineering, and strain modulations, the $FAPbI_3$ layer still possessed thermodynamic stability at its non-photovoltaic phase (2H). In this context, we elucidated a rational additivisation strategy using a multi-functional molecule containing diammonium ends and a sulphur-hetero atom. The cumulative impacts from the diammonium and sulphur atoms delivered micron-sized grains with higher crystallinity and preferred (h00) facet orientation at the macroscopic level. Most importantly, the strategy demonstrated exceptional stability against high humidity environments, direct water immersion, and shelf life aging experiments. Through systematic structural, morphological, and elemental analyses, we decipher the role of the sulphur element in stabilizing the $FAPbI_3$ system and in shifting the thermodynamic stability from the non-photovoltaic phase to the photoactive phase. The knowledge accumulated in this thesis are important contributions towards stabilizing and upscaling the state-of-art single-junction perovskite solar cells.

ABSTRAZIOAK

Berotegi-efektuko gasen emisioaren gorakada handia eta mundu mailako energia-eskariaren hazkunde esponentzialaren ondorioz, eguzki-energia bezalako energia-baliabide garbi eta berdeen berrikuntza eta ezarpena piztu zuten. Azken mendean sartutako sistema *fotovoltaiko* (PV) ezberdinen artean, halogenuro metaliko perovskita jaioberriak PV teknologi komertzialen lehiakide potentzial gisa ezarri ziren beren optoelektronika, kostu-lehiakortasuna, fabrikatzeko erraztasuna eta irtenbideen prozesagarritasun propietateengatik. . Juntura bakarreko perovskita eguzki-zelulak (PSC) txapeldunak % 26tik gorako potentzia bihurtzeko eraginkortasun (PCE) nabarmena erregistratu zuen 15 urteko ikerketan laborategi eskalan. Arrakasta azkarra izan duten arren, egungo PSC-k, formamidinio berun triioduroa ($FAPbI_3$) argi xurgatzaile gisa duen, erronka larri batzuei aurre egiten die produktua komertzializatzea eragozten dietenak. $FAPbI_3$-ek banda baxuagoko eta Shockley-Queisser-en eraginkortasun teoriko handiagoa izan arren, % 32,3ra arte, beren giro-tenperaturako polimorfismoak eta termodinamikoki egonkorra den fase ez fotoaktiboa izateak PV komertzialetan ezartzea mugatzen du. Tesi honek $FAPbI_3$ oinarritutako PSC fotoaktiboetan egitura-egonkortasuna-errendimenduaren korrelazioak egonkortzeko eta ulertzeko egokitutako gure ikuspegi berritzaileak deskribatzen ditu.

Lehenik eta behin, giro-tenperaturan prozesatu eta kostu-lehiakorra den hauts ingeniaritza protokolo bat garatu genuen zesio (Cs) amalgamatutako $FAPbI_3$ (δ-$Cs_{0.1}FA_{0.9}PbI_3$), non Cs txertatzeak fabrikazio-tenperatura 150 ºC-tik 80 ºC-ra murriztu zuen. Kristalinitate handiagoaren eta argiaren xurgapen hobearen ondorioz, δ-$Cs_{0.1}FA_{0.9}PbI_3$ hautsez egindako PSC txapeldunak % 17ss baino gehiagoko PCE hobetua eman zuen histeresi murriztuarekin δ-$FAPbI_3$ parekoarekin alderatuta. Ondoren, hautsaren ingeniaritza protokoloa zabaldu genuen α-$FAPbI_3$ hauts beltza garatzeko δ-$FAPbI_3$ hautsaren anneatze sinplearen bidez eta sistematikoki bi hauts metodoak ohiko bidearekin alderatu genituen. Hiru metodoen egiturazko eta optoelektronikoen azterketa sakon baten bidez frogatu genuen mikro-tentsioa, egitura-nahastea adierazten duena, eta Urbach-en energia, nahaste elektronikoa adierazten duena, α-$FAPbI_3$ < δ-$FAPbI_3$ < ohiko ordenan murrizten zirela. Mikrostrain murriztuak fase-egonkortzea hobetu zuen eta Urbach-en energia murriztuak zirkuitu irekiko tentsioa (V_{OC})-a areagotu zuen. Laburbilduz, hautsaren ingeniaritza-estrategiek $FAPbI_3$-ren fase-egonkortasun hobetua frogatu zuten giro-biltegiratzean eta

zahartze termikoan denbora luzeagoan gailuaren fidagarritasunarekin batera. Hala ere, PSCen bizitza errealean ezartzea kontuan hartuta, haien ura hartzeko gaitasuna funtsezkoa da eta hidrogenoaren migrazioaren jarraipena ohiko irudien edo masa-espektroskopia tresnen bidez erronka da. Eszenatoki honetan, protoi-difusioa frogatu genuen zeharkako hidrogenoaren migrazioa probatzeko, etxean aldatutako transmisio infragorriaren espektroskopia erabiliz, eta horrek hezetasunaren perovskita geruzaren narriaduraren jarraipen zuzena ahalbidetu zuen. Perovskita geruzaren hezetasuna/ura blokeatzeko gaitasuna $Cs_{0.1}FA_{0.9}PbI_3$ > $FAPbI_3$ > $MAPbI_3$ ordenakoa dela aurkitu dugu. Gainera, $Cs_{0.1}FA_{0.9}PbI_3$-ren ura blokeatzeko gaitasuna $FAPbI_3$ arena baino 5 aldiz handiagoa zela kuantifikatu genuen.

Hauts-metodoez gain, gehigarritasun-estrategia ezberdinak erabili ditugu $FAPbI_3$-n oinarritutako PSCen egonkortasuna eta errendimendua hobetzeko. Lehenik eta behin, bi likido ioniko ultra-hidrofobo erabili ditugu $FAPbI_3$ gailuetako gehigarri gisa eta PCE-k %16tik %18ra igo zen. Sortutako F-Pb elkarrekintza erdiionikoak gainazaleko pasibazioa eta egonkortzea eragin zuen. Konposizioaren ingeniaritza, interfazearen ingeniaritza eta tentsio modulazioak barne estrategia ezberdinak izan arren, $FAPbI_3$ geruzak egonkortasun termodinamikoa zuen oraindik bere fase ez fotovoltaikoan (2H). Testuinguru honetan, aditivizazio estrategia arrazional bat argitu genuen diamonio-muturrak eta sufre-heteroatomoa dituen funtzio anitzeko molekula bat erabiliz. Diammlonioaren eta sufre atomoaren inpaktu metatuek mikrometroko aleak eman zituzten kristalintasun handiagoarekin eta (h00) fazeta orientazio-orientazio hobetsiarekin maila makroskopikoan. Garrantzitsuena, estrategiak aparteko egonkortasuna frogatu zuen hezetasun handiko ingurunearen, ur-murgiltze zuzenaren eta apal-bizitzaren zahartze esperientzien aurrean. Azterketa estruktural, morfologiko eta elemental sistematikoen bidez, sufre-elementuak $FAPbI_3$ sistema egonkortzeko eta egonkortasun termodinamikoa fase ez fotovoltaikotik fase fotoaktibora aldatzeko eginkizuna deszifratzen dugu. Tesi honetan pilatutako ezagutzak ekarpen garrantzitsuak dira perovskitako juntura bakarreko perovskita eguzki-zelulak egonkortzeko eta eskalatzeko.

RESUMEN

El fuerte aumento de las emisiones de gases de efecto invernadero y el aumento exponencial de la demanda mundial de energía impulsaron la innovación y la implementación de recursos energéticos limpios y verdes, como la energía solar. Entre los diversos sistemas fotovoltaicos (PV) introducidos durante el último siglo, las películas delgadas fotovoltaicas basadas en perovskita de haluro metálico recién nacidas se establecieron como un competidor potencial para las tecnologías fotovoltaicas comerciales debido a sus excelentes propiedades optoelectrónicas, rentables, fáciles de fabricar y de procesabilidad de la solución. . La célula solar de perovskita (PSC) de unión única campeona registró una eficiencia de conversión de energía (PCE) excepcional superior al 26 % en solo 15 años de investigación a escala de laboratorio. A pesar de su rápida historia de éxito, el actual PSC de última generación, con triyoduro de plomo y formamidinio ($FAPbI_3$) como absorbente de luz, se enfrenta a serios desafíos que les impiden comercializar el producto. Aunque el $FAPbI_3$ posee una banda prohibida inferior ventajosa y una mayor eficiencia teórica de Shockley-Queisser de hasta el 32,3%, su polimorfismo a temperatura ambiente y la existencia de una fase no fotoactiva termodinámicamente estable restringe su implantación en PV comerciales.

En esta tesis, arrojamos luz sobre los aspectos fundamentales y prácticos de la perovskita $FAPbI_3$ de última generación. El aspecto fundamental incluye la comprensión del mecanismo de cristalización, la cinética de transición de fase y el modelado teórico junto con las caracterizaciones estructurales, ópticas y eléctricas en profundidad. Por otro lado, el aspecto práctico contiene varias estrategias de ingeniería de procesos y aditivación para transferir el conocimiento, adquirido a partir de investigaciones fundamentales, hacia la realización de células solares de perovskita estables y eficientes. Al hacerlo, intentamos abordar el problema crítico de inestabilidad de fase del absorbente $FAPbI_3$. Esta disertación describe el conocimiento fundamental que se correlaciona entre la condición del proceso, especialmente el papel del material precursor, el dopaje y los aditivos en la conversión de luz solar en electricidad y la estabilidad intrínseca y extrínseca tanto de la capa absorbente como de los dispositivos. Anticipamos que este estudio extiende pruebas sólidas para varias hipótesis existentes en la comunidad y abre una nueva dirección para las futuras posibilidades de investigación en el campo.

Los *capítulos 1* y *2* analizan el estado del arte de las células solares híbridas de perovskita, comenzando con la historia del material, la estructura, las propiedades optoelectrónicas, la integración fotovoltaica, los pros y los contras de las perovskitas híbridas empleadas anteriormente, el surgimiento y los desafíos con las perovskitas calientes $FAPbI_3$, además de incluir la herramientas de fabricación y caracterización utilizadas en esta tesis.

En los *Capítulos 3*, *4* y *5*, demostramos la aplicabilidad universal de nuestras estrategias de ingeniería de polvos desarrolladas al garantizar la mejora del rendimiento del dispositivo junto con la reducción de los costos de producción. En el *Capítulo 3*, desarrollamos un polvo de $FAPbI_3$ amalgamado con cesio procesado a temperatura ambiente (δ-$Cs_{0.1}FA_{0.9}PbI_3$) y lo empleamos como material precursor en lugar de precursores convencionales como PbI_2. FAI y CsI. La fusión de Cs redujo la temperatura de procesamiento de la película absorbente de perovskita de 150 ºC a 80 ºC. Además, registramos una mayor eficiencia del PSC fabricado con polvo δ-$Cs_{0.1}FA_{0.9}PbI_3$ que con el polvo δ-$FAPbI_3$. Atribuimos el PCE observado del 17 % con histéresis insignificante a la cristalinidad mejorada observada en las mediciones de PXRD y SEM, y a una mayor absorción de luz visible en las mediciones de absorción. Luego, realizamos espectroscopía de admitancia térmica a temperatura variable para revelar la densidad de defectos superficiales y profundos y la distribución de energía de captura dentro de la brecha de banda de los PSC basados en $CsFAPbI_3$ fabricados a 80 ºC y 150 ºC, y justificamos el incremento observado para el PSC procesado a baja temperatura. a través de cálculos de densidad de trampas. Además, avanzamos hacia la síntesis de polvo negro de α-$FAPbI_3$ a través del recocido simple del polvo de δ-$FAPbI_3$ y comparamos sistemáticamente los dos métodos de polvo con la ruta convencional en el *Capítulo 4*. Al comparar las tres rutas de precursores, demostramos que nuestras estrategias de ingeniería de polvo mejoró la estabilidad de fase intrínseca de $FAPbI_3$ y el rendimiento del dispositivo correspondiente. A través de análisis fundamentales en profundidad, identificamos que son los valores reducidos de microdeformación los que contribuyeron directamente a la estabilización de $FAPbI_3$ en polvo bajo el envejecimiento de la vida útil. Luego, mostramos que la energía reducida de Urbach mejoró aún más el PCE al reducir el déficit de Abra el circuito de voltaje (V_{OC}). En busca de una fabricación rentable de PSC, usamos PbI_2 de baja pureza (99 %) en el proceso de ingeniería de polvo y luego

fabricamos PSC que entregaron un PCE ligeramente más alto en comparación con la contraparte convencional fabricada con un precursor de PbI_2 de alta pureza. Dado el hecho de que se espera que los PSC funcionen en una atmósfera ambiente en el escenario de la vida real y la estabilidad de cada capa, especialmente la capa de perovskita, contra el ataque de la humedad es de suma importancia. Aunque muchos informes aclaran las vías de degradación de la capa de perovskita, específicamente $FAPbI_3$, la cuantificación de la capacidad de absorción de agua de la capa de perovskita no está bien demostrada. En el *Capítulo 5* demostramos la difusión de protones para analizar la migración indirecta de hidrógeno utilizando una espectroscopia infrarroja de transmisión modificada en el hogar, que permitió el monitoreo directo del deterioro de la capa de perovskita por la humedad. Encontramos que la capacidad de bloqueo de humedad/agua de la capa de perovskita es del orden de $Cs_{0.1}FA_{0.9}PbI_3 > FAPbI_3 > MAPbI_3$. Además, cuantificamos la capacidad de bloqueo de agua de $Cs_{0.1}FA_{0.9}PbI_3$ como 5 veces mayor que la de $FAPbI_3$. Sin embargo, no observamos ningún cambio significativo en la tasa de difusión de protones para la capa de perovskita de nuestros polvos δ-$FAPbI_3$ y α-$FAPbI_3$. A partir de los análisis de microdeformación y difusión de protones, creemos que los valores de microdeformación podrían regular la estabilidad intrínseca de la capa de $FAPbI_3$ pero no el ataque de humedad en la superficie de $FAPbI_3$.

Teniendo en cuenta el hecho de que el ataque de humedad/agua en la superficie $FAPbI_3$ acelera la transición de fase desfavorable de la fase α fotoactiva a la fase δ fotoactiva, preseleccionamos varias estrategias de aditivación como se analiza en los *Capítulos 4*, *5* y *6*. En busca de los materiales hidrofóbicos como aditivos, optamos por líquidos iónicos no volátiles (IL) como aditivos debido a su naturaleza ultrahidrofóbica, alta estabilidad química y térmica, procesabilidad a baja temperatura y excelentes propiedades electroquímicas. El *Capítulo 4* demuestra el uso de dos IL a base de fosfato de perfluoroalquilo con cationes de imidazolio funcionalizados con etilo (EMIFAP) y hexilo (HMIFAP) como aditivos. A partir del análisis XPS, observamos que la interacción semiiónica F-Pb surgida estabiliza eficazmente los átomos de Pb poco coordinados en la superficie $FAPbI_3$. También rastreamos los cambios de microdeformación inducidos por la aditivación en el sistema. Mediante mediciones de PXRD y XRD dependientes de la profundidad, encontramos que los valores de microdeformación se redujeron drásticamente de $1{,}95 \times 10^{-4}$ a $1{,}87 \times 10^{-4}$ y $1{,}67 \times 10^{-4}$ para las películas de referencia

$FAPbI_3$, EMIFAP y HMIFAP, respectivamente. Esto se confirmó aún más a través de la mayor cristalinidad observada en los análisis PXRD y SEM. Luego, rastreamos el desorden electrónico, la energía de Urbach, e identificamos una reducción de 13,22 a 12,98 y 12,47 meV para las películas de referencia $FAPbI_3$, EMIFAP y HMIFAP, respectivamente. Con esta comprensión y conocimiento en la mano, avanzamos para fabricar los PSC correspondientes y registramos un incremento de PCE de 16,37 a 17,49 y 18,26 % para las películas de referencia $FAPbI_3$, EMIFAP y HMIFAP, respectivamente. La naturaleza hidrofóbica de los IL parece proporcionar una mejor estabilidad para los PSC frente a las tensiones ambientales en las condiciones de almacenamiento y operación. De manera similar, luego empleamos 1,3-bis(cianometil)imidazolio bis(trifluorometilsulfonil)imida (IL-TFSI), otra fracción IL con grupo TFSI como parte aniónica, en el sistema $Cs_{0.1}FA_{0.9}PbI_3$ como se detalla en el *Capítulo* 5 Junto con una mayor cristalinidad, la mayor duración del portador lograda debido a la pasivación de los estados de trampa por parte de IL impulsó la PCE de 19,27 a 20,55 %.

Aunque los métodos de polvo discutidos anteriormente, el tratamiento con IL y otra ingeniería de cepas informada, la modulación de facetas y las estrategias aditivas de amonio de cadena larga o bases de Lewis ayudaron a estabilizar $FAPbI_3$, el problema central permaneció intacto. A pesar de estos encomiables esfuerzos, la estabilidad de la fase termodinámica del sistema $FAPbI_3$ se mantuvo con la fase hexagonal fotoinactiva (δ-fase o 2H). Para abordar esta grave preocupación, demostramos una nueva ruta de aditivización multifuncional, donde la molécula de hidroyoduro de yoduro de S-(2-aminoetil)isotiouronio elegida racionalmente (*isothio*) que contiene dos extremos de amonio junto con un heteroátomo de azufre se usa como aditivo. La elección del heteroátomo de azufre fue defendida por los hallazgos de la literatura anterior que indicaban que el azufre tiene una propiedad de donación de electrones más fuerte que el oxígeno y el nitrógeno. Al emplear un catión de diamonio bifuncional con una heteroestructura de azufre, demostramos que la perovskita no regresa a la notoria fase 2H al envejecer. La fase termodinámicamente estable de nuestra película $FAPbI_3$ modificada se cambió de una fase 2H a una fase intermedia más cercana a la fase 3C cúbica. Atribuimos los créditos a la interacción emergente azufre-Pb y esto se confirmó aún más mediante análisis estructurales, ópticos y morfológicos sistemáticos. Los impactos sinérgicos del átomo de diammlonio y azufre generaron granos de tamaño micrométrico

con mayor cristalinidad y orientación de faceta preferida (h00) a nivel macroscópico. Curiosamente, nuestro estudio demostró una estabilidad excepcional frente a ambientes de alta humedad, inmersión directa en agua y experimentos de envejecimiento de vida útil. La adición de Isothio permitió que la película $FAPbI_3$ permaneciera en su fase 3C durante más tiempo de 250 horas en un entorno de alta humedad (75 % HR), mientras que la película $FAPbI_3$ de referencia experimentó una transición de fase en un par de horas. Luego, a partir de experimentos de incursión de agua en tiempo real, decodificamos una ruta de degradación diferente de nuestra película $FAPbI_3$, que ayudó a resistir la incursión de agua directa durante un tiempo de hasta 2 minutos, mientras que la película de referencia se degradaba en un par de segundos. A través de mediciones detalladas de XPS, identificamos que es la molécula de agua adsorbida en la superficie la que acelera la degradación de $FAPbI_3$ en presencia de agua/humedad. La excepcional estabilidad a la humedad de nuestra película fue corroborada por la supresión completa de la molécula de agua adsorbida en la superficie, incluso después de 250 horas de exposición a alta humedad. En comparación con la película de referencia, observamos una distribución estructural ordenada de largo alcance con dislocación de borde reducida y transición de fase a nivel nanoscópico para nuestra película a partir del análisis microscópico de emisión de transmisión de alta resolución.

En resumen, creemos que los conocimientos acumulados en esta tesis son contribuciones importantes para estabilizar y ampliar las células solares de perovskita de unión simple de última generación con $FAPbI_3$ como fotoabsorbente. Los conocimientos fundamentales dilucidados y los enfoques prácticos podrían extrapolarse aún más a las amplias aplicaciones de las perovskitas híbridas de haluro orgásssanico-inorgánico.

ACRONYMS & ABBREVIATIONS

3D	Three-Dimensional
2D	Two-Dimensional
AFM	Atomic Force Microscopy
AM 1.5G	Air Mass 1.5 Global
a-Si	Amorphous Silicon
BCP	Bathocuproine
Br	Bromide
BuLi	Butyl lithium/Hexane
CBM	Conduction Band Maximum
CBZ	Chlorobenzene
c-Si	Crystalline Silicon
CTL	Charge Transport Layer
DMF	*N*, *N*-dimethylformamide
DMSO	Dimethyl sulfoxide
DOS	Density of States
EQE	External Quantum Efficiency
ETL	Electron Transport Layer
FA	Formamidinium
FF	Fill Factor
FTO	Fluorine-doped Tin Oxide

HI	Hysteresis Index
HF	High Frequency
HOIP	Hybrid organic-inorganic perovskite
HOMO	Highest Occupied Molecular Orbital
HTL	Hole Transport Layer
I	Iodide
IF	Intermediate Frequency
ITO	Indium Tin Oxide
Li-TFSI	Bis (trifluoromethane) sulfonimide lithium salt
LF	Low Frequency
LUMO	Lowest Unoccupied Molecular Orbital
MA	Methylammonium
MoS_2	Molybdenum Disulfide
MPP	Maximum Power Point
NiOx	Nickel Oxide
P3HT	Poly(3-hexylthiophene-2,5-diyl)
Pb	Lead
$PC_{60}BM$	[6,6]-phenyl-C61-isomethyl butyrate
PCE	Power Conversion Efficiency
PEDOT:PSS	Poly (3,4-ethylenedioxythiophene): polystyrene sulfonate
PL	Photoluminescence

PSC	Perovskite Solar Cell
PV	Photovoltaics
PTAA	Poly(triaryl amine)
SEM	Scanning Electron Microscopy
Sn	Tin
SnO_2	Tin Oxide
Spiro-OMeTAD	2,2′,7,7′-tetrakis(N,N-di-p-methoxyphenylamine)-9,9′-spirobifluorene
*t*BP	4-tert-butylpyridine
TCO	Transparent Conducting Oxide
TEM	Transmission Electron Microscopy
TiO_2	Titanium Oxide
UV	Ultraviolet
UV-Vis	Ultraviolet-Visible
VB	Valence Band
XPS	X-ray Photoelectron Spectroscopy
XRD	X-ray Diffraction

LIST OF SYMBOLS

A	Device active area
J-V	Current density-Voltage
V_{OC}	Open-circuit voltage
I_{SC}	Short-circuit current
J_{SC}	Short-circuit current density
E_C	Conduction band
E_F	Fermi level
E_V	Valence band
E_{vac}	Vacuum level
Φ_F	Work function
J_{int}	Integrated current density
μ	octahedral factor
m_h	Hole effective Mass
m_e	Electron effective Mass
R_{sh}	Shunt resistance
R_S	Series resistance
h	Planck constant
E_a	Activation energy
K_B	Boltzmann constant
t	Goldschmidt tolerance factor

F	Frequency
f_{peak}	Peak frequency
C	Capacitance
V_{bi}	Built-in potential
W	Depletion layer thickness
q	Electron charge
ε	Dielectric constant
ε_0	Vacuum permittivity
t_{DOS}	Trap density of state
N_{Defects}	Defect density
J_D	Dar current density
J_{ph}	Photocurrent density
J_{sat}	Saturation current density
V_{eff}	Effective voltage
V_{app}	Applied-bias voltage
τ	Charge lifetime

LIST OF FIGURES

LIST OF TABLES

CHAPTER 1

1

INTRODUCTION

1.1 History of Lead halide perovskites

The history of perovskites (Figure 1.1) starts with its first discovery in a piece of chlorite-rich skarn in the Ural Mountains in Russia in 1839 by Gustav Rose[1] and the compound was named after the renowned Russian mineralogist Count, Lev Perovski. Since then the calcium titanate ($CaTiO_3$) compound became the reference and any compound following a similar structure is named a perovskite. From the first experimental attempt to synthesize $CaTiO_3$ in 1851 and the first successful laboratory synthesis in 1882 by Danish crystallographer Haldor Topsoe, the metal oxide perovskite attracted enormous research interests due to their ferroelectric, piezoelectric, dielectric and pyroelectric applications etc.[2,3] However, a few metal oxide perovskite compounds demonstrated photovoltaic properties owing to their ferroelectric polarization. The lack of good semiconducting properties prevented them from further PV applications. In the late 18th century and early 19th century, the halide counterparts of oxide perovskites were discovered and Weber and co-workers ignited the field right after the introduction of a new composition of hybrid organic inorganic halide perovskite (HOIP) material in 1978.[4,5] In their first ever crystallographic study on HOIP materials they chose methylammonium (CH_3NH_3, MA) cation as organic part, Lead (Pb) and Tin (Sn) cation as inorganic part and iodide (I), bromide (Br) anion as halide part.[6] Taking this attempt forward, David Mitzi synthesized a large number of HOIPs with varying compositions and studied their physical properties in the late 1990s.[7-9]

1.2 Structure of 3D HOIPs

The traditional three-dimensional (3D) HOIP materials have the structure of ABX_3, where A is an organic cation, B is an inorganic cation and X is a halide anion that is connected to both the cations. In a unit cell motif depicted in Figure 1.2 A, the A cation occupies the central site of the unit cell and is surrounded by twelve X-anions, and the B cation is

octahedrally coordinated in a BX_6 configuration. The structural stability and possible 3D HOIP library can be determined by Goldschmidt's tolerance factor, octahedral factor and charge balance constrains.[10-12]

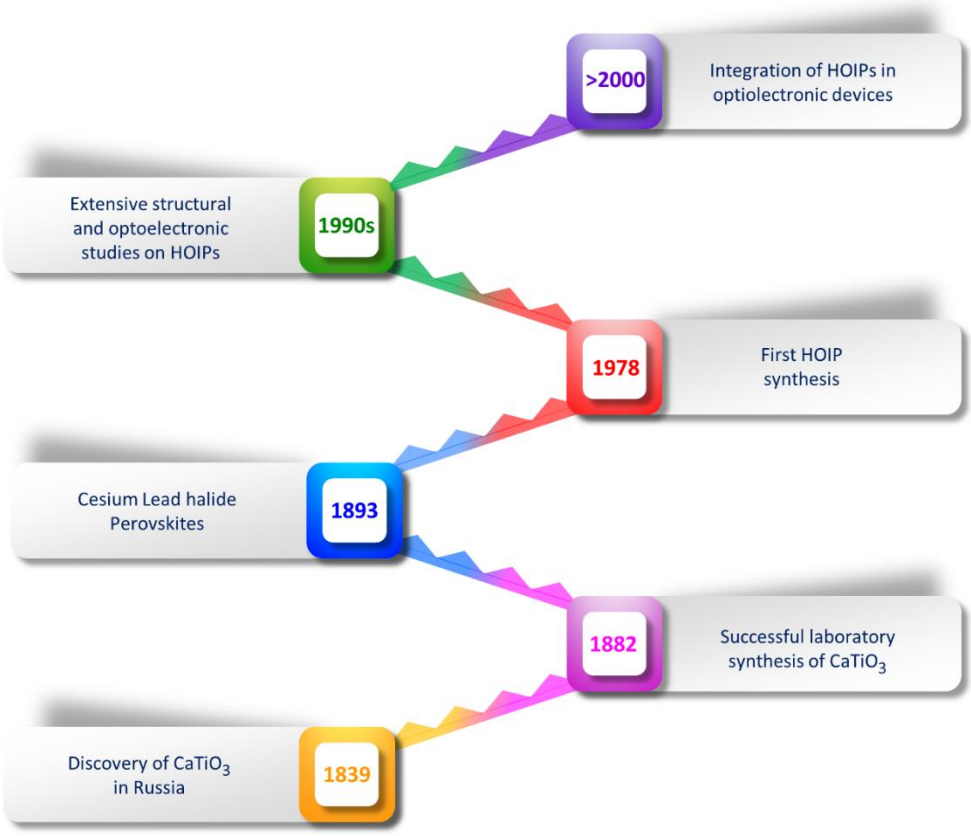

Figure 1. 1 Timeline of research and discoveries into optoelectronic behaviours of HOIPs.

For instance, the structural stability of ABX_3 perovskite is determined using the Goldschmidt tolerance factor (t) by the formula,

$$t = ((r_A + r_X)) \,/\, (\sqrt{2}(r_B + r_X)) \quad \text{.....(1.1)}$$

where r_A, r_B, and r_X represent the ionic radii of A, B, and X, respectively. Arguably, the value of $0.81 < t < 1$ is the ideal tolerance factor range to form the 3D perovskite structure. It can be deduced from Figure 1.2 B that any deviation from this range will lead to structural distortion and unfavourable phase transition, i.e., typically, hexagonal structures are formed when $t > 1$, and non-perovskite structures are formed when $t < 0.8$.[13]

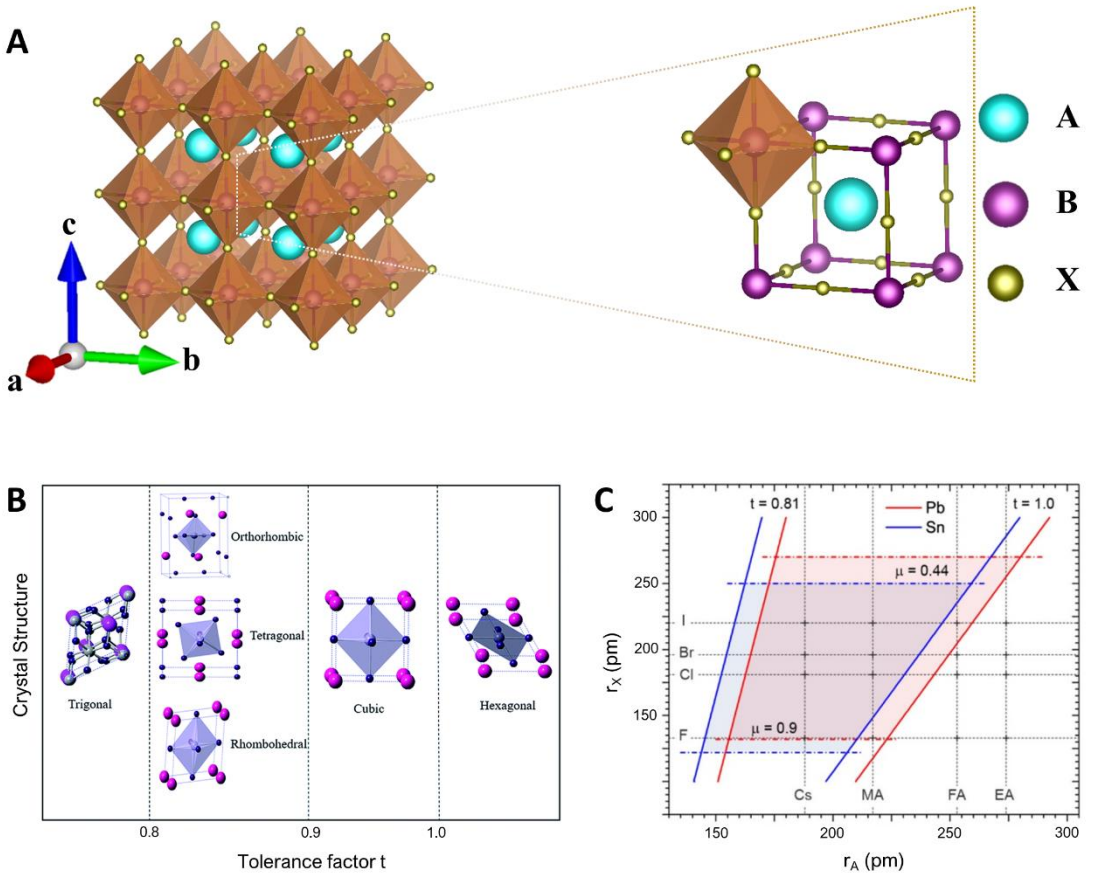

Figure 1. 2 (A) Extended 3D structure of HOPIs with corner shared PbI_6 octahedra (left) and zoom-in view of unit cell representation (right), where A, B, and X represents a monovalent cation, divalent metal cation, and monovalent halide anion, respectively. (B) relationship between the tolerance factor and crystal structures of HOIPs, Reproduced with permission from Ref.[13] (C) The formability of 3D lead (red) and tin (blue) HOIPs, in relation to the A-site cation and halide anion radii, is depicted in the graph. The solid and dashed lines represent the limits of the tolerance and octahedral factors, respectively. Reproduced with permission from Ref.[10]

While the octahedral factor (μ), given by $\mu = r_B/r_X$ and normally lies in the range of $0.44 \leq \mu \leq 0.9$, is a measure of octahedral stability and, together with the tolerance factor, provides a parameter space for perovskite formability (Figure 1.2 C). Additionally, the charge balance constrain restricts the A cation as monovalent, B cation as divalent, and X anion as monovalent for 3D HOIPs. However, these three constraints provide limited A-B combinations for 3D HOIPs. Typically, dications from group IVA of the periodic table such as Ge^{2+}, Sn^{2+}, and Pb^{2+} can fill the B site, in which Pb based ($APbX_3$) system displayed better performance in optoelectronic devices owing to their stability against oxidation. On the other hand, MA, formamidinium (FA) Cesium (Cs), or their combinations can fill the A site.[14]

1.3 Optoelectronic properties of 3D HOIPs

HOIP semiconductor materials have outstanding optoelectronic characters, particularly direct optical bandgap, high absorption coefficient, high photoluminescence quantum yield, long charge-carrier diffusion length, low exciton binding energy, and high carrier mobility, which helps the efficient conversion of both light-to-electricity and electricity-to-light. The fundamental understanding of the optical properties of HOIPs is often discussed through their band structure and density of states (DOS). For instance, 5p orbitals from halogen (X) and 6s orbitals from metallic cation (Pb) in a 3:1 ratio comprise the valence band maximum (VBM), whereas the conduction band minimum (CBM) constituted from majority Pb 6p along with X 5p components, suggesting the predominant role of halide anion substitution tuning the bandgap through the modulation of the VBM [15] (Figure 1.3 A). This enabled the tunability of optical bandgap via simple halide substitution as in Figure 1.3 B and C, where the bandgap follows the trend I < Br < Cl. Though the A site cations do not contribute directly to the band structures, they influence indirectly the optical bandgap by altering the octahedral bond angles.[16,17] Theoretical studies demonstrated that the degree of octahedral tilting (X-B-X bond angle variation) changes the Pb 6p contribution to the CBM and finally changes the optical bandgap of HOIPs.[18] Moreover, the halide-*p* -to- metal-*p* band edge transition induces a high absorption coefficient compared to the *p* -to- *s* band edge transition in GaAs system as in Figure 1.3 D, allowing HOIPs to absorb more light and produce higher photocurrent output from submicron thick films.[19]

Unlike many other semiconductor materials, HOIPs possess antibonding nature in both the VBM and CBM levels. Strong antibonding coupling between Pb 6s and I 5p orbitals expands the VBM bandwidth and the point defects were brought close to the VBM edge and form non-detrimental shallow defects (Figure 1.3 E). However, on the other hand, in other semiconductors with antibonding and bonding characters in VBM and CBM levels, the point defects formed by vacancies lead to deep defects within the bandgap, which acts as the origin of non-radiative recombination. The formation of shallow defects instead of deep trap states in HOIPs is suggested as the defect tolerance property.[20,21]

In addition, the inorganic semiconductors require high-temperature processing and high-purity precursors for optimal optoelectronic properties, whereas the HOIPs deliver similar properties through inexpensive wet-chemistry and low-temperature processes.

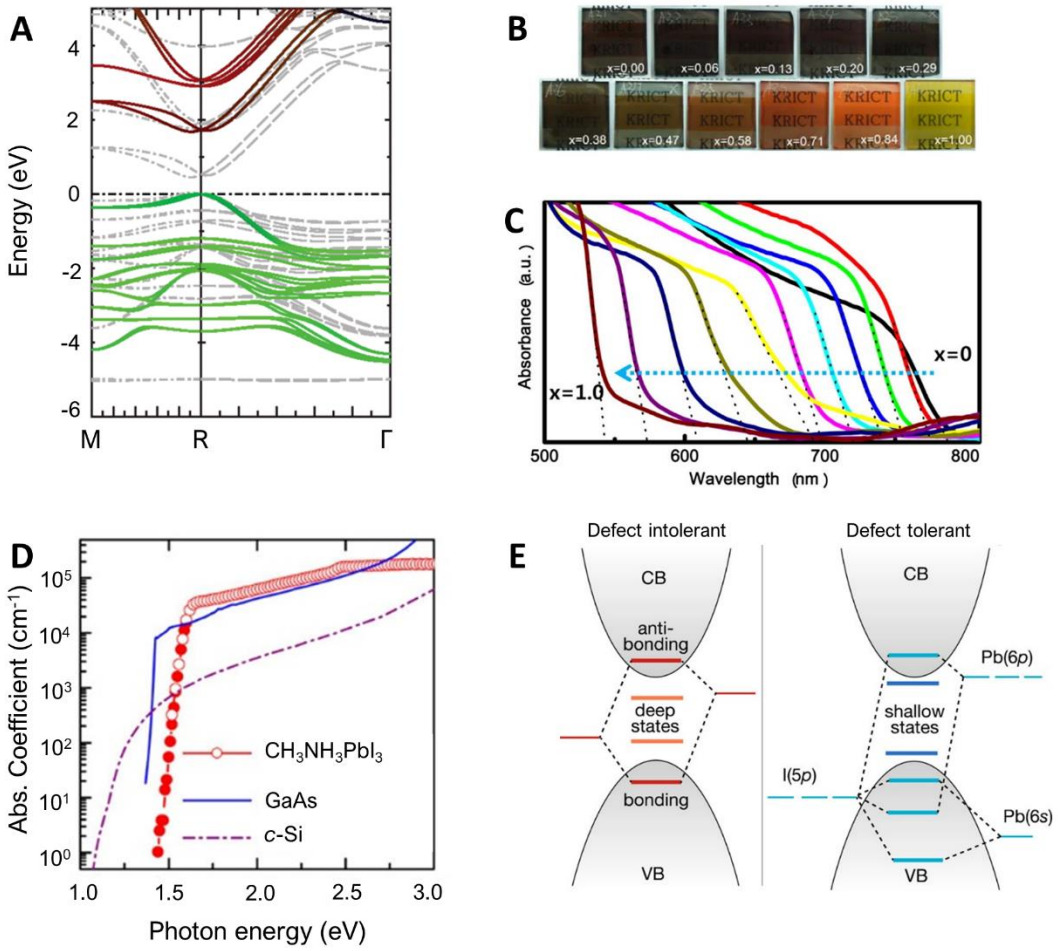

Figure 1. 3 (A) The calculated electronic band structure of $MAPbI_3$ from Quasiparticle Self-Consistent GW formalism. In the plot, the green, red, and blue lines represent the orbital contributions of I 5p, Pb 6p, and Pb 6s, respectively. Reprinted with permission from Ref [15]. (B) digital image and (C) PL spectra of $MAPb(I_{1-x}Br_x)_3$ perovskite thin films with varying halide composition demonstrating halide dependent optical bandgap for HOIP. Reproduced with permission from Ref.[16]. (D) Absorption coefficients over photon energy for $MAPbI_3$, GaAs, and single crystal silicon semiconductors. Reproduced with permission from Ref.[19]. (E) Electronic band structures of the typical defect-intolerant semiconductor (left) and the defect-tolerant $MAPbI_3$ perovskite (right). Reproduced with permission from Ref.[20].

1.4 Applications of 3D HOIPs

Thanks to the exceptional structural, optical, electronic, and defect properties, HOIPs found applications in solar cells, light emitting diodes,[22,23] photodetectors,[24] lasers,[25] X-ray imaging,[26,27] memory devices,[28,29] sensors,[30,31] energy storage devices,[32] water splitting,[33] radiation detection,[34,35] thermoelectric devices,[36] optical filters[37] and biomedical imaging applications.[38]

1.5 Photovoltaic devices

Solar energy has been identified as one of the most equitably distributed energy resources in the world, due to its availability in every location, and is intermittent, unlike coal and other energy sources. It addresses the exponentially growing global energy demand due to rapid urbanisation and advancements in the field of technology. Apart from the non-renewability and paucity of widely dependent fossil fuels, oils, gases, and coal sources, their inverse implications on the global climate and human livelihood emerged as the single biggest zeal for the progression from non-renewable to renewable green energy sources.

As a potential contender, the sun delivers about 174,000 TW of energy to the upper level of the earth's atmosphere at an average power density of 1366 W m^{-2}, which is a vast amount of energy that could meet the world's energy demands. However, this value is reduced to a global-average solar irradiance over the land of 183 W m^{-2} due to atmospheric absorption and scattering, as well as latitude-dependent oblique incidence, seasonal variation, diurnal variation, and cloud cover.[39] Moreover, over these decades, solar harvesting or photovoltaic technologies evolved as the popular alternative despite the fluctuations in solar energy availability. As of 2019, photovoltaics accounted for 3.1% of global electricity production, according to analysis by the International Energy Agency (IEA) in 2022. However, the potential of solar power as a major power source is enormous, with projections indicating it could reach 10% of global electricity production by the year 2050.[40] The critical challenge would lie in the efficient and sustainable transformation of solar energy into electricity and it highlights the surge in demand for novel PV technologies.

1.5.1 Working principles of photovoltaics

The photovoltaic effect reported by Alexandre Becquerel in 1839 is the fundamental principle behind the conversion of sunlight to electricity.[41] Briefly, when a p-n junction is formed by bringing p-type and n-type semiconductors in close contact, an electric field is formed near the junction by the movement of electrons and holes to the opposite sides to form a depletion zone with a thermal equilibrium at the p-n junction as depicted in Figure 1.4 A. On light irradiation on the semiconductor, the photon energy is transferred to the atoms of the semiconducting material and generates electron-hole pairs (also known as excitons). The electron-hole pair generated within and close to the depletion region can

be separated and migrate to opposite terminals to generate electrical power as represented in Figure 1.4 B.[42]

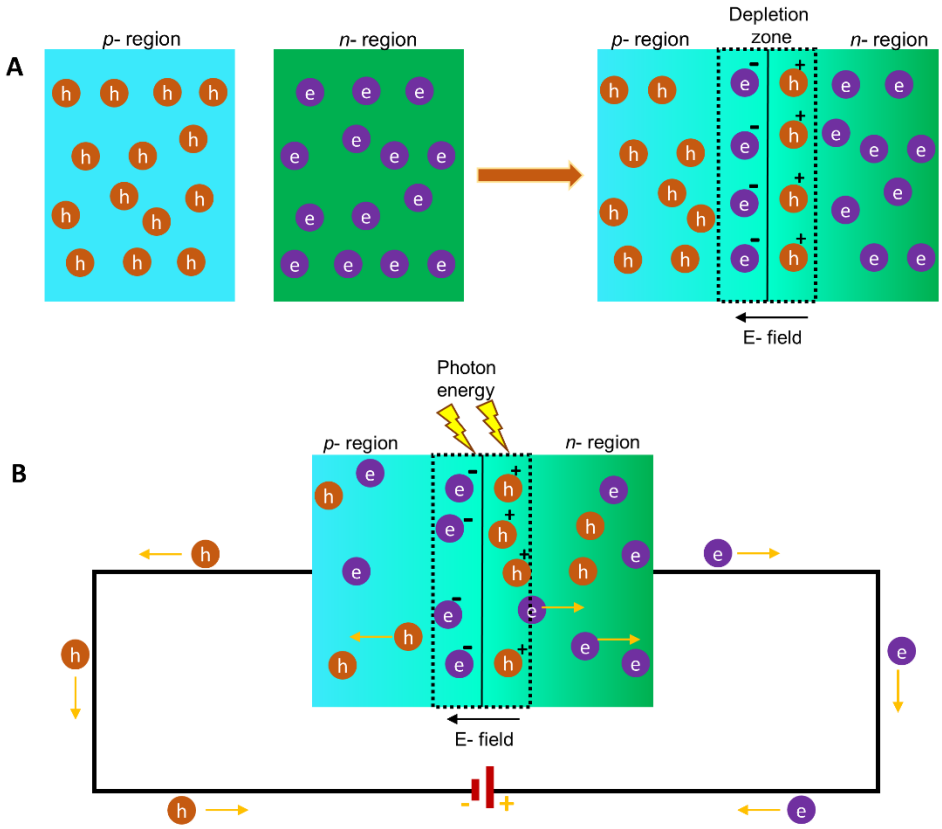

Figure 1. 4 (A) Schematic illustration of majority carrier diffusion and the creation of a depletion zone at a *p-n* junction. The Figure depicts the *p*-type region, depletion zone, and *n*-type region. Through the process of diffusion, the majority of carriers (electrons in the n-type region and holes in the p-type region) migrate across the junction, resulting in the formation of the depletion zone. (B) Schematic diagram demonstrating the photovoltaic effect.

1.5.2 Types of PV Technologies

Categorically, three main generations of solar cells can be identified, where each generation employs different materials and designs to convert light energy to electricity. The first-generation solar cell is made up of crystalline silicon (c-Si) as light-absorbing material and is the most common commercially available solar cell with an average efficiency of 15-22%.[43] However, their high manufacturing cost and complexity are identified as the major limitation. Next, the thin film materials like amorphous silicon (a-Si) cadmium telluride (CdTe) and copper indium gallium selenide (CIGS) evolved as the alternative light absorber and the new subgroup categorized as second-generation solar cells.[44] Though emerged as cost-effective compared to the c-Si solar cells but displayed

a lower efficiency and costly materials. The third-generation solar cells include dye-sensitized cells, multi-junction cells, organic photovoltaics, quantum-dot based solar cells, and recently emerged perovskite solar cells (PSCs).[45,46]

1.6 Perovskite Solar cells

It was back in 2006 when Miyasaka and co-workers utilised the methylammonium lead tribromide ($CH_3NH_3PbBr_3$) perovskite for the first time as a sensitizer in a dye-sensitized solar cell and achieved the light-to-electricity conversion efficiency of 2.2%. In 2009, they increased the efficiency to 3.8% using the iodide counterpart of $CH_3NH_3PbBr_3$ in the system.[47] Despite lower efficiencies achieved in DSSC using HOIP as a sensitizer, significant advancements have been made through introducing solid-state hole conductor in perovskite solar cells in breakthrough reports published in 2012-13,[48-50] which displayed a sharp spike with the efficiency from 3.8 to 10-12%. With the consistent focus and rapid advancements in material engineering and device designing pathways, PSCs witnessed an unprecedented efficiency boost from 12% to over 26% nearly in a decade.[45]

1.6.1 Device architectures

A PSC comprises of a transparent conductive oxide (TCO) coated glass and metal electrode as the charge collector, perovskite as the light absorber, and hole and electron selective layers as efficient charge extractors. Depending on the arrangement of different thin film stacks, PSCs are classified into two types, namely *n-i-p*, and *p-i-n*. *n*, *p*, here *i* indicates electron selective layer, hole selective layer, and perovskite absorber layer respectively. $n - i - p$ device architecture is further sub-classified to planar and mesoporous configuration while the $p - i - n$ configuration is commonly popular as inverted planar configuration, (Figure 1.5 A-C).[51] Upon light irradiation, electron-hole pair is created in the absorber layer, which dissociates and transports to their respective charge-selective layers, i.e., the electrons travel to the electron transport layer (ETL), while the positive charge (holes) travel to the hole transporting layer (HTL); thus collected charge carriers at the transparent electrode and metal electrode generates photocurrent at the outer circuit, (Figure 1.5 D).[51]

1.6.1.1 Transparent conductive oxide

In PSCs, the primary challenge is the selection of an optimal TCO with outstanding transparency and conductivity, which allows as many photons as possible to reach the

perovskite layer through adjacent stacks. To address various energy losses and stability concerns, further considerations including i) band energy alignment with the neighboring layer to maximise the charge carrier transport, ii) material and processing compatibility with other layers, iii) high chemical stability, and iv) low-cost fabrication has been identified for an ideal TCO. To meet these requirements, TCOs including Indium Tin Oxide (ITO), Fluorine-doped Tin Oxide (FTO), Zinc Oxide (ZnO), and Aluminium-doped Zinc Oxide (AZO) are widely employed in PSCs.[52,53]

1.6.1.2 Electron transporting materials

The fundamental role of an ideal ETL is to extract electronic charge carriers from the perovskite absorber and transport them to the respective electron collecting electrode with minimal leakage. In real conditions, the potential ETL should satisfy a set of prerequisites to achieve high device performance. Firstly, the ETL should cater a cascading energy level, where the lowest unoccupied molecular orbital (LUMO) level situates between perovskite and electron collecting electrode layers, ensuring seamless energy transfer. Next, the highest occupied molecular orbital (HOMO) level of the ETL must be sufficiently deep to hinder the hole transport and minimize exciton recombination. Here, the quality of the ETL layer, such as its transparency, pinhole-free, and chemical resistance nature, also contributes to the device's performance.[54]

Metal oxide semiconductors such as titanium dioxide (TiO_2), zinc oxide (ZnO), tin (IV) oxide (SnO_2), tungsten (IV) oxide (WO_3), niobium pentoxide (Nb_2O_5) and zinc stannate (Zn_2SnO_4); Metal sulfide/selenide semiconductor namely cadmium selenide (CdSe), zinc sulfide (ZnS), and molybdenum disulfide (MoS_2);[55,56] Organic semiconductors particularly [6,6]-phenyl-C_{61}-butyric acid methyl ester (PCBM), buckminsterfullerene (C_{60}) and other fullerene derivatives are the prominent ETL materials currently employed in PSC architectures.[57] Due to the higher bandgap and chemical resistance properties, TiO_2 has been widely used in the past for *n – i – p* configuration. However, considering the high-temperature necessity and time-consuming process of TiO_2, the SnO_2 layer with moderate temperature processability, deep conduction band, and high electron mobility gaining momentum in recent years.[58,59] Conversely organic semiconductor materials were employed as the ETL in *p – i – n* configured PSCs.

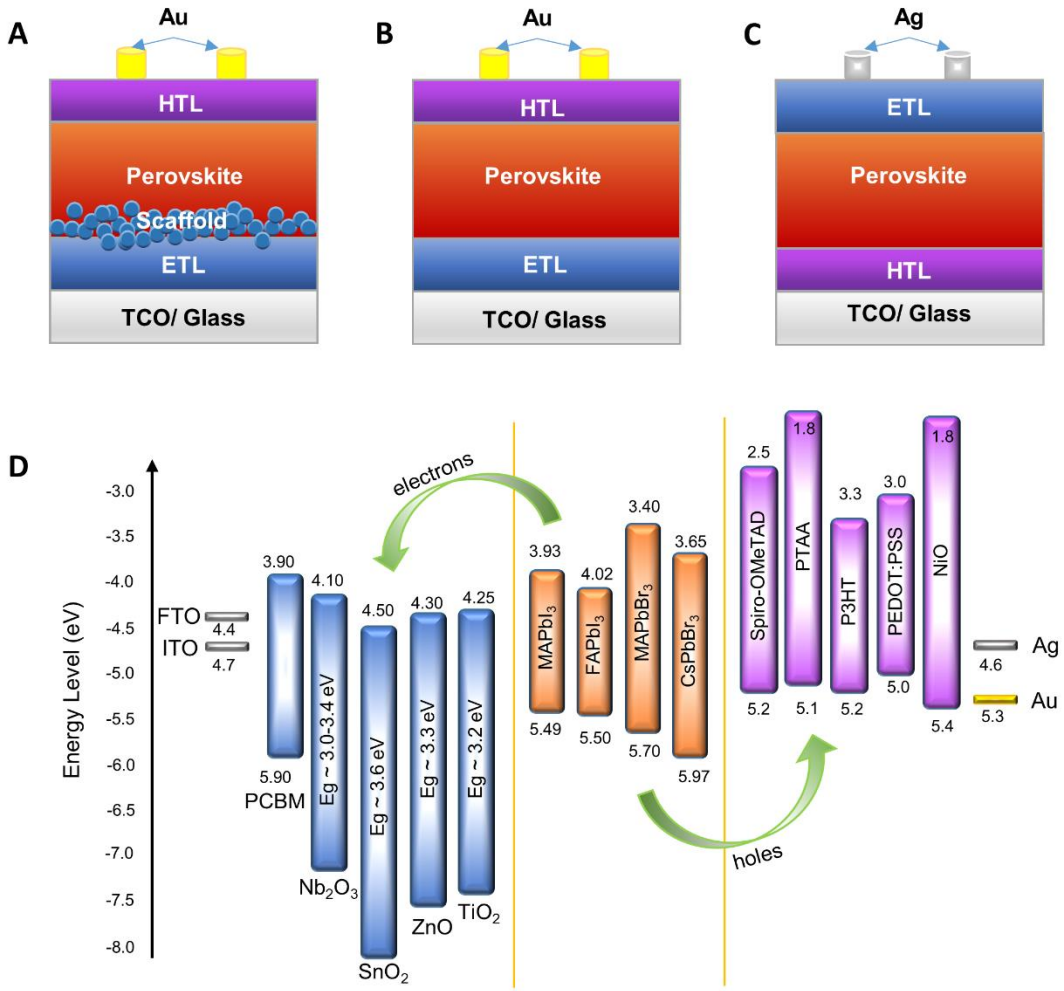

Figure 1. 5 (A-C) Schematic representation of PSC device architectures, (A) *n- i- p* mesoporous, (B) *n- i- p* planar, and (C) *p- i- n* inverted planar. (D) Energy level diagram of the materials used in PSCs.

1.6.1.3 Hole transporting materials

Akin to the ETL, an ideal HTL is also bound to satisfy some general requirements including i) suitable energy-level alignment ensuring the easy passage for holes from perovskite absorber to hole collecting electrode while blocking the electron transport through the materials, ii) high-quality thin film formation and iii) good solubility in common solvents specifically which does not interact with perovskite layer and excellent stability against the moisture, air, optical, chemical and thermal stresses, particularly in the case of *n – i – p* system.[60]

Despite the vast efforts made over the years, doped Spiro-OMeTAD [2,2′,7,7′-tetrakis(N,N-di-p-methoxyphenylamine)-9,9′-spirobifluorene] remains the most favoured candidate among the community for high-performance PSCs in *n – i – p*

configuration. Besides various conjugated polymers like PTAA [poly(triaryl amine)] and P3HT [poly(3-hexylthiophene-2,5-diyl)] have also been employed as the HTL mainly owing to their hydrophobic nature. On the contrary, polymeric materials such as PEDOT:PSS [poly (3,4-ethylenedioxythiophene): polystyrene sulfonate]; inorganic materials such as NiOx, CuS, CuCrO2, MoOx, CuOx, CuI, Ta-WOx, and CuSCN; and new generation transition metal dichalcogenides and Mxene materials were mainly utilized for HTL in *p – i – n* architectures.[61]

1.7 Recent developments in perovskite solar cells

As discussed above in section 1.6, perovskite solar cell research skyrocketed in terms of PCE, stability, scalability etc. in the past 15 years.

1.7.1 Pros and cons of methylammonium-rich perovskite absorbers

Historically, the $MAPbI_3$ is the first ever-developed HOIP material for photovoltaic applications. With the MA as the A-site cation with a 217 pm ionic radius, $MAPbI_3$ with a tolerance factor of 0.91 crystallizes into a tetragonal perovskite structure with optical bandgap around 1.55 eV.[62] Additionally, the calculated lower effective masses for both holes (0.25 m_h) and electrons (0.19 m_e) corroborate their higher charge carrier mobility (1−70 cm^2/ V s) in polycrystalline thin films.[63] The continuous efforts on crystal growth and defect engineering enabled the fabrication of uniform high-quality $MAPbI_3$ thin films to achieve PCEs exceeding 20%. Considering the direct contributions of X-site halogen into the band edge states, octahedral factors, and electronegativity or the bond-length with Pb^{2+} cation of perovskite materials, the partial substitution of I^- with Br^- and/or Cl^- was, therefore, employed to tune the optoelectronic, structural properties and stability of $MAPbI_3$ perovskite layer. In addition to the mixed halide composition route, a well-strategized mixed-A site cation combination has been introduced, where the MA cation co-exists with cations with similar ionic radii such as formamidinium (FA), cesium (Cs) and rubidium (Rb), and the corresponding PSCs displayed higher certified PCEs over 22% along with improved long-term stability.[51,14] However, despite the emergence of MA-based perovskite absorbers as the potential candidate for PV applications, some critical stability concerns are hindering their commercialization. For a commercial PV module, it is necessary to withstand stringent yardsticks such as high relative humidity,

light illumination including the UV part of the spectrum, and electric and gradient thermal stress.

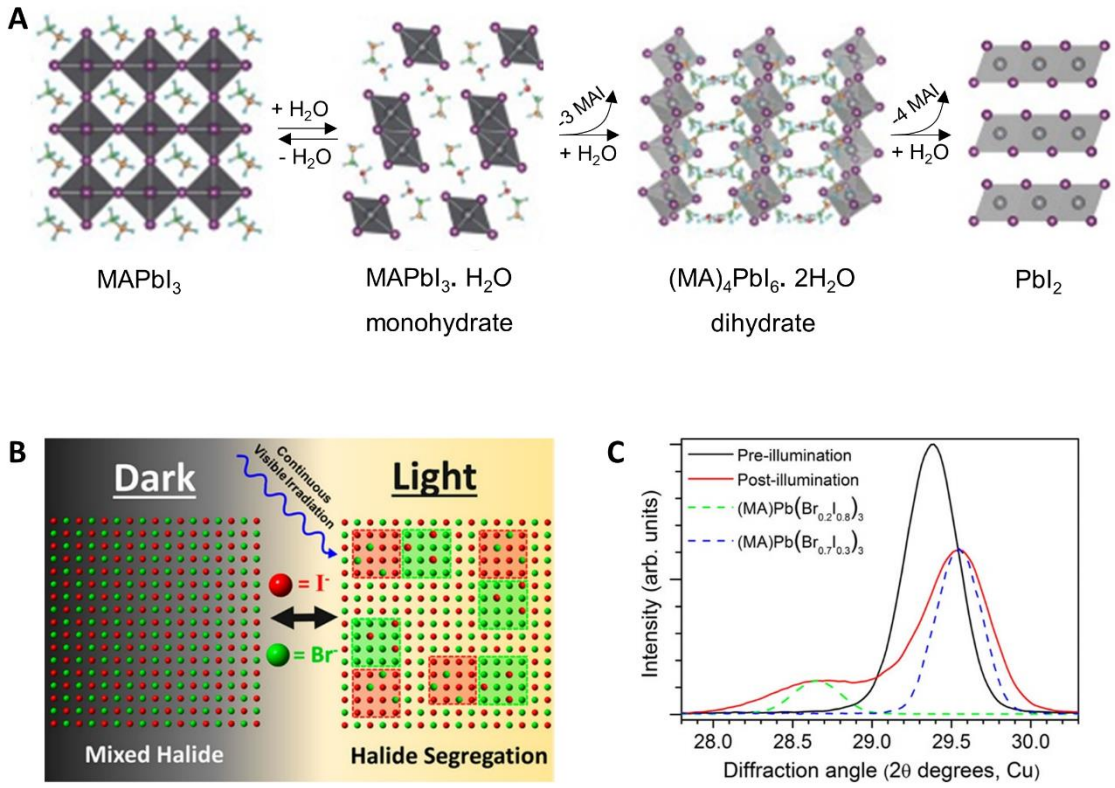

Figure 1. 6 (A) Humidity induced phase transition (degradation) of $MAPbI_3$ system. Reproduced with permission from Ref.[64]. (B) Schematic representation of halide segregation under light irradiation on mix-perovskites. Reproduced with permission from Ref.[70]. (C) PXRD patterns of a $MAPb(I_{0.4}Br_{0.6})_3$ thin film (200) Bragg reflection before (unbroken black line) and after (unbroken red line) 300 seconds of illumination. Broken green (x = 0.2) and blue (x = 0.7) lines represent individual $MAPb(I_{1-x}Br_x)_3$ thin film (200) reflections. The change in the PXRD reflection indicates the photoinduced phase segregation in mix-perovskites. Reproduced with permission from Ref.[71].

The thermal and humidity stresses are highly critical for MA-based perovskites. Primarily, humidity attack on the $MAPbI_3$ layer generates secondary hydrated products such as monohydrated $MAPbI_3.H_2O$ at lower moisture ingression and dehydrated $(MA)_4PbI_6.2H_2O$ at intense moisture ingression and finally, it converts to PbI_2 and other volatile compounds,[64] Figure 1.6 A. At elevated temperatures around 54 - 57 ºC, MA-rich perovskite materials undergo a phase transition from tetragonal to a cubic or pseudo-cubic phase, and the re-orientation nature of MA cation further weakens their bonding with the PbX_6 octahedra. This easy volatilization of MA cation leads to the fast degradation of perovskite materials under thermal stress.[65-67] On the other side, the light

illumination can also induce degradation both in perovskite as well as in the device stacks. Various studies reported the UV-light sensitized degradation of the mesoporous TiO_2 layer and further photo-activated TiO_2 mediated perovskite degradation.[68,69] Most importantly, the highly promising MA-based perovskite with mixed-halide composition shows a notorious phase segregation into low-band-gap-I-rich and high-band-gap-Br-rich domains as depicted in Figure 1.6 B and C under illumination eventually leading to degradation for corresponding PSCs.[70,71]

1.7.2 Emergence and Challenges of $FAPbI_3$

1.7.2. 1 Optoelectronic properties

In 2014, Baikie and co-workers introduced a perovskite with a broader absorption spectrum and improved thermal stability than the MA-rich counterpart, Figure 1.7 A and B.[62,72,73] The replacement of the MA cation by a larger Formamidinium (FA) cation with an ionic radius of 253 pm maintained the ABX_3 symmetry with a higher *t* value (~1.04) eventually reducing the band-gap to ~1.47 eV which is closer to the optimum value of ~1.4 eV. Along with the reduced optical bandgap, a longer charge carrier diffusion length and lifetime was displayed by the $FAPbI_3$ than the former $MAPbI_3$.[62] Figure 1.7 C depicts the theoretical Shockley-Queisser (SQ) limit efficiency of various PV materials calculated based on bandgap values, and the SQ limit efficiency is expected to be around ~33% for those light-harvesting materials with bandgap values lies in the range of 1.1-1.45 eV.[74] Capitalizing these factors Snaith et al. reported a champion PCE of 14.2% and suggested $FAPbI_3$ as the future alternative for the degradation prone $MAPbI_3$.[75]

1.7.2.2 Polymorphism in $FAPbI_3$

Despite the superior optoelectronic properties over the MA-counterpart, $FAPbI_3$ struggles due to its inherent temperature-dependent polymorphism. Typically, $FAPbI_3$ structures have different polymorphs such as α-phase (cubic), β-phase (tetragonal), γ-phase (orthorhombic), and δ-phase (hexagonal), where α-, β- and γ-structures comes with a photoactive black phase. On the contrary, the δ-phase corresponds to a photo-inactive non-perovskite yellow phase. Among the three photoactive phases, the α-phase stabilizes at a temperature range of 150 to 180 °C whereas the other two photoactive polymorphs, β- and γ-phases form at a relatively lower temperature of -122 and -182 °C, respectively.[76,77] However, the photoactive α-phase is not thermodynamically stable at room temperature where it slowly transforms to non-perovskite δ-phase owing to the anisotropic strain relaxation associated to the larger *t* value,[78,79] Figure 1.7 D. This

inherent unfavourable phase transition accelerates further in the presence of humidity, which again boost the degradation rate of the $FAPbI_3$ and corresponding PSCs.

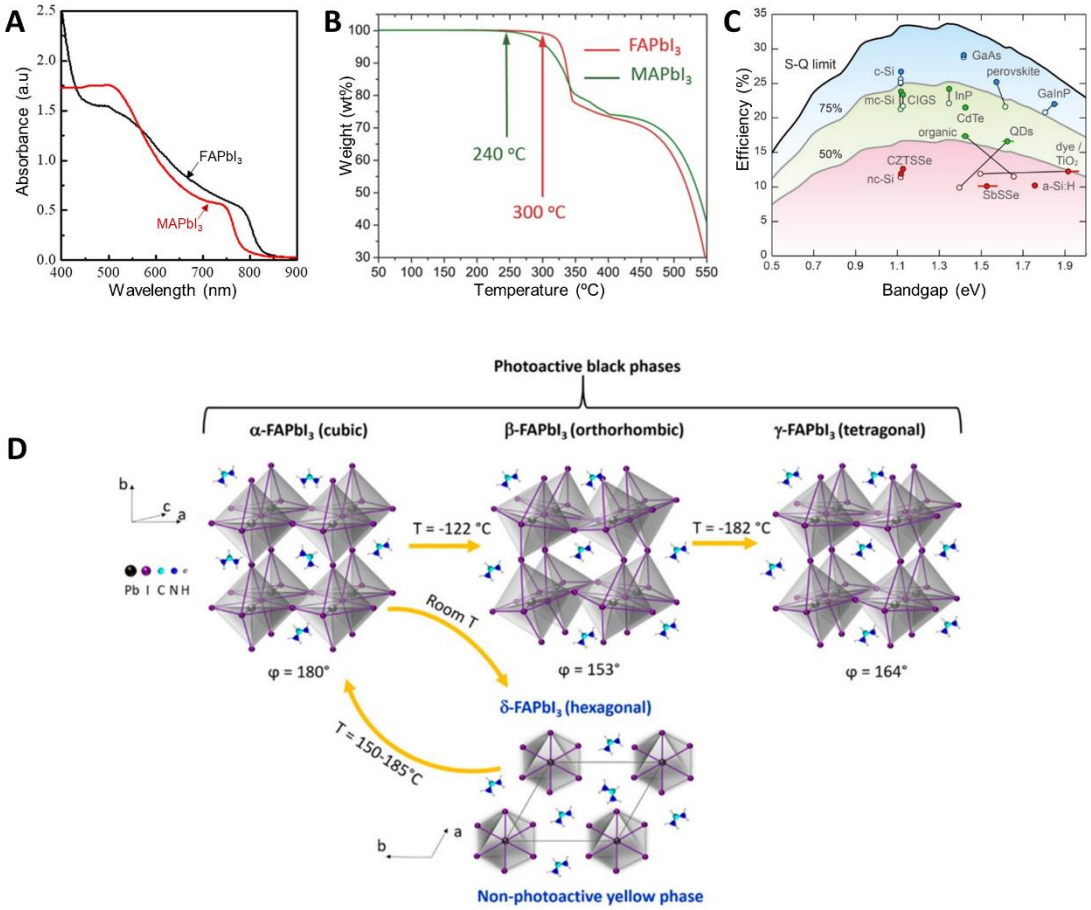

Figure 1. 7 (A) UV-Vis absorption of $MAPbI_3$ and $FAPbI_3$ thin films. Reproduced with permission from Ref.[62]. (B) Thermogravimetric analysis of $MAPbI_3$ and $FAPbI_3$ perovskites. Reproduced with permission from Ref.[73]. (C) Calculated theoretical Shockley-Queisser (SQ) limit efficiency of various PVs based on the bandgap of the light absorber materials. Reproduced with permission from Ref.[74]. (D) Polymorphic phases and phase transition in $FAPbI_3$ perovskites. Reproduced with permission from Ref.[79].

(Section 1.7.2.3 has been published in *Physical Chemistry Chemical Physics* journal entitled: ¨Substance and shadow of formamidinium lead triiodide based solar cells¨.

Muhammed P. U. Haris, Samrana Kazim, Meenakshi Pegu, M. Deepa and Shahzada Ahmad.

M. P. U. Haris et al. *Phys. Chem. Chem. Phys.*, 2021, 23, 9049, DOI: 10.1039/d1cp00552a)

1.7.2.3 Current strategies to mitigate instability of $FAPbI_3$

1.7.2.3.1 Compositional and Dimensional Engineering:

Compositional engineering of 'A', 'X', and 'B' sites in ABX_3 is an effective pathway to improve the physical and structural properties without significantly altering the optoelectronic properties. Partial substitution by MA, Cs, Rb, Br, and Cl in $FAPbI_3$ or their combinations are well explored and yield performance and stability enhancement in devices.[80-82] Partial doping with smaller cations such as MA, Cs, and Rb was demonstrated to lower the tolerance factor from 1.04 to the ideal range.[72,83] Initial reports with MA doping formed stable $FAPbI_3$ without any phase segregation at room temperature, where, Bein et al. attributed the stabilisation of $FA_xMA_{1-x}PbI_3$ to the higher dipole moment magnitude of MA which creates stronger hydrogen bond interaction with the inorganic cage and optimised the MA content to <20% of FA.[84] Though the MA content improved the phase stability and the efficiency of $FAPbI_3$, the chemical instability of MA cation due to its photo- and thermal sensitivity hindered its employment in PSCs. Akin to $MAPbI_3$, the formation of volatile methylamine through the reversible acid-base decomposition induced the deprotonation of MA cations which is reported in MA doped FAPbI3.[85,86] The ^{1}H NMR studies on precursor solutions (Figure 1.8 A-C) demonstrated that only a small amount of volatile methylamine leaves the system and the remainder immediately condensates with formamidinium iodide (FAI) to form the unwanted N-methyl FAI and *N*,*N*-dimethyl FAI. Figure 1.8 C clearly shows the gradual increase in the N-methyl FAI upon aging of the precursor solution.[85] By capitalizing the reported knowledge on the compositional engineering of $MAPbI_3$, Cs, K or Rb amalgamated $FAPbI_3$ along with the Br or Cl doping delivered improved device performances at the expense of higher bandgap though the device long-term stability under harsh testing conditions remains untouched. The enhanced photo- and moisture-stabilities demonstrated by Park et al., through smaller Cs amalgamation into $FAPbI_3$ opened a new pathway whereby they demonstrated the contraction of cubo-octahedral volume (Figure 1.9 A) and a reduction of trap density (Figure 1.9 B) by an order of magnitude thus increasing the open circuit voltage (V_{OC}) and the fill factor (FF), leading to PCE and stability hike.[87]

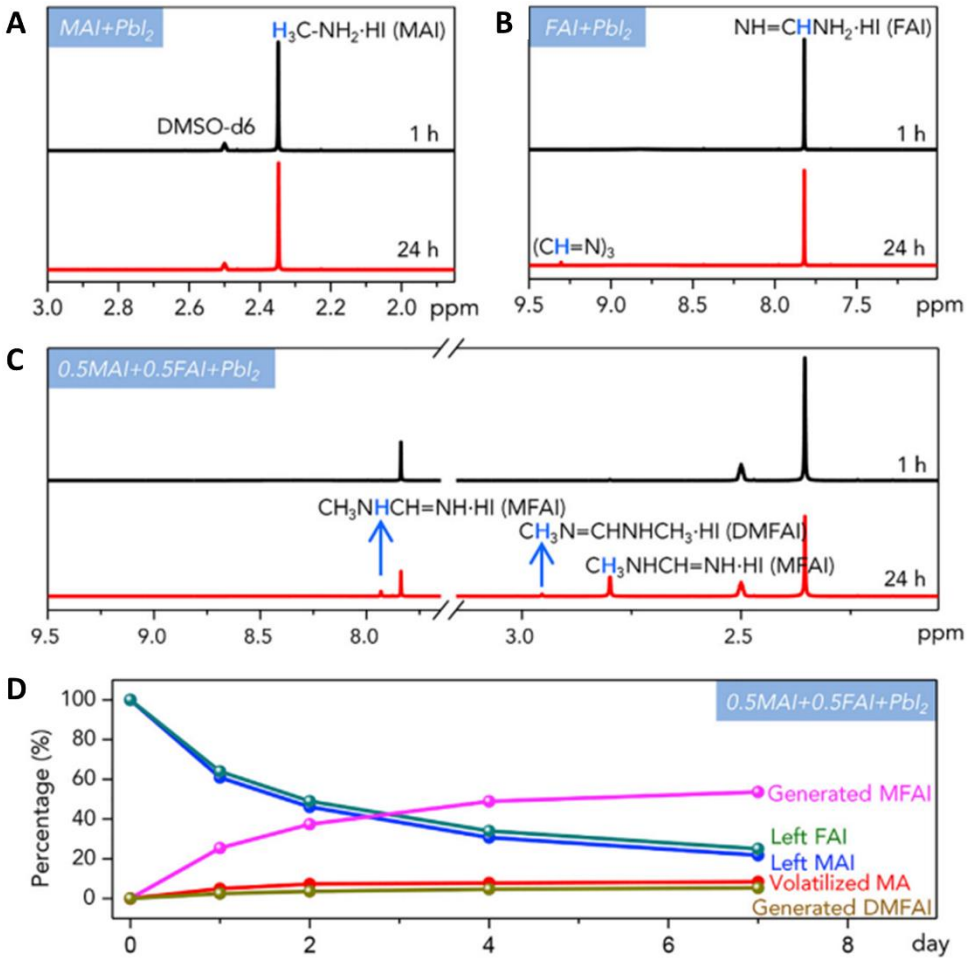

Figure 1. 8 (A-C) 1H NMR spectra of different perovskite precursor solutions with aging and D) compositional evaluation from 1H NMR data. Reproduced with permission (A-D) from Ref.[85]

The inclusion of Cs motivated researchers to expand the cationic dopant pool with Rb and K, and although it improves the device performance marginally, only Cs displayed structural incorporation.[88] Various methodologies were adopted for Cs amalgamation and >20% of PCEs were reported.[89] The understanding of mechanisms and dynamics with Cs inclusion is of significant interest. The microscopic understanding of the structural energy landscape revealed that higher entropy contribution from an organic cation reduces the Gibbs free energy thereby assisting in circumventing phase transitions. FA cation in $FAPbI_3$ was reported to have an isotropic orientation with a large entropy at higher temperatures and upon cooling to room temperature it adopts a strong preferential orientation with a lower entropy.[90] The entropy enhancement and reduction of annealing temperature upon Cs inclusion which was optimized over a range of 3% - 20% to balance the bandgap widening and the increase of density of states (DOS) below the VBM.[91] In

addition to the phase stability, different imaging or mapping techniques such as Synchrotron-based nanoscale X-ray fluorescence (n-XRF),[92] PL, hyperspectral imaging[93] showed that inorganic Cs doping homogenizes the halide distribution between Cl, I, and Br and reduces the heterogeneity in the charge carrier dynamics[93,94] which eventually highlighted the ability of the triple-cation-mixed halide perovskites to function as capable light harvesters. The addition of dopants as additives in the precursor solution, a non-uniform distribution at perovskite surface and bulk has been reported in thin films which significantly affects the structural, optoelectronic, and device properties.[95,96] The dopant impacts at the grain and grain boundaries have been studied for device improvements, understanding dopant distribution and the effects at $FAPbI_3$ surface and bulk will be of paramount importance for future optimisation.

Moreover, the intrinsic lattice strain, which stems from the twisting and tilting of the PbI_6 octahedra and lattice expansion or contraction, is detrimental to the successful working of PSCs. The A or X site doping stabilizes the α-$FAPbI_3$ phase at the expense of lattice expansion or contraction which eventually generates the residual strain and influences the optoelectronic properties. Although strain engineering was initially reported for low dimensional and $MAPbI_3$ perovskites, Kim et al., reported a strain relaxation strategy of using smaller and larger cations together as dopants to reduce tensile strain and comprehensive strain in the $FAPbI_3$ lattice.[97] The grazing-incidence wide-angle X-ray scattering (GIWAXS) patterns of $FAPbI_3$ modified with equal mole % of smaller (Cs) cation and larger (methylene diammonium) cation showed a reduction of lattice strain and trap density to deliver an unparalleled device PCE of 24.4% through prolonged carrier lifetime and reduced Urbach energy. Additionally, the non-encapsulated devices showed superior thermal stability of retaining >80% of the initial PCE after 1300 h of annealing at 85 ºC.[97] In addition to the single site doping, co-doping strategies have been introduced to relax the residual strain. The anisotropic strain on the (111) lattice plane of $FAPbI_3$ is reported as the driving force for the phase transition and a co-doping strategy where both the A and X sites get doped with comparatively smaller ions (MA+, Br-) which reduced the strain along (111) plane through lattice shrinkage as depicted in Figure 1.9 C.[98] The micro-strain (Figure 1.9 D) calculated from the Williamson−Hall plot where MABr alloying reduced the strain at the (111) lattice plane of α-$FAPbI_3$ where they found MA contributes more towards the phase stabilization. However, the current limitation to

obtaining a defect-free strained $FAPbI_3$ or defect rich $FAPbI_3$ without strain restricts the individual study of strain and defects and their relationships.

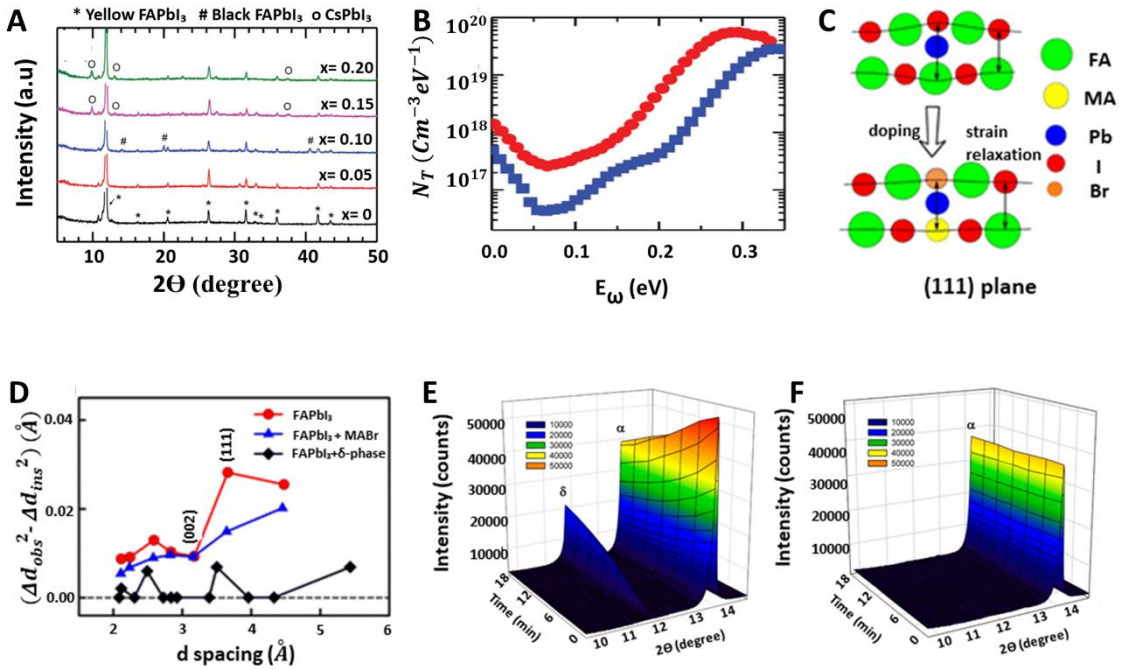

Figure 1. 9 (A) X-ray diffraction (XRD) patterns of the $FA_{1-x}Cs_xPbI_3$ films, (B) calculated trap density for $FAPbI_3$ (red) and $FA_{0.9}Cs_{0.1}PbI_3$ (blue) perovskite solar cells. (A,B) Reproduced with permission from Ref.[87] (C) schematic representation of strain relaxation of (111) plane after MABr alloying, (D) Williamson−Hall plot extracted from diffraction profiles and (E,F) Time-dependent XRD measurements of (E) $FAPbI_3$ with phase transition and (F) stabilized $FAPbI_3$-MABr without phase transition under a humid atmosphere with a RH of ~50% at 23 °C. (C-F) Reproduced with permission from Ref. [98]

The usage of long organic spacer cations will address partially the existing stability concerns in PSCs. The low dimensional/layered perovskites (in scientific literature also referred to as 2D or quasi 2D) derived from large organic spacers with high intrinsic and extrinsic structural as well as thermal stability will enhance the physico-chemical properties, whereas, its poor charge-transport properties owing to the large quantum well and narrow light absorption ability impede its development. Moreover, the 2D perovskite surface is known to increase the hydrophobicity and the contact angle measurements with water droplet has been used to probe the same. As depicted in Figure 1.10 A and B, layered $FAPbI_3$ perovskite film showed higher hydrophobicity than the pristine $FAPbI_3$ surface.[99] Apparently, the employment of alternate layers of layered (2D) and conventional (3D) i.e., 2D/3D hybrid perovskites was reported to align the interface in

order to maximize charge collection and transportation.[100-103] The approach of having a perpendicular orientation of the layered perovskites atop of 3D (conventional) perovskite to allow uni-directional charge transport and collection was adopted. This bilayer approach was optimized by structural and interfacial packaging control to maximize light harvesting and induced stability.[104] Researchers focussed on the tuning of opto-electrical and structural properties of the layered, bilayer, and layered passivation by manipulating the elemental composition, organic spacer, layer thickness, and crystallization routes of MA based system, and demonstrated reduced exciton binding energy, improved charge carrier dissociation and conductivity. FA cations with a low band gap were also employed in layered PSCs and a PCE of >19% was achieved.[105] Liu et al. showed the superior absorption ability of FA over MA that led to high photocurrent and PCE along with superior stability of the layered perovskite over the $FAPbI_3$ under harsh moisture and thermal testing conditions. In another report, Chen et al., compared the MA and FA based layered PSCs and the $(PDA)(FA)_3Pb_4I_{13}$ demonstrated superior stability. The authors annealed both the perovskite films at 150 ºC under N_2 and the digital images were compared as shown in Figure 1.10 C. $(PDA)(MA)_3Pb_4I_{13}$ films turned brown within 1 hour and gradually changed to a non-perovskite yellow phase after 3 hours while the FA counterpart showed exceptional stability until 12 hours of continuous thermal stress. Further, the corresponding PSCs were tested for thermal stability at 85 ºC under an N_2 atmosphere in the dark as shown in Figure 1.10 D.[106] The knowledge capitalization from the MA system, it is vital to focus more on the rational selection of organic spacer and crystallization routes to optimize the FA systems. To this end, the employment of an organic spacer with an electron-donating or an electron-withdrawing group or hetero-atoms can improve the charge transport. Another approach introduced was the functional donor groups on the cations to fine-tune the electrical properties of the layered perovskite. Such organic cations can actively participate in the energy band structure of the layered perovskite, in the charge-transfer processes, and subsequently contribute to the optimization of device performance. The incorporation of cations tailored for π–π stacking is imperative for improving charge-transport properties in low-dimensional perovskites.[107,108] Cations can be tailored to stabilize lead iodide based perovskites through stronger hydrogen bonding coupled with π–π stacking interactions. However, most of the reports on low-dimensional PSCs are restricted to MA cations while the FA cations have rarely been studied and much effort are needed to elucidate the charge carrier dynamics and thereby boost the PCE for future commercialisation.

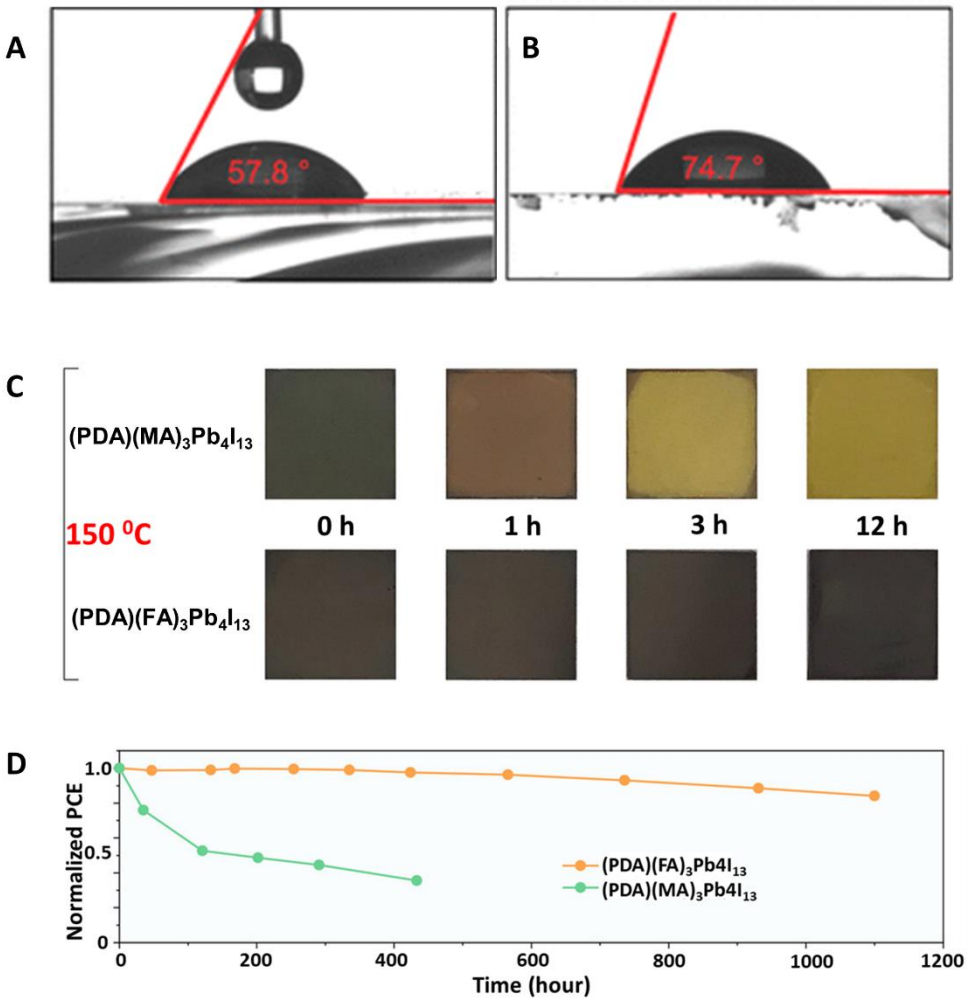

Figure 1. 10 (A, B) Contact angle measurements of the (A) $FAPbI_3$ and (B) $(PDMA)FA_2Pb_3I_{10}$ perovskite films with a water droplet. (A, B) Reproduced with permission from ref.[99] (C) Images of the $(PDA)(MA)_3Pb_4I_{13}$ and $(PDA)(FA)_3Pb_4I_{13}$ perovskite films taken at various intervals during annealing at 150 °C, (D) Thermal stability tests at 85 °C for corresponding solar cells. Reproduced with permission from Ref. [106]

1.7.2.3.2 Controlled crystallization:

Defects at the grain boundaries and surfaces of polycrystalline perovskite layers are sensitive to moisture and ion migration, these promote intrinsic as well as extrinsic instability of PSCs under operando conditions. Any methodology to decrease the super-saturation of perovskite solution by increasing the precursor-solvent interaction will limit the nucleation rate and thereby control the defects at grain boundaries. The use of oxygen-, sulphur- and nitrogen-donor Lewis bases/acids with high dipole moment is a well-explored methodology to increase the molecular interactions and the nucleation energy

barrier to slow down the crystallization.[109-111] The choice of non-volatile additives induces uniform layer formation by residing at grain boundaries and passivating charged point defects. In recent years, ionic liquids (ILs) have been employed as non-volatile additives due to high hydrophobicity, high surface tension properties, low-toxicity, and excellent electrochemical properties and among them, the imidazolium based ILs are preferred owing to their high ionic-conductivity.[112-117] Enhancement in the PCE of $FAPbI_3$ from 17.1 to 20.06% with a 1-hexyl-3-methylimidazolium iodide (HMII) additive was reported. HMII addition improved the carrier lifetime from 229 ns to 1382 ns along with an increase in the PL emission suggesting the reduced non-radiative recombination and authors attributed this to the passivation of vacancies through ionic interactions of HMII.[116] Improved crystallinity and phase purity were observed from morphological and structural analysis. The low trap density of the modified device calculated from space charge limit current (SCLC) measurements supported the crystallinity improvements and reduced non-radiative recombination, which resulted in higher V_{OC} and photocurrent. Moreover, HMII enhanced the stability and the device retained 85% of its initial PCE after 250 hours of maximum power point tracking (MPPT) under the ISOS-L-1 protocol. A polymerized ionic liquid (PIL) in a PSC achieved a PCE of 21.4% and excellent long-term operational stability of maintaining 92% of its initial PCE after 1200 hours under 1 sun illumination at 70-75 ºC.[118] The synthesized PIL (Figure 1.11 A and B) containing multi-anchoring sites form high-quality films with large grains. The authors reported that the PIL species were immobilized at the grain boundaries and passivate the under-coordinated Pb ion defects, which eventually resulted in excellent stability under harsh conditions. Though the role of the alkyl chain on the imidazole ring has been well studied, the understandings of the effects of the anionic part and the interactions with $FAPbI_3$ require further investigation. The spin coating method followed by an anti-solvent dripping and high temperature (150 ºC) annealing is the way to fabricate high quality $FAPbI_3$ layers. The higher thermal expansion coefficient of $FAPbI_3$ over the substrate and the temperature gradient between the bottom and top surface of the $FAPbI_3$ layer upon annealing will induce large residual strain.[119,120]

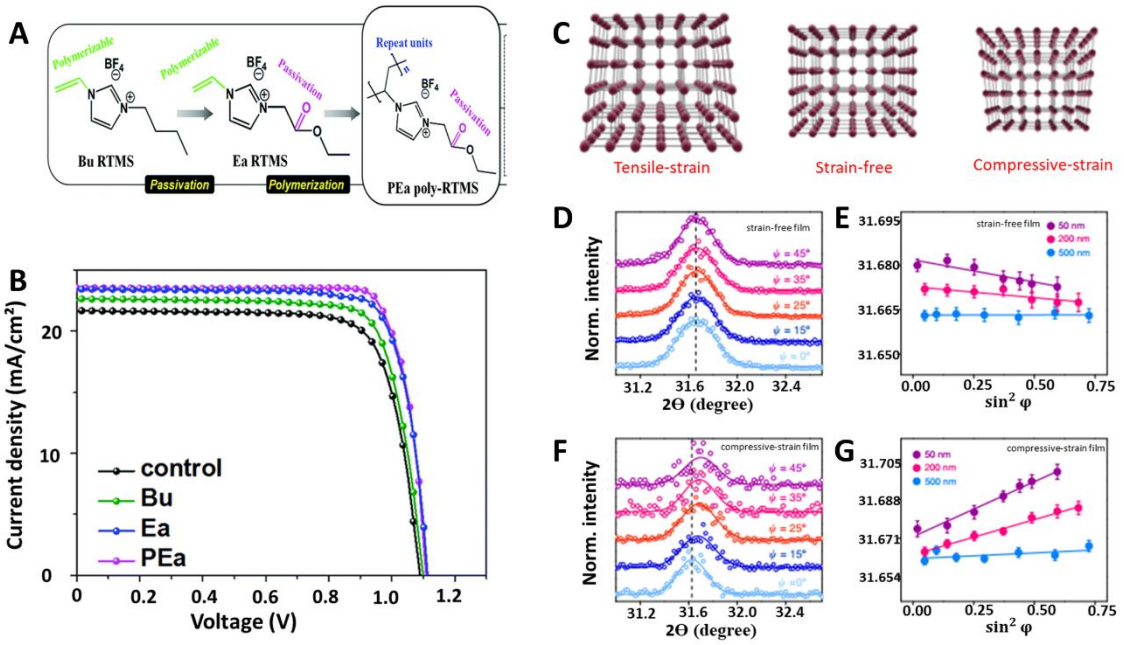

Figure 1. 11 (A) Schematic representation of ILs and PIL, (B) J-V characteristics of devices with modified perovskite absorbers. (A, B) Reproduced with permission from Ref. [118] (C) Schematic representation of different strain state at the perovskite surface, (D, F) GIXRD spectrum at different tilt angles at the depth of 50 nm for the strain-free film and the compressive strained film. (E, G) Residual strain distribution at depths of 50, 200, and 500 nm for the strain-free film, compressively strained film (measured (points) and Gauss fitted (line) diffraction strain data as a function of Sin 2θ). The error bar indicates a standard deviation of 2θ. (C-G) Reproduced with permission from Ref.[121].

The faster annealing or expansion at the bottom surface and faster cooling from the top surface of $FAPbI_3$ due to temperature gradient leads to tensile strain on the surface and comprehensive strain in the bulk (Figure 1.11 C).[121] Moreover, the thermal coefficient gradient between the perovskite and the substrate induces an additional tensile strain to the bulk eventually leading to a gradient residual strain in the perovskite layer to affect the optoelectronic properties. A novel strategy to minimize the gradient residual tensile strain of the perovskite layer by a flipping method, where the spun-coated perovskite film was annealed from the perovskite surface instead of the substrate surface, has been introduced.[121] The residual strain distribution was calculated from GIXRD measurement as depicted in Figure 1.11 D and F for pristine and flipped thin films, respectively, where a smaller strain gradient was visible for the film fabricated through the flipping method. The detailed analysis of strain distribution across the film thickness showed a homogeneous lattice parameter for the flipped film and a vertical gradient lattice structure for the pristine film as depicted in Figure 1.11 G and E, respectively. To this end, it is

crucial to design effective strategies to reduce the annealing temperature of $FAPbI_3$ film and to introduce new substrate materials with thermal coefficients similar to that of $FAPbI_3$, which could synergically lower the temperature and strain gradients throughout the perovskite layer.

1.8 Research Gaps and Scope of the Thesis

Exploiting the unique optoelectronic and ease of fabrication properties, HOIPs have evolved as the promising alternative for commercially available photovoltaic light absorbers such as Silicon and various thin-films. The past 15 years of efforts from the photovoltaic community have shortlisted different HOIP materials such as $MAPbI_3$, $CsPbI_3$, mix-perovskites, and $FAPbI_3$ to function as the promising light absorber in a single junction PSC. Considering the low band gap and superior thermal stability, $FAPbI_3$ has been considered to be in the pole position in the race for the efficient light absorber material. However, the proposed $FAPbI_3$ suffers from various intrinsic and extrinsic challenges such as unfavourable phase transition, instability against environmental stresses etc. Moreover, the necessity of an inert atmosphere, high fabrication temperature, and high-purity chemicals increases the production cost, which hampers the commercialization of PSCs along with the stability concerns.

Through this dissertation, we aim to address some of the exsisting challenges for the commercialization of promising $FAPbI_3$ based single junction solar cells.

Our object goals were as follows:

1. Understand the fundamental structure-stability-performance correlations in $FAPbI_3$ based perovskite thin films and solar cells.
2. Realise the phase stabilization for $FAPbI_3$ thin films under harsh environmental conditions.
3. Design and develop cost-competative device fabrication and upscaling strategies.

1.9 Thesis Outline

The main intention of this thesis is to understand the origin of the instability of $FAPbI_3$ and to develop cost-effective pathways to overcome phase-instability concerns. Various plans, including i) Process engineering and ii) additive engineering strategies, were

designed to ensure the phase stability and high efficiency of $FAPbI_3$ PSCs. This thesis is written in accordance with the compilation of scientific research publications. A brief description of each chapter is presented below.

Chapter 1 briefs the history and basic properties of hybrid organic-inorganic perovskites and their photovoltaic applications followed by a short literature review discussion on the current challenges and possible mitigating strategies that emerged over these years.

Chapter 2 discusses the experimental and characterization tools employed in this thesis.

Chapter 3 describes the newly developed powder engineering strategy to stabilize the $FAPbI_3$ layer at a reduced temperature. The pre-synthesized δ-$Cs_{0.1}FA_{0.9}PbI_3$ with high phase purity reduces the annealing temperature from 150 ºC to 80 ºC and the corresponding PSCs displayed an improved PCE of 17% with negligible hysteresis. We discuss the role of Cs in improving the crystallinity and defect management of pristine $FAPbI_3$.

Chapter 4 demonstrates another novel approach where the pre-synthesized α-$FAPbI_3$ perovskite powder is employed as the precursor source instead of conventional precursors. On comparing the conventional and previously reported δ -$FAPbI_3$ powder methods, we noticed superior crystallinity and phase stability for our α-$FAPbI_3$ powder precursor method. Moreover, we demonstrated cost-effectiveness through the employment of low-grade PbI_2 in the powder method without compromising the final device performance. Further, we have studied the role of hydrophobic ionic liquids as additives in $FAPbI_3$ based PSCs. The additivisation of imidazolium based ILs with bulky fluorine-rich anionic parts reduced the microstrain and Urbach energy of the pristine $FAPbI_3$ system to improve the device performance.

Next, in *Chapter 5*, we discuss a custom-modified transmission infrared spectroscopic tool to track the indirect hydrogen migration, which allowed the direct monitoring of the deterioration of perovskite surface by moisture. We were able to quantify the moisture/water blocking ability of different perovskite surfaces.

In *Chapter 6*, we propose a rational additivisation strategy to overcome the unwanted phase transition in $FAPbI_3$. Our multifunctional ammonium salt containing sulfur hetero-atom shifts the thermodynamic stability from the δ-phase to an intermediate phase closer to the α-phase. Along with the high crystallinity, micron-sized grains with preferred (00h)

facet orientation, stems Pb….S interaction to offer exceptional stability against high relative humidity, direct water incursion, and shelf life aging. Our findings through experimental and theoretical studies substantiate the role of Pb….S interaction in stabilizing the perovskite cubic phase and the stoichiometric distribution of elemental components.

Finally, *Chapter 7* delivers a summary of the thesis and a short discussion on the outlook for the large area and multi-junction PSCs for commercialisation.

1.10 References

(1) Chakhmouradian, A.R., Woodward, P.M., 2014. Celebrating 175 years of perovskite research: A tribute to Roger H. Mitchell. Physics and Chemistry of Minerals 41, 387–391. doi:10.1007/s00269-014-0678-9

(2) Brenner, T.M., Egger, D.A., Kronik, L., Hodes, G., Cahen, D., 2016. Hybrid Organic-Inorganic Perovskites: Low-Cost Semiconductors with Intriguing Charge-Transport Properties. Nature Reviews Materials 1. doi:10.1038/natrevmats.2015.7

(3) Yuan, Y., Xiao, Z., Yang, B., Huang, J., 2014. Arising applications of ferroelectric materials in photovoltaic devices. Journal of Materials Chemistry A 2, 6027–6041. doi:10.1039/c3ta14188h

(4) Weber, D., 1978. $CH_3NH_3SnBr_xI_{3-x}$ (x = 0-3), ein Sn(II)-System mit kubischer Perowskitstruktur / $CH_3NH_3SnBr_xI_{3-x}$(x = 0-3), a Sn(II)-System with Cubic Perovskite Structure. Zeitschrift für Naturforschung B 33, 862–865. doi:10.1515/znb-1978-0809

(5) MØLLER, CHR.KN., 1957. A phase transition in Cæsium plumbochloride. Nature 180, 981–982. doi:10.1038/180981a0

(6) MØLLER, CHR.KN., 1958. Crystal structure and photoconductivity of Cæsium plumbohalides. Nature 182, 1436–1436. doi:10.1038/1821436a0

(7) Mitzi, D.B., 2007. Synthesis, structure, and properties of organic-inorganic perovskites and related materials. Progress in Inorganic Chemistry 1–121. doi:10.1002/9780470166499.ch1

(8) Mitzi, D.B., 2000. Organic−Inorganic Perovskites Containing Trivalent Metal Halide Layers: The Templating Influence of the Organic Cation Layer. Inorganic Chemistry 39, 6107–6113. doi:10.1021/ic000794i

(9) Mitzi, D.B., Wang, S., Feild, C.A., Chess, C.A., Guloy, A.M., 1995. Conducting layered organic-inorganic halides containing 〈110〉-oriented perovskite sheets. Science 267, 1473–1476. doi:10.1126/science.267.5203.1473

(10) Kieslich, G., Sun, S., Cheetham, A.K., 2014. Solid-state principles applied to organic–inorganic perovskites: New tricks for an old dog. Chemical Science 5, 4712–4715. doi:10.1039/c4sc02211d

(11) Travis, W., Glover, E.N., Bronstein, H., Scanlon, D.O., Palgrave, R.G., 2016. On the application of the tolerance factor to inorganic and hybrid halide perovskites: A revised system. Chemical Science 7, 4548–4556. doi:10.1039/c5sc04845a

(12) Li, C., Lu, X., Ding, W., Feng, L., Gao, Y., Guo, Z., 2008. Formability of ABX_3 (X = F, Cl, Br, I) halide perovskites. Acta Crystallographica Section B Structural Science 64, 702–707. doi:10.1107/s0108768108032734

(13) Yi, Z., Ladi, N.H., Shai, X., Li, H., Shen, Y., Wang, M., 2019. Will organic–inorganic hybrid halide lead perovskites be eliminated from optoelectronic applications? Nanoscale Advances 1, 1276–1289. doi:10.1039/c8na00416a

(14) Manser, J.S., Christians, J.A., Kamat, P.V., 2016. Intriguing optoelectronic properties of metal halide perovskites. Chemical Reviews 116, 12956–13008. doi:10.1021/acs.chemrev.6b00136

(15) Brivio, F., Butler, K.T., Walsh, A., van Schilfgaarde, M., 2014. Relativistic quasiparticle self-consistent electronic structure of hybrid halide perovskite photovoltaic absorbers. Physical Review B 89. doi:10.1103/physrevb.89.155204

(16) Noh, J.H., Im, S.H., Heo, J.H., Mandal, T.N., Seok, S.I., 2013. Chemical management for colorful, efficient, and stable inorganic–organic hybrid nanostructured solar cells. Nano Letters 13, 1764–1769. doi:10.1021/nl400349b

(17) Byranvand, M.M., Otero-Martínez, C., Ye, J., Zuo, W., Manna, L., Saliba, M., Hoye, R.L., Polavarapu, L., 2022. Recent progress in mixed a-site cation halide

perovskite thin-films and nanocrystals for solar cells and light-emitting diodes. Advanced Optical Materials 10, 2200423. doi:10.1002/adom.202200423

(18) Amat, A., Mosconi, E., Ronca, E., Quarti, C., Umari, P., Nazeeruddin, Md.K., Grätzel, M., De Angelis, F., 2014. Cation-induced band-gap tuning in organohalide perovskites: Interplay of spin–orbit coupling and octahedra tilting. Nano Letters 14, 3608–3616. doi:10.1021/nl5012992

(19) De Wolf, S., Holovsky, J., Moon, S.-J., Löper, P., Niesen, B., Ledinsky, M., Haug, F.-J., Yum, J.-H., Ballif, C., 2014. Organometallic halide perovskites: Sharp optical absorption edge and its relation to photovoltaic performance. The Journal of Physical Chemistry Letters 5, 1035–1039. doi:10.1021/jz500279b

(20) Brandt, R.E., Poindexter, J.R., Gorai, P., Kurchin, R.C., Hoye, R.L., Nienhaus, L., Wilson, M.W., Polizzotti, J.A., Sereika, R., Žaltauskas, R., Lee, L.C., MacManus-Driscoll, J.L., Bawendi, M., Stevanović, V., Buonassisi, T., 2017. Searching for "defect-tolerant" photovoltaic materials: Combined theoretical and experimental screening. Chemistry of Materials 29, 4667–4674. doi:10.1021/acs.chemmater.6b05496

(21) Maiti, A., Chatterjee, S., Peedikakkandy, L., Pal, A.J., 2020. Defects and their passivation in hybrid halide perovskites toward solar cell applications. Solar RRL 4, 2000505. doi:10.1002/solr.202000505

(22) Yang, X., Zhang, X., Deng, J., Chu, Z., Jiang, Q., Meng, J., Wang, P., Zhang, L., Yin, Z., You, J., 2018. Efficient green light-emitting diodes based on quasi-two-dimensional composition and phase engineered perovskite with Surface Passivation. Nature Communications 9. doi:10.1038/s41467-018-02978-7

(23) Wang, J., Wang, N., Jin, Y., Si, J., Tan, Z.-K., Du, H., Cheng, L., Dai, X., Bai, S., He, H., Ye, Z., Lai, M.L., Friend, R.H., Huang, W., 2015. Interfacial control toward efficient and low-voltage perovskite light-emitting diodes. Advanced Materials 27, 2311–2316. doi:10.1002/adma.201405217

(24) Dong, R., Fang, Y., Chae, J., Dai, J., Xiao, Z., Dong, Q., Yuan, Y., Centrone, A., Zeng, X.C., Huang, J., 2015. High-gain and low-driving-voltage photodetectors based on organolead triiodide perovskites. Advanced Materials 27, 1912–1918. doi:10.1002/adma.201405116

(25) Zhang, Q., Shang, Q., Su, R., Do, T.T., Xiong, Q., 2021. Halide perovskite semiconductor lasers: Materials, cavity design, and low threshold. Nano Letters 21, 1903–1914. doi:10.1021/acs.nanolett.0c03593

(26) Yakunin, S., Sytnyk, M., Kriegner, D., Shrestha, S., Richter, M., Matt, G.J., Azimi, H., Brabec, C.J., Stangl, J., Kovalenko, M.V., Heiss, W., 2015. Detection of X-ray photons by solution-processed lead halide perovskites. Nature Photonics 9, 444–449. doi:10.1038/nphoton.2015.82

(27) Wei, W., Zhang, Y., Xu, Q., Wei, H., Fang, Y., Wang, Q., Deng, Y., Li, T., Gruverman, A., Cao, L., Huang, J., 2017. Monolithic integration of hybrid perovskite single crystals with heterogenous substrate for highly sensitive X-ray imaging. Nature Photonics 11, 315–321. doi:10.1038/nphoton.2017.43

(28) Kim, H., Han, J.S., Kim, S.G., Kim, S.Y., Jang, H.W., 2019. Halide perovskites for resistive random-access memories. Journal of Materials Chemistry C 7, 5226–5234. doi:10.1039/c8tc06031b

(29) Park, Y., Lee, J.-S., 2022. Metal halide perovskite-based memristors for emerging memory applications. The Journal of Physical Chemistry Letters 13, 5638–5647. doi:10.1021/acs.jpclett.2c01303

(39) Shellaiah, M., Sun, K.W., 2020. Review on sensing applications of perovskite nanomaterials. Chemosensors 8, 55. doi:10.3390/chemosensors8030055

(31) Seol, M.J., Hwang, S.H., Han, J.W., Jang, H.W., Kim, S.Y., 2023. Recent progress of halide perovskites applied to five senses sensors. ACS Applied Electronic Materials. doi:10.1021/acsaelm.2c01329

(32) Zhang, L., Miao, J., Li, J., Li, Q., 2020. Halide perovskite materials for energy storage applications. Advanced Functional Materials 30, 2003653. doi:10.1002/adfm.202003653

(33) Huang, H., Pradhan, B., Hofkens, J., Roeffaers, M.B., Steele, J.A., 2020. Solar-driven metal halide perovskite photocatalysis: Design, stability, and performance. ACS Energy Letters 5, 1107–1123. doi:10.1021/acsenergylett.0c00058

(34) He, X., Deng, Y., Ouyang, D., Zhang, N., Wang, J., Murthy, A.A., Spanopoulos, I., Islam, S.M., Tu, Q., Xing, G., Li, Y., Dravid, V.P., Zhai, T., 2023. Recent

development of halide perovskite materials and devices for ionizing radiation detection. Chemical Reviews 123, 1207–1261. doi:10.1021/acs.chemrev.2c00404

(35) Wei, H., Huang, J., 2019. Halide lead perovskites for ionizing radiation detection. Nature Communications 10. doi:10.1038/s41467-019-08981-w

(36) Zhou, Y., Wang, J., Luo, D., Hu, D., Min, Y., Xue, Q., 2022. Recent progress of Halide Perovskites for thermoelectric application. Nano Energy 94, 106949. doi:10.1016/j.nanoen.2022.106949

(37) Zhou, Yongfeng, Parkes, M.A., Zhang, J., Wang, Y., Ruddlesden, M., Fielding, H.H., Su, L., 2022. Single-crystal organometallic perovskite optical fibers. Science Advances 8. doi:10.1126/sciadv.abq8629

(38) Butey, B., Butey, S., Patankar, B., Raut, V.D., Dambhare, M., Moharil, S.V., 2021. Current status of perovskite in X-ray detection for Medical Imaging Technology. Journal of Physics: Conference Series 1913, 012055. doi:10.1088/1742-6596/1913/1/012055

(39) Archer, D., 2012. Global warming: Understanding the forecast. Blackwell, Malden, Mass.

(40) Iea, n.d. Electricity market report 2023 – analysis [WWW Document]. IEA. URL https://www.iea.org/reports/electricity-market-report-2023 (accessed 7.10.23).

(41) A. E. Becquerel, "Memoire sur les Effects d'Electriques Produits Sous l'Influence des Rayons Solaires," Comptes Rendus de l'Academie des Sciences, Vol. 9, 1839, pp. 561-567

(42) M., S.A.H., Jäger, K., Isabella, O., van, S.R.A., Zeman, M., 2016. Solar energy: The physics and engineering of photovoltaic conversion, technologies and systems. UIT Cambridge Ltd., Cambridge, England.

(43) Le Donne, A., Scaccabarozzi, A., Tombolato, S., Marchionna, S., Garattini, P., Vodopivec, B., Acciarri, M., Binetti, S., 2013. State of the art and perspectives of Inorganic Photovoltaics. ISRN Renewable Energy 2013, 1–8. doi:10.1155/2013/830731

(44) Jackson, P., Hariskos, D., Lotter, E., Paetel, S., Wuerz, R., Menner, R., Wischmann, W., Powalla, M., 2011. New World Record Efficiency for

$Cu(In,Ga)Se_2$ thin-film solar cells beyond 20%. Progress in Photovoltaics: Research and Applications 19, 894–897. doi:10.1002/pip.1078

(45) NREL. Efficiency Chart, http://www.nrel.gov/ncpv

(46) Meng, L., Zhang, Y., Wan, X., Li, C., Zhang, X., Wang, Y., Ke, X., Xiao, Z., Ding, L., Xia, R., Yip, H.-L., Cao, Y., Chen, Y., 2018. Organic and solution-processed tandem solar cells with 17.3% efficiency. Science 361, 1094–1098. doi:10.1126/science.aat2612

(47) Kojima, A., Teshima, K., Shirai, Y., Miyasaka, T., 2009. Organometal halide perovskites as visible-light sensitizers for photovoltaic cells. Journal of the American Chemical Society 131, 6050–6051. doi:10.1021/ja809598r

(48) Kim, H.-S., Lee, C.-R., Im, J.-H., Lee, K.-B., Moehl, T., Marchioro, A., Moon, S.-J., Humphry-Baker, R., Yum, J.-H., Moser, J.E., Grätzel, M., Park, N.-G., 2012. Lead iodide perovskite sensitized all-solid-state submicron thin film mesoscopic solar cell with efficiency exceeding 9%. Scientific Reports 2. doi:10.1038/srep00591

(49) Lee, M.M., Teuscher, J., Miyasaka, T., Murakami, T.N., Snaith, H.J., 2012. Efficient hybrid solar cells based on meso-superstructured organometal halide perovskites. Science 338, 643–647. doi:10.1126/science.1228604

(50) Im, J.-H., Lee, C.-R., Lee, J.-W., Park, S.-W., Park, N.-G., 2011. 6.5% efficient perovskite quantum-dot-sensitized solar cell. Nanoscale 3, 4088. doi:10.1039/c1nr10867k

(51) Kim, J.Y., Lee, J.-W., Jung, H.S., Shin, H., Park, N.-G., 2020. High-efficiency perovskite solar cells. Chemical Reviews 120, 7867–7918. doi:10.1021/acs.chemrev.0c00107

(52) Fortunato, E., Ginley, D., Hosono, H., Paine, D.C., 2007. Transparent conducting oxides for photovoltaics. MRS Bulletin 32, 242–247. doi:10.1557/mrs2007.29

(53) Wang, X., Zhi, L., Müllen, K., 2007. Transparent, conductive graphene electrodes for dye-sensitized solar cells. Nano Letters 8, 323–327. doi:10.1021/nl072838r

(54) Lin, L., Jones, T.W., Yang, T.C., Duffy, N.W., Li, J., Zhao, L., Chi, B., Wang, X., Wilson, G.J., 2020. Inorganic Electron Transport Materials in perovskite solar cells. Advanced Functional Materials 31, 2008300. doi:10.1002/adfm.202008300

(55) Singh, T., Singh, J., Miyasaka, T., 2016. Role of metal oxide electron-transport layer modification on the stability of high performing perovskite solar cells. ChemSusChem 9, 2559–2566. doi:10.1002/cssc.201601004

(56) Lian, J., Lu, B., Niu, F., Zeng, P., Zhan, X., 2018. Electron-transport materials in perovskite solar cells. Small Methods 2, 1800082. doi:10.1002/smtd.201800082

(57) Said, A.A., Xie, J., Zhang, Q., 2019. Recent progress in organic electron transport materials in inverted perovskite solar cells. Small 15, 1900854. doi:10.1002/smll.201900854

(58) Wali, Q., Iqbal, Y., Pal, B., Lowe, A., Jose, R., 2018. Tin Oxide as an emerging electron transport medium in perovskite solar cells. Solar Energy Materials and Solar Cells 179, 102–117. doi:10.1016/j.solmat.2018.02.007

(59) Xiong, L., Guo, Y., Wen, J., Liu, H., Yang, G., Qin, P., Fang, G., 2018. Review on the application of SnO_2 in perovskite solar cells. Advanced Functional Materials 28, 1802757. doi:10.1002/adfm.201802757

(60) Yin, X., Song, Z., Li, Z., Tang, W., 2020. Toward Ideal Hole Transport Materials: A review on recent progress in Dopant-free hole transport materials for fabricating efficient and stable perovskite solar cells. Energy & Environmental Science 13, 4057–4086. doi:10.1039/d0ee02337j

(61) Farokhi, A., Shahroosvand, H., Monache, G.D., Pilkington, M., Nazeeruddin, M.K., 2022. The evolution of triphenylamine hole transport materials for efficient perovskite solar cells. Chemical Society Reviews 51, 5974–6064. doi:10.1039/d1cs01157j

(62) Wei, Q., Zi, W., Yang, Z., Yang, D., 2018. Photoelectric performance and stability comparison of $MAPbI_3$ and $FAPbI_3$ perovskite solar cells. Solar Energy 174, 933–939. doi:10.1016/j.solener.2018.09.057

(63) Umari, P., Mosconi, E., De Angelis, F., 2014. Relativistic GW calculations on $CH_3NH_3PbI_3$ and $CH_3NH_3SnI_3$ perovskites for solar cell applications. Scientific Reports 4. doi:10.1038/srep04467

(64) Song, Z., Abate, A., Watthage, S.C., Liyanage, G.K., Phillips, A.B., Steiner, U., Graetzel, M., Heben, M.J., 2016. Perovskite Solar Cell Stability in Humid Air: Partially Reversible Phase Transitions in the PbI_2-CH_3NH_3I-H_2O System. Advanced Energy Materials 6, 1600846. doi:10.1002/aenm.201600846

(65) Manser, J.S., Saidaminov, M.I., Christians, J.A., Bakr, O.M., Kamat, P.V., 2016. Making and breaking of lead halide perovskites. Accounts of Chemical Research 49, 330–338. doi:10.1021/acs.accounts.5b00455

(66) Philippe, B., Park, B.-W., Lindblad, R., Oscarsson, J., Ahmadi, S., Johansson, E.M., Rensmo, H., 2015. Chemical and electronic structure characterization of lead halide perovskites and stability behavior under different exposures—a photoelectron spectroscopy investigation. Chemistry of Materials 27, 1720–1731. doi:10.1021/acs.chemmater.5b00348

(67) Juarez-Perez, E.J., Ono, L.K., Uriarte, I., Cocinero, E.J., Qi, Y., 2019. Degradation mechanism and relative stability of methylammonium halide based perovskites analyzed on the basis of acid–base theory. ACS Applied Materials & Interfaces 11, 12586–12593. doi:10.1021/acsami.9b02374

(68) Leijtens, T., Eperon, G.E., Pathak, S., Abate, A., Lee, M.M., Snaith, H.J., 2013. Overcoming ultraviolet light instability of sensitized TiO_2 with Meso-superstructured organometal tri-halide perovskite solar cells. Nature Communications 4. doi:10.1038/ncomms3885

(69) Wei, D., Wang, T., Ji, J., Li, M., Cui, P., Li, Y., Li, G., Mbengue, J.M., Song, D., 2016. Photo-induced degradation of lead halide perovskite solar cells caused by the hole transport layer/metal electrode interface. Journal of Materials Chemistry A 4, 1991–1998. doi:10.1039/c5ta08622a

(70) Brennan, M.C., Draguta, S., Kamat, P.V., Kuno, M., 2017. Light-induced anion phase segregation in mixed halide perovskites. ACS Energy Letters 3, 204–213. doi:10.1021/acsenergylett.7b01151

(71) Slotcavage, D.J., Karunadasa, H.I., McGehee, M.D., 2016. Light-induced phase segregation in halide-perovskite absorbers. ACS Energy Letters 1, 1199–1205. doi:10.1021/acsenergylett.6b00495

(72) Koh, T.M., Fu, K., Fang, Y., Chen, S., Sum, T.C., Mathews, N., Mhaisalkar, S.G., Boix, P.P., Baikie, T., 2013. Formamidinium-containing metal-halide: An alternative material for near-IR absorption perovskite solar cells. The Journal of Physical Chemistry C 118, 16458–16462. doi:10.1021/jp411112k

(73) Liu, Y., Sun, J., Yang, Zhou, Yang, D., Ren, X., Xu, H., Yang, Zupei, Liu, S.F., 2016. 20-mm-large single-crystalline formamidinium-perovskite wafer for mass production of integrated photodetectors. Advanced Optical Materials 4, 1829–1837. doi:10.1002/adom.201600327

(74) Ehrler, B., Alarcón-Lladó, E., Tabernig, S.W., Veeken, T., Garnett, E.C., Polman, A., 2020. Photovoltaics reaching for the Shockley–Queisser Limit. ACS Energy Letters 5, 3029–3033. doi:10.1021/acsenergylett.0c01790

(75) Eperon, G.E., Stranks, S.D., Menelaou, C., Johnston, M.B., Herz, L.M., Snaith, H.J., 2014. Formamidinium lead trihalide: A broadly tunable perovskite for efficient planar heterojunction solar cells. Energy & Environmental Science 7, 982. doi:10.1039/c3ee43822h

(76) Weber, O.J., Ghosh, D., Gaines, S., Henry, P.F., Walker, A.B., Islam, M.S., Weller, M.T., 2018. Phase behavior and polymorphism of formamidinium lead iodide. Chemistry of Materials 30, 3768–3778. doi:10.1021/acs.chemmater.8b00862

(77) Fabini, D.H., Stoumpos, C.C., Laurita, G., Kaltzoglou, A., Kontos, A.G., Falaras, P., Kanatzidis, M.G., Seshadri, R., 2016. Reentrant structural and optical properties and large positive thermal expansion in perovskite formamidinium lead iodide. Angewandte Chemie International Edition 55, 15392–15396. doi:10.1002/anie.201609538

(78) Ibaceta-Jaña, J., Muydinov, R., Rosado, P., Vinoth Kumar, S.H., Gunder, R., Hoffmann, A., Szyszka, B., Wagner, M.R., 2021. Hidden polymorphism of $FAPbI_3$ discovered by Raman spectroscopy. Physical Chemistry Chemical Physics 23, 9476–9482. doi:10.1039/d1cp00102g

(79) Masi, S., Gualdrón-Reyes, A.F., Mora-Seró, I., 2020. Stabilization of black perovskite phase in $FAPbI_3$ and $CSPbI_3$. ACS Energy Letters 5, 1974–1985. doi:10.1021/acsenergylett.0c00801

(80) Saliba, M., Matsui, T., Seo, J.-Y., Domanski, K., Correa-Baena, J.-P., Nazeeruddin, M.K., Zakeeruddin, S.M., Tress, W., Abate, A., Hagfeldt, A., Grätzel, M., 2016. Cesium-containing triple cation perovskite solar cells: Improved stability, reproducibility and high efficiency. Energy & Environmental Science 9, 1989–1997. doi:10.1039/c5ee03874j

(81) Pellet, N., Gao, P., Gregori, G., Yang, T.-Y., Nazeeruddin, M.K., Maier, J., Grätzel, M., 2014. Mixed-organic-cation perovskite photovoltaics for enhanced solar-light harvesting. Angewandte Chemie International Edition 53, 3151–3157. doi:10.1002/anie.201309361

(82) Yin, W.-J., Shi, T., Yan, Y., 2014. Unusual defect physics in $CH_3NH_3PbI_3$ perovskite solar cell absorber. Applied Physics Letters 104. doi:10.1063/1.4864778

(83) Turren-Cruz, S.-H., Hagfeldt, A., Saliba, M., 2018. Methylammonium-free, high-performance, and stable perovskite solar cells on a planar architecture. Science 362, 449–453. doi:10.1126/science.aat3583

(84) Binek, A., Hanusch, F.C., Docampo, P., Bein, T., 2015. Stabilization of the trigonal high-temperature phase of formamidinium lead iodide. The Journal of Physical Chemistry Letters 6, 1249–1253. doi:10.1021/acs.jpclett.5b00380

(85) Wang, X., Fan, Y., Wang, L., Chen, C., Li, Z., Liu, R., Meng, H., Shao, Z., Du, X., Zhang, H., Cui, G., Pang, S., 2020. Perovskite solution aging: What happened and how to inhibit? Chem 6, 1369–1378. doi:10.1016/j.chempr.2020.02.016

(86) Kim, Hyeonwoo, Lee, S., Lee, D.Y., Paik, M.J., Na, H., Lee, J., Seok, S.I., 2019. Optimal Interfacial Engineering with different length of alkylammonium halide for efficient and stable perovskite solar cells. Advanced Energy Materials 9, 1902740. doi:10.1002/aenm.201902740

(87) Lee, J.-W., Kim, D.-H., Kim, H.-S., Seo, S.-W., Cho, S.M., Park, N.-G., 2015. Formamidinium and cesium hybridization for photo- and moisture-stable

perovskite solar cell. Advanced Energy Materials 5, 1501310. doi:10.1002/aenm.201501310

(88) Kubicki, D.J., Prochowicz, D., Hofstetter, A., Zakeeruddin, S.M., Grätzel, M., Emsley, L., 2017. Phase segregation in Cs-, Rb- and K-doped mixed-cation $(MA)_x(FA)_{1-x}PbI_3$ hybrid perovskites from solid-state NMR. Journal of the American Chemical Society 139, 14173–14180. doi:10.1021/jacs.7b07223

(89) Peng, Z., Wei, Q., Chen, H., Liu, Y., Wang, F., Jiang, X., Liu, W., Zhou, W., Ling, S., Ning, Z., 2020. $Cs_{0.15}FA_{0.85}PbI_3/Ca_XFA_{1-x}PbI_3$ core/shell heterostructure for highly stable and efficient perovskite solar cells. Cell Reports Physical Science 1, 100224. doi:10.1016/j.xcrp.2020.100224

(90) Chen, T., Foley, B.J., Park, C., Brown, C.M., Harriger, L.W., Lee, J., Ruff, J., Yoon, M., Choi, J.J., Lee, S.-H., 2016. Entropy-driven structural transition and kinetic trapping in formamidinium lead iodide perovskite. Science Advances 2. doi:10.1126/sciadv.1601650

(91) Yi, C., Luo, J., Meloni, S., Boziki, A., Ashari-Astani, N., Grätzel, C., Zakeeruddin, S.M., Röthlisberger, U., Grätzel, M., 2016. Entropic stabilization of mixed A-cation ABX_3 metal halide perovskites for high performance perovskite solar cells. Energy & Environmental Science 9, 656–662. doi:10.1039/c5ee03255e

(92) Correa-Baena, J.-P., Luo, Y., Brenner, T.M., Snaider, J., Sun, S., Li, X., Jensen, M.A., Hartono, N.T., Nienhaus, L., Wieghold, S., Poindexter, J.R., Wang, S., Meng, Y.S., Wang, T., Lai, B., Holt, M.V., Cai, Z., Bawendi, M.G., Huang, L., Buonassisi, T., Fenning, D.P., 2019. Homogenized halides and alkali cation segregation in alloyed organic-inorganic perovskites. Science 363, 627–631. doi:10.1126/science.aah5065

(93) Bercegol, A., Ramos, F.J., Rebai, A., Guillemot, T., Puel, J.-B., Guillemoles, J.-F., Ory, D., Rousset, J., Lombez, L., 2018. Spatial inhomogeneity analysis of cesium-rich wrinkles in triple-cation perovskite. The Journal of Physical Chemistry C 122, 23345–23351. doi:10.1021/acs.jpcc.8b07436

(94) Correa-Baena, J.-P., Luo, Y., Brenner, T.M., Snaider, J., Sun, S., Li, X., Jensen, M.A., Hartono, N.T., Nienhaus, L., Wieghold, S., Poindexter, J.R., Wang, S.,

Meng, Y.S., Wang, T., Lai, B., Holt, M.V., Cai, Z., Bawendi, M.G., Huang, L., Buonassisi, T., Fenning, D.P., 2019. Homogenized halides and alkali cation segregation in alloyed organic-inorganic perovskites. Science 363, 627–631. doi:10.1126/science.aah5065

(95) Jiang, Y., Leyden, M.R., Qiu, L., Wang, S., Ono, L.K., Wu, Z., Juarez-Perez, E.J., Qi, Y., 2017. Combination of hybrid CVD and cation exchange for upscaling Cs-substituted mixed cation perovskite solar cells with high efficiency and stability. Advanced Functional Materials 28, 1703835. doi:10.1002/adfm.201703835

(96) Luo, L., Zhang, Y., Chai, N., Deng, X., Zhong, J., Huang, F., Peng, Y., Ku, Z., Cheng, Y.-B., 2018. Large-area perovskite solar cells with $Cs_xFA_{1-x}PbI_{3-y}Br_y$ thin films deposited by a vapor–solid reaction method. Journal of Materials Chemistry A 6, 21143–21148. doi:10.1039/c8ta06557h

(97) Kim, G., Min, H., Lee, K.S., Lee, D.Y., Yoon, S.M., Seok, S.I., 2020. Impact of strain relaxation on performance of α-formamidinium lead iodide perovskite solar cells. Science 370, 108–112. doi:10.1126/science.abc4417

(98) Zheng, X., Wu, C., Jha, S.K., Li, Z., Zhu, K., Priya, S., 2016. Improved phase stability of formamidinium lead triiodide perovskite by strain relaxation. ACS Energy Letters 1, 1014–1020. doi:10.1021/acsenergylett.6b00457

(99) Li, Y., Milić, J.V., Ummadisingu, A., Seo, J.-Y., Im, J.-H., Kim, H.-S., Liu, Y., Dar, M.I., Zakeeruddin, S.M., Wang, P., Hagfeldt, A., Grätzel, M., 2018. Bifunctional Organic Spacers for Formamidinium-based hybrid Dion–Jacobson two-dimensional perovskite solar cells. Nano Letters 19, 150–157. doi:10.1021/acs.nanolett.8b03552

(100) Grancini, G., Nazeeruddin, M.K., 2018. Dimensional tailoring of hybrid perovskites for photovoltaics. Nature Reviews Materials 4, 4–22. doi:10.1038/s41578-018-0065-0

(101) Thrithamarassery Gangadharan, D., Ma, D., 2019. Searching for stability at Lower Dimensions: Current trends and future prospects of layered perovskite solar cells. Energy & Environmental Science 12, 2860–2889. doi:10.1039/c9ee01591d

(102) Huang, P., Kazim, S., Wang, M., Ahmad, S., 2019. Toward phase stability: Dion–Jacobson layered perovskite for solar cells. ACS Energy Letters 4, 2960–2974. doi:10.1021/acsenergylett.9b02063

(103) Smith, I.C., Hoke, E.T., Solis-Ibarra, D., McGehee, M.D., Karunadasa, H.I., 2014. A layered hybrid perovskite solar-cell absorber with enhanced moisture stability. Angewandte Chemie International Edition 53, 11232–11235. doi:10.1002/anie.201406466

(104) Tsai, H., Nie, W., Blancon, J.-C., Stoumpos, C.C., Asadpour, R., Harutyunyan, B., Neukirch, A.J., Verduzco, R., Crochet, J.J., Tretiak, S., Pedesseau, L., Even, J., Alam, M.A., Gupta, G., Lou, J., Ajayan, P.M., Bedzyk, M.J., Kanatzidis, M.G., Mohite, A.D., 2016. High-efficiency two-dimensional ruddlesden–popper perovskite solar cells. Nature 536, 312–316. doi:10.1038/nature18306

(105) Lai, H., Lu, D., Xu, Z., Zheng, N., Xie, Z., Liu, Y., 2020. Organic-salt-assisted Crystal Growth and orientation of quasi-2d ruddlesden–popper perovskites for solar cells with efficiency over 19%. Advanced Materials 32, 2001470. doi:10.1002/adma.202001470

(106) Cheng, L., Liu, Z., Li, S., Zhai, Y., Wang, X., Qiao, Z., Xu, Q., Meng, K., Zhu, Z., Chen, G., 2020. Highly thermostable and efficient formamidinium-based low-dimensional perovskite solar cells. Angewandte Chemie International Edition 60, 856–864. doi:10.1002/anie.202006970

(107) Maheshwari, S., Savenije, T.J., Renaud, N., Grozema, F.C., 2018. Computational design of two-dimensional perovskites with functional organic cations. The Journal of Physical Chemistry C 122, 17118–17122. doi:10.1021/acs.jpcc.8b05715

(108) El-Ballouli, A.O., Bakr, O.M., Mohammed, O.F., 2020. Structurally tunable two-dimensional layered perovskites: From confinement and enhanced charge transport to prolonged hot carrier cooling dynamics. The Journal of Physical Chemistry Letters 11, 5705–5718. doi:10.1021/acs.jpclett.0c00359

(109) Liu, T., Zong, Y., Zhou, Y., Yang, M., Li, Z., Game, O.S., Zhu, K., Zhu, R., Gong, Q., Padture, N.P., 2017. High-performance formamidinium-based perovskite

solar cells via microstructure-mediated δ-to-α phase transformation. Chemistry of Materials 29, 3246–3250. doi:10.1021/acs.chemmater.7b00523

(110) Lee, J.-W., Kim, H.-S., Park, N.-G., 2016. Lewis acid–base adduct approach for high efficiency perovskite solar cells. Accounts of Chemical Research 49, 311–319. doi:10.1021/acs.accounts.5b00440

(111) Zhang, F., Zhu, K., 2019. Additive Engineering for efficient and stable perovskite solar cells. Advanced Energy Materials 10, 1902579. doi:10.1002/aenm.201902579

(112) Bai, S., Da, P., Li, C., Wang, Z., Yuan, Z., Fu, F., Kawecki, M., Liu, X., Sakai, N., Wang, J.T.-W., Huettner, S., Buecheler, S., Fahlman, M., Gao, F., Snaith, H.J., 2019. Planar perovskite solar cells with long-term stability using Ionic liquid additives. Nature 571, 245–250. doi:10.1038/s41586-019-1357-2

(113) Zhang, K., Zhang, X., Brooks, K.G., Ding, B., Kinge, S., Ding, Y., Dai, S., Nazeeruddin, M.K., 2023. Role of ionic liquids in perovskite solar cells. Solar RRL 7. doi:10.1002/solr.202300115

(114) Xia, R., Fei, Z., Drigo, N., Bobbink, F.D., Huang, Z., Jasiūnas, R., Franckevičius, M., Gulbinas, V., Mensi, M., Fang, X., Roldán-Carmona, C., Nazeeruddin, M.K., Dyson, P.J., 2019. Retarding thermal degradation in hybrid perovskites by Ionic liquid additives. Advanced Functional Materials 29, 1902021. doi:10.1002/adfm.201902021

(115) Wang, S., Li, Z., Zhang, Y., Liu, X., Han, J., Li, X., Liu, Z., (Frank) Liu, S., Choy, W.C., 2019. Water-soluble triazolium ionic-liquid-induced surface self-assembly to enhance the stability and efficiency of perovskite solar cells. Advanced Functional Materials 29, 1900417. doi:10.1002/adfm.201900417

(116) Akin, S., Akman, E., Sonmezoglu, S., 2020. $FAPbI_3$-Based Perovskite Solar Cells Employing Hexyl-Based Ionic Liquid with an Efficiency Over 20% and Excellent Long-Term Stability. Advanced Functional Materials 30, 2002964. doi:10.1002/adfm.202002964

(117) Wang, S., Yang, B., Han, J., He, Z., Li, T., Cao, Q., Yang, J., Suo, J., Li, X., Liu, Z., Liu, S. (Frank), Tang, C., Hagfeldt, A., 2020. Polymeric room-temperature molten salt as a multifunctional additive toward highly efficient and stable

inverted planar perovskite solar cells. Energy & Environmental Science 13, 5068–5079. doi:10.1039/d0ee02043e

(118) Wang, J., Ye, X., Wang, Y., Wang, Z., Wong, W., Li, C., 2019. Halide perovskite based on hydrophobic ionic liquid for stability improving and its application in high-efficient photovoltaic cell. Electrochimica Acta 303, 133–139. doi:10.1016/j.electacta.2019.02.071

(119) Zhao, J., Deng, Y., Wei, H., Zheng, X., Yu, Z., Shao, Y., Shield, J.E., Huang, J., 2017. Strained hybrid perovskite thin films and their impact on the intrinsic stability of perovskite solar cells. Science Advances 3. doi:10.1126/sciadv.aao5616

(120) Haeger, T., Heiderhoff, R., Riedl, T., 2020. Thermal properties of metal-halide perovskites. Journal of Materials Chemistry C 8, 14289–14311. doi:10.1039/d0tc03754k

(121) Zhu, C., Niu, X., Fu, Y., Li, N., Hu, C., Chen, Y., He, X., Na, G., Liu, P., Zai, H., Ge, Y., Lu, Y., Ke, X., Bai, Y., Yang, S., Chen, P., Li, Y., Sui, M., Zhang, L., Zhou, H., Chen, Q., 2019. Strain engineering in perovskite solar cells and its impacts on carrier dynamics. Nature Communications 10. doi:10.1038/s41467-019-08507-4

CHAPTER 2

2

METHODOLOGY

In order to understand the solution-to-thin film-to-device properties of perovskite materials, various processing and characterization tools were used to i) synthesize and fabricate required perovskite materials, thin films, and devices, ii) investigate photo-physical, chemical, morphological, and kinetic parameters of perovskite and corresponding PSCs.

This chapter briefs the material and instrumental parameters used throughout this thesis. Work-specific experimental details could be found in the relevant chapters under the supporting information sections.

2.1 Materials

Titanium diisopropoxide bis(acetylacetonate) (TAA), 4-*tert*-butylpyridine (tbp), tin(IV) chloride pentahydrate, bis(trifluoromethane) sulfonamide lithium salt, and [tris(2-(1*H*-pyrazol-1-yl)-4-*tert*-butylpyridine)-cobalt(III) tris(bis(trifluoromethylsulfonyl)imide)] (FK209), chlorobenzene (CB), dimethylsulphoxide (DMSO), N,N-dimethylformamide (DMF), methylammonium hydrochloride (MACl) and Low-grade Lead iodide (99%) were supplied from Sigma-Aldrich. High-purity Lead iodide (>99.999%) (PbI_2), Formamidine acetate, Formamidinium chloride (FACl), hydriodic acid and cesium iodide (CsI) were purchased from TCI. Acetonitrile (HPLC grade), ethanol, diethyl ether and Chlorobenzene were supplied from Alfa Aeser. 2,2′,7,7′-Tetrakis(*N*, *N*-di-4-methoxyphenylamine)-9,9′-spirobifluorene (spiro-OMeTAD) was purchased from Merck. 30-NRT was purchased from GreatCell. All of the purchased chemicals were used as received without further purification unless and otherwise stated in each relevant chapter.

2.2 Material Synthesis

New materials synthesized in each work have been explained in detail in the respective chapters under the supporting information sections.

2.3 Fabrication Techniques

2.3.1 Substrate cleaning

Plane glass and Fluorine-doped tin oxide (FTO) coated glasses were used throughout this thesis as substrates and specified wherever necessary. Substrates were cleaned with a sequential treatment in 2% Hellmanex solution, deionised water, acetone, and isopropanol in the ultrasonic bath for 15 min each. This is followed by a UV-Ozone treatment for 30 min before being used.

2.3.2 Precursor solution preparation

The parent solution used for the spin-coating technique is termed a precursor solution throughout the thesis. The preparation of each precursor solution has been explained in detail in respective chapters under the supporting information section.

2.3.3 Spin Coating

Spin-coating tool, the most common solution-processible deposition technique at the laboratory scale, operates using a rotational centrifugal force to form uniform thin films on flat substrates. Figure 2.1 illustrates the simple procedure of the spin-coting process. Initially, a specific amount of precursor solution is dropped on the cleaned substrate, preferably covering the top surface. Then the stage starts rotating to make uniform coverage of the solution on the surface with the help of centrifugal force. Finally, the substrate spins at a fixed rate, and uniform thin film forms due to the evaporation of solvents.

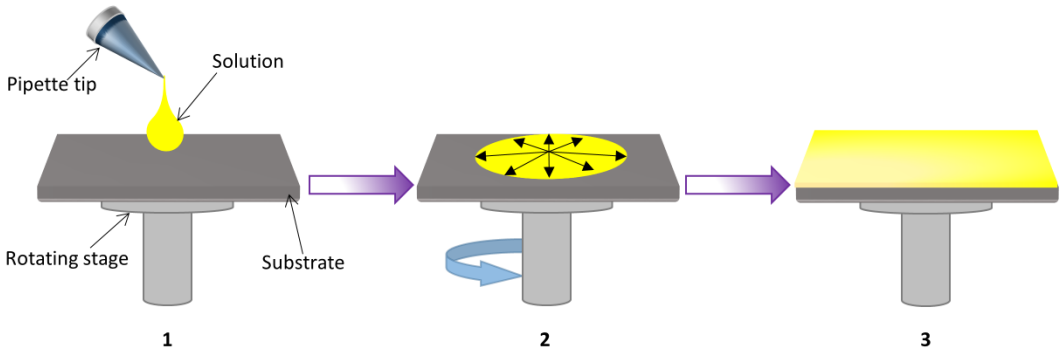

Figure 2. 1 Spin-coating mechanism steps: (1) Precursor solution is dropped onto the substrate, (2) stage starts to rotate spreading the solution over the entire surface, and (3) solvents evaporate and a uniform thin layer forms.

This easy setup helps to control the thickness of the fabricated thin film by varying the solution concentration, rotational speed, spinning time etc. However, the large amount of solvent wastage during the spinning process hinders this method from applying in mass production.

2.3.4 Spray pyrolysis

Spray pyrolysis is another tool for thin film fabrication where the process involves the decomposition f precursor solution through rapid heating and subsequent deposition onto the substrate. As schematically illustrated in Figure 2.2, initially the precursor solution is atomized into tiny droplets via a nebulizer or an aerosol generator. These droplets are transported to heated substrates through carrier gas like nitrogen or compressed air. As the droplets travel through the carrier gas at a high-temperature zone, the solvent evaporates, and the remaining solute coats the substrates. The high temperature of substrates helps to alter the solute status through decomposition, oxidation, or reduction depending on the specific requirements. Spray pyrolysis has been employed to coat compact-titanium dioxide (c-TiO_2) layer as electron transporting material in this thesis.

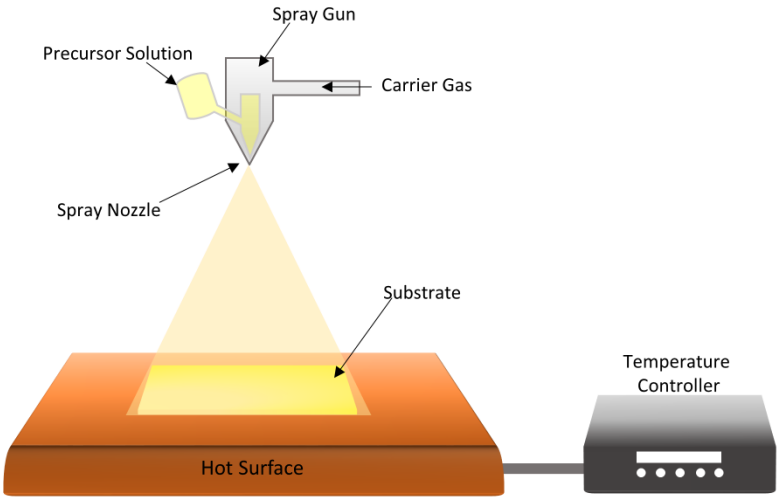

Figure 2. 2 Schematic representation of working of spray pyrolysis.

2.4 Characterization Techniques

This section explains the parameters of various instruments employed in the thesis for characterizing materials, thin films, and PSCs.

2.4.1 Material and thin film analysis

2.4.1.1 Powder X-ray diffraction:

Room temperature PXRD: Room temperature X-ray powder diffraction patterns were collected by using a Philips X'pert PRO automatic diffractometer operating at 40 kV and 40 mA, in theta-theta configuration, secondary monochromator with Cu-Kα radiation (λ = 1.5418 Å) and a PIXcel solid-state detector (active length in 2θ 3.347º). Data were collected from 2θ =10 to 50° (step size = 0.026 and time per step = 300s.) at RT. 1º fixed soller slit and divergence slit giving a constant volume of sample illumination were used.

Temperature dependent PXRD: Temperature dependent XRD data were collected on a Bruker D8 Advance diffractometer operating at 30 kV and 20 mA, equipped with a Cu tube (λ = 1.5418 Å), a Vantec-1 PSD detector, and an Anton Parr HTK2000 high-temperature furnace. The powder patterns were recorded in 2θ steps of 0.033º in the 10 ≤2θ ≤ 50 range, counting for 0.6s per step (total time for each temperature 36 min.). Data sets were recorded from 30-150 ºC each 10 ºC at 0.033 ºC s-1 heating rate.

Depth-dependent PXRD: The depth-dependent XRD data were collected on a Bruker D8 Advance diffractometer equipped with a Cu tube, Ge (111) incident beam monochromator (λ = 1.5406 Å), and 1-D LynxEye detector (active length in 2θ 2.7º). The sample was mounted on a zero-background silicon wafer embedded in a generic sample holder. Data were collected as detector scans, for different incident angles, from 10 to 30° 2θ (step size 0.02 and time per step = 0.5 s) at RT. A fixed divergence and anti-scattering slit of 0.1º of sample illumination were used.

2.4.1.2 X-ray photoelectron spectroscopy:

X-ray photoelectron spectroscopy (XPS) data were collected using a SPECS system (Berlin, Germany) equipped with phoibos 150 1D-DLD analyser with monochromated Al Kα radiation (1486.7 eV).

2.4.1.3 Opto-electronic analysis:

The UV-Visible absorption spectra were collected with a Varian Cary 50 UV−vis spectrophotometer and steady-state photoluminescence (PL) measurement was made using a spectrophotometer (PerkinElmer Instrument LS55).

2.4.1.4 Morphological analysis:

Surface and cross-sectional SEM morphological analysis was done by a Hitachi S-4800 SEM machine and the AFM topographical images were recorded with the help of scanning probe microscopy (CSI Nano observer) and an NSG10 cantilever (NTMDT) was used; data were processed through Gwyddion software. TITAN (Analytical) was used for ultra-high resolution imaging in Scanning-Transmission mode (HRSTEM) using a convergent beam and the lamella was made and processed for sample characterization. For the TRPL measurements, samples were excited with a 408-nm pulsed laser (MDL 300, PicoQuant) with 40 $\mu m \cdot cm^{-2}$ pulse energy density (pulse width 180 ps). SPM images were acquired with the help of an Autoprobe CP-Research microscope (VEECO).

2.4.2 Device analysis

Current-voltage (*J- V*)characteristics were recorded by applying an external potential bias to the cell while recording the generated photocurrent with a digital source meter (Keithley Model 2400). The light source was a 450 W xenon lamp (Oriel) equipped with a SchottK113 Tempax sunlight filter (Praezisions Glas & Optik GmbH) to match the emission spectrum of the lamp to the AM 1.5G standard. Before each measurement, the exact light intensity was determined using a calibrated Si reference diode equipped with

an infrared cutoff filter (KG-3, Schott). The cells were masked with the active area of 0.09 cm^2 to fix the active area and reduce the influence of the scattered light on the small device. The *J-V* characteristics under dark conditions were performed using a Keithley 2400 source meter adjusted to a 100 mV/s scan rate.

Incident photon to current efficiency (IPCE) measurements were carried out using a 150W Xenon lamp attached to with Bentham PVE300 motorized 1/4m monochromator as the light source.

Frequency-dependent capacitance (*C-f)* measurements at different temperatures were acquired using an LCR meter (Keysight, E4980A) and the temperature was controlled by LabVIEW software using Linkam (LTS420) sample heating control system.

.

CHAPTER 3

3

LOW-TEMPERATURE-PROCESSED PEROVSKITE SOLAR CELL FABRICATED FROM PRE-SYNTHESIZED $CsFAPbI_3$ POWDER

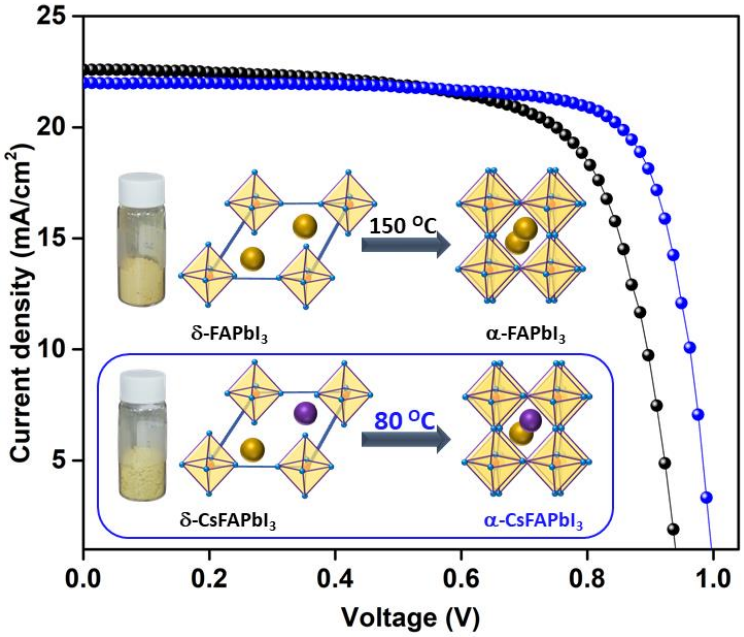

This chapter has been published in *ACS Applied Energy Materials* entitled:

Low-Temperature-Processed Perovskite Solar Cells Fabricated from Presynthesized $CsFAPbI_3$ Powder

Muhammed. P. U. Haris, Samrana Kazim, Shahzada Ahmad

M. P. U. Haris et al. ACS Applied Energy Materials 2021 4 (3), 2600-2606.
DOI: 10.1021/acsaem.0c03160

3.1 Abstract

Investigating methylammonium (MA) and bromide (Br) -free perovskite structure is paramount to reducing thermal diffusion and phase segregation, which has plagued the rapid development of perovskite solar cells. Such engineered compositions are intrinsically stable and compatible with single and multijunction solar cells. We demonstrate a δ-phase free formamidinium based solar cells, derived from a powder perovskite precursor with $Cs_{0.1}FA_{0.9}PbI_3$ fabricated at a modest temperature of 80 ºC, to yield a competitive performance >17% with negligible hysteresis. Importantly, these fabricated PSCs show enhanced stability and efficiency over the conventional $FAPbI_3$ which demands high temperature (150 ºC) processing for solar cell fabrication. We put forward a strategy for substantial materials synthesis, which can be effectively processable at low temperatures.

3.2 Introduction

As we discussed in *Chapter 1*, the rapid unprecedented improvements in the power conversion efficiency (PCE) from a mere 3.8 to over 26% in just a 12-year span boosted solution processed hybrid lead halide perovskite as a promising light harvester for photovoltaics (PVs). [1–3] Methylammonium lead iodide ($MAPbI_3$) perovskite based solar cells enjoy the privilege of intense investigation owing to its high PCE value, though also represents severe intrinsic degradation of perovskite under light, moisture, heat, and oxygen that impeded its rapid commercial aspects. Recently, the formamidinium lead iodide ($FAPbI_3$) are attracting significant attention due to its lower band gap of ~1.47 eV, and the possibility of strong secondary hydrogen bond formation with PbI_6 octahedra along with higher thermal stability, as compared to thermally unstable $MAPbI_3$ or mixed halide perovskites which display phase segregation. Notably, $FAPbI_3$ are photostable as compared to $MAPbI_3$.

However, $FAPbI_3$ undergoes a polymorphic transformation from the photoactive black α-phase (~1.47 eV) to the inactive yellow δ-phase (~2.43 eV) at room temperature. Moreover, α-$FAPbI_3$ phase is thermodynamically unstable below 150 ºC and its degradation to FAI and PbI_2 starts at similar temperatures [4–8], which makes use of $FAPbI_3$ in perovskite solar cells (PSC) challenging, see section *1.7.2.2* for detailed discussion. Strategies have been developed to overcome such issues in recent years. The most

common methods are the alloying at the FA site with small cations such as methylammonium (MA^+), Cesium (Cs^+), rubidium (Rb^+), potassium (K^+) and the addition of large organic cations to form 2D/3D mixed phases. [9–15] Initial reports showed the introduction of MA to form a mixed perovskites $(MAPbBr_3)_x$ $(FAPbI_3)_{1-x}$ to enhance PCE, phase stability and lower the transition temperature to 100 °C. Triple cation based mixed perovskites (MA, FA and Cs) were reported to improve the PSC performance. In a seminal work, Gratzel et. al showed methylammonium thiocyanate vapour assisted conversion of δ- $FAPbI_3$ to the desired α-phase. The strong affinity of Pb^{2+} ions with the surface thiocyanate anions induces the disintegration of δ-phase at the top surface and penetration of MA^+ into the PbI_6 chains, which eventually stabilise the α-phase and gave a high performance.[16] However, the volatile nature of MA hinders the long-term stability of devices. [17] Thus MA-free, low-temperature processed and phase pure α-$FAPbI_3$ will be the promising candidate for long-term stable PSCs. The fabrication of δ/α phase junction $Cs_{0.2}FA_{0.8}PbI_3$ films at 60 ºC [18] PSCs fabricated with $Cs_xFA_{(1-x)}PbI_3$ film at 100 ºC gave a PCE of 15.7%.[12] Moreover, phase stabilization with high device performance at 85 ºC was achieved with the addition of PbS quantum dots. [19,20] Although, improved phase stability was reported, the device stability remained unaddressed. Compositional engineering at the FA site induces structural distortions and relaxation of lattice strain through a strain-compensation strategy was observed by introducing smaller and larger ions together with a certified PCE of 24.4%.[21]

Pre-synthesized $FAPbI_3$ powder as precursor over the conventional route stemmed device long-term stability and can reduce device hysteresis by suppressing the trap states. [22–24] Precursor engineering with the perovskite single crystals or powders over the commercially available cost-ineffective materials could reduce the manufacturing cost of PSCs without affecting their performance. In the past, $MAPbX_3$ (X=Br, Cl or I) single crystals and powders were employed as the precursor and the fabricated PSCs demonstrated reproducibility and reduced interfacial trap density.[25,26] Recently, improved stability and device performance with δ-$FAPbI_3$ powder perovskite precursor synthesized at room temperature precipitation method over the conventional method was explored. [22]

To address such challenges, we undertook the synthesis of MA, Br-free, Cs amalgamated δ-$FAPbI_3$ powder perovskite precursor employing low-grade PbI_2 (99%), process at room temperature and annealing at 80 °C. Further, Cs inclusion in $FAPbI_3$ powder perovskite

precursor can extend the longevity significantly. The fabricated PSCs performed competitively and gave a PCE of >17%, as compared to their conventional counterparts, while adopting a milder synthetic protocol.

3.3 Results and discussion

3.3.1 Precursor powder engineering

We synthesized non-perovskite δ-$Cs_xFA_{(1-x)}PbI_3$ powder through the precipitation method, for this CsI and FAI were dissolved in acetonitrile in varying ratios. Yellow colour perovskite powder (yield 92%) was precipitated by the employment of low-grade PbI_2 followed by 24 hr stirring (Figure 3.1). The complete removal of acetonitrile was ensured by vacuum drying the precipitation for 24 hr. The high Cs concentration imposes larger distortions to the perovskite lattice and thereby inhibits the PV performance,[12] to eliminate such behaviour we limited the concentration to $x \leq 0.1$. The phase purity of synthesized powders was monitored by powder X-ray diffraction (XRD) technique.

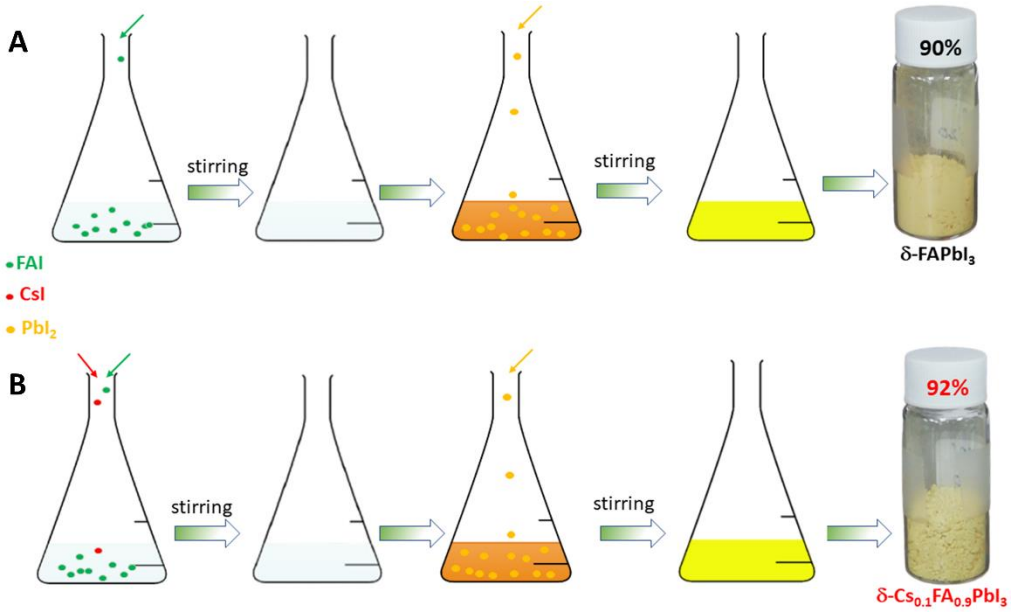

Figure 3. 1 Schematic illustration of synthetic procedure of non-perovskite powder precursors of (A) δ-$FAPbI_3$ and (B) δ-$Cs_{0.1}FA_{0.9}PbI_3$ along with the product yields.

Figure 3.2 A illustrates the diffractograms of synthesized δ-$FAPbI_3$ and δ-$Cs_{0.1}FA_{0.9}PbI_3$ powders at room temperature and compared with the diffractograms of δ-$CsPbI_3$[25]. The diffraction peaks at (010), (011), (-120), (002), (012), (021), (-122), (-130), (022) and (240) indicate the hexagonal non-perovskite δ-phase of $FAPbI_3$. The absence of α-$FAPbI_3$

and δ-$CsPbI_3$ peaks signal the phase purity of synthesized powders. The noted blue shift in the diffraction patterns of δ-$Cs_{0.1}FA_{0.9}PbI_3$ suggests an increase in the inter-planar distance, this was also validated by the absence of any additional peak. This point towards the structural incorporation of Cs into the δ-$FAPbI_3$ powder. We carried out the X-ray photoelectron spectroscopy (XPS) measurements for both non-perovskite powders and identified the elemental composition and the nature of their chemical bonding. The survey spectrum and signals from core levels are presented (Figure 3.2 B and Figure S3.1 A-C, supporting information, SI). The signals from Cs 3d core level (Figure 3.2 B) for both samples are the characteristic peaks at 721.8 eV and 735.77 eV corresponding to Cs $3d_{5/2}$ and Cs $3d_{3/2}$ respectively, only visible in δ-$Cs_{0.1}FA_{0.9}PbI_3$. It can be deduced that the shift in the binding energy (Figure S3.1 B-C, see SI), of Pb 4f and I 3d core level signals, emerge from the Cs inclusion. [27] We attribute the shift of Pb 4f peaks towards higher binding energy to the increase in the cationic charge of Pb ions, which is also evident from the diffractograms.

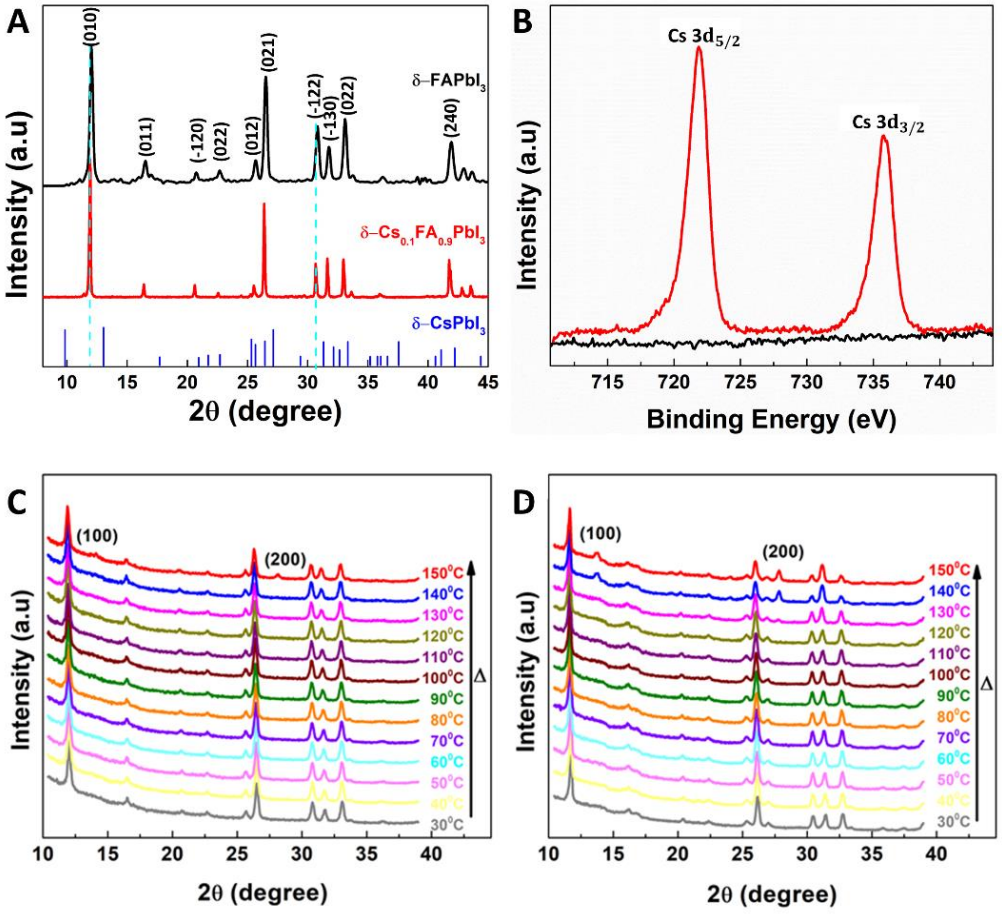

Figure 3. 2 (A) Diffractograms of synthesized non-perovskite powders, (B) XPS core level signals from Cs 3d. (C, D) Temperature dependent *in situ* XRD measurements for (C) δ-

$FAPbI_3$ and (D) δ-$Cs_{0.1}FA_{0.9}PbI_3$ powders respectively. Samples were heated from 30 − 150 ºC at 2 ºC/ min.

The influence of Cs incorporation on the phase transition temperature (δ to α conversion), was systematically probed by means of in-situ XRD analysis for these non-perovskite powders (Figure 3.2 C and D) and ex-situ XRD analysis of perovskite thin films at varying temperatures. For the in-situ temperature dependent XRD analysis, the powders were heated gradually from 30 ºC − 150 ºC at a rate of 2 ºC per minute and the diffractograms were collected at 10 °C intervals. The detailed analysis of collected diffractograms shows that the characteristic peaks for α-phase at ~ 14° (100) and ~28° (200) start to emerge at 130 ºC for δ-$Cs_{0.1}FA_{0.9}PbI_3$ powder (Figure 3.2 C)while it appears at 150 ºC in the case of control δ-$FAPbI_3$ powder(Figure 3.2 D). Our results are in agreement with previous reports validating Cs incorporation into perovskite film through lowering of the phase transition temperature. [12] In the case of thin films, the smaller ionic radius of Cs than FA cation helps to reduce the Goldschmidt tolerance factor from 1.04 to the ideal range and there by induces extra phase stability at a moderately lower temperature. Similarly, δ-$Cs_{0.1}FA_{0.9}PbI_3$ powder undergoes a phase transition at a lower temperature compared to its FA analogue. In future, the lower transition temperature of our δ-$Cs_{0.1}FA_{0.9}PbI_3$ powder could be further employed in the defect-tolerant, solvent-free vacuum-processed perovskite solar cells from a single source instead of widely used multi-sourced co-sublimation.

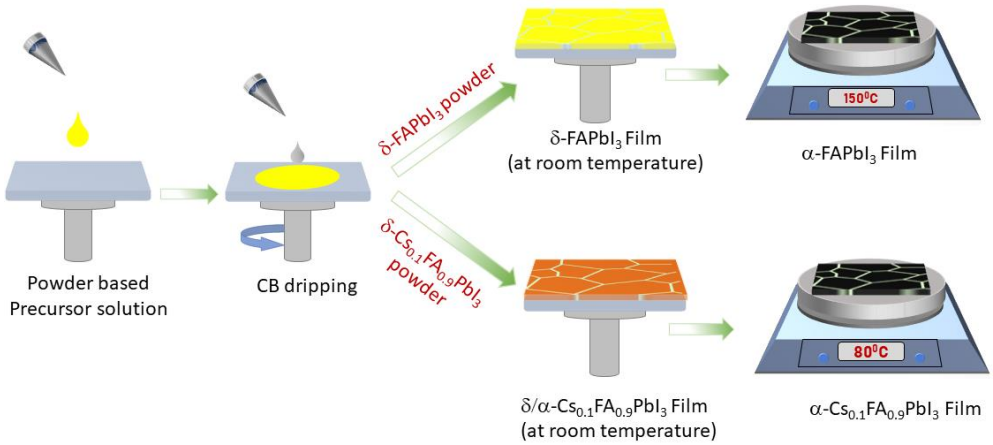

Figure. 3 Schematic illustration of the thin-film fabrication procedure for FAPI-150 and CsFAPI-80.

3.3.2 Thin film analysis

Yellow non-perovskite powders were dissolved in DMF:DMSO mixture (4:1) and the solution was stirred for 3 hr to complete the dissolution. The spin coated thin films were annealed at varying temperatures for 20 minutes as illustrated in Figure 3.3. To decipher the phase transition temperature, XRD studies of thin films deposited at diverse temperatures (Figure 3.4 A, B) was carried out. $FAPbI_3$ films were annealed at 60, 100 and 150 ºC (Figure 3.4 A) and we noted the formation of α- $FAPbI_3$ phase only at 150 ºC, and below 150 ºC it only represents the δ-$FAPbI_3$ signature diffractions (010) and (002).

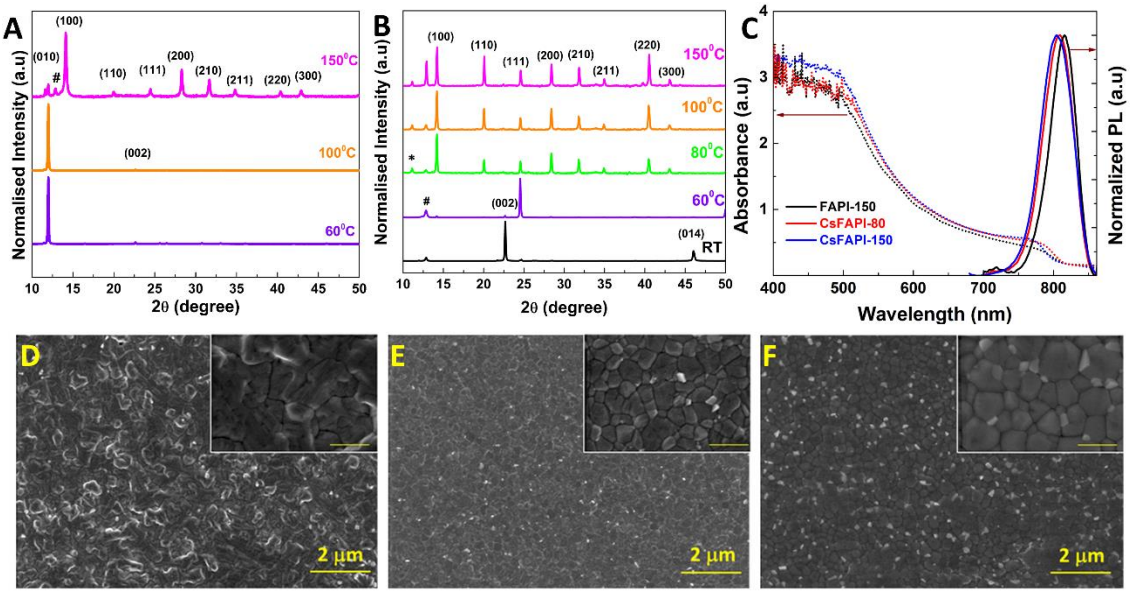

Figure 3. 4 (A, B) XRD measurements for perovskite thin films annealed at different temperatures, (A) $FAPbI_3$ films and (B) $Cs_{01}FA_{0.9}PbI_3$ films. The reflections indicated by * and # represent Bragg reflections associated with FAI and PbI_2, respectively. (C) Normalized UV-Vis absorption and steady-state photoluminescence spectra of FAPI-150 (black), CsFAPI-80 (red) and CsFAPI-150 (blue) perovskite films. (D-F) top view of SEM images of perovskite films (D) FAPI-150, (E) CsFAPI-80, and (F) CsFAPI-150; the insets are the corresponding zoom-in images with a scale bar of 500 nm.

XRD spectra of $Cs_{0.1}FA_{0.9}PbI_3$ films annealed at 25, 60, 80, 100 and 150 ºC are shown (Figure 3.4 B). At RT, we observed diffractions corresponding to δ-phase at (002), (014) and a weak diffraction corresponding to α-phase at (111), i.e. Cs incorporation enables the phase transition from room temperature to form a δ/α phase junction where the major fraction is from δ-$FAPbI_3$. The diffraction peak at 12.8° indicates the presence of excess

PbI_2. By annealing at 60 ºC, (111) diffraction peak becomes intense and (100), (110), (200) and (210) diffractions also emerge. The presence of weak (002) diffraction specifies the formation of δ/α phase junction with a major fraction of the α-phase. The diffraction peaks for δ-$FAPbI_3$ disappeared and the highly oriented α-$FAPbI_3$ phase is formed by annealing at 80 ºC. We noted a weaker diffraction peak at ~110, signalling the presence of FAI. [28] The trivial amounts of PbI_2 and FAI will improve the crystal quality by passivating the grain boundaries and vacancies.[29,30] δ-$FAPbI_3$ phase remains fully inhibited even at high temperatures. Notably, we observed a difference in preferential orientation for low temperature processed films (LT≤ 60 ºC) and high temperature processed films (HT ≥ 80 ºC). HT films have strong diffractions from (hk0) planes while the low temperature films show diffractions from the (hkl) planes. Arguably, these infer that strongly textured δ-phase free perovskite can be formed from 80 ºC.

The powder diffractograms (Figure S3.2, see SI) of $FAPbI_3$ at 150 ºC (FAPI-150), $Cs_{0.1}FA_{0.9}PbI_3$ fabricated at 80 ºC (CsFAPI-80) and 150 ºC (CsFAPI-150) was recorded. We observed the δ-phase (010) diffraction in $FAPbI_3$ disappeared on Cs incorporation. The diffraction peak intensities are higher for $Cs_{0.1}FA_{0.9}PbI_3$ as compared to the $FAPbI_3$ film. The (100) diffractions of the above three cases are compared in the inset. The full width at half maximum (FWHM) decreases from 0.24° to 0.11° and 0.10° for FAPI-150, CsFAPI-80 and CsFAPI-150 respectively. The increase in relative intensity of diffraction peaks and narrowing of FWHM indicates higher crystallinity. It is in agreement with the previous reports of Cs induced crystallinity enhancement in perovskites.[31] UV-Visible absorption spectra and the steady state photoluminescence spectra were measured to deduce the changes in absorption and fluorescence (Figure 3.4 C), and the bandgap was calculated from the tauc plot (Figure S3.3, see SI). Cs incorporation induces a blue shift in the emission, an increment in the bandgap and the absorption coefficient. [28] The blue shifting in the fluorescence spectra of CsFAPI-150 than of CsFAPI-80 indicates the concentration of Cs amalgamation. At high temperatures (150 °C), more Cs ions are structurally incorporated into $FAPbI_3$, also supported by the shifted (100) diffraction peak (Figure 3.2 D). Next, microstructure analysis was made by performing scanning electron microscopy (SEM) experiments (Figure 3.4 D-F). Large area uniformity in the microstructure can be inferred, while the inset represents images at a scale bar of 500 nm to gaze the crystallinity and grain size. It can be deduced from the micrographs that Cs insertion reduces the grain boundaries, grain size and pinholes while inducing higher

crystallinity. Cs incorporation increases the density of crystal nuclei in the film formation to reduce the grain size and the absence of agglomeration of crystallites enhances the perovskite crystallinity.[32] Grain size increment refers to higher crystallinity and the presence of PbI_2 was noted for CsFAPI-150 as compared to CsFAPI-80, in agreement with PXRD data (Figure S3.2, see SI). Further, we have studied the influence of Cs concentration, where $FAPbI_3$ and $Cs_xFA_{(1-x)}PbI_3$ (x = 0.05, 0.1) films were annealed at 150 and 80 ºC respectively (Figure S3.4, see SI). On varying the x = 0 − 0.1, the δ-phase (010) gradually disappears and the PbI_2 phase becomes weaker. High phase purity and low annealing temperature of CsFAPI-80 allow low-temperature processed solar cells employing $FAPbI_3$ and choice of the substrates.

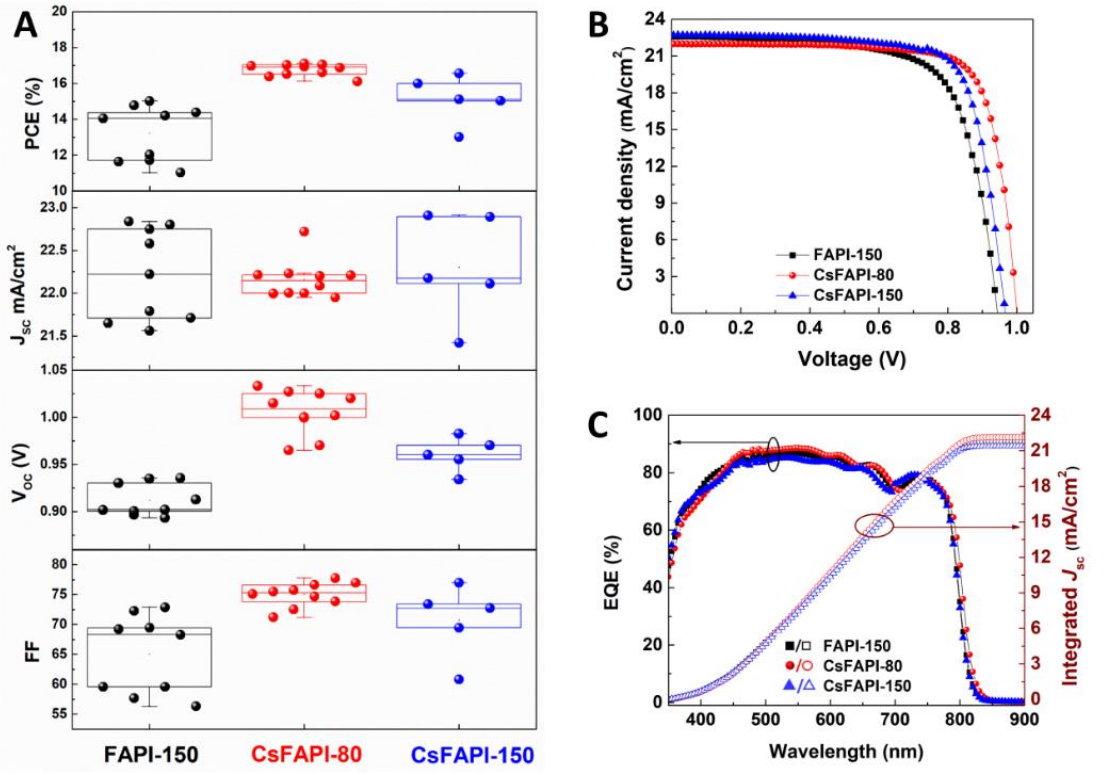

Figure 3. 5 (A) Statistical deviation of the photovoltaic parameters for the devices prepared from the different perovskite layers. The data were obtained under AM 1.5G, one sun illumination at reverse scan (V_{OC} to J_{SC}). (B) *J*−*V* curves for FAPI-150, CsFAPI-80, and CsFAPI-150 PSCs fabricated through the powder method, (C) the corresponding IPCE spectra and integrated currents.

3.3.3 Photovoltaic evaluation

To unravel the merits of the synthesized perovskite powder, PSCs were fabricated using a device architecture of FTO/c-TiO_2/SnO_2-QD/perovskite/Spiro-OMeTAD/Au. Firstly, the device parameters with pre-synthesized perovskite powder-based PSCs was evaluated and the corresponding device statistics are summarised (Figure 3.5 A and Table A1-A3, Appendix A). The pristine FAPI-150 based PSCs gave an average PCE of 13.196% (±1.56) with an open-circuit voltage (V_{OC}) of 912.06 (±17.06) mV, short-circuit current (J_{SC}) of 22.22 (±0.55) $mAcm^{-2}$ and fill factor (FF) of 65.04% (±6.63) and the Cs incorporation boosted the efficiency of CsFAPI-150 to 15.14% (±1.22) with V_{OC} of 959.39 (±15.7) mV, J_{SC} of 22.41 (±0.57) $mAcm^{-2}$ and FF of 70.43% (±5.22). Remarkably, the champion device fabricated from CsFAPI-80 absorber layer gave the average PCE of 16.75 % (±0.32) with a V_{OC} of 1005.7 (±23.2) mV, J_{SC} of 22.16 (±0.21) $mAcm^{-2}$ and FF of 75.20% (±2.06). *J-V* characteristics (Figure 3.5 A) under AM 1.5G illumination for devices with PCE of 15.01% (V_{OC} = 912.7mV, J_{SC} = 22.75 $mAcm^{-2}$, FF = 72.30%), 16.60% (V_{OC} = 965 mV, J_{SC} = 22.71 $mAcm^{-2}$, FF = 75.73) and 17.11% (V_{OC} = 1000 mV, J_{SC} = 22.00 $mAcm^{-2}$, FF = 77.76%) for FAPI-150, CsFAPI-150 and CsFAPI-80, respectively, are presented. The PCE improvements on Cs inclusion is ascribed to the significant increment in V_{OC} and *FF*. The series (R_S) and shunt resistance (R_{sh}) calculated from the inverse slope near zero J_{SC} and V_{OC} region respectively, can influence the V_{OC} and *FF*. [24] Pristine FAPI-150 showed higher value of R_S (5.03 $\Omega.cm^2$) as compared to CsFAPI-150 (3.86 $\Omega.cm^2$). Lowering the annealing temperature to 80 ºC further decreases the R_S and achieved 3.25 $\Omega.cm^2$ for CsFAPI-80. R_{sh} showed by FAPI-150 (2.02 $k\Omega cm^2$) increases to 3.64 and 7.27 $k\Omega.cm^2$ for CsFAPI-150 and CsFAPI-80 respectively. The V_{OC} and *FF* increment in CsFAPI-80 is attributed to the 35.4% and 23.3% decline in R_S and ~400% and ~200% increase in R_{sh} over FAPI-150 and CsFAPI-150 respectively. We calculated the hysteresis index (Table 3.1 and Figure S3.5, see SI) using the standard equation,[33] Cs incorporation lower the hysteresis, notably CsFAPI-80 exhibited a lower (0.02) than CsFAPI-150 (0.06).

Table 3. 1 *J-V* parameters for the best performing PSCs fabricated through powder method.

Samples		V_{OC} **(V)**	J_{SC} **(mAcm^{-2})**	**FF (%)**	**PCE (%)**	R_S **(Ω.cm^2)**	R_{sh} **(kΩ.cm^2)**	**HI**
FAPI-150	RS	0.913	22.75	72.30	15.01	5.03	2.02	
	FS	0.913	22.55	63.82	13.13	6.96	1.60	
	Average	0.913	22.65	68.06	14.07			0.15
CsFAPI-80	RS	1.000	22.00	77.76	17.11	3.25	7.27	
	FS	1.014	22.05	73.69	16.47	4.03	2.85	
	Average	1.007	22.02	75.72	16.79			0.02
CsFAPI-150	RS	0.965	22.71	75.73	16.60	3.86	3.64	
	FS	0.969	22.63	69.97	15.34	4.35	1.03	
	Average	0.967	22.67	72.85	15.97			0.06

Spectral dependence of the external quantum efficiencies (EQEs) (Figure 3.5 B) for all the PSCs displayed a similar flat nature across the 450-700nm range and the usage of same transport layers ended up with similar EQEs of >80%. In agreement with the UV-VIS absorption spectra, CsFAPI-80 showed moderately lower EQE response at lower wavelength, and a slightly higher EQE (>85%) at 450-700nm which can be attributed to improved film quality. The superior EQEs and the moderate drops near ~720nm signals the lower recombination. The calculated integrated J_{SC} estimated from EQE data (Figure 3.5 B) are 21.79, 22.14 and 21.40 mAcm^{-2} for FAPI-150, CsFAPI-80 and CsFAPI-150 respectively, are in accordance with the J_{SC} obtained from *J-V* measurements. On comparing the effect of the annealing temperature of perovskite layers on the device performance, we infer that the low temperature processed CsFAPI-80 (80 ºC) is higher than CsFAPI-150 (150 ºC). They can be synthesized in a large scale in powder form to unify the results or for its commercial endeavour.

Reduced performance from conventional $FAPbI_3$ was reported due to the poor interface and higher trap densities than the powder analogue which ultimately lowers the V_{OC} and *FF*.[23] To decipher the advantages of powder method over the conventional method of Cs incorporated $FAPbI_3$, we compared the PSCs fabricated through the conventional method employing same grade PbI_2 (99%), and the *J-V* characteristics are presented (Figure 3.6, Table S3.1- S3.3, see SI). The best performing PSCs from conventional method showed lower PCE of 12.62% (V_{OC} = 875.7 mV, J_{SC} = 22.71 $mAcm^{-2}$, *FF* = 63.46%), 15.18% (V_{OC} = 883.50 mV, J_{SC} = 23.17 $mAcm^{-2}$, *FF* = 73.83%) and 14.03% (V_{OC} = 934.8 mV, J_{SC} = 21.59 $mAcm^{-2}$, FF = 69.52%) for FAPI-150, CsFAPI-150 and CsFAPI-80 respectively. In all the configurations, V_{OC} and *FF* decreases significantly as compared to our developed powder method. High V_{OC} deficit of 81.5 and 65.2 mV for conventional CsFAPI-150 and CsFAPI-80 respectively from their powder analogues are attributed to poor interface.[23] Arguably, it can be concluded that the powder method is superior over the conventional method to fabricate the MA, Br-free PSCs that can also be processable at low temperature.

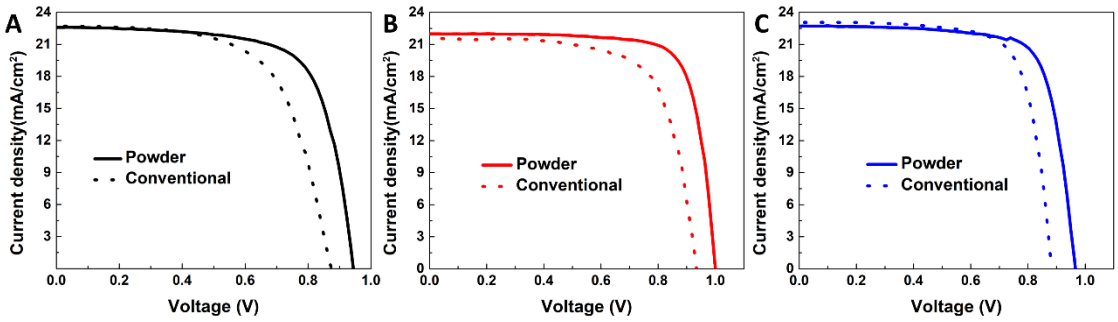

Figure 3. 6 *J-V* curves of PSCs fabricated through powder and conventional methods, (A) FAPI-150, (B) CsFAPI-80 and (C) CsFAPI-150.

We performed thermal admittance spectroscopy at varying temperature to reveal the shallow and deep defect density and trap energy distribution within the band gap of $CsFAPbI_3$ based PSCs.[34,35] Briefly, dark capacitance-frequency (*C-f*) measurements were measured at different temperatures on the $CsFAPbI_3$ based fabricated PSCs from pre-synthesized powder without applying bias voltage (Figure S3.6 and S3.7, see SI). The frequency (*f*) ranges from 20 to 10^6 Hz. The trap density of state ($t\text{-}_{DOS}$) and energy distribution at room temperature can be derived from the frequency dependent capacitance measurement [36] and the detailed procedure can be found in the Appendix A

(Figure S3.6, 3.7 and Note S1, see SI). Figure 3.7 A shows the extracted trap density profile (t_{DOS}) as a function of frequency-related energy (E_ω) for CsFAPI-80 and CsFAPI-150. In both types of devices, the trap density profile (t_{DOS}) shows the broad distribution with two peak maximums at lower and higher energies. In CsFAPI-150 based devices the peak maximum of t_{DOS} (1.175×10^{17} $eV^{-1}cm^{-3}$) was found at E_ω = 0.119 eV which shifts toward lower energy regimes and shows a maximum at 0.053 eV in CsFAPI-80 based devices with an almost similar value of t_{DOS} ($1.579 \times 10^{17} eV^{-1}cm^{-3}$).

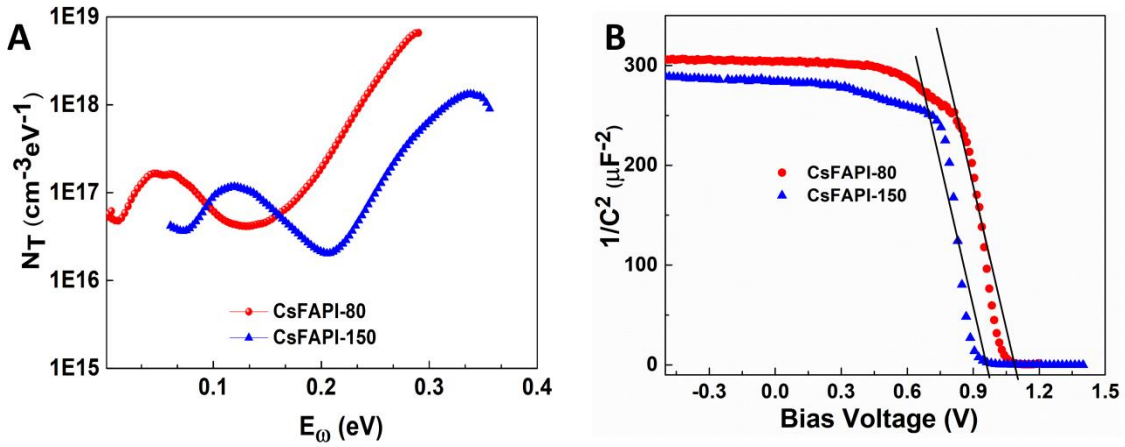

Figure 3. 7 (A) calculated trap density of state (N_T) at RT (25 ºC) of $CsFAPbI_3$ based perovskite solar cells, i.e., CsFAPI-80 and CsFAPI-150 and (B) C^{-2} vs. bias voltage measured on CsFAPI-80 and CsFAPI-150 solar cells at room temperature.

Further t_{DOS} profile of CsFAPI-150 based devices showed another Gaussian peak at higher energy around 0.34 eV, which corresponds to deeper defect states with a density of $1.32 \times 10^{18} eV^{-1}cm^{-3}$. In the case of CsFAPI-80, the onset of this high energy second Gaussian peak noted at 0.29 eV. The trap density of the state peak near to 0.119 eV is generally ascribed to the shallow defects near to valence band edge, while the peak at >0.3 eV corresponds to a deeper defect in $CsFAPbI_3$, which shows a similar value of $CsFAPbI_3$ perovskite. The shift of t_{DOS} towards lower energy in CsFAPI-80 devices signals that the charge carriers captured by these traps near the valence band edge can be thermally activated and participate in the charge transportation and extraction, which leads to improvement in V_{OC} and *FF* for CsFAPI-80 based devices. Moreover, an improved build-in potential of 1.10 V for the CsFAPI-80 based PSCs at 10 kHz, while CsFAPI-150 gave a value of 0.97 V from Mott-Schottky analysis as seen in Figure 3.7 B.

The fabricated PSCs were kept at maximum power point (MPP) tracking under operational conditions (continuous 1 sun illumination under 40-45% relative humidity at room temperature) (Figure 3.8). The CsFAPI-80 and CsFAPI-150 based devices retained ~100% whereas FAPI-150 showed decrement from their original PCEs after 1000s. The achieved device stability for both CsFAPI-80 with CsFAPI-150 supports the merit of pre-synthesized powder based PSCs, while CsFAPI-80 also allows choice of substrates. We have also noted the stability of PSCs fabricated through conventional PSCs was significantly lowered as compared to the devices fabricated through the powder method under MPP tracking, see Figure S3.8, SI.

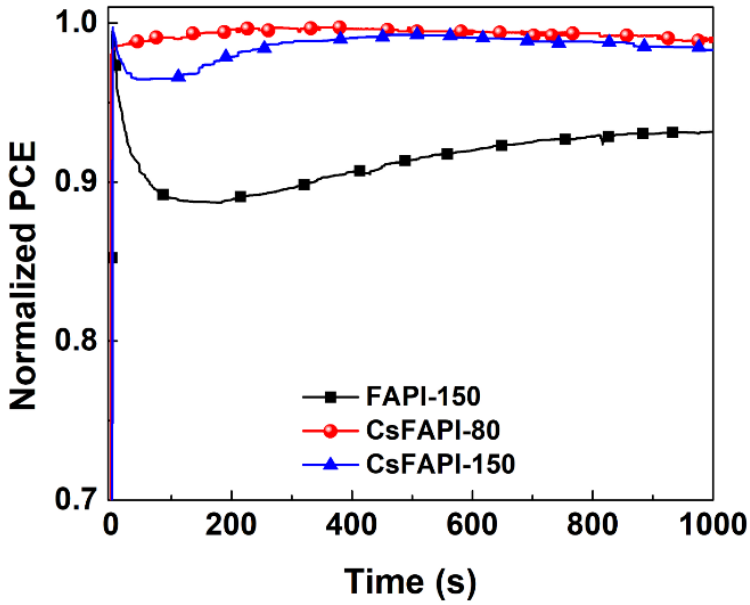

Figure 3. 8 Normalized PCE for 1000 s of continuous MPP tracking under operational condition at ambient atmosphere for the fabricated PSCs from powder precursors.

3.4 Conclusion

To summarize, we demonstrated room-temperature synthesis of MA and Br-free, δ-$Cs_{0.1}FA_{0.9}PbI_3$ powder perovskite precursor from low-grade PbI_2 (99%) and fabricated the perovskite solar cells. The fabricated devices gave lower hysteresis value and a 100% PCE retainment under MPP tracking for 1000s along with a competitive power conversion efficiency in excess of 17%. The Cs alloying resulted in a δ-phase free, perovskite absorber fabricated at a temperature as low as 80 °C. The low-temperature

annealing will prevent the perovskite from degradation and push perovskites solar cells towards cost-effective large-scale production and can adapt the roll-to-roll manufacturing process on flexible substrates.

3.5 Experimental Procedures

3.5.1 Materials

All chemicals were purchased from Sigma Aldrich unless and otherwise stated and were used as received without any further purification.

3.5.2 Perovskite powder synthesis

Synthesis of δ-$Cs_xFA_{(1-x)}PbI_3$ powder: δ-$Cs_xFA_{(1-x)}PbI_3$ was synthesized through a room temperature precipitation method where, CsI (>99%, TCI) and FAI (Greatcell Solar Ltd.) was dissolved in 100 ml of acetonitrile (HPLC grade, Alfa Aeser) by stirring. CsI content was varied from 0 mmol for x=0 to 1 mmol for x= 0.1 and the total iodide salt concentration kept always 10 mmol. 8.3 mmol of PbI_2 (99%, Sigma-Aldrich) was added to the stirring solution and allowed the stirring to continue for 24 hours. The yellow powders were filtered and washed five times with acetonitrile solvent to remove the unreacted precursors. The final product was dried under a continuous vacuum for another 24 hours and stored in Ar filled glove box. The yield of synthesized powders was calculated in mole percentage with respect to the PbI_2 concentration used. All the procedures were done under ambient environmental conditions, see the schematic representation in Figure 3.1.

3.5.3 Device fabrication

Cleaned FTO substrates (see section 2.3.1 for details) were then heated gradually to 500 ºC on a hotplate and TiO_2 compact layer (c-TiO_2) was deposited by spray pyrolysis (see section 2.3.4) with a pre-diluted titanium diisopropoxide bis-(acetylacetonate) solution in ethanol (1:19 volume ratio). The samples were allowed to cool after 30 minutes annealing. SnO_2 quantum dots synthesized by a previously reported method [33] was spun coated (see section 2.3.3) on FTO/c-TiO_2 substrate followed by 45 minute annealing at 150 ºC. The FTO/c-TiO_2/QD-SnO_2 substrates was treated with UV-Ozone for 20 minutes and transferred to the Ar filled glove box for perovskite and HTM deposition. For powder

method, 1.25 M perovskite solutions were prepared by dissolving 1.25 mmol synthesized precursor powders in a 1 ml DMF:DMSO mix solvent (4:1 volume ratio). For the conventional method, the precursor solutions was prepared by stoichiometric mixing of PbI_2 (1.25 mmol), FAI (1.25 and 1.125 mmol for FAPI and CsFAPI respectively) and CsI (0, 0.125 mmol for FAPI and CsFAPI respectively) in 1 ml DMF:DMSO mix solvent (4:1 volume ratio). The solutions were stirred overnight at 50 ºC in order to complete the dissolution. The perovskite solution was filtered via a PTFE filter with 0.45µm pore size and spin-coated in two steps: 1000 rpm for 5 s and 5000 rpm for 20 s. 100 µl chlorobenzene (CB) was dropped on the surface 5 s prior to the end of the program. The substrates were immediately transferred to a hotplate and annealed at 150 ºC for FAPI-150, CsFAPI-150 respectively, and 80 ºC for CsFAPI-80. Afterward, a solution of 60 mM spiro-OMeTAD in 0.8 mL CB is prepared by adding 23 µL of 4-tert-butylpyridine and 14 µL from the solution of bis(trifluoromethylsulfonyl)imide lithium salt (520 mg LITFSI in 1 mL acetonitrile). The HTM solution is spun-coated on top of the perovskite layer at 4000 rpm for 30 s. Finally, the device is completed by thermal evaporation of a 70 nm thick gold layer as a back-contacted electrode.

3.5.4 Characterization Techniques

Instrumental details has been explained in detail in section 2.4.

3.6 Supporting information

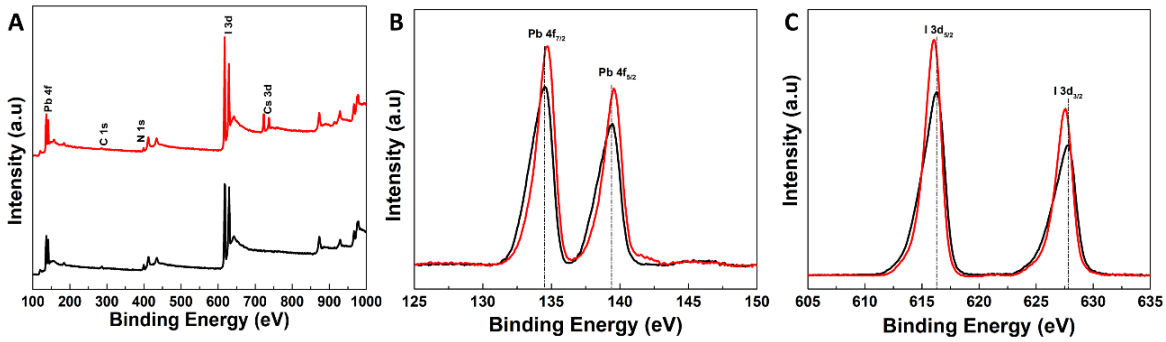

Figure S3. 1 (A-C) XPS spectra of δ-$FAPbI_3$ (black) and δ-$Cs_{0.1}FA_{0.9}PbI_3$ (red) powder precursors, (A) survey spectrum, (B) core level spectra of Pb 4f and (C) I 3d signals.

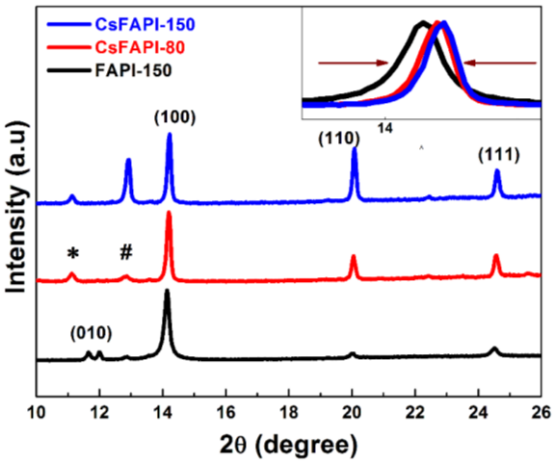

Figure S3. 2 XRD patterns for FAPI-150, CsFAPI-80 and CsFAPI-150 films. Inset represents magnified view of (100) diffraction. The reflections marked with * and # corresponds to FAI and PbI_2, respectively.

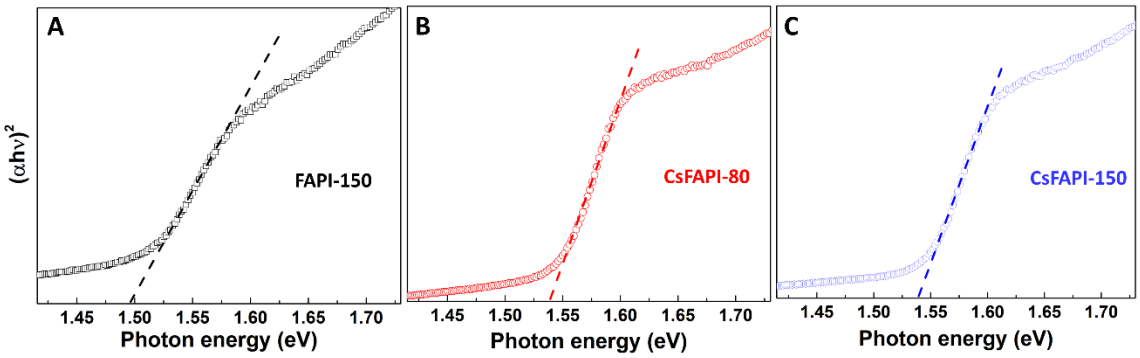

Figure S3. 3 Tauc plots of perovskite absorbers from powder method, (A) FAPI-150, (B) CsFAPI-80 and (C) CsFAPI-150.

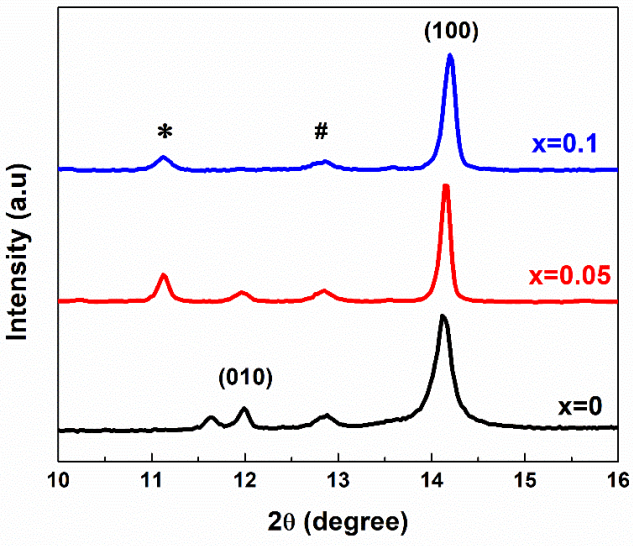

Figure S3. 4 Diffractograms for $Cs_xFA_{(1-x)}PbI_3$ perovskite where Cs concentration was varied from x = 0 − 0.1. The Cs containing perovskites layers were fabricated at 80 ºC

and $FAPbI_3$ at 150 ºC. The reflections marked with * and # corresponds to FAI and PbI_2, respectively.

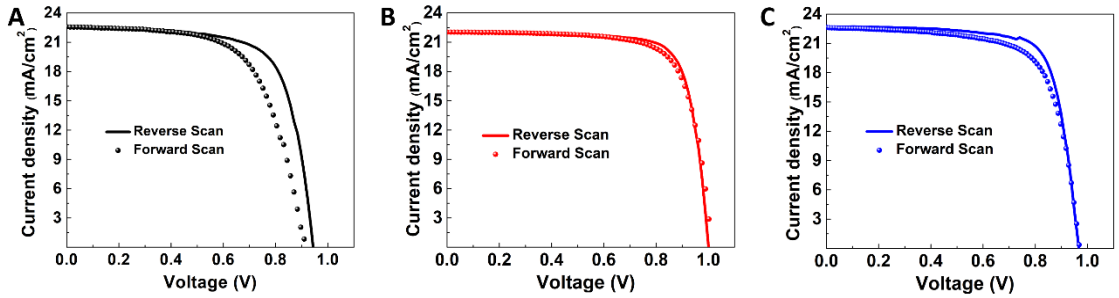

Figure S3. 5 *J-V* hysteresis curves of (A) FAPI-150, (B) CsFAPI-80 and (C) CsFAPI-150 PSCs.

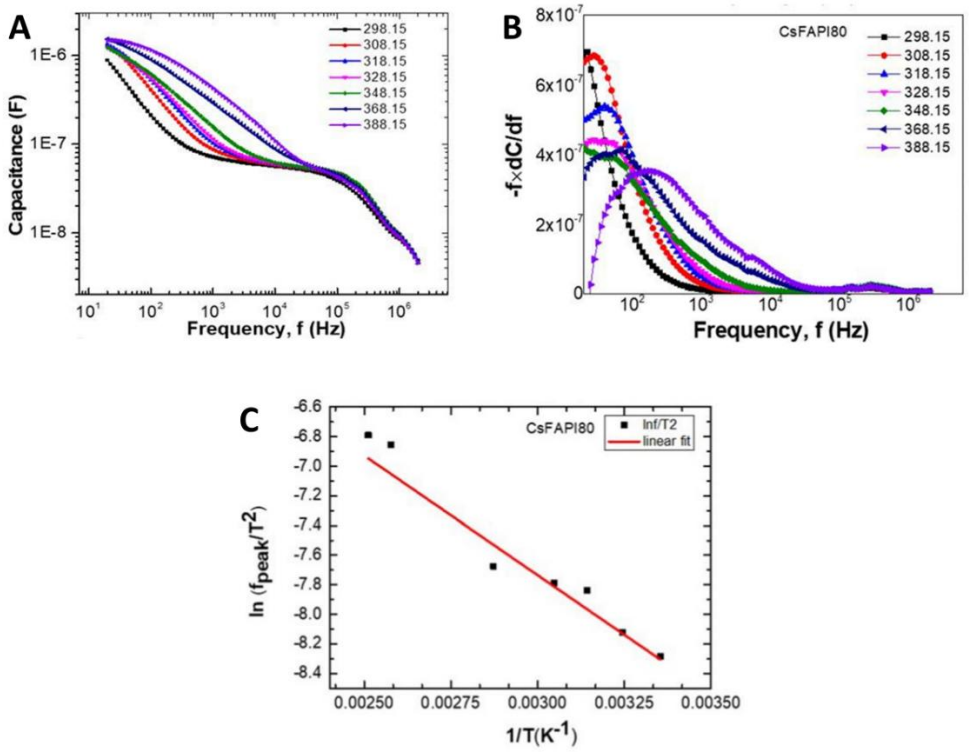

Figure S3. 6 (A) Capacitance-frequency (*C-f*) plots for CsFAPbI-80 based PSC in the dark at different temperatures, (B) *–f dC/df* versus frequency at variable temperature and (C) Arrhenius plot of ln(f_{peak}/T^2) vs. 1/T .

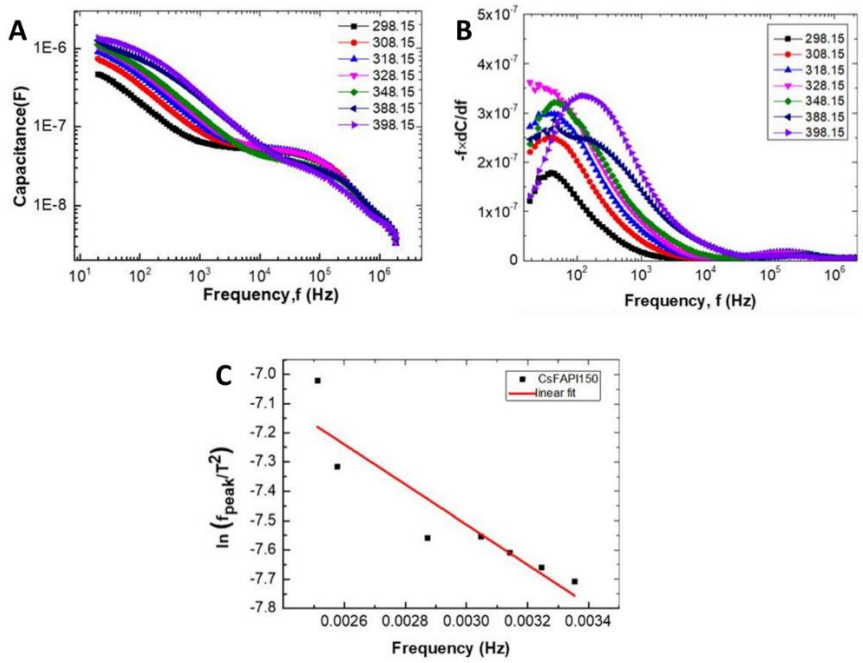

Figure S3. 7 (A) Capacitance-frequency (*C-f*) plots for CsFAPbI-150based PSC in the dark at different temperatures, (B) *–f dC/df* versus frequency at variable temperature and (C) Arrhenius plot of $\ln(f_{peak}/T^2)$ vs. 1/T .

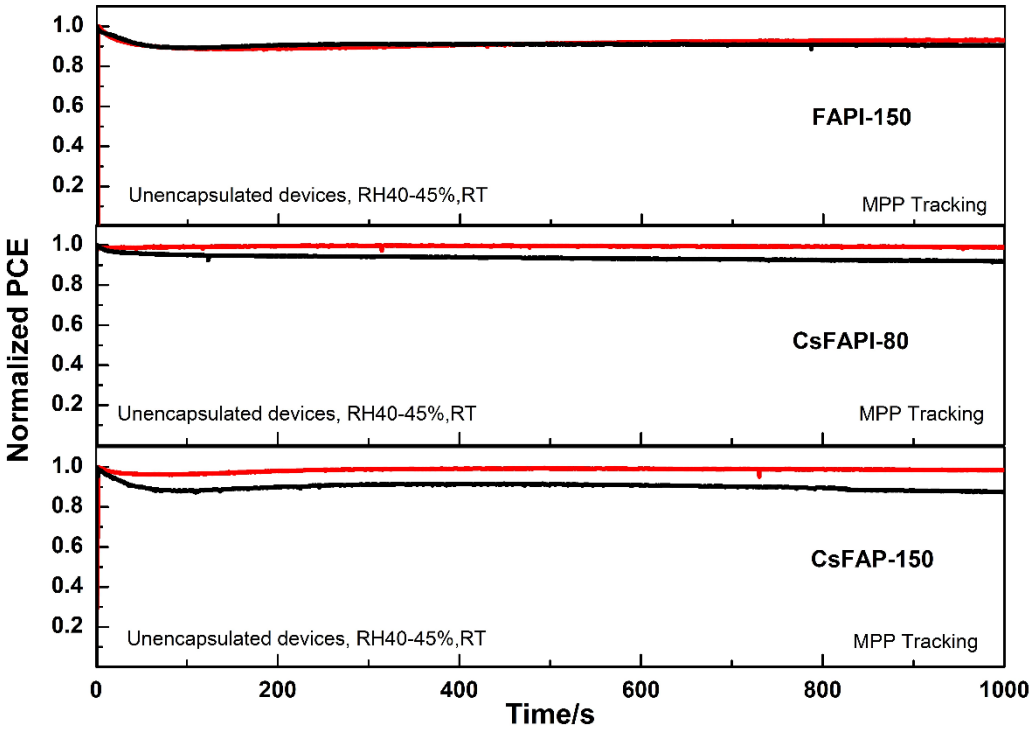

Figure S3. 8 Normalized PCE of PSCs from conventional (black curves) and powder method (red curves) for 1000 s of continuous MPP tracking under operational condition at ambient atmosphere.

Table S3. 1 Open circuit voltage (V_{OC}), short-circuit current density (J_{SC}), fill factor (FF) and power conversion efficiency (PCE) of the perovskite solar cell incorporating

FAPI-150 (powder method). The data were obtained under AM 1.5G one-sun illumination at reverse scan.

	Device ID	V_{OC} **[V]**	J_{SC} **[mAcm^{-2}]**	***FF*** **[%]**	**PCE [%]**
1	A-1	0.89	22.88	69.44	14.20
2	A-2	0.90	22.59	72.90	14.77
3	A-3	0.93	22.22	69.22	14.37
4	A-4	0.90	21.79	59.58	11.71
5	A-5	0.90	22.84	68.31	14.05
6	A-6	0.93	21.65	57.68	11.62
7	A-7	0.91	22.75	72.30	15.01
8	A-8	0.90	21.71	56.32	11.02
9	A-9	0.93	21.56	59.58	12.02
	Average	0.91	22.22	65.04	13.19
	STDEV	0.01	0.55	6.63	1.56

Table S3. 2 Open circuit voltage (V_{OC}), short-circuit current density (J_{SC}), fill factor (FF) and power conversion efficiency (PCE) of the perovskite solar cell incorporating CsFAPI-80 (powder method). The data were obtained under AM 1.5G one-sun illumination at reverse scan.

	Device ID	V_{OC} **[V]**	J_{SC} **[mAcm^{-2}]**	***FF*** **[%]**	**PCE [%]**
1	B-1	1.03	22.09	74.71	16.93
2	B-2	0.97	22.20	76.63	16.50
3	B-3	0.97	22.72	75.73	16.60
4	B-4	1.00	22.00	77.77	17.11
5	B-5	1.00	22.00	77.46	17.03
6	B-6	1.02	22.23	72.54	16.39

7	B-7	1.03	22.21	73.86	16.86
8	B-8	1.00	22.00	77.00	16.96
9	B-9	1.02	22.21	71.22	16.11
10	B-10	1.03	21.95	75.08	17.04
	Average	1.01	22.16	75.20	16.75
	STDEV	0.02	0.21	2.06	0.32

Table S3. 3 Open circuit voltage (V_{OC}), short-circuit current density (J_{SC}), fill factor (FF) and power conversion efficiency (PCE) of the perovskite solar cell incorporating CsFAPI-150 (powder method). The data were obtained under AM 1.5G one-sun illumination at reverse scan.

	Device ID	V_{OC} **[V]**	J_{SC} **[mAcm^{-2}]**	***FF*** **[%]**	**PCE [%]**
1	C-1	0.98	22.12	69.46	15.10
2	C-2	0.97	22.71	75.73	16.60
3	C-3	0.96	22.89	72.73	15.99
4	C-4	0.96	21.42	73.42	15.02
5	C-5	0.93	22.91	60.80	13.01
	Average	0.96	22.41	70.43	15.14
	STDEV	0.02	0.57	5.22	1.22

Note S1.

Derivation for the density of traps (t_{DOS}) and energy distribution:

The trap density of state (N_T) and energy distribution can be derived from the frequency dependent capacitance measurement (Figure S3.6 A and S3.7 A) using the equations 1 and 2:

$$N_T\,(E_\omega) = \frac{V_{bi}}{qW\,k_BT}\left(-f\frac{dC}{df}\right) \text{.....(S3.1)}$$

$$E_\omega = k_B\,T ln\left(\frac{v_o}{f}\right) \text{.....(S3.2)}$$

Where N_T is the trap density of state (t_{DOS}), V_{bi} is the built in potential, W is the depletion width, q is elemental charge, K_B is Boltzmann constant, T is temperature in Kelvin, C is the capacitance, and $\omega = 2\,\pi f$ is the applied angular frequency and E_ω is the demarcation energy. v_0 is the attempt-to-escape frequency (ATEF), which was derived from frequency differential capacitance spectra (-f × dc/df) (Figure S3.7 B and S3.8 B) as reported. [33,36,37]

In short, ln (f_{peak}/T^2) vs. 1/T plot is shown in Figure S3.7 C & 3.8 C from which the value of v_0 can be determined. The f_{peak} was extracted from the plot of frequency differential capacitance spectra (–fdC/df) as a function of *f*, see Figure S3.7 B and S3.8 B. V_{bi} and W are extracted from the capacitance-voltage (from C^{-2}-V) measurements through Mott-Schottky analysis, see Figure 3.7 B.

3.7 References

(1) Kojima, A., Teshima, K., Shirai, Y., Miyasaka, T., 2009. Organometal halide perovskites as visible-light sensitizers for photovoltaic cells. Journal of the American Chemical Society 131, 6050–6051. doi:10.1021/ja809598r.

(2) Kim, H.-S., Lee, C.-R., Im, J.-H., Lee, K.-B., Moehl, T., Marchioro, A., Moon, S.-J., Humphry-Baker, R., Yum, J.-H., Moser, J.E., Grätzel, M., Park, N.-G., 2012. Lead iodide perovskite sensitized all-solid-state submicron thin film mesoscopic solar cell with efficiency exceeding 9%. Scientific Reports 2. doi:10.1038/srep00591.

(3) Best research-cell efficiency chart [WWW Document], n.d. . NREL.gov. URL https://www.nrel.gov/pv/cell-efficiency.html (accessed 7.8.23).

(4) Manser, J.S., Saidaminov, M.I., Christians, J.A., Bakr, O.M., Kamat, P.V., 2016. Making and breaking of lead halide perovskites. Accounts of Chemical Research 49, 330–338. doi:10.1021/acs.accounts.5b00455.

(5) Abdelmageed, G., Jewell, L., Hellier, K., Seymour, L., Luo, B., Bridges, F., Zhang, J.Z., Carter, S., 2016. Mechanisms for light induced degradation in $MAPbI_3$ perovskite thin films and solar cells. Applied Physics Letters 109. doi:10.1063/1.4967840.

(6) Juarez-Perez, E.J., Ono, L.K., Uriarte, I., Cocinero, E.J., Qi, Y., 2019. Degradation mechanism and relative stability of methylammonium halide based perovskites analyzed on the basis of acid–base theory. ACS Applied Materials & Interfaces 11, 12586–12593. doi:10.1021/acsami.9b02374.

(7) Lee, J.-W., Seol, D.-J., Cho, A.-N., Park, N.-G., 2014. High-efficiency perovskite solar cells based on the black polymorph of $HC(NH_2)_2PbI_3$. Advanced Materials 26, 4991–4998. doi:10.1002/adma.201401137.

(8) Jesper Jacobsson, T., Correa-Baena, J.-P., Pazoki, M., Saliba, M., Schenk, K., Grätzel, M., Hagfeldt, A., 2016. Exploration of the compositional space for mixed lead halogen perovskites for high efficiency solar cells. Energy & Environmental Science 9, 1706–1724. doi:10.1039/c6ee00030d.

(9) Pellet, N., Gao, P., Gregori, G., Yang, T.-Y., Nazeeruddin, M.K., Maier, J., Grätzel, M., 2014. Mixed-organic-cation perovskite photovoltaics for enhanced solar-light harvesting. Angewandte Chemie International Edition 53, 3151–3157. doi:10.1002/anie.201309361.

(10) Conings, B., Drijkoningen, J., Gauquelin, N., Babayigit, A., D'Haen, J., D'Olieslaeger, L., Ethirajan, A., Verbeeck, J., Manca, J., Mosconi, E., Angelis, F.D., Boyen, H.-G., 2015. Intrinsic thermal instability of methylammonium lead trihalide perovskite. Advanced Energy Materials 5, 1500477. doi:10.1002/aenm.201500477.

(11) Salado, M., Kazim, S., Ahmad, S., 2018. The role of Cs^+ inclusion in formamidinium lead triiodide-based perovskite solar cell. Chemical Papers 72, 1645–1650. doi:10.1007/s11696-017-0373-7.

(12) Yi, C., Luo, J., Meloni, S., Boziki, A., Ashari-Astani, N., Grätzel, C., Zakeeruddin, S.M., Röthlisberger, U., Grätzel, M., 2016. Entropic stabilization of mixed A-cation ABX_3 metal halide perovskites for high performance perovskite solar cells. Energy & Environmental Science 9, 656–662. doi:10.1039/c5ee03255e.

(13) Yao, D., Zhang, C., Pham, N.D., Zhang, Y., Tiong, V.T., Du, A., Shen, Q., Wilson, G.J., Wang, H., 2018. Hindered formation of photoinactive δ-$FAPbI_3$ Phase and hysteresis-free mixed-cation planar heterojunction perovskite solar cells with enhanced efficiency

via potassium incorporation. The Journal of Physical Chemistry Letters 9, 2113–2120. doi:10.1021/acs.jpclett.8b00830.

(14) Saliba, M.; Matsui, T.; Domanski, K.; Seo, J.-Y.; Ummadisingu, A.; Zakeeruddin, S. M.; Correa-Baena, J.-P.; Tress, W. R.; Abate, A.; Hagfeldt, A.; Gratzel, M. 2016. Incorporation of Rubidium Cations into Perovskite Solar Cells Improves Photovoltaic Performance. Science 354, 206-209. 10.1126/science.aah555.

(15) Salado, M., Calio, L., Berger, R., Kazim, S., Ahmad, S., 2016. Influence of the mixed organic cation ratio in lead iodide based perovskite on the performance of Solar Cells. Physical Chemistry Chemical Physics 18, 27148–27157. doi:10.1039/c6cp03851d.

(16) Lu, H., Liu, Y., Ahlawat, P., Mishra, A., Tress, W.R., Eickemeyer, F.T., Yang, Y., Fu, F., Wang, Z., Avalos, C.E., Carlsen, B.I., Agarwalla, A., Zhang, X., Li, X., Zhan, Y., Zakeeruddin, S.M., Emsley, L., Rothlisberger, U., Zheng, L., Hagfeldt, A., Grätzel, M., 2020. Vapor-assisted deposition of highly efficient, stable black-phase $FAPbI_3$perovskite solar cells. Science 370. doi:10.1126/science.abb8985.

(17) Jeon, N.J., Noh, J.H., Yang, W.S., Kim, Y.C., Ryu, S., Seo, J., Seok, S.I., 2015. Compositional Engineering of perovskite materials for high-performance solar cells. Nature 517, 476–480. doi:10.1038/nature14133.

(18) Ma, F., Li, J., Li, W., Lin, N., Wang, L., Qiao, J., 2017. Stable α/δ phase junction of formamidinium lead iodide perovskites for enhanced near-infrared emission. Chemical Science 8, 800–805. doi:10.1039/c6sc03542f.

(19) Masi, S., Gualdrón-Reyes, A.F., Mora-Seró, I., 2020. Stabilization of black perovskite phase in $FAPbI_3$ and $CSPbI_3$. ACS Energy Letters 5, 1974–1985. doi:10.1021/acsenergylett.0c00801.

(20) Ruan, S., Fan, R., Pai, N., Lu, J., Webster, N.A., Ruan, Y., Cheng, Y.-B., McNeill, C.R., 2019. Incorporation of γ-butyrolactone (GBL) dramatically lowers the phase transition temperature of formamidinium-based metal halide perovskites. Chemical Communications 55, 11743–11746. doi:10.1039/c9cc05753f.

(21) Kim, G., Min, H., Lee, K.S., Lee, D.Y., Yoon, S.M., Seok, S.I., 2020. Impact of strain relaxation on performance of α-formamidinium lead iodide perovskite solar cells. Science 370, 108–112. doi:10.1126/science.abc4417.

(22) Zhang, Y., Kim, S.-G., Lee, D.-K., Park, N.-G., 2018. $CH_3NH_3PbI_3$ and $HC(NH_2)_2PbI_3$ powders synthesized from low-grade PbI_2: Single Precursor for high-efficiency perovskite solar cells. ChemSusChem 11, 1813–1823. doi:10.1002/cssc.201800610.

(23) Zhang, Y., Seo, S., Lim, S.Y., Kim, Y., Kim, S.-G., Lee, D.-K., Lee, S.-H., Shin, H., Cheong, H., Park, N.-G., 2019. Achieving reproducible and high-efficiency (21%) perovskite solar cells with a presynthesized $FAPbI_3$ powder. ACS Energy Letters 5, 360–366. doi:10.1021/acsenergylett.9b02348.

(24) Wang, J.; Meng, F.; Li, R.; Chen, S.; Huang, X.; Xu, J.; Lin, X.; Chen, R.; Wu, H.; Wang, H.-L. 2020. Boosting Efficiency and Stability of Planar Inverted $(FAPbI_3)_x(MAPbBr_3)_{1-x}$ Solar Cells via $FAPbI_3$ and $MAPbBr_3$ Crystal Powders. Sol. RRL 4, 2000091. 10.1002/solr.202000091

(25) Prochowicz, D., Yadav, P., Saliba, M., Saski, M., Zakeeruddin, S.M., Lewiński, J., Grätzel, M., 2017. Reduction in the interfacial trap density of mechanochemically synthesized $MAPbI_3$. ACS Applied Materials & Interfaces 9, 28418–28425. doi:10.1021/acsami.7b06788.

(26) Heo, J.H., Im, S.H., 2016. Highly reproducible, efficient hysteresis-less $CH_3NH_3PbI_{3-x}Cl_x$ planar hybrid solar cells without requiring heat-treatment. Nanoscale 8, 2554–2560. doi:10.1039/c5nr08458j.

(27) Straus, D.B., Guo, S., Cava, R.J., 2019. Kinetically stable single crystals of perovskite-phase $CsPbI_3$. Journal of the American Chemical Society 141, 11435–11439. doi:10.1021/jacs.9b06055.

(28) Petrov, A.A., Goodilin, E.A., Tarasov, A.B., Lazarenko, V.A., Dorovatovskii, P.V., Khrustalev, V.N., 2017. Formamidinium iodide: Crystal Structure and Phase Transitions. Acta Crystallographica Section E Crystallographic Communications 73, 569–572. doi:10.1107/s205698901700425x.

(29) Lee, J.-W., Kim, D.-H., Kim, H.-S., Seo, S.-W., Cho, S.M., Park, N.-G., 2015. Formamidinium and cesium hybridization for photo- and moisture-stable perovskite solar cell. Advanced Energy Materials 5, 1501310. doi:10.1002/aenm.201501310.

(30) Jia, Y.; Neutzner, S.; Zhou, Y.; Yang, M.; Tapia, J. M. F.; Li, N.; Yu, H.; Cao, J.; Wang, J.; Petrozza, A.; Wong, C.; Zhao, N. Role of Excess FAI in Formation of High-Efficiency

$FAPbI_3$ -Based Light-Emitting Diodes. Advanced Functional Materials 2020, 30, 1906875. 10.1002/adfm.201906875

(31) Wu, Z.Y., Jian, B.-L., Hsu, H.-C., 2019. Photoluminescence characterizations of highly ambient-air-stable $CH_3NH_3PbI_3/PbI_2$ heterostructure. Optical Materials Express 9, 1882. doi:10.1364/ome.9.001882.

(32) Yu, Y., Wang, C., Grice, C.R., Shrestha, N., Chen, J., Zhao, D., Liao, W., Cimaroli, A.J., Roland, P.J., Ellingson, R.J., Yan, Y., 2016. Improving the performance of Formamidinium and cesium lead triiodide perovskite solar cells using lead thiocyanate additives. ChemSusChem 9, 3288–3297. doi:10.1002/cssc.201601027.

(32) Kim, H.-S., Park, N.-G., 2014. Parameters affecting i–v hysteresis of $CH_3NH_3PbI_3$ Perovskite Solar Cells: Effects of perovskite crystal size and mesoporous TiO_2 layer. The Journal of Physical Chemistry Letters 5, 2927–2934. doi:10.1021/jz501392m.

(33) Hemasiri, N.H., Kazim, S., Ahmad, S., 2020. Reduced trap density and mitigating the interfacial losses by placing 2D dichalcogenide material at perovskite/HTM interface in a dopant free perovskite solar cells. Nano Energy 77, 105292. doi:10.1016/j.nanoen.2020.105292.

(34) Salado, M., Andresini, M., Huang, P., Khan, M.T., Ciriaco, F., Kazim, S., Ahmad, S., 2020. Interface Engineering by thiazolium iodide passivation towards reduced thermal diffusion and performance improvement in Perovskite Solar Cells. Advanced Functional Materials 30, 1910561. doi:10.1002/adfm.201910561.

(35) Shao, Y., Xiao, Z., Bi, C., Yuan, Y., Huang, J., 2014. Origin and elimination of photocurrent hysteresis by fullerene passivation in $CH_3NH_3PbI_3$ planar heterojunction solar cells. Nature Communications 5. doi:10.1038/ncomms6784.

(36) Samiee, M., Konduri, S., Ganapathy, B., Kottokkaran, R., Abbas, H.A., Kitahara, A., Joshi, P., Zhang, L., Noack, M., Dalal, V., 2014. Defect density and dielectric constant in perovskite solar cells. Applied Physics Letters 105. doi:10.1063/1.4897329.

(37) Khan, M.T., Salado, M., Almohammedi, A., Kazim, S., Ahmad, S., 2019. Elucidating the impact of charge selective contact in halide perovskite through impedance spectroscopy. Advanced Materials Interfaces 6, 1901193. doi:10.1002/admi.201901193.

CHAPTER 4

4

MICROSTRAIN AND URBACH ENERGY RELAXATION IN $FAPbI_3$ BASED SOLAR CELLS THROUGH POWDER ENGINEERING AND PERFUOROALKYL PHOSPHATE IONIC LIQUID ADDITIVES

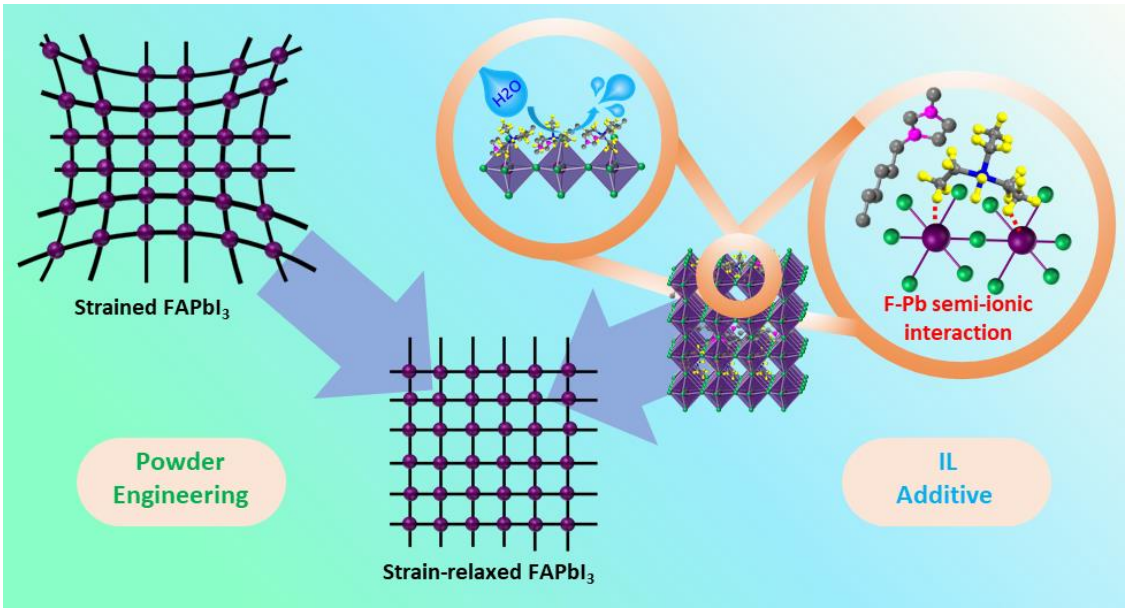

This chapter has been published in *ACS Applied Materials & Interfaces* entitled:

Microstrain and Urbach Energy Relaxation in $FAPbI_3$-Based Solar Cells through Powder Engineering and Perfluoroalkyl Phosphate Ionic Liquid Additives

Muhammed. P. U. Haris, Samrana Kazim, Shahzada Ahmad

M. P. U. Haris et al. ACS Appl. Mater. Interfaces 2022, 14, 21, 24546–24556.
DOI: 10.1021/acsami.2c01960

4.1 Abstract

The structural and electronic imperfections are the origin of the defects and lead to the non-radiative recombination that is detrimental to fabricating efficient perovskite solar cells (PSCs). Here we propose a powder engineering methodology for α-$FAPbI_3$ as a precursor material. Our developed methodology of α-$FAPbI_3$ synthesis mitigates the notorious structural and electronic imperfections evidenced by a significant decline in the microstrain and Urbach energy as compared to reported δ-$FAPbI_3$ powder and conventional precursor routes. In addition to the performance enhancement in photovoltaics, our engineered powder showed remarkable thermal and moisture stability along with cost-effectiveness through the employment of low-grade PbI_2. Further, through additive engineering, with the use of ultra-hydrophobic perfluoroalkyl phosphate anion-based ionic liquid, the microstrain and Urbach energy achieved the lowest value of 1.67×10^{-4} and 12.47 meV respectively as a result of defect passivation and a semi-ionic F-Pb interaction that stabilizes the surface.

4.2. Introduction

Reports suggests reduced defect density and improved stability in a single-crystalline perovskite when compared to polycrystalline.[1,2] Capitalizing on this opportunity, research is being carried out to achieve defect-free $FAPbI_3$ based PSCs through precursor engineering. In this direction, similar to our findings in the chapter 3, pre-synthesized non-perovskite δ-$FAPbI_3$ powder as the precursor material was employed to fabricate reproducible PSCs.[3,4] On comparing the performance between the δ-$FAPbI_3$ powder and α-$FAPbI_3$ powder as precursor material, in the literature, authors noted α-$FAPbI_3$ prepared from 3-methoxypropionitrile lags behind the δ-$FAPbI_3$ in terms of PSC performances.[3] Improved PCE of >21% was achieved from the δ-$FAPbI_3$ powder-based PSCs with the MACl additive, and the improved PCE was attributed to a 22% decrease in the defect density as compared to the conventional counterpart.[4] Recently, pre-synthesized α-$FAPbI_3$ powder-based PSCs with an octyl ammonium iodide passivation was reported, and the performance was further improved with a formate anion treatment which suppresses the anion vacancies at the grain boundaries.[5] The report describes the use of 35 mol% of MACl as an additive, while the compositional analysis suggests the structural incorporation of 5% MA^+ cation. It is worth noting that the $FAPbI_3$ based PSCs with >21%

PCE is achieved by the incorporation of excess MACl which comes with notorious instability and bandgap widening. Thus, the fabrication of MA-free $FAPbI_3$ based PSCs is of paramount importance.

Moreover, reports suggest that conventional partial doping or additive engineering with larger molecules can induce stress on the perovskite structure and thus produce microstrain impacts on structural stability, defects generation, and charge carrier dynamics.[6-8] Variations in the microstrain of the perovskite can create the disorder near the band edge. Thus, the qualitative analyses of the structural and energetic disorder of perovskite can be estimated from the microstrain and Urbach energy calculations.[9,10]

On the other hand, ionic liquids (ILs) have emerged as a promising non-volatile additive in PSCs due to their hydrophobic nature, high chemical and thermal stability, low-temperature processability, and excellent electrochemical properties. The introduction of ILs has been reported to assist in perovskite crystal growth, improving the crystallinity, and adjusting the surface defect, which in turn improves the open-circuit voltage (V_{OC}) and the stability against atmospheric stresses. However, most of the studies are focused on the imidazolium-based ILs as cations with hexyl side chains.[11-14] Mostly, the anionic combinations have been limited to hexafluorophosphate (PF_6), tetrafluoroborate (BF_4), and halides which show limited hydrophobicity. The perfluoroalkyl phosphate (PAP) anion-based ILs possess ultra-hydrophobicity with improved thermal and electrochemical stability as compared to their PF_6, BF_4, and halide counterparts.[15] Arguably, their utilization in PSCs can be an effective strategy to fabricate long-term stable PSCs.

Here, we adopted a powder engineering methodology to synthesize methyl ammonium (MA), Br^- free α-$FAPbI_3$ powder and probed its opto-electrical, structural, and PV properties, and made a comparative analysis with the conventional and δ-$FAPbI_3$ powder processed perovskites. We noted a drastic reduction in structural and energetic disorders for α-$FAPbI_3$ powder-based perovskites over the conventional and δ-$FAPbI_3$ powder. This in turn enhanced the phase stability and PV performances. We further employed two perfluoroalkyl phosphate-based ILs with ethyl and hexyl functionalized imidazolium cations, and the fabricated PSCs gave improved performance along with reliability. From spectroscopic analysis, we decipher an F-Pb semi-ionic interaction that immobilizes the under-coordinated Pb atoms at the surface, which is favorable for stability. Moreover, the synergy created using hexyl-imidazolium cation and perfluoroalkyl phosphate anion yielded enhanced thermal and shelf-life stability, which allowed retaining over 70% of

initial PCE after 500 min of max power point tracking whereas the control device lost 80% of initial performance within 200 min of testing.

4.3 Results and Discussion

4.3.1 Powder Engineering

4.3.1.1 α-$FAPbI_3$ powder synthesis

We derived α-$FAPbI_3$ powder by annealing the as-synthesized δ-$FAPbI_3$ powder[3] at 150 °C for 1 hour in an inert atmosphere (detailed in experimental procedures). Notably, here we synthesized the $FAPbI_3$ powders from low-grade PbI_2 (99%, Sigma Aldrich), which will reduce the cost significantly as compared to the sublimed grade costly PbI_2 routinely employed for solar cells fabrication.[16] We identified the phase purity of synthesized α-$FAPbI_3$ powder using diffuse reflectance spectroscopy (DRS), scanning electron microscopy (SEM) imaging, and powder X-ray diffraction (PXRD) techniques. The DRS spectrum was converted to the pseudo-absorption spectrum using the widely accepted Kubelka−Munk function {F(R)}[17] (Figure S4.1, supporting information, SI) and, we derived the Tauc plot from the Kubelka−Munk transformed data and the estimated optical band gap is noted to be 1.47 eV (Figure 4.1 A). We noted rod-like structures with smooth surfaces from the microscopy image depicted in Figure 4.1 B. The indexed diffractogram of α-$FAPbI_3$ powder is shown (Figure 4.1 C) suggesting high phase purity. Further Figure 4.1 D represents the diffractograms of precursor materials, lead iodide (PbI_2), formamidine hydroiodide (FAI), and the synthesized δ-$FAPbI_3$, α-$FAPbI_3$ powders, where α-$FAPbI_3$ powder showed no residual FAI which appeared in δ-$FAPbI_3$ powder (weak peak at $2\Theta = 25.5°$). We attribute the appearance of two weak peaks ($2\Theta < 14°$) in α-$FAPbI_3$ to the Kβ and W lines from instrumental contaminations. In short, the sharp band edge, clear SEM image, crystalline diffractograms and visual black colour of synthesized α-$FAPbI_3$ asserts their phase purity at the macroscopic level.

4.3.1.2 Thin film characterizations

The deposition of high-quality perovskite film is the critical step to achieving high performance. Here we compared spin-coated perovskite layers of δ-$FAPbI_3$ and α-$FAPbI_3$ powders to the well-established conventional method.

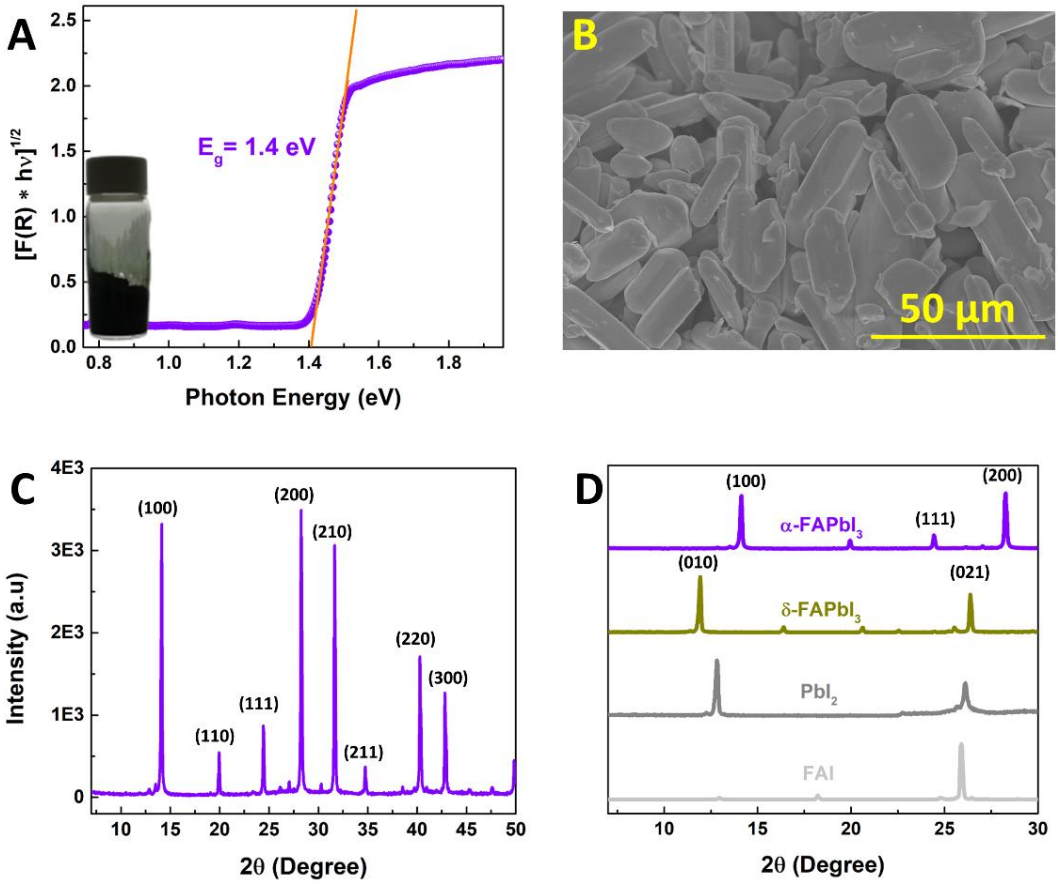

Figure 4. 1 (A) Tauc plot estimated for α-$FAPbI_3$ powder from DRS spectra, digital image, (B) SEM surface image of synthesized α-$FAPbI_3$ powder, (C) indexed XRD spectra of α-$FAPbI_3$ powder, and (D) XRD diffractogram from PbI_2, FAI, δ-$FAPbI_3$, and α-$FAPbI_3$ powders.

As schematically depicted in Figure 4.2, for the conventional method, commercial FAI and PbI_2 (high-grade, 99.99% TCI) were dissolved in DMF: DMSO solvent mixture, whereas for δ-$FAPbI_3$ and α-$FAPbI_3$, 1.4 M pre-synthesized δ-$FAPbI_3$ and α-$FAPbI_3$ powder was dissolved in the solvent mixture and spin-coated. The deposited thin films were annealed at 150 °C for 20 minutes (min) to ensure the complete phase conversion. Formamidine hydrochloride (FACl) was used in all the precursor solutions to produce larger grains.[5] An induced higher crystallinity in $FAPbI_3$ perovskite layers can be observed from the diffractograms (Figure S4.2 A, SI) at an optimized 0.42 M FACl addition. The magnified view of the (100) plane (Figure S4.2 B, SI) shows no shifting in the 2Θ value and the UV-Vis absorption spectra (Figure S4.3 A, SI) suggest a similar bandgap. Arguably, the size of chloride (Cl^-) is smaller than iodide (I^-), and the incorporation of Cl^- in the perovskite structure can induce peak shifting in the

diffractograms and blue shifting in absorbance spectra. However, no changes in the spectra with FACl addition were noted suggesting the absence of Cl^- in the perovskite layers. Cl^- may leave the perovskite surface upon annealing due to its lower sublimation temperature.[18] Moreover, the absence of Cl^- was confirmed from the XPS analysis where no Cl^- was detected (Figure S4.3 B and C, SI).

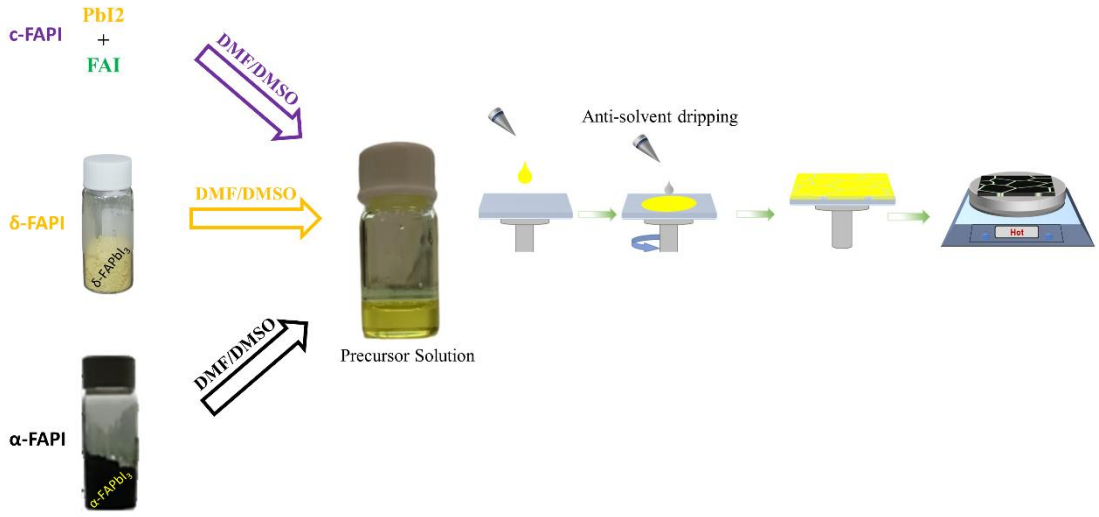

Figure 4. 2 Schematic representation of thin film fabrication from conventional (c-FAPI), δ-$FAPbI_3$ (δ-FAPI), and α-$FAPbI_3$ (α-FAPI) precursor routes.

To harmonize the terminology, hereafter, the perovskite layer deposited from the conventional method, δ-$FAPbI_3$, and α-$FAPbI_3$ powders were termed as c-FAPI, δ-FAPI, and α-FAPI respectively, see Figure 4.2. To investigate the role of different precursor materials on the performance of PSCs, we decipher their optoelectronic and structural properties. In the UV-Vis absorption spectra (Figure 4.3 A), α-FAPI shows the maximum absorption onset than δ-FAPI and c-FAPI indicating improved crystallinity. We further estimated the tauc plots and noted a similar bandgap of 1.49 eV for all three perovskites, see Figure S4.4, SI. We attribute the slightly, higher bandgap for the thin films to the possible presence of multiple absorptions, reflections, and scattering in the thin film geometry.[19] A closer examination of absorption onsets displays the sub-bandgap absorption edges for the three perovskites just below their band gaps, this is known as the Urbach tails and is characterized by the Urbach energy (E_U) in the literature[20] where the absorption coefficient and the E_U are related by,

$$\alpha(E) = \alpha_0 \exp\left\{\frac{E-E_C}{E_U}\right\} \quad \text{(4.1)}$$

where α is the absorption coefficient, E_C and α_0 are constants, and E is the photon energy. We calculated the exponential relation between the absorption coefficient and the photon energy and the E_U from the slope of the exponential decay of the absorption onset (Figure 4.3 B-D).

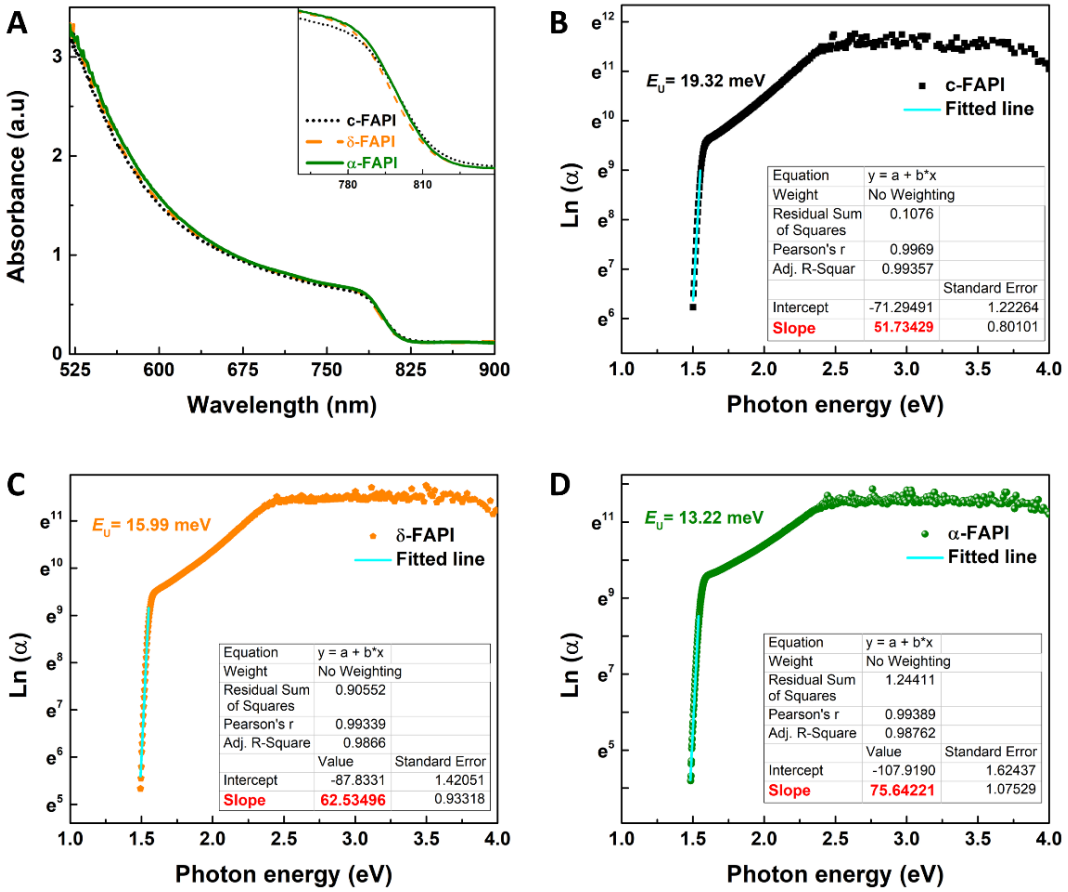

Figure 4. 3 (A)UV-Vis absorption spectra of conventional and powder engineered perovskite thin films. (B-D) Co-relationship of absorption coefficient (α) and photon energy for the Urbach energy calculation for (B) c-FAPI, (C) δ-FAPI, and (D) α-FAPI perovskite thin films.

α-FAPI registered the lowest E_U of 13.22 meV while the δ-FAPI and c-FAPI exhibited higher values of 15.99 meV and 19.32 meV respectively. A reduction in the E_U is significant as the E_U is a measure of energetic disorder at the band edge and impedes the PV performance by reducing the diffusion length, carrier mobility, and the open-circuit voltage deficit.[21,22] In this context, the synthesized α-FAPI with a lower E_U by 6.10 and 2.77 meV than c-FAPI and δ-FAPI respectively, are a promising alternative for $FAPbI_3$ based PSCs. Diffractograms depicted in Figure 4.4 A suggest no shifting of peak and completely inhibited δ-phase in all three cases, however, the presence of unreacted PbI_2

in δ-FAPI is observed. Remarkably, the peak intensities increase substantially for α-FAPI and δ-FAPI than for c-FAPI suggesting the enhanced crystallinity, which is in agreement with the SEM micrographs (Figure S4.5, SI). The induced intrinsic and extrinsic strains were reported to contribute to the phase transformation where the tensile strained α-$FAPbI_3$ quickly rearranges to the δ-$FAPbI_3$ as depicted schematically in Figure 4.4 B.[6,7] We further quantified the microstrain using the Williamson-Hall (W-H) equation[8],

$$\beta \text{ Cos } \theta = \frac{k\lambda}{D} + 4\varepsilon \text{ Sin } \theta \quad \text{.....(4.2)}$$

where β, λ, k, D, and ε denote the full width at half maximum (FWHM) of XRD peak, the wavelength of X-ray radiation, Scherrer constant, crystallite size, and the microstrain respectively. β Cos θ was plotted as a function of 4 Sin θ and the corresponding slopes were estimated as the microstrains. The microstrain dropped from 5.16×10^{-4} to 3.16×10^{-4} for δ-FAPI as compared to c-FAPI and it shows further decrement to achieve the lowest value of 1.95×10^{-4} for the synthesized α-FAPI, see Figure 4.4 C and S4.6, SI. We attribute the origin of the microstrain to the slightly higher Goldschmidt tolerance factor (t >1) of $FAPbI_3$ and the thermal expansion coefficient gradient at the perovskite-substrate interface. We performed depth-dependent diffractograms for c-FAPI and α-FAPI thin films to unravel the crystal structure inhomogeneity, i.e., structural imperfections along with the perovskite thickness (detailed in the experimental procedures). A gradual shift of diffraction peaks towards lower angles across the depths profile, suggests the crystal structure inhomogeneity along with the film thickness.[23,24] We noted reduced diffraction plane peak shifting (100) for α-FAPI as compared to c-FAPI in Figure 4.4 D and E, pointing towards the versatility of our powder methodology that effectively mitigates the structural imperfections.

4.3.1.3 Degradation kinetics

To acquire insights into the perovskite under different environmental stresses, we investigated the structural variation under thermal and moisture conditions. $FAPbI_3$ layers are reported to go through two degradation pathways, first the decomposition to PbI_2, and second, the perovskite can undergo phase transition against environmental stresses such as temperature, moisture, and light. The degradations against the atmospheric stresses have been tracked with structural evaluations such as X-ray and neutron powder diffractions.[25,26]

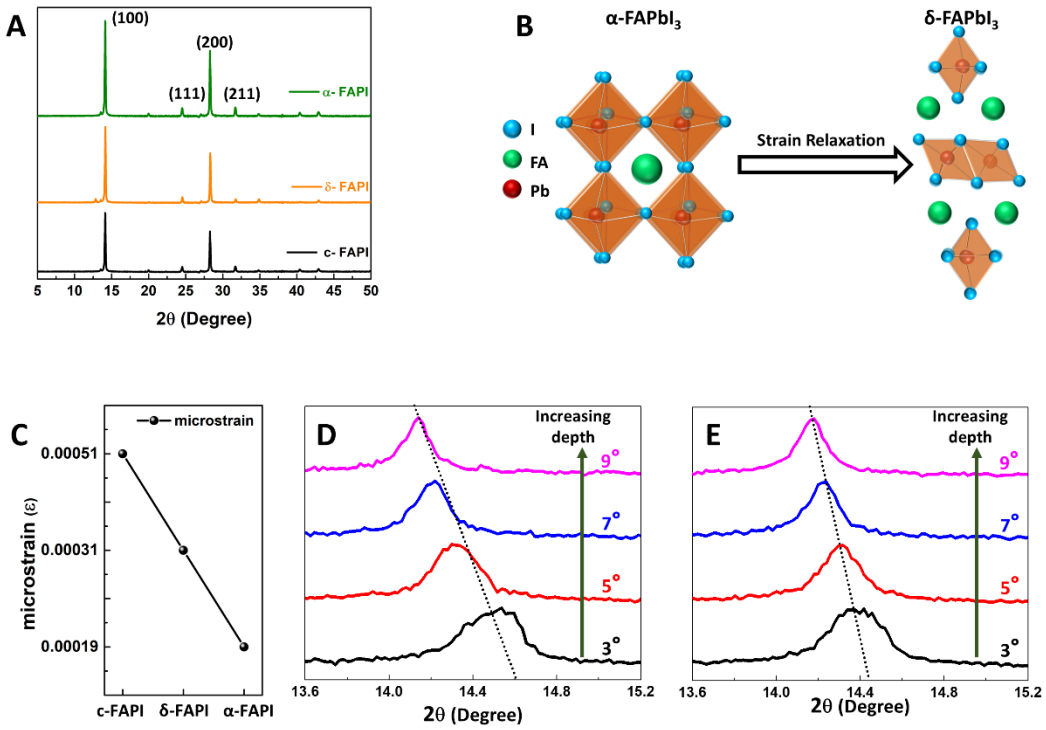

Figure 4. 4 (A)diffractograms of conventional and powder engineered perovskite thin films, (B) schematic representation of α to δ phase-transition, (C) microstrain calculated for different perovskite layers, (D, F) zoom-in-view of (100) plane in depth depended on XRD spectra of (D) c-FAPI, and (E) α-FAPI thin film along with the film thickness. The diffractograms were collected at different incident angles from 3° to 9°.

The thin films were annealed at 85 °C for the thermal stability test and kept at 45-50 % relative humidity (RH) under the dark condition at room temperature for the moisture stability test, and the corresponding diffractograms (Figure S4.7 and S4.8, SI) and digital photographs (Figure 4.5) are shown. The normalized diffractograms collected for the thin films before and after the thermal annealing at 85 °C for 500 hr (Figure S4.7) depict the decomposition of the perovskite phase to PbI_2 for c-FAPI while the δ-FAPI and α-FAPI display improved thermal stability by retaining the perovskite structure. Simultaneously, we tracked the influence of moisture (Figures 4.5 and S4.8, SI). Upon moisture stress, c-FAPI showed a rapid conversion to δ-phase within 24 hr and almost full conversion was realized <100 hr of exposure. Expectedly,[3,4] δ-FAPI is more stable, however, the (010) (δ-phase) plane emerged after 24 hr, and further evolved after 100 hr. Notably, the (010) plane did not appear even after 24 hr for α-FAPI, suggesting improved phase stability, and the (010) reflection emerged only after 100 hr of exposure for α-FAPI. Remarkably, the intensity of (100) α-phase perovskite peak drastically dropped for c-FAPI and recorded a significant decrease for δ-FAPI, but in the case of α-FAPI, it retained the

intensity even after 100 hr of moisture exposure. The powder-engineered methodology induced tensile strain-relaxation, effectively stabilizing the α-phase also in harsh conditions. Moreover, α-FAPI shows higher crystallinity and lowest Urbach energy, which will promote PV performances.

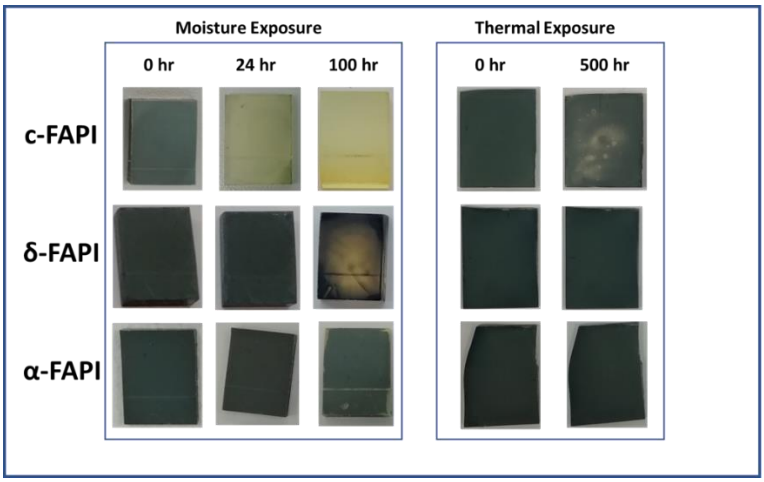

Figure 4. 5 Digital photographs of perovskite thin films upon moisture and thermal exposure taken over time.

4.3.1.4 Photovoltaic Properties

The PV parameters were collected from a PSC with a mesoscopic architecture of FTO/c-TiO_2/mp-TiO_2/Perovskite/Spiro-OMeTAD/Au as illustrated in Figure 4.6 A. Figure 4.6 B depicts the current density–voltage (*J-V*) characteristics under AM 1.5G illumination (100 mW cm^{-2}). The fabricated α-FAPI device displayed a PCE of 16.37 % with an open-circuit voltage (V_{OC}) of 962 mV, a short-circuit current density (J_{SC}) of 23.80 mA cm^{-2} and a fill factor (FF) of 71.44%, whereas δ-FAPI and c-FAPI displayed a reduced PCEs of 16.09% (V_{OC} = 958 mV, J_{SC} = 23.63 and FF = 71.05%) and 15.93% (V_{OC} = 948 mV, J_{SC} = 23.42 and FF = 71.72%) respectively. The improved PCEs of powder-based α-FAPI were attributed to the V_{OC} and J_{SC} values enhancement. We ascribed the marginal increment in J_{SC} to the improved crystallinity, which is evident from the structural and morphological analyses, Figure 4.4 A and S4.5, SI. Additionally, the V_{OC} deficit was minimized by 10 mV for δ-FAPI and 14 mV for α-FAPI than conventional c-FAPI. As discussed in the earlier section *4.3.1.2*, the decrease in the E_U value can boost PV performance. Since J_{SC} is primarily dependent on the bandgap of thin-film absorber, E_U does not have any close relation with J_{SC} but it defines the $V_{OC,def}$ (i.e., the difference between bandgap and open-circuit voltage), and reduction in the E_U leads to a decrease

in the $V_{OC,def}$.[21,27] Figure 4.6 C compares the E_U and V_{OC} where the gradual reduction of E_U in α-FAPI (6.10 meV) and δ-FAPI (2.77 meV) than of the c-FAPI resulted in the lower $V_{OC,def}$ and registered higher V_{OC}. The c-FAPI based PSCs gave a higher performance during a reverse scan with a nominal hysteresis of 0.088 while the δ-FAPI and α-FAPI gave high performance under forward scans with an inverted hysteresis of -0.058 and -0.046 respectively[26] (Figure S4.9, SI).[27,28] The advances in the PV parameters of α-FAPI based PSCs are further established by the external quantum efficiency (EQE) and stabilized photocurrent analyses as in Figure 4.6 D and E, respectively. Compared to the δ-FAPI and c-FAPI, synthesized α-FAPI based PSC exhibited a higher EQE across the complete spectral region. The integrated J_{SC} was calculated from the EQE spectra as 22.48, 22.58, and 23.20 mA cm^{-2} for c-FAPI, δ-FAPI, and α-FAPI respectively, which is in agreement with the J_{SC} values derived from *J-V* measurements and support the crystallinity improvements. For reliable reporting, we collected stabilized photocurrent under a voltage bias near the maxima power point (MPP) tracking, see Figure 4.6 E. We propose the synthesized α-$FAPbI_3$ powder as a promising precursor material over the conventional and δ-$FAPbI_3$ powders owing to its improved PV parameters and cost-competitiveness due to the employment of low-grade PbI_2.

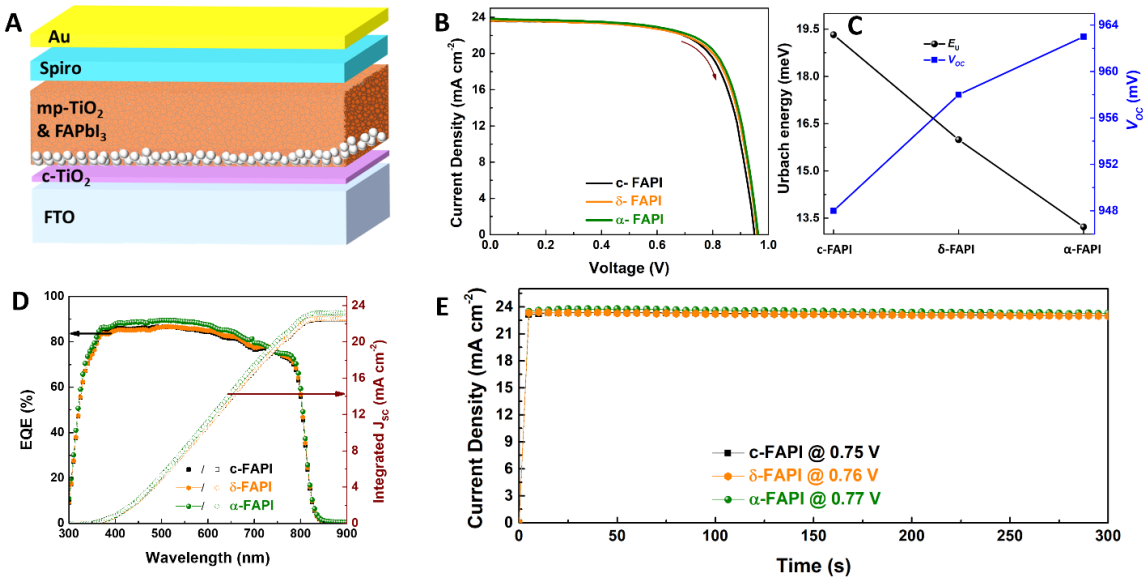

Figure 4. 6 Photovoltaic parameters of powder engineered PSCs: (A) schematic diagram of fabricated PSC, (B) *J-V* curve under forward bias (C) relationship between E_U and corresponding V_{OC} for c-FAPI, δ-FAPI, and α-FAPI films, (D) EQE and integrated photocurrent spectra, and (E) steady-state photocurrent measurements at maximum power point (MPP) for best-performing devices from powder engineered PSCs.

4.3.2 IL Additive Engineering

4.3.2.1 Thin film analysis

To impart ultra-hydrophobicity to our α-FAPI, we realized the additive engineering with 3.5 mM EMIFAP (1-ethyl-3-methylimidazolium tris(pentafluoroethyl)trifluorophosphate) and HMIFAP (1-hexyl-3-methylimidazolium tris(pentafluoroethyl)trifluorophosphate) with PAP anion (Figure S4.10, SI) and the effect of ILs on the optoelectrical, structural and morphological properties of $FAPbI_3$ were monitored. As an effective method to probe the inclusion and the molecular interactions of the PAP based ionic liquids with the α-FAPI perovskite, XPS has been employed to collect the core level spectra of C 1s, N 1s, F 1s, I 3d, and Pb 4f (Figure 4.7, and S4.11-4.13, SI). Figure S4.11 depicts the collected survey spectra for the aforementioned perovskite absorber surfaces. For the core level spectral analyses, all the elemental peaks were corrected with Aliphatic hydrocarbon (C-H/C-C) at 284.6 eV, C=O at 532 eV, and C-O peak at 533 eV, and the fitting was undertaken with a Shirley type background and Gaussian-Lorentzian (30-35% Gaussian) functions.[29] We have calculated the component compositions of deconvoluted peaks from the corresponding peak areas, and the elemental composition of the perovskite surface using equation 3,[30]

$$C_A = \frac{I_A/S_A}{\sum_i \left(I_i/S_i\right)} \quad \ldots\ldots\ldots\ldots\ldots\ldots\ldots\ldots\ldots\ldots\ldots\ldots\ldots\ldots\ldots\ldots\ldots\ldots\ldots\ldots\ldots\ldots\ldots\ldots (4.3)$$

Where, C_A, I_A, and S_A are the required concentration, measured peak intensity and sensitivity factor of atomic species A. I_i and S_i are the peak intensity and sensitivity factor of atomic species i. The deconvoluted C 1s peaks (Figure S4.12 A-C, SI) depict, where the labeled C-H and C-N components are assigned to the aliphatic hydrocarbon and carbon bonded to nitrogen atom respectively, in FA cation. Upon EMIFAP and HMIFAP addition, three new components emerged at 287.3, 288.96, and 292.6 eV and ascribed to imidazolium ring (N-C-N), CF_2, and CF_3 respectively.[31] In the N 1s core-level XPS spectra (Figure S4.12 D-F, SI), the peaks labeled as C-N and C=N are attributed to the FA while the Im-N peak is assigned to the imidazolium ring indicating the presence of IL cationic part.[32] The emerged F 1s peak (Figure 4.7 A) suggests the inclusion of the fluorine-rich anionic part of IL into the $FAPbI_3$ surface. The deconvoluted characteristics of fluorine peaks exhibited the bound state of fluorine with carbon and a semi-ionic

interaction with the lead, see Figure 4.7 B and C.[33] The effect of strong F-Pb interaction was observed in the Pb core level spectra (Figure 4.7 D).

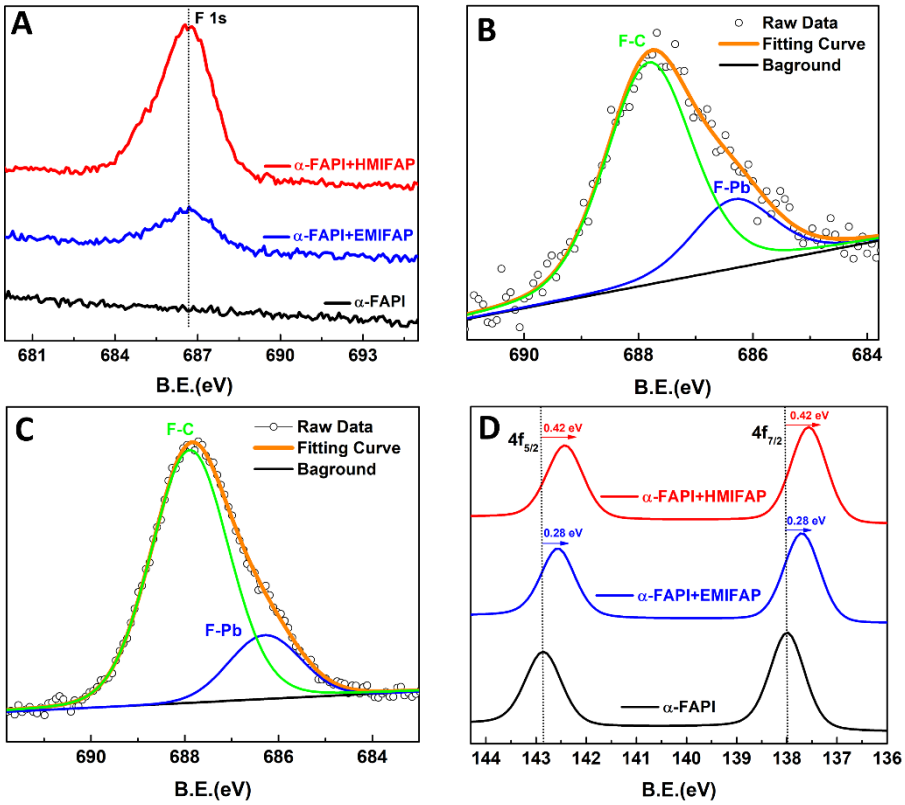

Figure 4. 7 XPS analyses of $FAPbI_3$ surfaces: (A) F 1s core-level spectra of α-FAPI, α-FAPI+EMIFAP, and α-FAPI+HMIFAP thin films, (B, C) deconvoluted F 1s core-level spectra of, (B) α-FAPI+EMIFAP and (C) α-FAPI+HMIFAP thin films, and d) Pb 4f core-level spectra.

The main peaks of Pb $4f_{7/2}$ and $4f_{5/2}$ at 142.85 and 138.0 eV showed a strong shift of 0.28 and 0.42 eV towards the lower binding energy for modified α-FAPI+EMIFAP and α-FAPI+HMIFAP layers respectively.[34] In the deconvoluted peaks of pristine α-FAPI (Figure S4.13, SI), besides the main peaks of Pb $4f_{5/2}$ and $4f_{7/2}$ at 142.85 and 138.0, two weak peaks at 141.9 and 137.09 eV respectively, ascribed to the metallic Pb (Pb^o),[35] which disappeared in reformed α-FAPI+EMIFAP and α-FAPI+HMIFAP perovskite. The identified F-Pb semi-ionic interaction effectively stabilizes the under-coordinated Pb atoms at the surface. The shift of Pb^{2+} peaks towards the lower binding energy indicates the lowering of the oxidation state due to the electron donation from the PAP-based EMIFAP and HMIFAP to the uncoordinated Pb^{2+} ions.[35] We observed a similar peak shift for core level spectra of I 3d (Figure S4.13 D, SI), demonstrating the interaction between the iodide ions and PAP-based ILs that interact with the $FAPbI_3$ surface. To understand

the F-Pb interaction in detail, we probed the elemental composition of Pb, I, and F (F-Pb component) for all three perovskite surfaces, see Table S4.1 and S4.2. We calculated the Pb:I:F ratio as 1:3.19:0, 1:3.03:0.09, and 1:2.93:0.28 for α-FAPI, α-FAPI+EMIFAP, and α-FAPI+HMIFAP surfaces respectively, suggesting a weakening of Pb-I interactions with increasing the F-Pb interaction. The reduced iodide content and emerged F-Pb component in F 1s core-level spectra suggest a semi-ionic F-Pb interaction inhibiting the migration of ions that also passivate the surface, to enhance the PV parameters.[36]

To access the effects of PAP-based ILs on the optoelectronic properties of the α-FAPI film, we collected the UV-Vis absorption spectra (Figure 4.8 A) and noted an improved absorption onset in α-FAPI+EMIFAP and α-FAPI+HMIFAP as compared to the α-FAPI. Expectedly, the calculated E_U was further reduced by additivization and acquired a value of 12.98 and 12.47 meV for α-FAPI+EMIFAP and α-FAPI+HMIFAP films respectively (Figure S4.14, SI). The normalized diffractograms for the perovskite layers depicted in Figure 4.8 B show enhanced crystallinity after additivization as compared to the α-FAPI. Upon the EMIFAP and HMIFAP addition, the (100) and (200) planes significantly intensify as compared to the other reflections such as (110) and (111). Compared with pristine α-FAPI, the diffractograms showed no peak shifting for α-FAPI+EMIFAP and α-FAPI+HMIFAP, indicating the absence of elemental substitutions, However, the FWHM of α-FAPI shows a decrement from 0.14^o to 0.13^o and 0.11^o with α-FAPI+EMIFAP and α-FAPI+HMIFAP usage respectively. This implies that the addition of EMIFAP and HMIFAP did not alter the perovskite crystal structure, however, the size of the grain can increase due to the surface chemistry and interaction with ILs. Affirmatively, the absence of any peak shifting in the diffractogram endorses the semi-ionic F-Pb interaction instead of iodide substitution as indicated by F 1s XPS core level spectral compositions. Additionally, residual peaks (PbI_2 and δ-phase peaks) were inhibited by additivization (IL treatments). The enhanced peak intensity and reduced FWHM infer the crystallinity enhancement.

The additivization (IL treatment) alters the crystallization growth through interaction with the perovskite structure and mitigates the external strain induced by the temperature gradients along with the bulk of $FAPbI_3$ thin film as schematically represented in Figure 4.8 C. α-FAPI+EMIFAP and α-FAPI+HMIFAP registered significantly reduced microstrains of 1.87×10^{-4} and 1.67×10^{-4} respectively, see Figure 4.8 D and E.

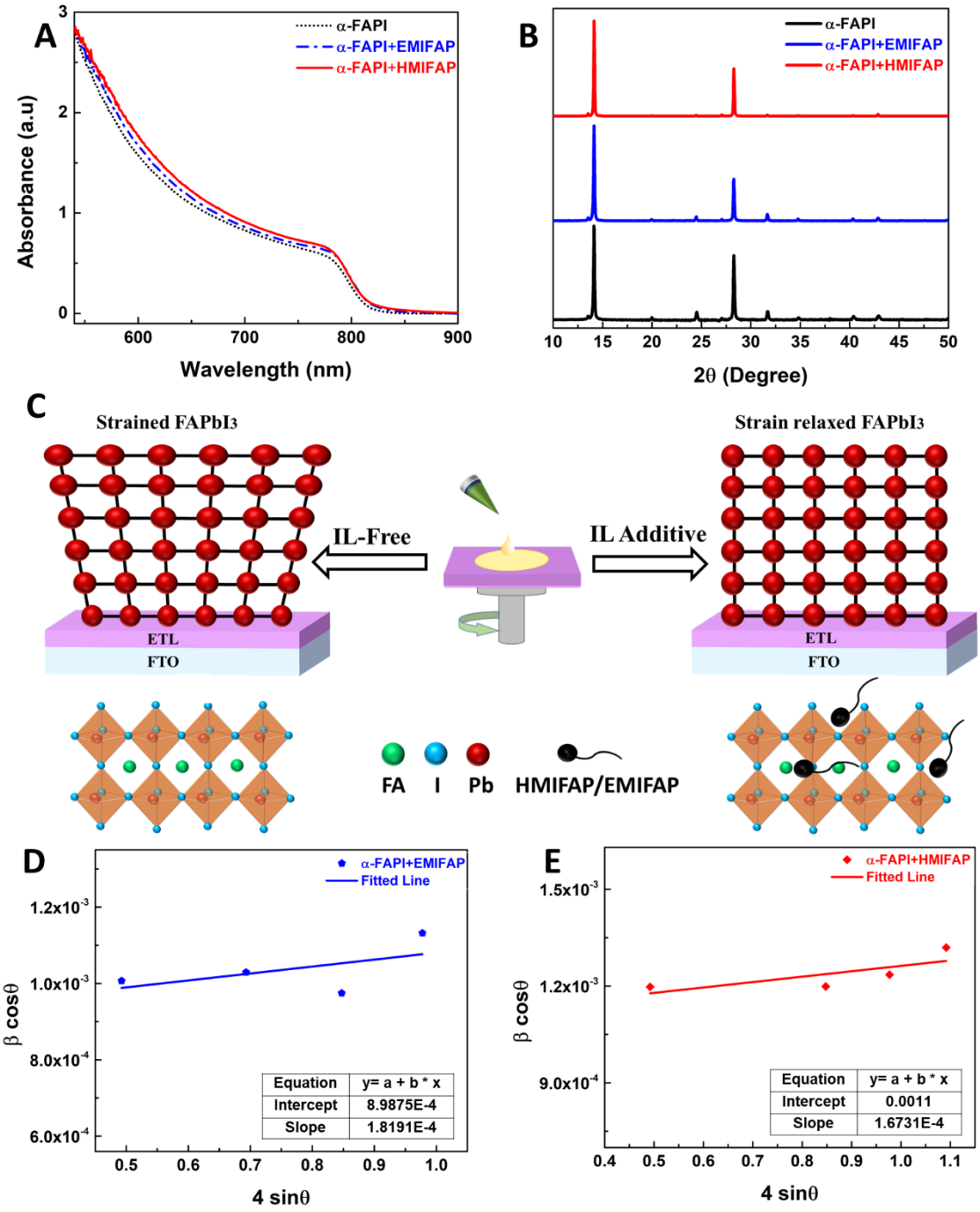

Figure 4. 8 Structural and optoelectronic properties of EMIFAP and HMIFAP treated α-FAPI perovskite layers: (A) comparison of UV-Vis absorption spectra and (B) diffractograms of α-FAPI, α-FAPI+EMIFAP, and α-FAPI+HMIFAP perovskite layers, (C) schematic representation of microstrain induced by external stress before and after the IL treatment, (D, E) Williamson−Hall plots for microstrain calculation for (D) α-FAPI+EMIFAP, (E) α-FAPI+HMIFAP perovskite layers.

We measured depth-dependent diffractograms for α-FAPI+HMIFAP thin film (Figure S4.15, SI), and the reduced peak shifting of (100) diffraction plane in depth-profiling

diffractograms supports our hypothesis. The HMIFAP additivization mitigates the temperature gradient-induced structural inhomogeneity along with the film thickness and induces structural perfection. The effective crystal growth can be visualized through the SEM micrographs (Figure S4.16, SI). The microstructure suggests that the additivization improved the uniformity and crystalline size as compared to the pristine α-FAPI. Reports suggest that the PAP-based ILs show higher hydrophobicity than the corresponding PF_6 and BF_4 anion based ILs with the same cations.[37,38] The hydrophobicity of PAP-based IL as additives was monitored by goniometry experiments to measure the contact angle and displayed in Figure S4.17, SI. For the α-FAPI a showed a value of 92º, while for the α-FAPI+EMIFAP and α-FAPI+HMIFAP added layers, it increases to 98º and 101º.

Table 4. 1 Photovoltaic parameters of α-FAPI, α-FAPI+EMIFAP, and α-FAPI+HMIFAP based PSC under both forward and reverse scan at a rate of 100 mV/s.

Perovskite	**direction**	V_{OC} **(mV)**	J_{SC} **(mA cm^{-2})**	**FF (%)**	**PCE (%)**	**HI**	R_s **(Ω cm^2)**	R_{sh} **(kΩcm^2)**
α-FAPI	FS	962	23.81	71.43	16.37	0.046	3.79	1.64
	RS	955	23.44	69.46	15.56		3.65	1.04
α-FAPI+EMIFAP	FS	973	23.96	75.03	17.49	0.029	3.47	2.36
	RS	960	23.85	73.18	16.77		3.60	2.83
α-FAPI+HMIFAP	FS	990	24.29	76.11	18.26	0.005	3.15	5.78
	RS	974	24.43	74.88	17.82		3.27	5.54

4.3.2.2 Fabrication and analysis of PSCs

The improved optoelectronic and structural properties of IL treated α-FAPI absorbers, prompt us to fabricate PSCs with α-FAPI (control device), and with α-FAPI+EMIFAP, and α-FAPI+HMIFAP. The additive engineering gave higher PV performance compared

to the control one, the EMIFAP additivization improved the PCE to 17.49% with a V_{OC} of 973 mV, J_{SC} of 23.96 mAcm^{-2}, and FF of 75.03% under forward scan. α-FAPI+HMIFAP based PSC registered a PCE of 18.26% with a boosted V_{OC} of 990 mV, J_{SC} of 24.29 mA cm$^{-2,}$ and FF of 76.11% under similar conditions, Figure 4.9 A and Table 4.1. A substantial increment in the PV parameters was registered with the HMIFAP additivization, along with a negligible hysteresis (Figure S4.18, SI and Table 4.1). The steady-state photocurrent measurements at maximum power points are shown in Figure S4.19, SI. Following the *J-V* measurements, improved EQE spectra were noted over the entire measured range, and the integrated photocurrent was estimated as 23.2, 23.7, and 23.96 mA cm^{-2} for α-FAPI, α-FAPI+EMIFAP, and α-FAPI+HMIFAP devices respectively, see Figure 4.9 B). The statistical analysis of PV parameters for the α-FAPI, α-FAPI+EMIFAP, and α-FAPI+HMIFAP based PSCs are presented in Figure 4.10.

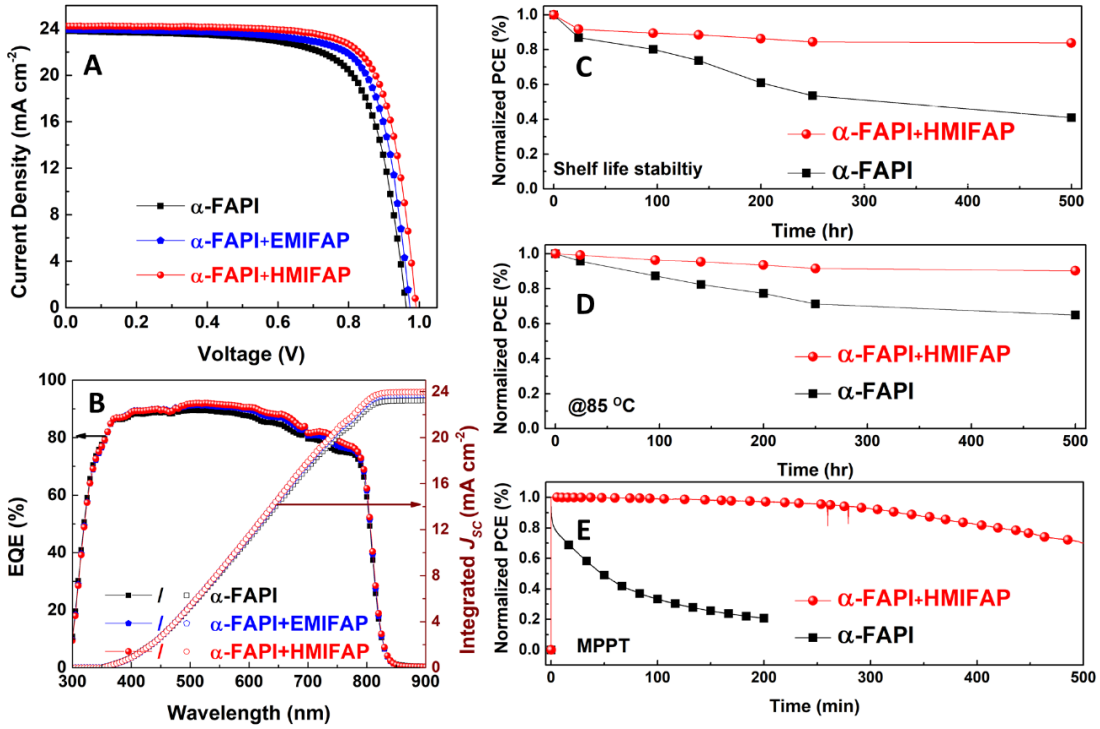

Figure 4. 9 Photovoltaic performance and stability of EMIFAP and HMIFAP treated PSCs: (A) *J-V* characteristics under forward scan, (B) EQE and integrated photocurrent of corresponding PSCs, (C) normalized PCEs of α-FAPI and α-FAPI+HMIFAP devices (unencapsulated) normalized to initial efficiencies as a function of shelf life in a dark and ambient atmosphere with a relative humidity of 45-50%, (D) stability curve of devices aged on a hot plate kept at 85 °C at ambient atmosphere and (E) MPP tracking profiles of unencapsulated devices exposed to continuous light illumination in ambient atmosphere.

We measured the Mott–Schottky (M-S) plots of PSCs (Figure S4.20 A-C, SI) at 10 kHz in the dark to extract built-in potential (V_{bi}) and depletion width (W), see section *3.3.3* for details.[16,39] We noted the higher build-in potential through additivization (IL-treated PSC) as compared to the control device, which is in agreement with the V_{OC} enhancement. The IL-treated PSC gave an increased build-in potential (V_{bi}) of 1.11 V (EMIFAP) and 1.19 V (HMIFAP) and a corresponding increased depletion width (W) of 90.2 nm and 119.3 nm compared to the control α-FAPI based PSC (0.98 V and 53.9 nm) respectively. The increased depletion width allows increased charge separation and collection thus inhibiting the charge recombination and leading to an enhanced photocurrent. In addition to the increment in V_{OC} contribution from the reduced E_U, the lower series (R_S) and higher shunt resistance (R_{sh}) obtained suggest a considerable increment in the FF and V_{OC} due to the reduced charge carrier recombination, which is supported by dark J –V measurements of IL-treated PSCs, see Figure S4.21, SI. We calculated a lower reverse leakage current of 4×10^{-8} mA cm^{-2} and 4.28×10^{-8} mA cm^{-2} for HMIFAP and EMIFAP based PSC while α-FAPI based PSC showed the highest leakage current (1.45×10^{-7} mA cm^{-2}), in agreement to its lower R_{sh} and high R_S value obtained from *J-V* measurement under illumination (Table 4.1). The lower reverse saturation current density with EMIFAP and HMIFAP additive compared to the pristine α-FAPI, leads to higher J_{SC}, attributed to the higher crystallinity in IL-treated perovskite films as revealed by UV-Vis absorption and XRD spectra (Figure 4.8 A and B).

We investigated the stability of fabricated PSCs against the shelf life, thermal and operational stresses. Similar to α-FAPI (Figure 4.5, S4.7 and S4.8, SI) it displayed improved stability, over the c-FAPI and δ-FAPI based absorbers, under moisture and thermal stresses. Here we compared the α-FAPI based PSCs with the α-FAPI+HMIFAP. To estimate the shelf-life stability, we kept the unencapsulated PSCs under the dark condition at room temperature, and 45-50% RH, while for thermal stability, the PSCs were annealed at 85 °C under a dark and open atmosphere, and the corresponding *J-V* parameters were collected at regular intervals. The α-FAPI+HMIFAP based PSCs (Figure 4.9 C) retained 85% of initial PCE after 500 hr of atmospheric exposure while the pristine α-FAPI lost 60% of initial PCE. We noted a similar trend of surface hydrophobicity of α-FAPI+HMIFAP (101°) than the α-FAPI (92^o), see Figure S4.17, SI. The pristine α-FAPI displayed thermal stability (Figure S4.7, SI) and with the additivization (HMIFAP

treatment), it showed further improvements by retaining 90% of the initial PCE while the α-FAPI was able to retain 70% (Figure 4.9 D). We attribute these merits to the higher thermal stability of PAP-based ILs, ultra-hydrophobicity, and its coordination. We further monitored the operational stability of unencapsulated α-FAPI and α-FAPI+HMIFAP based PSCs under MPP tracking with a continuous one-sun illumination under atmospheric conditions. α-FAPI+HMIFAP based PSCs showed considerable stability by retaining 70% of the original PCE after 500 min whereas the α-FAPI lost 80% of its initial PCE within 200 min (Figure 4.9 E). Such improvements can be attributed to the collective effect of improved interactions from hexyl-imidazolium cation with the perovskite absorber and the developed hydrophobicity and thermal stability of the perfluoroalkyl phosphate anion.

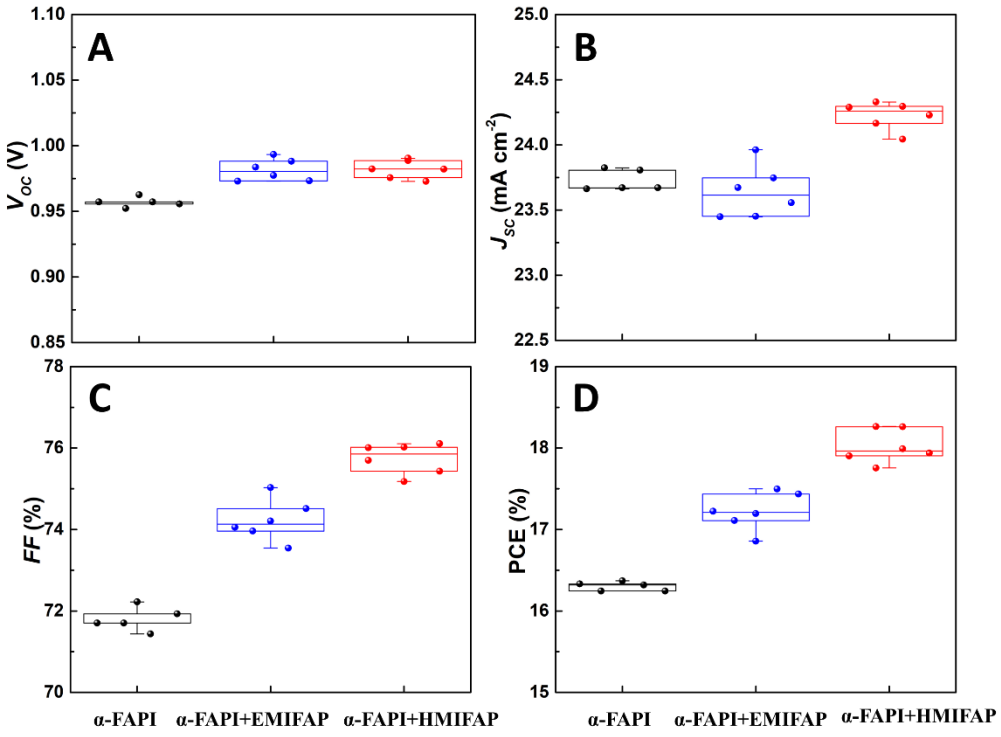

Figure 4. 10 Statistical deviation of the photovoltaic parameters (A) V_{OC}, (B) J_{SC}, (C) FF, and (D) PCE for the PSCs prepared from the different perovskite. The data were obtained under AM 1.5G one-sun illumination at forward scan (J_{SC} to V_{OC}).

4.4 Conclusion

We achieved a significant decrement in the Urbach energy and microstrain through the $FAPbI_3$ powder engineering methodology. The α-$FAPbI_3$ powder displayed an improved performance by minimizing the open-circuit voltage deficit. We noted that the microstrain

relaxation effectively mitigated the phase instability under atmospheric conditions. Further, through additive engineering, by employing two ultra-hydrophobic perfluoroalkyl phosphate anion-based ionic liquids as additives, the hexyl-imidazolium cationic counterpart registered the efficiency of >18% owing to reduced microstrain, Urbach energy, induced F-Pb semi-ionic interaction, and improved crystallinity. The unencapsulated device showed promising thermal and shelf-life stability along with high operational stability by retaining 70% of original PCE after 500 min of MPP tracking at atmospheric conditions.

4.5 Experimental Procedure

4.5.1 Chemical materials

All chemicals were purchased from Sigma Aldrich and were used as received without any further purification unless and otherwise stated.

4.5.2 Synthesis of $FAPbI_3$ powders

Non-perovskite δ-$FAPbI_3$ was synthesized through a previously reported room temperature precipitation method[16] where, 10.7 mmol FAI was dissolved in 100 ml of acetonitrile (HPLC grade, Alfa Aesar) by stirring. 8.3 mmol of PbI_2 (99%) was added to the stirring solution and allowed the stirring to continue for 24 hours. The yellow powders were filtered and the residual PbI_2 and FAI were removed by five times washing with acetonitrile solvent followed by a one-time wash with diethyl ether. The final product was dried under a continuous vacuum for another 24 hours and taken for α-$FAPbI_3$ synthesis.

Synthesis of α-$FAPbI_3$ powder: The photo-active α-$FAPbI_3$ powder was synthesized by annealing the δ-$FAPbI_3$ powder in a tube furnace at 150 °C for 1 hour in an inert atmosphere. Then obtained α-$FAPbI_3$ powder was transferred to a clean vial and kept in the glovebox until further use.

4.5.3 Device fabrication

Cleaned FTO substrates were then heated gradually to 500 ºC on a hotplate and TiO_2 compact layer (c-TiO_2) was deposited by spray pyrolysis with a pre-diluted titanium diisopropoxide bis-(acetylacetonate) solution in ethanol (1:19 volume ratio). The samples were allowed to cool after 30 minutes of annealing. Mesoporous TiO_2 (mp-TiO_2, Dyesol

30 NR) dispersed in ethanol at 1:8 (mp- TiO_2:ethanol, v/v ratio) was spun coated on FTO/c-TiO_2 substrate at 4000 rpm for 30 s, and annealed at 500 ºC for another 30 min. The FTO/c-TiO_2/mp-TiO_2 substrates were treated with UV-Ozone for 20 minutes and transferred to the Ar-filled glove box for perovskite and HTM deposition. Perovskite precursor solutions were prepared as follows,

c-FAPI: conventional precursor solution was prepared by dissolving equi molecular amount (1.4 mmol) of FAI (TCI) and PbI_2 (99.99%, TCI) in 1 ml precursor solvent.

δ-FAPI: 886.2 mg of δ-$FAPbI_3$ powder was dissolved in 1 ml precursor solvent.

α-FAPI: 886.2 mg of α-$FAPbI_3$ powder was dissolved in 1 ml precursor solvent.

α-FAPI+EMIFAP: 886.2 mg of α-$FAPbI_3$ and 1.15 µl EMIFAP (1-Ethyl-3-methylimidazolium tris(pentafluoroethyl)trifluorophosphate,) ionic liquid were mixed in 1 ml precursor solvent.

α-FAPI+HMIFAP: 886.2 mg of α-$FAPbI_3$ and 1.3 µl HMIFAP (1-Hexyl-3-methylimidazolium tris(pentafluoroethyl)trifluorophosphate) ionic liquid were mixed in 1 ml precursor solvent.

We have opted for a mixed solvent of DMSO: DMF (1:8 v/v ratio) as the 0.42 M formamidine hydrochloride (FACl) was added to all the precursor solutions. The perovskite solutions were filtered via a PTFE filter with 0.45 µm pore size and spin-coated in two steps: 1000 rpm for 5 s and 5000 rpm for 20 s. 100 µl chlorobenzene (CB) was dropped on the surface 5 s before the end of the program. The substrates were immediately transferred to the hotplate and annealed at 150℃ for 20 min. Afterward, a solution of 60 mM spiro-OMeTAD in 0.8 mL CB is prepared by adding 23 µL of 4-tert-butylpyridine and 14 µL from the solution of bis(trifluoromethylsulfonyl)imide lithium salt (520 mg LiTFSI in 1 mL acetonitrile). The HTM solution is spun-coated on top of the perovskite layer at 4000 rpm for 30 s. Finally, the device is completed by thermal evaporation of 70 nm thick gold layer as a back-contacted electrode.

4.5.4 Characterizations Techniques

Instrumental details have been explained in detail in section 2.4.

4.6 Supporting Information

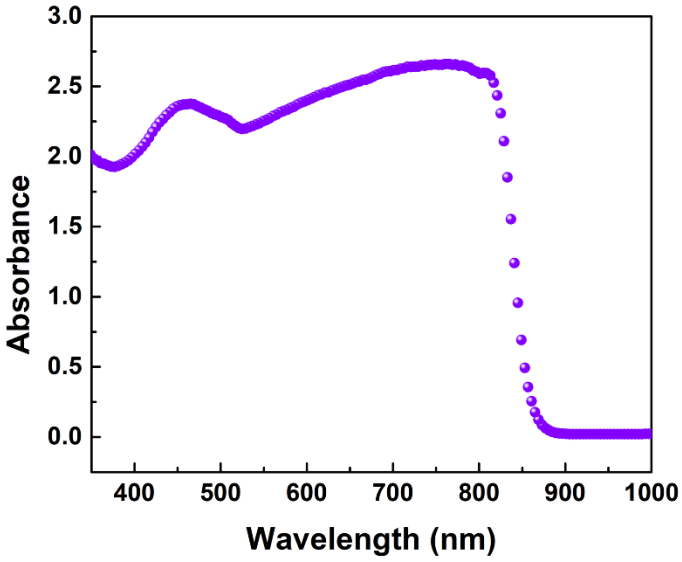

Figure S4. 1 Kubelka-Munk transformed pseudo-absorption spectra of α-$FAPbI_3$ powder.

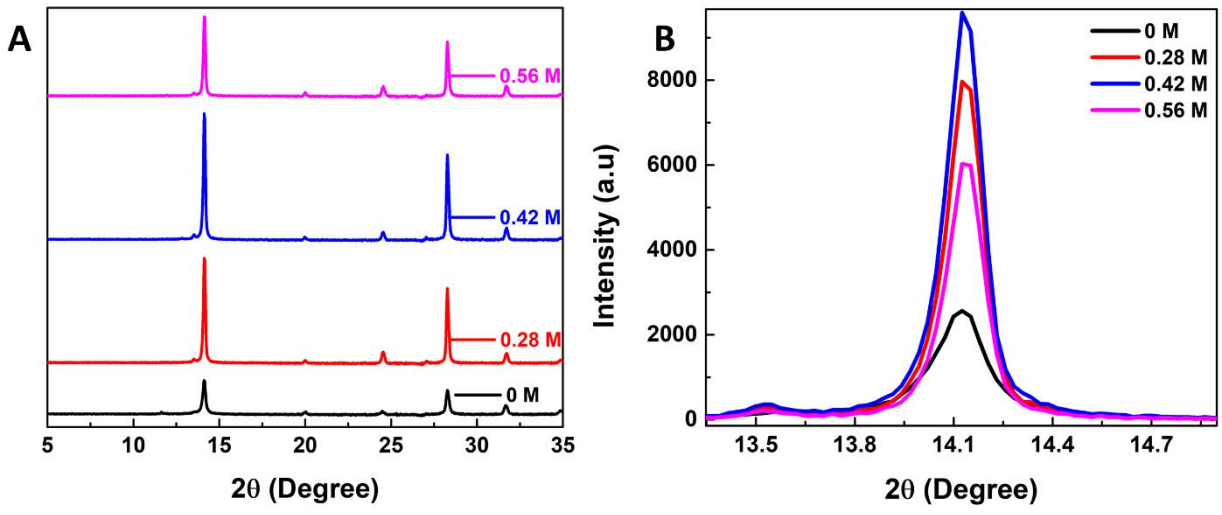

Figure S4. 2 (A) Diffractograms of FACl treated $FAPbI_3$ thin films, and (B) zoom-in view of (100) plane.

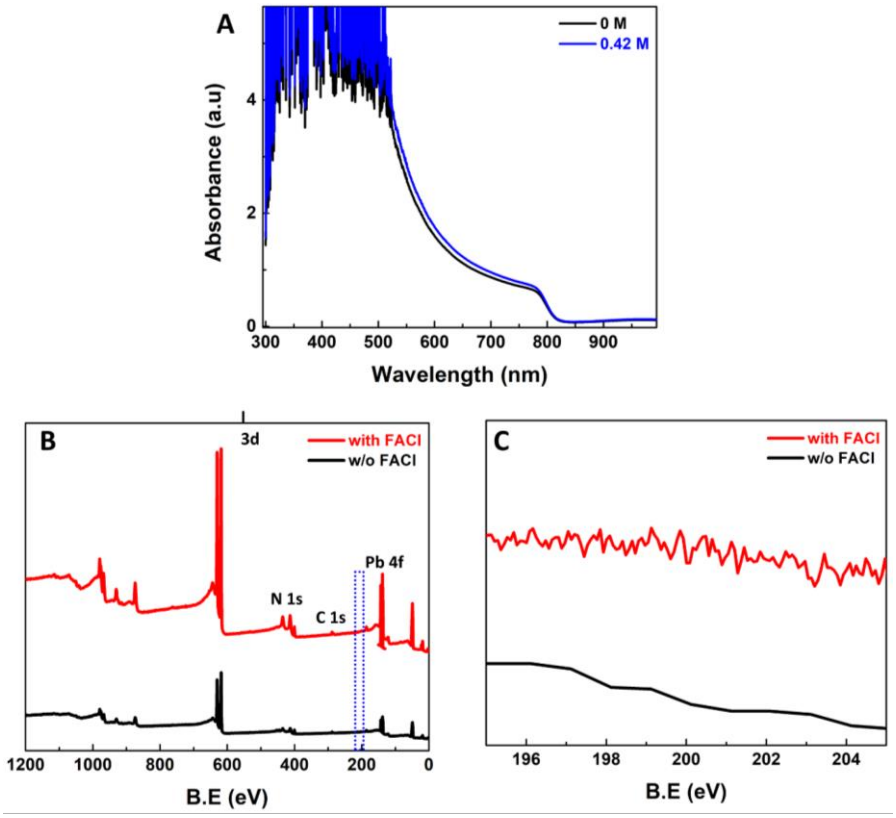

Figure S4. 3 (A)UV-Vis absorption spectra of $FAPbI_3$, and with optimized FACl content. XPS (B) survey and (C) Cl 2p core-level spectra of $FAPbI_3$ thin films with and without FACl.

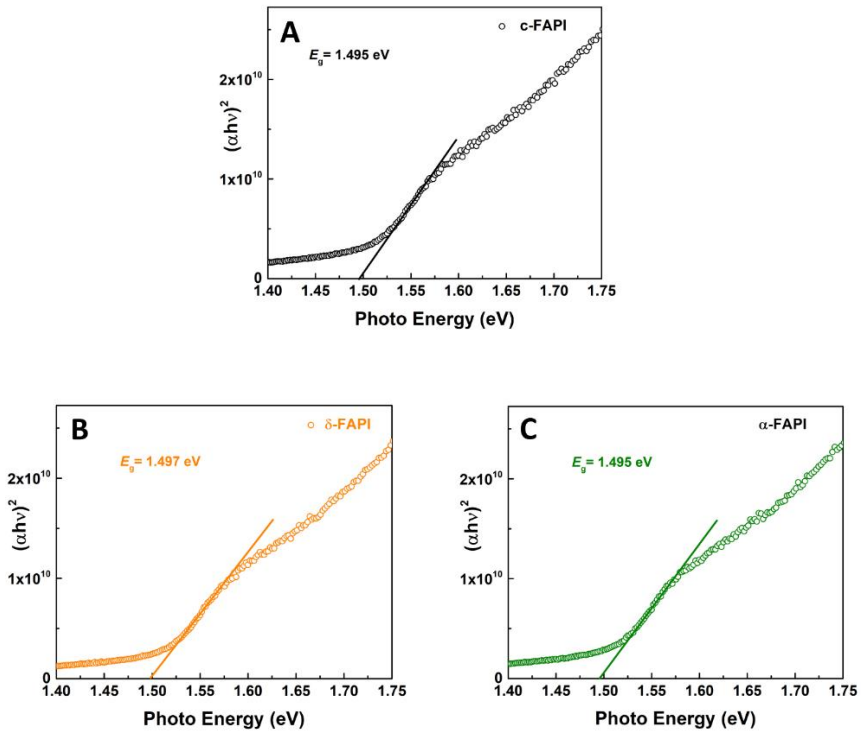

Figure S4. 4 (A-C) Tauc plots calculated from the UV-Vis absorption for (A) c-FAPI, (B) δ-FAPI, and (C) α-FAPI thin films.

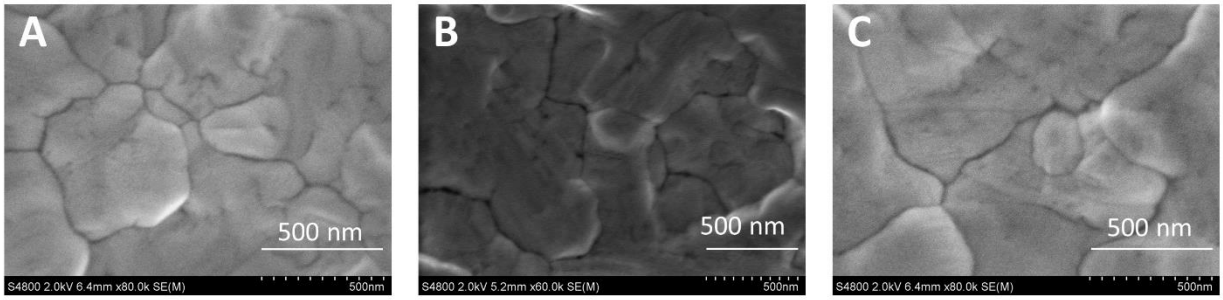

Figure S4. 5 SEM images (top view) of (A) c-FAPI, (B) δ-FAPI and (C) α-FAPI thin films. The scale bar is 500 nm.

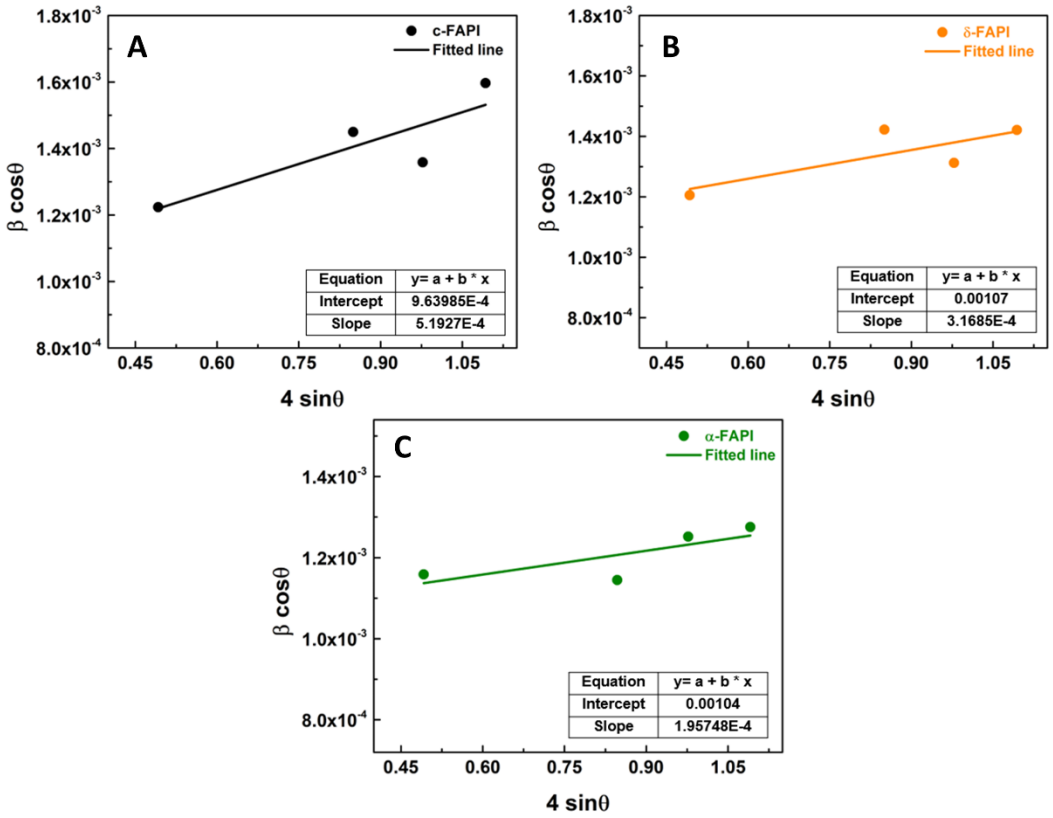

Figure S4. 6 Microstrain calculation from Williamson−Hall plots for (A) c-FAPI, (B) δ-FAPI, and (C) α-FAPI perovskite layers.

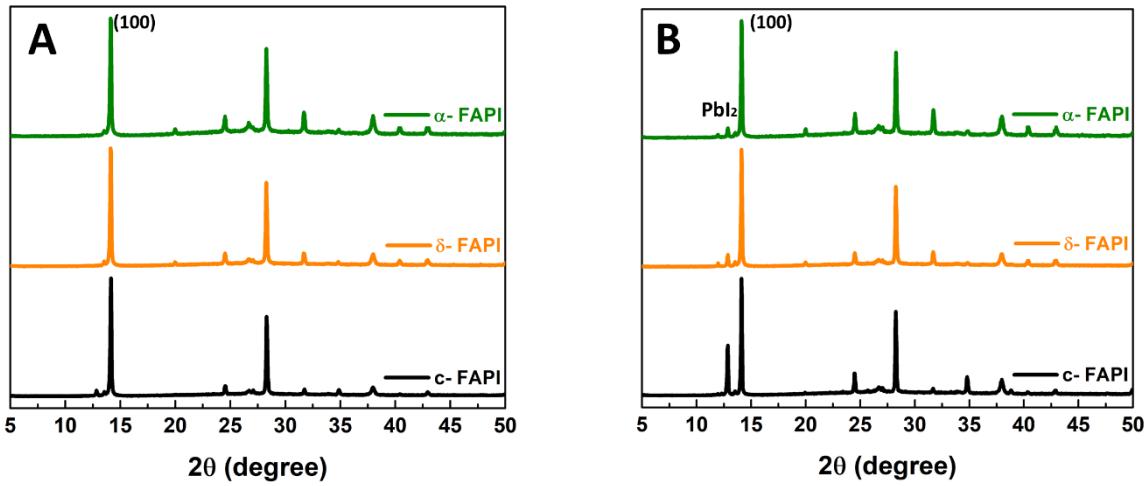

Figure S4. 7 Diffractograms of perovskite thin films (A) before, and (B) after thermal aging for 500 hr at 85 °C.

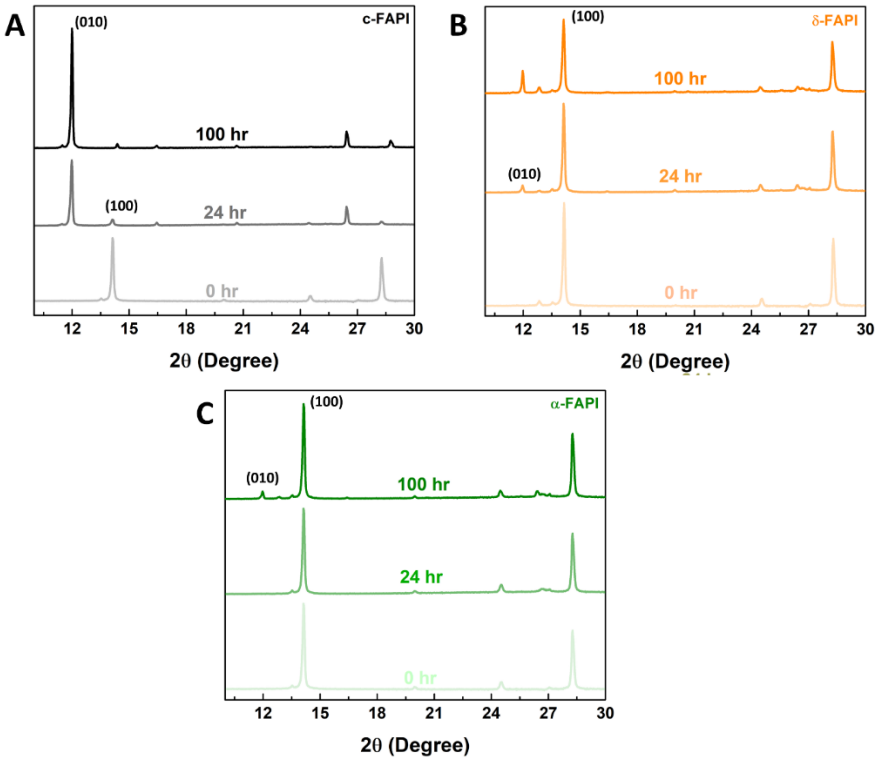

Figure S4. 8 Diffractograms from moisture stability test for (A) c-FAPI, (B) δ-FAPI, and (C) α-FAPI thin films.

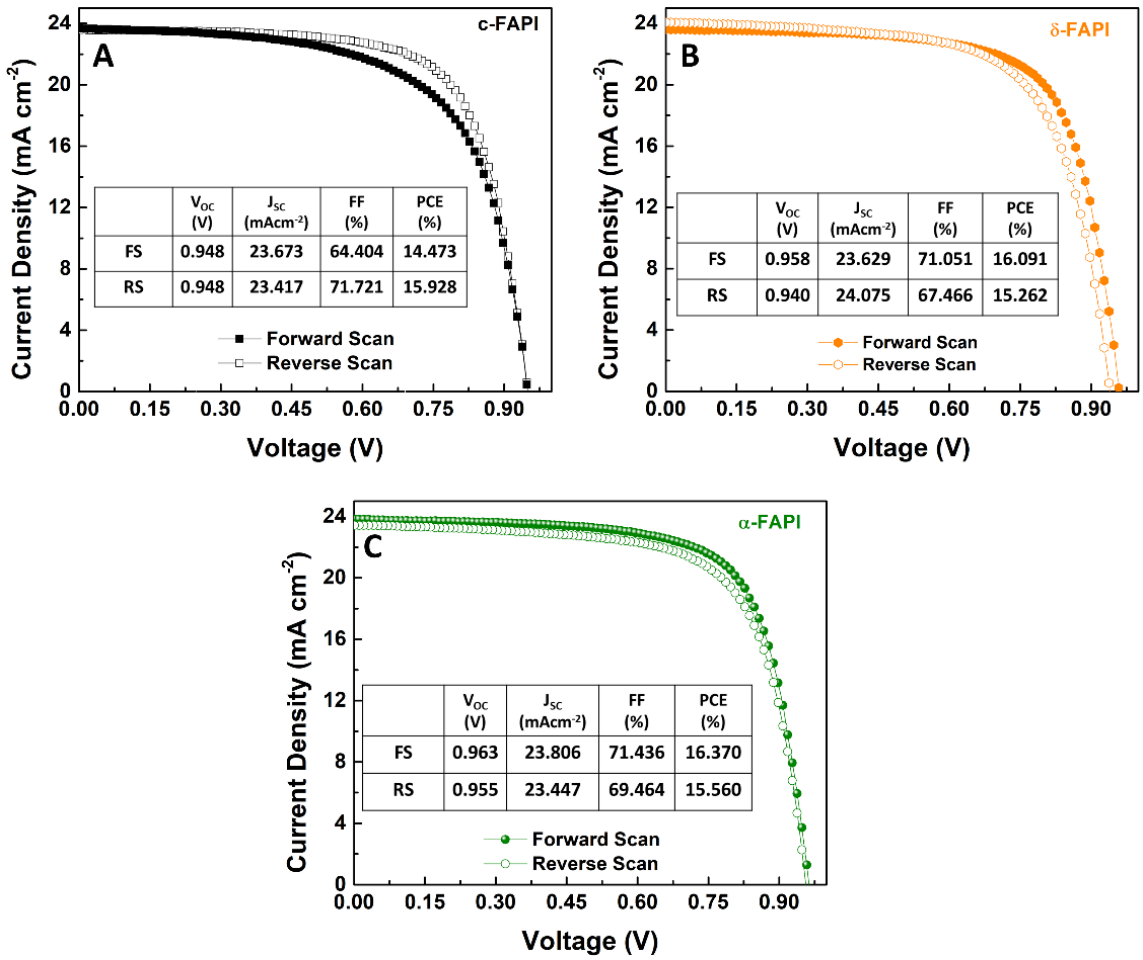

Figure S4. 9 *J-V* curves of powder-engineered PSCs, (A) c-FAPI, (B) δ-FAPI, and (C) α-FAPI under both forward and reverse scans.

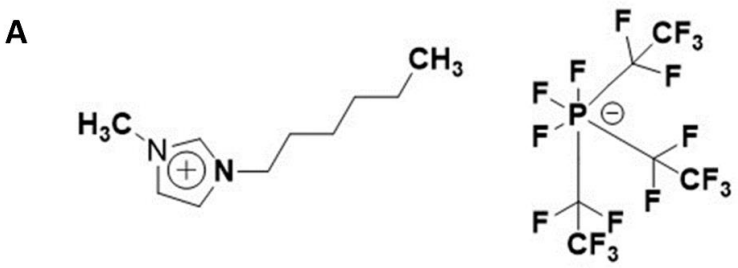

1-Hexyl-3-methylimidazolium tris(pentafluoroethyl)trifluorophosphate
(HMIFAP)

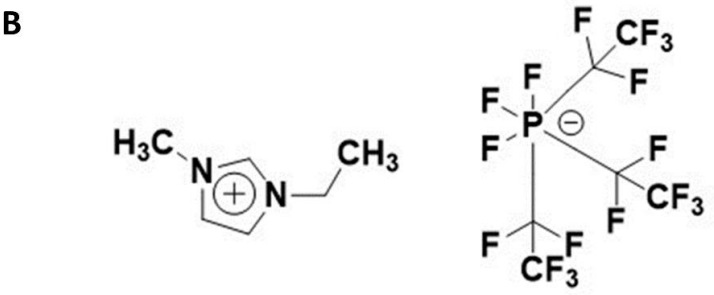

1-Ethyl-3-methylimidazolium tris(pentafluoroethyl)trifluorophosphate
(EMIFAP)

Figure S4. 10 Molecular structure of ionic liquid additives. (A) 1-hexyl-3-methylimidazolium tris(pentafluoroethyl) trifluorophosphate), and (B) 1-ethyl-3-methylimidazolium tris(pentafluoroethyl) trifluorophosphate).

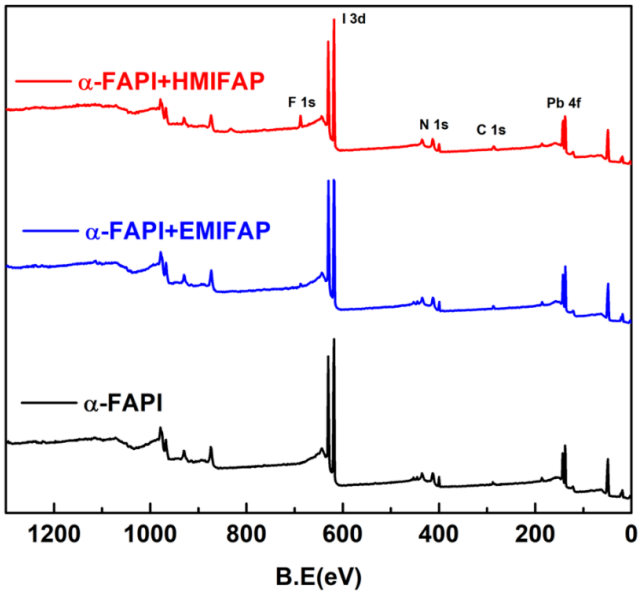

Figure S4. 11 XPS survey spectra of α-FAPI, α-FAPI+EMIFAP, and α-FAPI+HMIFAP thin films.

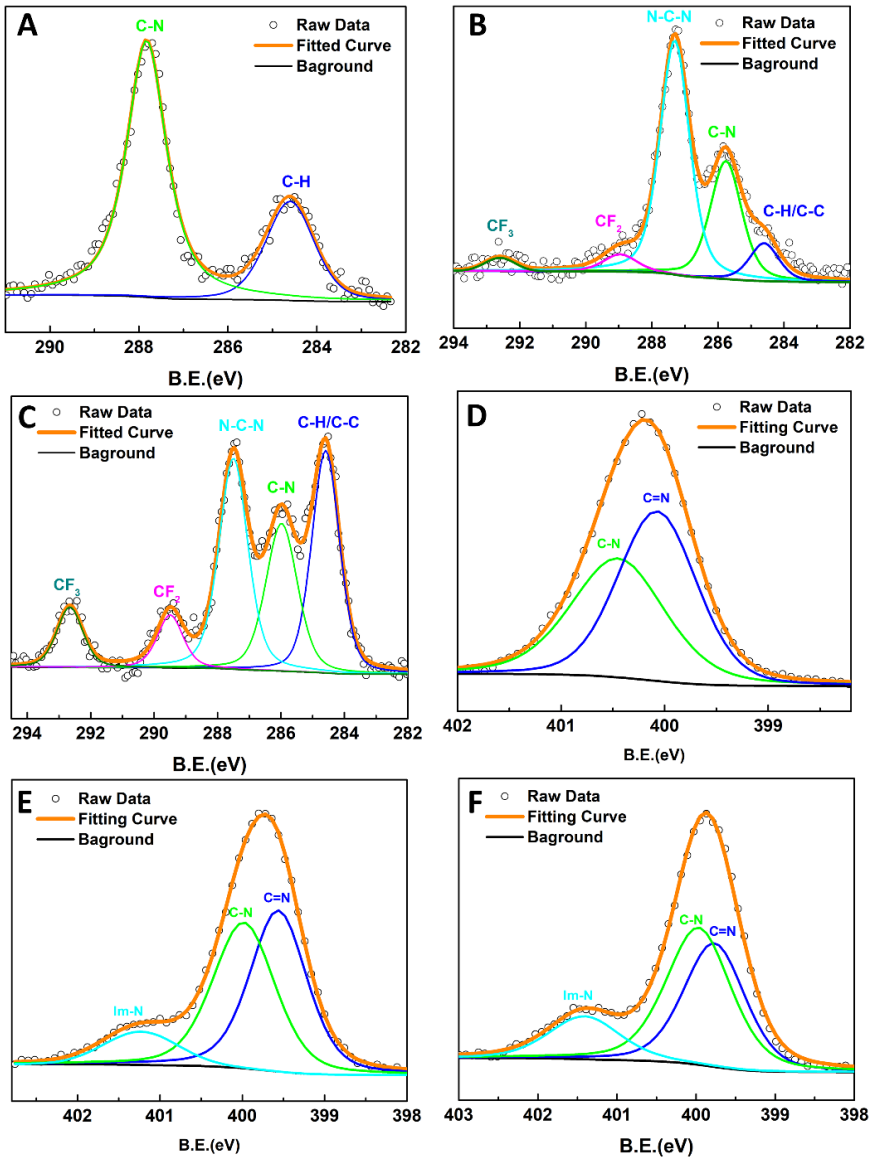

Figure S4. 12 XPS C 1s core-level spectra of (A) α-FAPI, (B) α-FAPI+EMIFAP, and (C) α-FAPI+HMIFAP thin films, and XPS N 1s core-level spectra of (D) α-FAPI, (E) α-FAPI+EMIFAP, and (F) α-FAPI+HMIFAP thin films.

Table S4. 1 Calculated elemental composition of Pb 4f and I 3d core-level spectra

	Core level	Measured Area	Sensitivity Factor	Corrected area	Elemental Ratio
α-FAPI	Pb 4f	140212.001	22.7	6176.740132	**1**
	I 3d	665971.8649	33.6	19761.77641	**3.199386081**
α-FAPI+EMIFAP	Pb 4f	145332.61	22.7	6402.317621	**1**
	I 3d	653948.326	33.6	19404.99484	**3.030932857**
α-FAPI+HMIFAP	Pb 4f	144071	22.7	6346.740088	**1**
	I 3d	628443.5762	33.6	18648.17733	**2.938229245**

Table S4. 2 Calculated elemental composition of Pb 4f and F 1s (F-Pb) core level spectra

	Core level	Measured Area	Sensitivity Factor	Corrected area	Elemental Ratio
α-FAPI+EMIFAP	Pb 4f	140212.001	22.7	6176.740132	**1**
	F 1s (F-Pb)	2567.68	4.3	579.45	**0.09**
α-FAPI+HMIFAP	Pb 4f	145332.61	22.7	6402.317621	**1**
	F 1s (F-Pb)	7681.8	4.3	1726	**0.28**

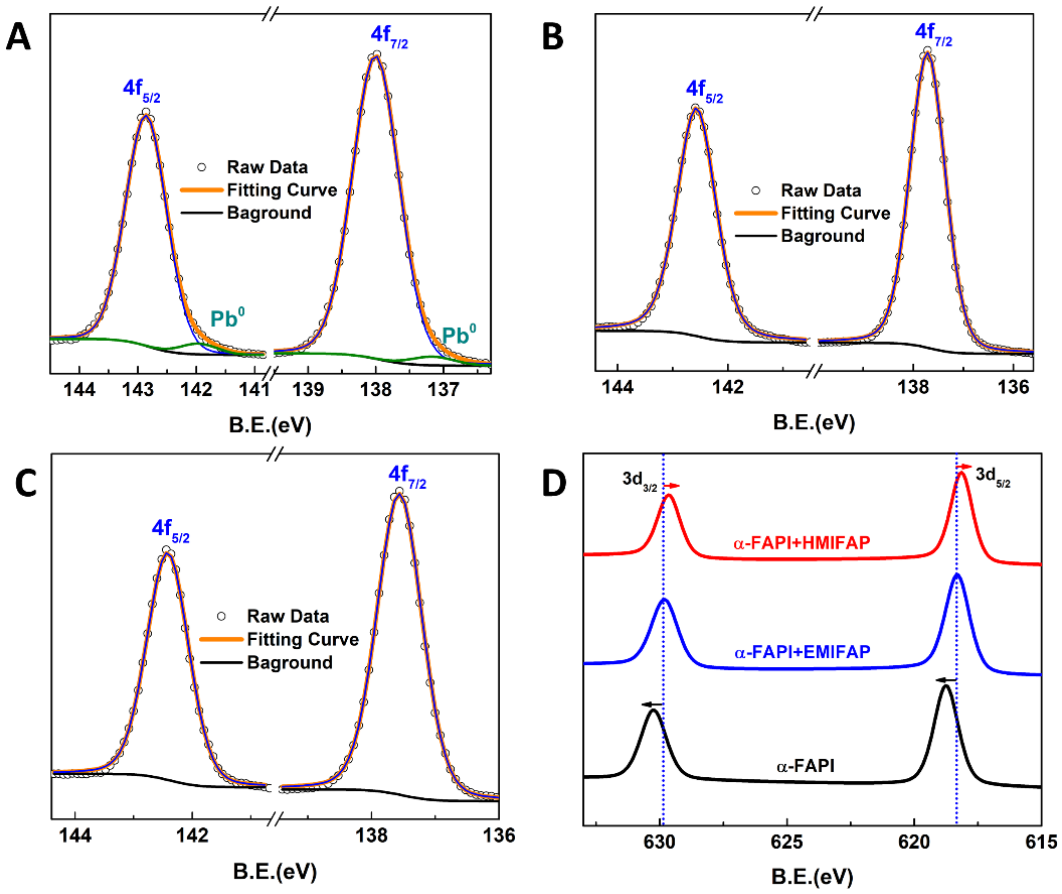

Figure S4. 13 Deconvoluted Pb 4f core-level spectra of (A) α-FAPI, (B) α-FAPI+EMIFAP and (C) α-FAPI+HMIFAP thin films. (D) XPS core spectra of I 3d for the discussed perovskite surfaces.

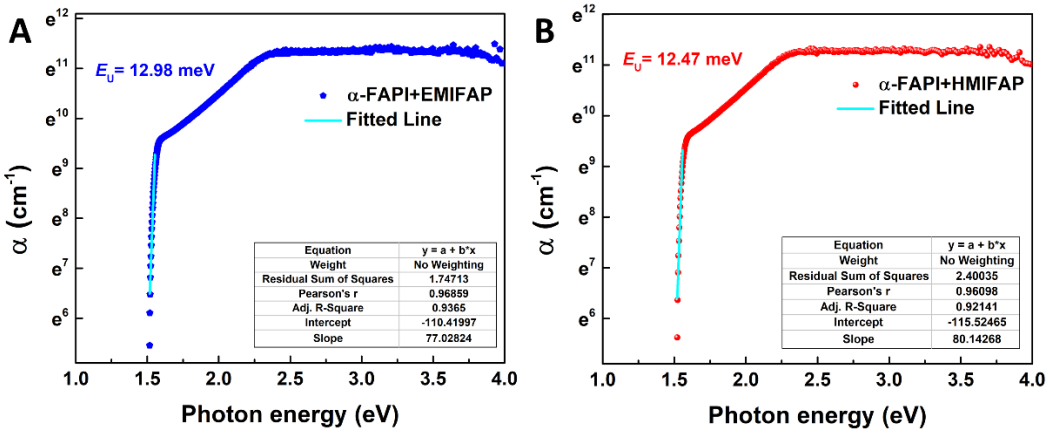

Figure S4. 14 (A, B) Relationship of absorption coefficient (α) and photon energy for the Urbach energy calculation for (A) α-FAPI+EMIFAP, (B) α-FAPI+HMIFAP thin films.

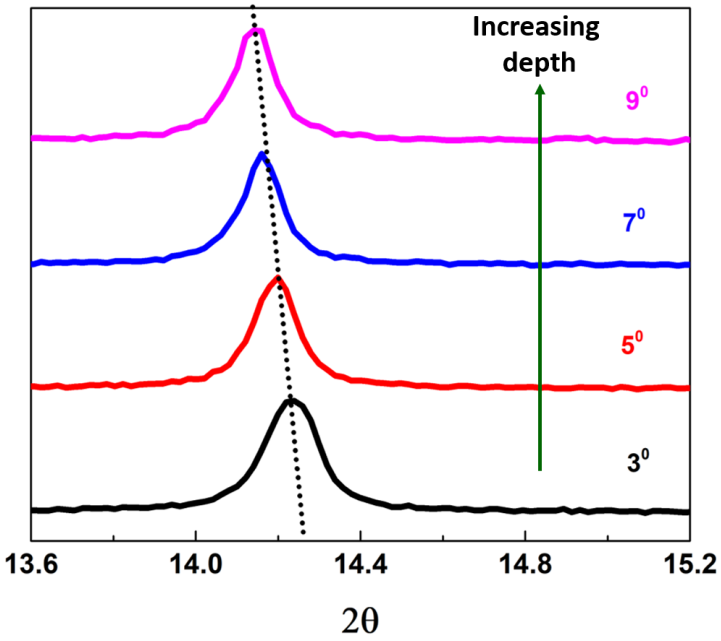

Figure S4. 15 Zoom-in-view of (100) plane in Depth dependent XRD spectra of the α-FAPI+HMIFAP thin film along with the film thickness. The diffractograms were collected at different incident angles from 3° to 9°.

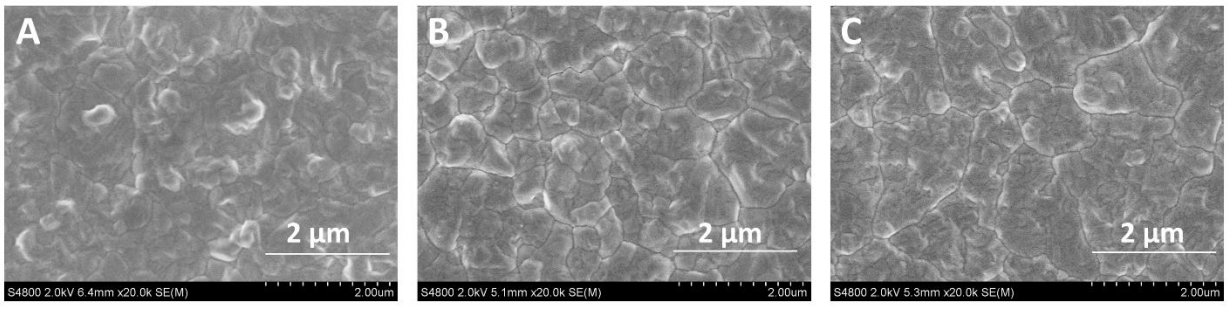

Figure S4. 16 Surface microstructure of (A) α-FAPI, (B) α-FAPI+EMIFAP, and (C) α-FAPI+HMIFAP thin films. The scale bar in SEM images is 2 µm.

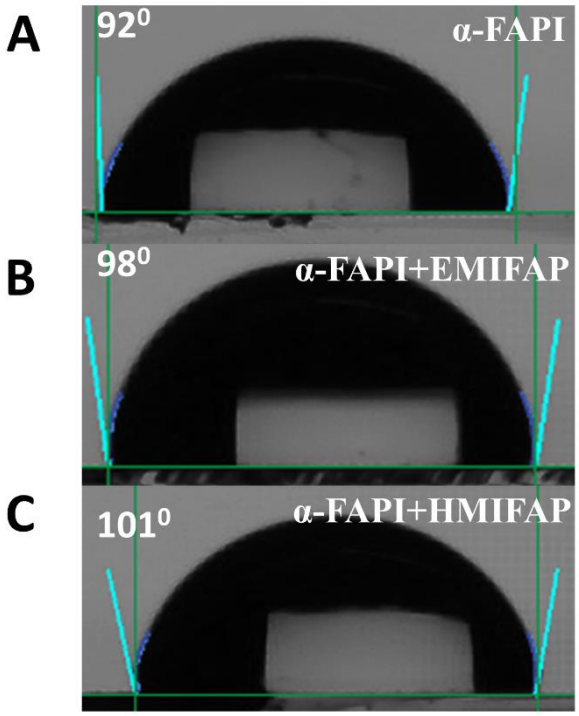

Figure S4. 17 Contact angle measurements of the water droplet on the (A) α-FAPI, (B) α-FAPI+EMIFAP, and (C) α-FAPI+HMIFAP thin films.

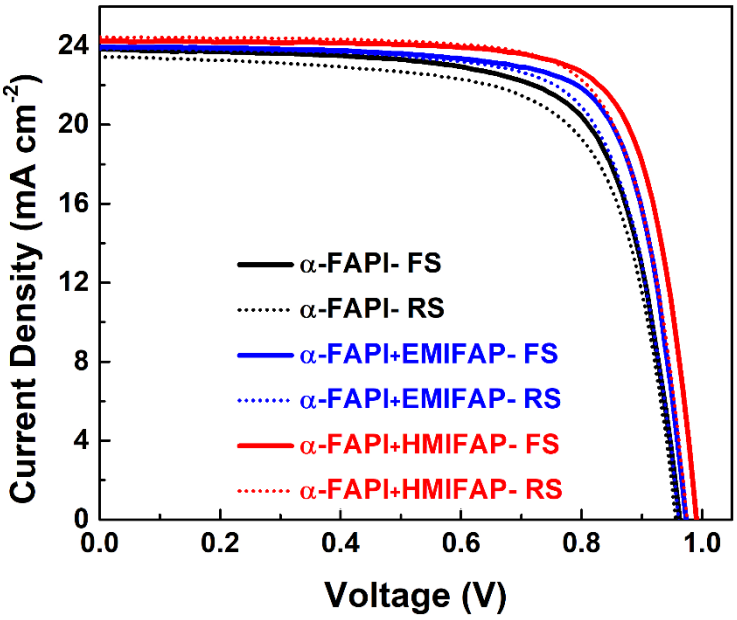

Figure S4. 18 *J-V* curves of best-performing devices under both the forward (FS) and reverse (RS) scans at 100mV/s rate.

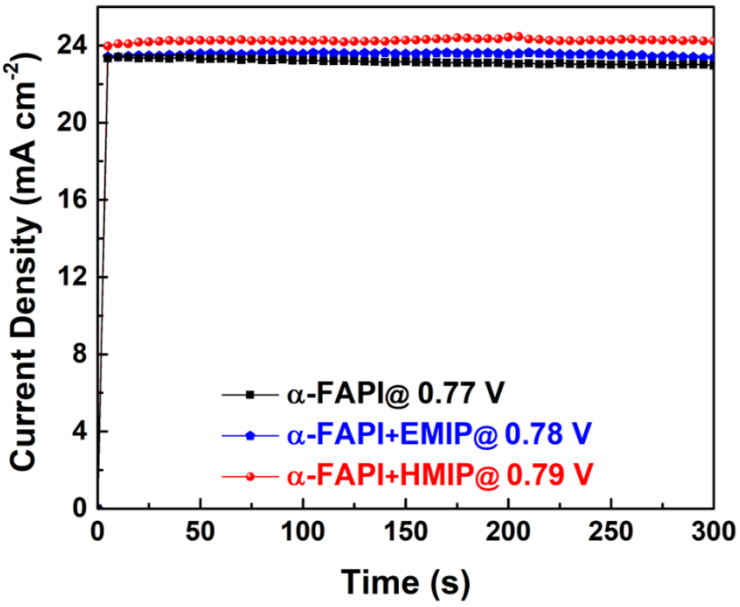

Figure S4. 19 The steady-state photocurrent measurements at maximum power point α-FAPI, α-FAPI+EMIFAP, and α-FAPI+HMIFAP based PSCs.

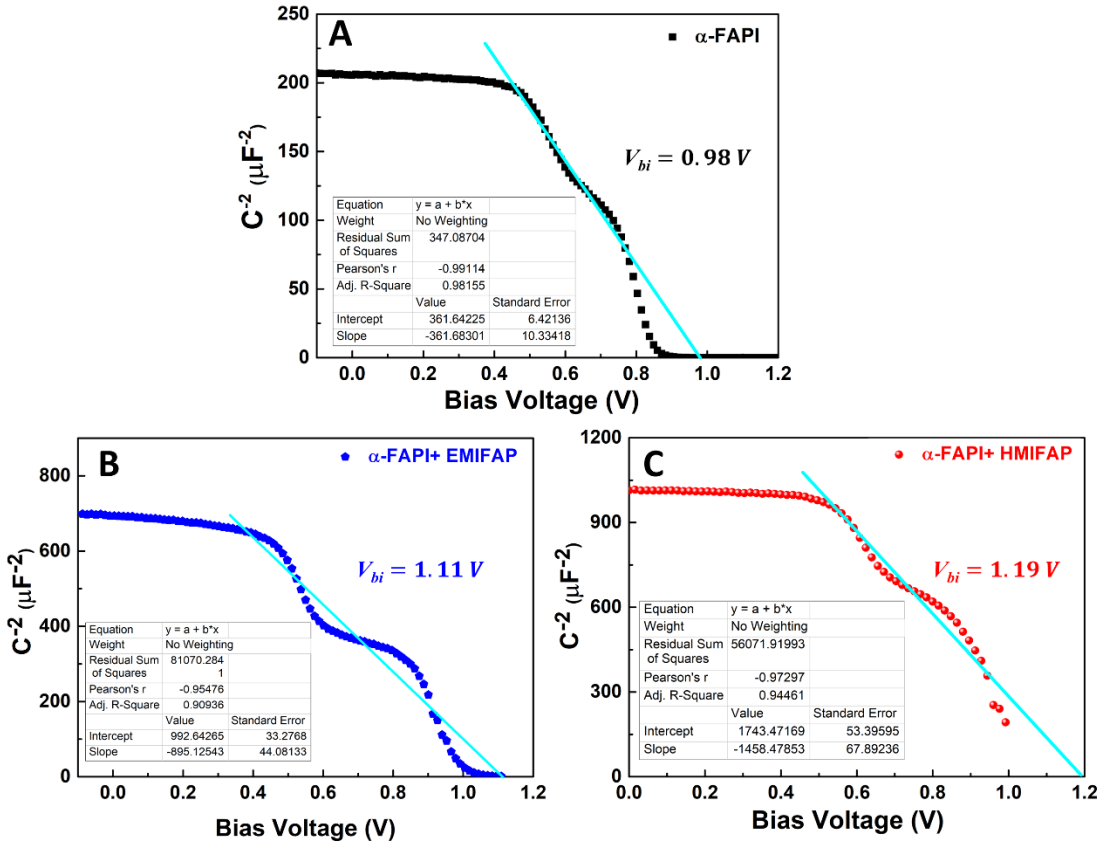

Figure S4. 20 Mott-Schottky analysis at 10 kHz (A) α-FAPI, (B) α-FAPI+EMIFAP, and (C) α-FAPI+HMIFAP based PSCs.

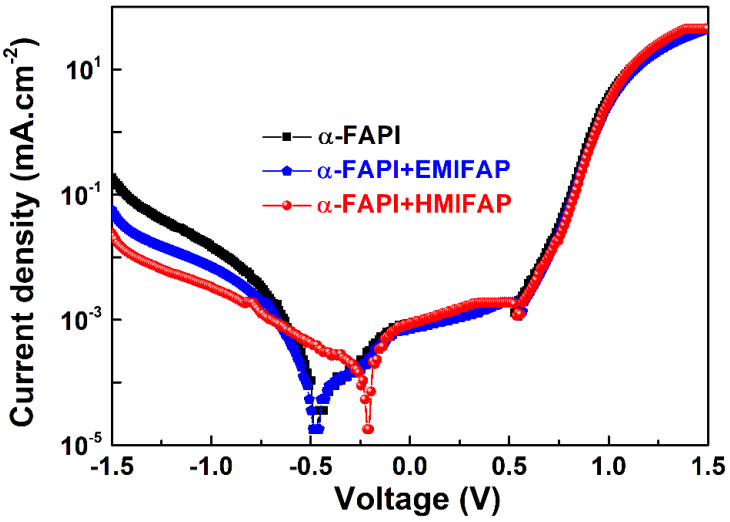

Figure S4. 21 The dark *J-V* characteristics of the PSCs based on α-FAPI, α-FAPI+EMIFAP, and α-FAPI+HMIFAP.

4.7 References

(1) Murali, B., Kolli, H.K., Yin, J., Ketavath, R., Bakr, O.M., Mohammed, O.F., 2019. Single crystals: The next big wave of perovskite optoelectronics. ACS Materials Letters 2, 184–214. doi:10.1021/acsmaterialslett.9b00290

(2) Chen, Z., Turedi, B., Alsalloum, A.Y., Yang, C., Zheng, X., Gereige, I., AlSaggaf, A., Mohammed, O.F., Bakr, O.M., 2019. Single-Crystal Mapbi3 Perovskite solar cells exceeding 21% power conversion efficiency. ACS Energy Letters 4, 1258–1259. doi:10.1021/acsenergylett.9b00847

(3) Zhang, Y., Kim, S.-G., Lee, D.-K., Park, N.-G., 2018. Ch3nh3PBI3 and $HC(NH_2)_2PbI_3$ powders synthesized from low-grade PbI_2: Single Precursor for high-efficiency perovskite solar cells. ChemSusChem 11, 1813–1823. doi:10.1002/cssc.201800610.

(4) Zhang, Y., Seo, S., Lim, S.Y., Kim, Y., Kim, S.-G., Lee, D.-K., Lee, S.-H., Shin, H., Cheong, H., Park, N.-G., 2019. Achieving reproducible and high-efficiency (21%) perovskite solar cells with a presynthesized $FAPbI_3$ powder. ACS Energy Letters 5, 360–366. doi:10.1021/acsenergylett.9b02348.

(5) Jeong, J., Kim, Minjin, Seo, J., Lu, H., Ahlawat, P., Mishra, A., Yang, Y., Hope, M.A., Eickemeyer, F.T., Kim, Maengsuk, Yoon, Y.J., Choi, I.W., Darwich, B.P., Choi, S.J., Jo, Y., Lee, J.H., Walker, B., Zakeeruddin, S.M., Emsley, L.,

Rothlisberger, U., Hagfeldt, A., Kim, D.S., Grätzel, M., Kim, J.Y., 2021. Pseudo-halide anion engineering for α-$FAPbI_3$ perovskite solar cells. Nature 592, 381–385. doi:10.1038/s41586-021-03406-5

(6) Moloney, E.G., Yeddu, V., Saidaminov, M.I., 2020. Strain engineering in Halide Perovskites. ACS Materials Letters 2, 1495–1508. doi:10.1021/acsmaterialslett.0c00308.

(7) Gu, L., Li, D., Chao, L., Dong, H., Hui, W., Niu, T., Ran, C., Xia, Y., Song, L., Chen, Y., Huang, W., 2021. Strain engineering of metal–halide perovskites toward efficient photovoltaics: Advances and perspectives. Solar RRL 5, 2000672. doi:10.1002/solr.202000672

(8) Kim, G., Min, H., Lee, K.S., Lee, D.Y., Yoon, S.M., Seok, S.I., 2020. Impact of strain relaxation on performance of α-formamidinium lead iodide perovskite solar cells. Science 370, 108–112. doi:10.1126/science.abc4417

(9) Wehrspohn, R.B., Deane, S.C., French, I.D., Gale, I., Hewett, J., Powell, M.J., Robertson, J., 2000. Relative importance of the si–si bond and si–H bond for the stability of amorphous silicon thin film transistors. Journal of Applied Physics 87, 144–154. doi:10.1063/1.371836

(10) Stutzmann, M., 1989. The defect density in amorphous silicon. Philosophical Magazine B 60, 531–546. doi:10.1080/13642818908205926

(11) Bai, S., Da, P., Li, C., Wang, Z., Yuan, Z., Fu, F., Kawecki, M., Liu, X., Sakai, N., Wang, J.T.-W., Huettner, S., Buecheler, S., Fahlman, M., Gao, F., Snaith, H.J., 2019. Planar perovskite solar cells with long-term stability using Ionic liquid additives. Nature 571, 245–250. doi:10.1038/s41586-019-1357-2.

(12) Lin, Y.-H., Sakai, N., Da, P., Wu, J., Sansom, H.C., Ramadan, A.J., Mahesh, S., Liu, J., Oliver, R.D., Lim, J., Aspitarte, L., Sharma, K., Madhu, P.K., Morales-Vilches, A.B., Nayak, P.K., Bai, S., Gao, F., Grovenor, C.R., Johnston, M.B., Labram, J.G., Durrant, J.R., Ball, J.M., Wenger, B., Stannowski, B., Snaith, H.J., 2020. A piperidinium salt stabilizes efficient metal-halide perovskite solar cells. Science 369, 96–102. doi:10.1126/science.aba1628.

(13) Niu, T., Chao, L., Gao, W., Ran, C., Song, L., Chen, Y., Fu, L., Huang, W., 2021. Ionic liquids-enabled efficient and stable perovskite photovoltaics: Progress and challenges. ACS Energy Letters 1453–1479. doi:10.1021/acsenergylett.0c02696.

(14) Haris, M.P., Kazim, S., Pegu, M., Deepa, M., Ahmad, S., 2021. Substance and shadow of formamidinium lead triiodide based solar cells. Physical Chemistry Chemical Physics 23, 9049–9060. doi:10.1039/d1cp00552a.

(15) O'Mahony, A.M., Silvester, D.S., Aldous, L., Hardacre, C., Compton, R.G., 2008. Effect of water on the electrochemical window and potential limits of room-temperature ionic liquids. Journal of Chemical & Engineering Data 53, 2884–2891. doi:10.1021/je800678e.

(16) Haris, M.P., Kazim, S., Ahmad, S., 2021a. Low-temperature-processed perovskite solar cells fabricated from presynthesized $CsFAPbI_3$ powder. ACS Applied Energy Materials 4, 2600–2606. doi:10.1021/acsaem.0c03160.

(17) Sharma, M., Yangui, A., Whiteside, V.R., Sellers, I.R., Han, D., Chen, S., Du, M.-H., Saparov, B., 2019. $Rb_4Ag_2BiBr_9$: A lead-free visible light absorbing halide semiconductor with improved stability. Inorganic Chemistry 58, 4446–4455. doi:10.1021/acs.inorgchem.8b03623.

(18) Tavakoli, M.M., Yadav, P., Prochowicz, D., Sponseller, M., Osherov, A., Bulović, V., Kong, J., 2019. Controllable perovskite crystallization via antisolvent technique using chloride additives for highly efficient planar perovskite solar cells. Advanced Energy Materials 9, 1803587. doi:10.1002/aenm.201803587.

(19) Filip, M.R., Hillman, S., Haghighirad, A.A., Snaith, H.J., Giustino, F., 2016. Band gaps of the lead-free halide double perovskites $Cs_2BiAgCl_6$ and $Cs_2BiSAgBr_6$ from theory and experiment. The Journal of Physical Chemistry Letters 7, 2579–2585. doi:10.1021/acs.jpclett.6b01041.

(20) Caselli, V.M., Wei, Z., Ackermans, M.M., Hutter, E.M., Ehrler, B., Savenije, T.J., 2020. Charge carrier dynamics upon sub-bandgap excitation in methylammonium lead iodide thin films: Effects of urbach tail, deep defects, and two-photon absorption. ACS Energy Letters 5, 3821–3827. doi:10.1021/acsenergylett.0c02067.

(21) Chantana, J., Kawano, Y., Nishimura, T., Mavlonov, A., Minemoto, T., 2020. Impact of urbach energy on open-circuit voltage deficit of thin-film solar cells. Solar Energy Materials and Solar Cells 210, 110502. doi:10.1016/j.solmat.2020.110502.

(22) De Wolf, S., Holovsky, J., Moon, S.-J., Löper, P., Niesen, B., Ledinsky, M., Haug, F.-J., Yum, J.-H., Ballif, C., 2014. Organometallic halide perovskites: Sharp optical absorption edge and its relation to photovoltaic performance. The Journal of Physical Chemistry Letters 5, 1035–1039. doi:10.1021/jz500279b.

(23) Broadhurst, A., Rogers, K.D., Lowe, T.W., Lane, D.W., 2004. Determination of depth-dependent diffraction data: A new approach. Acta Crystallographica Section A Foundations of Crystallography 61, 139–146. doi:10.1107/s0108767304026881.

(24) Zhu, C., Niu, X., Fu, Y., Li, N., Hu, C., Chen, Y., He, X., Na, G., Liu, P., Zai, H., Ge, Y., Lu, Y., Ke, X., Bai, Y., Yang, S., Chen, P., Li, Y., Sui, M., Zhang, L., Zhou, H., Chen, Q., 2019. Strain engineering in perovskite solar cells and its impacts on carrier dynamics. Nature Communications 10. doi:10.1038/s41467-019-08507-4.

(25) Juarez-Perez, E.J., Ono, L.K., Qi, Y., 2019. Thermal degradation of formamidinium based lead halide perovskites into sym-triazine and hydrogen cyanide observed by coupled thermogravimetry-mass spectrometry analysis. Journal of Materials Chemistry A 7, 16912–16919. doi:10.1039/c9ta06058h.

(26) Tang, S., Huang, S., Wilson, G.J., Ho-Baillie, A., 2020. Progress and opportunities for Cs Incorporated perovskite photovoltaics. Trends in Chemistry 2, 638–653. doi:10.1016/j.trechm.2020.04.002.

(27) Ledinsky, M., Schönfeldová, T., Holovský, J., Aydin, E., Hájková, Z., Landová, L., Neyková, N., Fejfar, A., De Wolf, S., 2019. Temperature dependence of the Urbach Energy in lead iodide perovskites. The Journal of Physical Chemistry Letters 10, 1368–1373. doi:10.1021/acs.jpclett.9b00138.

(28) Kim, H.-S., Park, N.-G., 2014. Parameters affecting i–v hysteresis of $CH_3NH_3PbI_3$ Perovskite Solar Cells: Effects of perovskite crystal size and mesoporous TiO_2

layer. The Journal of Physical Chemistry Letters 5, 2927–2934. doi:10.1021/jz501392m.

(29) Thundiyil, S., Kurungot, S., Devi, R.N., 2021. Synergistic effect of B site co-doping with Co and Ce in bifunctional oxygen electrocatalysis by oxygen deficient brownmillerite $Ba_2In_2O_5$. Catalysis Today 375, 494–500. doi:10.1016/j.cattod.2020.05.046.

(30) Rajendra Kumar, G., Dennyson Savariraj, A., Karthick, S.N., Selvam, S., Balamuralitharan, B., Kim, H.-J., Viswanathan, K.K., Vijaykumar, M., Prabakar, K., 2016. Phase transition kinetics and surface binding states of methylammonium lead iodide perovskite. Physical Chemistry Chemical Physics 18, 7284–7292. doi:10.1039/c5cp06232b.

(31) Ikari, T., Keppler, A., Reinmöller, M., Beenken, W.J., Krischok, S., Marschewski, M., Maus-Friedrichs, W., Höfft, O., Endres, F., 2010. Surface electronic structure of imidazolium-based ionic liquids studied by electron spectroscopy. e-Journal of Surface Science and Nanotechnology 8, 241–245. doi:10.1380/ejssnt.2010.241.

(32) Caporali, S., Bardi, U., Lavacchi, A., 2006. X-ray photoelectron spectroscopy and low energy ion scattering studies on 1-buthyl-3-methyl-imidazolium bis(trifluoromethane) sulfonimide. Journal of Electron Spectroscopy and Related Phenomena 151, 4–8. doi:10.1016/j.elspec.2005.09.010

(33) Hayakawa, S., Osaka, A., Nishioka, H., Matsumoto, S., Miura, Y., 2000. Structure of lead oxyfluorosilicate glasses: X-ray Photoelectron and nuclear magnetic resonance spectroscopy and molecular dynamics simulation. Journal of Non-Crystalline Solids 272, 103–118. doi:10.1016/s0022-3093(00)00233-7.

(34) Conings, B., Baeten, L., De Dobbelaere, C., D'Haen, J., Manca, J., Boyen, H.-G., 2013. Perovskite-based hybrid solar cells exceeding 10% efficiency with high reproducibility using a thin film sandwich approach. Advanced Materials 26, 2041–2046. doi:10.1002/adma.201304803.

(35) Wang, S., Yang, B., Han, J., He, Z., Li, T., Cao, Q., Yang, J., Suo, J., Li, X., Liu, Z., Liu, S. (Frank), Tang, C., Hagfeldt, A., 2020. Polymeric room-temperature molten salt as a multifunctional additive toward highly efficient and stable

inverted planar perovskite solar cells. Energy & Environmental Science 13, 5068–5079. doi:10.1039/d0ee02043e.

(36) Niu, T., Lu, J., Jia, X., Xu, Z., Tang, M.-C., Barrit, D., Yuan, N., Ding, J., Zhang, X., Fan, Y., Luo, T., Zhang, Y., Smilgies, D.-M., Liu, Z., Amassian, A., Jin, S., Zhao, K., Liu, S., 2019. Interfacial Engineering at the 2D/3D heterojunction for high-performance perovskite solar cells. Nano Letters 19, 7181–7190. doi:10.1021/acs.nanolett.9b02781.

(37) Ignat'ev, N.V., Finze, M., Sprenger, J.A.P., Kerpen, C., Bernhardt, E., Willner, H., 2015. New hydrophobic ionic liquids with perfluoroalkyl phosphate and cyanofluoroborate anions. Journal of Fluorine Chemistry 177, 46–54. doi:10.1016/j.jfluchem.2015.03.007.

(38) Nieto de Castro, C.A., Ribeiro, A.P., Figueiras, A.O., Langa, E., Vieira, S.I., Lourenço, M.J., Santos, Â.F., Vieira dos Santos, F.J., Lampreia, I.M., Goodrich, P., Hardacre, C., 2021. Thermophysical Properties of 1-Butyl-3-methylimidazolium tris(pentafluoroethyl)trifluorophosphate, [C_4mim][$(C_2F_5)_3PF_3$], and of Its IoNanofluid with Multi-Walled Carbon Nanotubes. Journal of Chemical & Engineering Data 66, 1717–1729. doi:10.1021/acs.jced.0c01017.

(39) Hemasiri, N.H., Kazim, S., Ahmad, S., 2020. Reduced trap density and mitigating the interfacial losses by placing 2D dichalcogenide material at perovskite/HTM interface in a dopant free perovskite solar cells. Nano Energy 77, 105292. doi:10.1016/j.nanoen.2020.105292.

CHAPTER 5

5

PROBING PROTON DIFFUSION AS A GUIDE TO ENVIRONMENTAL STABILITY IN POWDER ENGINEERED $FAPbI_3$ AND $CsFAPbI_3$ PEROVSKITES

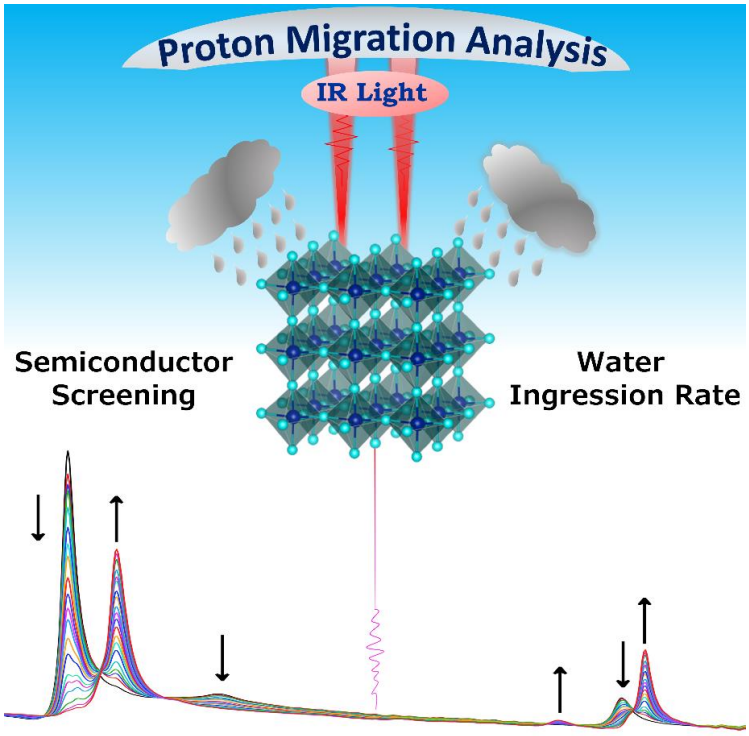

This chapter has been published in *Cell Reports Physical Science* entitled:

Probing proton diffusion as a guide to environmental stability in powder-engineered $FAPbI_3$ and $CsFAPbI_3$ perovskites

Muhammed P.U. Haris, Jianxing Xia, Samrana Kazim, Zuzanna Molenda, Lionel Hirsch,

Thierry Buffeteau, Dario M. Bassani, Mohammad Khaja Nazeeruddin and Shahzada Ahmad

M. P. U. Haris et al., Cell Reports Physical Science 4, 101304 March 15, 2023

D.O.I: 10.1016/j.xcrp.2023.101304

5.1 Abstract

Pre-synthesized perovskite powder is advantageous for device reliability. Arguably, the water uptake capability is critical for the stability of α-$FAPbI_3$ thin films, and the migration of hydrogen species is challenging to elucidate using routine techniques such as imaging or mass spectroscopy. Here, we decipher the proton diffusion to quantify indirect monitoring of H migration by following the N–D vibration using transmission infrared spectroscopy. Allows the direct assessment of the deterioration of perovskite by moisture. The inclusion of a minor amount of Cs in $FAPbI_3$, reveals significant differences in proton diffusion rates attesting to its impact. Its ability to access the active layer by water molecules is five times lower than $FAPbI_3$, which is lower than $MAPbI_3$. This protocol directly correlates with the local environment of the materials and engages with a range of semiconductors to identify the material's reliability and intrinsic degradation mechanisms toward its suitability for optoelectronic applications.

5.2 Introduction

In addition to the high power conversion efficiencies (PCEs), reliability is critical for perovskite solar cells (PSCs) to enter the markets, while the PV market relies broadly on operational costs. Moisture or humidity is the main factor for degradation while other environmental scenarios such as heat, light, and combinations of factors alleviate this.[1-5] Moisture-induced degradation accelerates intrinsic instability. With the herald, building abound formamidinium lead triiodide ($FAPbI_3$) as a material of choice, a direct, rapid, and reliable approach is paramount to investigating and developing fast and efficient screening of materials. Water ingress into the perovskite layer may proceed through i) mono-, di-hydrate formations, ii) strong water-organic amine interaction induced degradation through the weakening of cation-PbI_6 interaction, and iii) protonation of iodide to form hydroiodic acid leaving PbI_2 behind as the final decomposition product.[1] Understanding the reaction kinetics and mechanistic origin are pivotal to designing robust perovskite-based absorbers. Ion diffusion into the perovskite grains occurred as a result of ion migration at grain boundaries and in the bulk, this negatively affects the overall device performance.[6,7] Quantifying experimental approaches to monitor water uptake will be beneficial, although current techniques such as TOF-SIMS[8] do not apply to hydrogen species (H^+, H^0, and H^{-1}), it can be studied by neutron scattering experiments.[9] However,

this requires access to large-scale radiation facilities and planning. The development of experimental techniques for tracking the migration of hydrogen species is of significance to deciphering the stability of designed materials. One such technique is polarization-modulated infrared reflection–absorption spectroscopy (PM-IRRAS),[10] that can track the migration of hydrogen species in $MAPbI_3$ by registering the difference in the vibrational frequency of X–H vs X–D bonds during isotope exchange processes, where X is a heavier element such as carbon, oxygen, or nitrogen.[10] Alternatively, the H / D composition of the material can also be determined using NMR spectroscopy after the dissolution of the material.[11]

Here, we employ transmission infrared (IR) spectroscopy using a sealed cell to follow the isotope exchange under controlled conditions. We show that this is a particularly suitable technique as it allows direct probing of local environmental effects, such as relative humidity, on the migration of hydrogen species. Additionally, we have opted for powder-engineered perovskites as the choice of material owing to i) achieving the highest PCEs and reproducibility over their conventional counterpart,[11-14] ii) reduction in the microstrain and Urbach energy values for perovskite layers fabricated from the powder engineering process, indicating mitigated structural and electronic disorders.[14] Additionally, the powder methodology, would overcome the Pb impurities issue from the Pb precursors and eliminate the error in the weighing of the precursors. The indirect assessment of the protection against moisture induced by surface modification of the powder-engineered α-$FAPbI_3$ and α-$CsFAPbI_3$ can be obtained by simply monitoring the rate of hydrogen exchange within the active layer in the presence of ambient moisture. This knowledge can be used to predict the material´s propensity towards moisture-induced defect formation. Optimization of such process and materials design rule will suppress the non-radiative recombination of photo-generated charge carriers, paving the way for higher fill factor and the V_{OC} in PSCs. With this in hand, we further improve the performance of powder-engineered PSCs with promising fluorinated ionic liquids as an additive.

5.3 Results and Discussions

5.3.1 Preparation and characterization of thin films

Hereafter, akin to Chapter 4, we use the term ˙ δ-$FAPbI_3$', ˙α-$FAPbI_3$' and α-Cs $FAPbI_3$' for thin films fabricated from the pre-synthesized δ-$FAPbI_3$, α-$FAPbI_3$, and α-$CsFAPbI_3$ powders, respectively. See section *4.5.2* in *Chapter 4* for the detailed synthesis of δ-$FAPbI_3$, α-$FAPbI_3$ powders. Briefly δ-phase powder was precipitated by stirring lead iodide (PbI_2) with the formamidinium iodide containing acetonitrile solution at room temperature. The α-$FAPbI_3$ powder was realized by annealing the δ-phase powder at 150 °C. We used a modified synthesis protocol for α-$CsFAPbI_3$ powder, where acetonitrile solution containing CsI and FAI in a 1:9 ratio was used in this case, and the rest of the procedure is the same as the above for α-$FAPbI_3$ powder. Thin films of the perovskites were prepared by spin-coating precursor solutions onto a 2 mm thick BaF_2 disk (20 mm diameter). Upon annealing to 150 °C for 30 min, both $FAPbI_3$, i.e., δ-$FAPbI_3$ and α-$FAPbI_3$ films, gave dark brown films with identical UV-Vis spectra. Scanning probe microscopy (SPM) images (Figure S5.1) were collected on α-$FAPbI_3$ and α-$CsFAPbI_3$ to determine grain size.

5.3.2 Proton diffusion studies

The samples were placed in a home-built spectroscopic cell that hermetically seals the BaF_2 substrate inside a controlled environment. After measuring the transmission IR spectrum at $t = 0$, a saturated solution of K_2CO_3 in D_2O is injected into the cell to maintain the relative humidity fixed at 43%. Successive IR spectra are then taken to determine the proportion of H / D exchange taking place in the material over time. The spectral variation during the H / D exchange for the α-$FAPbI_3$ sample is shown in Figure 5.1 in the 1850-1250 cm^{-1} region. At t=0, the IR spectrum exhibits three main bands at 1712, 1613, and 1352 cm^{-1}, with strong, weak, and medium intensities, respectively. The 1712 and 1352 cm^{-1} bands are coupled modes involving νCN, δNH_2, and δCH vibrations; the 1712 cm^{-1} mode is dominated by the νCN (50%) and δNH_2 (40%) components whereas the 1352 cm^{-1} mode is dominated by the δCH (72%) component. The 1613 cm^{-1} mode is pure δNH_2 vibration.[15] Upon D_2O exposition, the 1712 and 1352 cm^{-1} bands decreased in favour of the increase of the 1681 and 1336 cm^{-1} bands, respectively, whereas the decrease of the

δNH_2 band at 1613 cm^{-1} mode is associated with the increase of the δND_2 band at 1393 cm^{-1} (Figure 5.1 A).

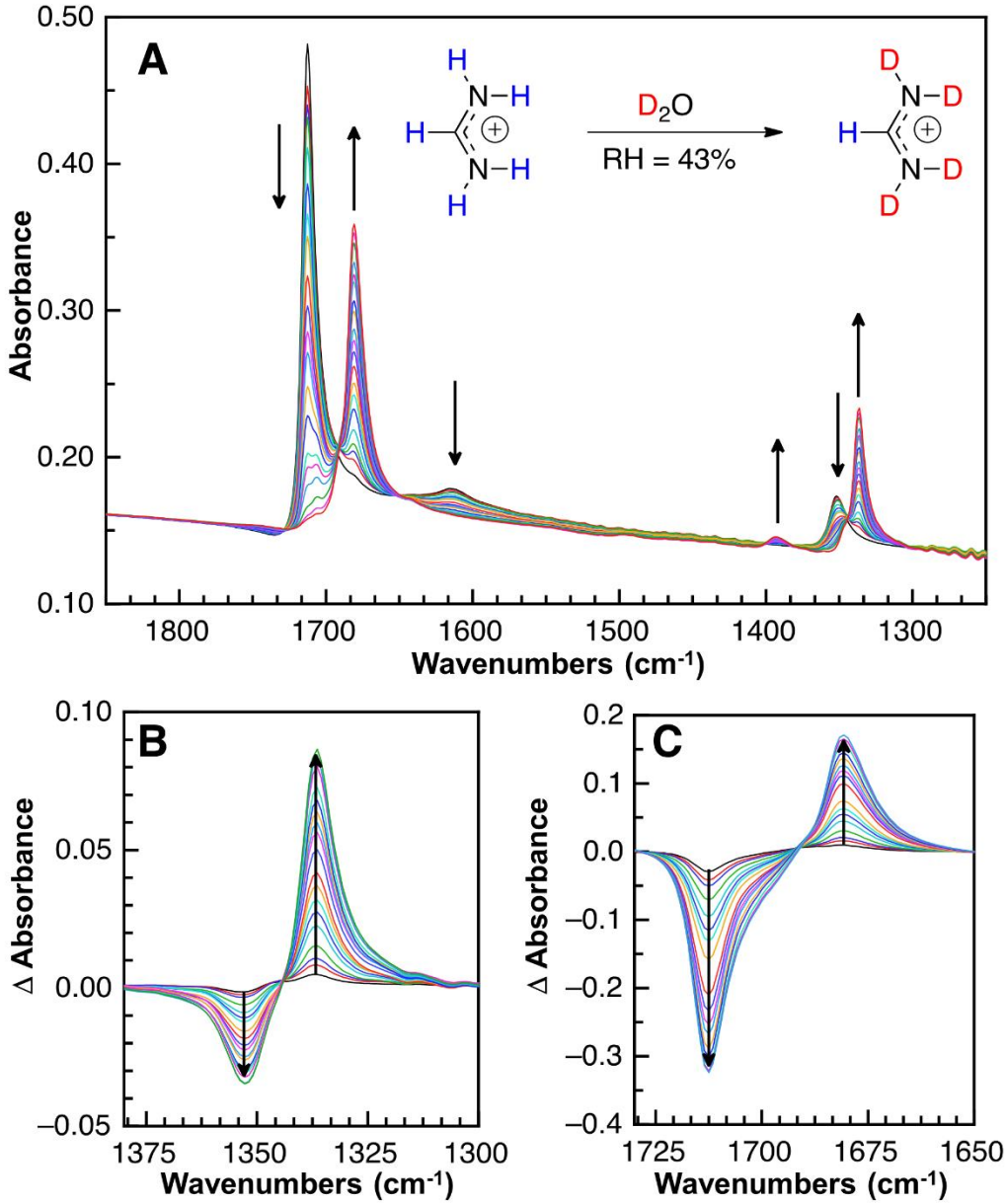

Figure 5. 1 Spectral variation during the H / D exchange. (A) Evolution of the transmission IR spectra of a film (200µm thick) prepared from α-$FAPbI_3$ exposed to 43% RH D_2O (t = 0 to 100 h) and (B and C) Zoom of differential absorption spectra (Abs_t – $Abs_{t\,=\,0}$). The presence of isosbestic points is visible in both the absolute (top) and differential (bottom) absorption spectra.

It is important to note that only the H in the NH_2 fragment will exchange with D_2O. The H / D exchange for the α-$FAPbI_3$ sample can be followed by either the spectral variation

of the pure δNH_2 mode or by the sum of the spectral variation of the two bands related to the coupled modes involving νCN, δNH_2, and δCH vibrations. Both were found to give identical kinetic profiles but, due to the weaker intensity of the δNH_2 mode, the spectral vibration of the coupled modes of νCN and δCH were selected. The variations in the spectral data are related to the exchange of the labile N–H protons in α-$FAPbI_3$ by deuterium, which causes a shift of the vibration to lower frequencies due to its higher mass. This is a complex process that we can decompose into 3 steps: (i) dissociation of D_2O on the surface of the substrate, (ii) diffusion of D^+ into the sample, and (iii) H / D substitution in the formamidinium cation. Both the dissociation of D_2O and isotopic substitution are expected to be fast with respect to ion diffusion in the solid, which should therefore be rate-limiting. The diffusion of a species in a solid follows Fink's law stating that the rate of diffusion of a species is proportional to the concentration gradient of that species. The exact solutions of Fink's law depend on the experimental conditions. For the diffusion in nano-crystalline perovskite thin films, we have evidenced that high-diffusivity pathways between grains are important in determining the diffusion rate. Indeed, the measured diffusion rates are relatively insensitive to sample thickness in agreement with a model in which diffusion occurs rapidly around the grains, and more slowly inside.[16] The individual grains can be modeled as spheres of radius R, and the bulk sample's H / D exchange is obtained by integrating over the thickness of the sample (equation 1):

$$m(t) = \frac{M}{M_{total}} = 1 - \frac{6}{\pi^2}\sum_{n=1}^{\infty}\frac{1}{n^2}e^{-D\frac{n^2\pi^2}{R^2}t} \quad \text{.....(5.1)}$$

Where $m(t)$ is the fraction of total deuterium present at time t, M is the intensity of the signal for the deuterated species present, D is the diffusion constant, and R is the radius of the sphere approximating the grain size or lattice domain.

Table 5. 1 Diffusion constants for protons (H) in pristine perovskite

Material	***R*** **(nm)**	***D*** **($cm^2\ s^{-1}$)[a]**
$FAPbI_3$ from α-powder	200	5.1×10^{-16}

$FAPbI_3$ from δ-powder	200	5.2×10^{-16}
$CsFAPbI_3$ from α-powder	140	1.1×10^{-16}

[a]Determined using eq(1) according to the average grain size (*R)* obtained from AFM and SEM analysis of the samples.

As mentioned above, the vibrations of the N–H(D) and C–H are strongly coupled. Because of this, it is not possible to individually discriminate between the partially deuterated species as is the case for $MAPbI_3$, where the sequential transformation of $CH_3NH_3^+ \rightarrow CH_3NH_2D^+ \rightarrow CH_3NHD_2^+ \rightarrow CH_3ND_3^+$ can be resolved. Furthermore, the contribution of the C–H vibrators (which do not undergo isotope exchange) should be deducted from the overall signals to obtain exclusively the changes resulting from the N–H to N–D exchange. To simplify this, we identified the vibration at 1,712, 1,681, 1,352, and 1,336 cm^{-1} to be exclusively (or nearly so) due to N–H/D vibrators. For these bands (Figure 5.2 A), the decrease in intensity of the N–H contribution (at 1,712 and 1,352 cm^{-1}) is fully compensated by the growth in of the signal of the N–D species (at 1,681 and 1,336 cm^{-1}). From this, it is possible to verify that the loss of H can be precisely quantified from the sum of the intensities of the vibrations at 1,712 and 1,352 cm^{-1}. The data may then be fitted to equation (1) using a value of R corresponding to the average grain size (Table 5.1) determined by SPM and surface SEM images for each sample (Figure S5.1).

The results for the analysis of the diffusion of D^+ into thin films of α-$FAPbI_3$ or α-$CsFAPbI_3$ exposed to D_2O are summarized in Table 5.1 and Figure 5.2 B. The diffusion constants were determined using the corresponding average grain size for each sample as derived from the analysis of the AFM and SEM images (Figure S5.1). Overall, the diffusion coefficients are smaller than that previously determined for $MAPbI_3$ ($D = 1.5 \times 10^{-15}$ $s.cm^{-2}$). As expected, both the α-$FAPbI_3$ and α-$CsFAPbI_3$ films prepared from either α-powder or δ-powder gave nearly identical results, in agreement with the observation that the nature of the precursor material does not affect the properties of the post-annealed active layer. It can also be seen that the rate of diffusion of protons into α-$CsFAPbI_3$ is only one-fifth that of α-$FAPbI_3$. Interestingly, the proton diffusion rate constants are greatest for $MAPbI_3$ and the smallest for α-CsFAPI , with $MAPbI_3 > FAPbI_3 > CsFAPbI_3$.

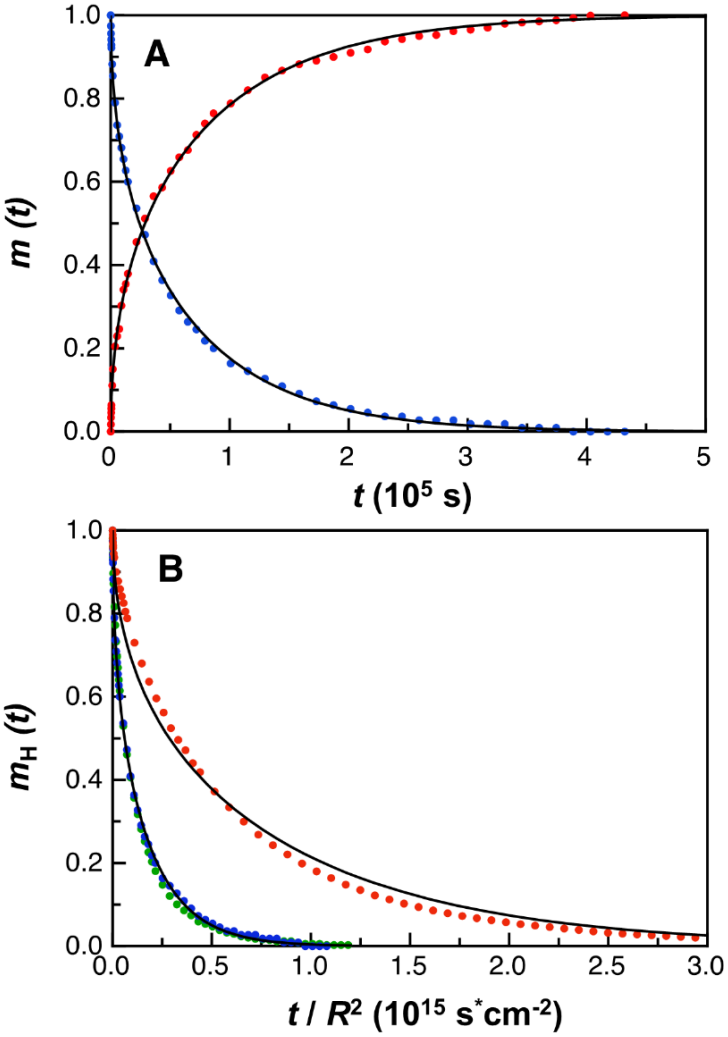

Figure 5. 2 Relative H/D composition. (A) Relative hydrogen (blue symbols) and deuterium (red symbols) composition of thin films of $FAPbI_3$ exposed to D_2O (RH = 43%) at room temperature determined from vibrations assigned to pure N–H or N–D modes. Solid black lines are the best fit for eq(1), (B) Comparison of the proportion of hydrogen present in thin films prepared from α-FAPI (blue symbols), δ-FAPI (green symbols), and α-CsFAPI (red symbols), as determined from the sum of the vibrations at 1712 cm^{-1} and 1352 cm^{-1}, exposed to D_2O (RH = 43%) at room temperature. Solid black lines are the best fit for equation (5.1).

This is also the same order that is generally observed for the propensity towards damage by ambient moisture in halide perovskite materials, and we may speculate that the propensity of lead halide perovskite materials towards damage by moisture is related to the proton diffusion rate for the material. A similar observation was earlier made from the comparison of $MAPbI_3$ active layers in the absence of different adlayers capable of reducing moisture degradation. In this case, the rate of isotope substitution was found to be slowest for those adlayers offering the greatest protection.[10] We also note that the fit

of the experimental data for the α-$CsFAPbI_3$ sample shows some deviation from equation (1) which may reflect intra-grain inhomogeneity due to the partial substitution of FA by Cs^+.

Though reports appear to suggest a performance enhancement in powder-engineered $FAPbI_3$ PSCs,[12-14,17] the reason for intrinsic stability remains undiscovered to an extent. While comparing the conventional and powder engineering methods, we speculate that the precursor solution step acts as a Y-junction in the perovskite fabrication process and their investigations are crucial.

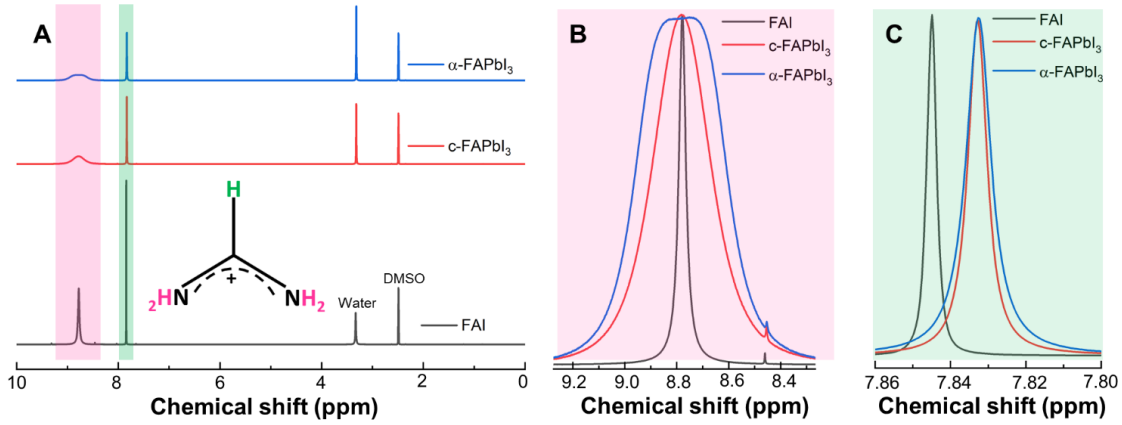

Figure 5. 3 ^{1}H-NMR characterization of precursor solutions. (A) Solution ^{1}H-NMR spectra of FAI, conventional-$FAPbI_3$ (c-$FAPbI_3$) and α-$FAPbI_3$ in DMSO-D_6 solvent at 25°C , the FA cation structure has been given in the inset; (B and C) Zoom-in view of Solution ^{1}H-NMR spectra of, (B) $–NH_2$ protons and, (C) –CH protons in all the three solutions.

It has been suggested that the perovskite precursor solution is a low-viscous solution that comprises polyiodide plumbates which drive the nucleation and crystallization upon further spin coating and annealing.[18] To unravel the different scenarios between conventional (c-$FAPbI_3$) and powder engineering (α-$FAPbI_3$) methods, we probed the corresponding $FAPbI_3$ precursor solutions using proton nuclear magnetic resonance spectroscopy. With the presence of PbI_2, the protons attached to two nitrogen atoms showed fast resonances, which lead to the peak broadening (Figure 5.3). A slight peak broadening of -CH protons was also visible in the powder method than in the conventional counterpart. Arguably, such observations are attributed to the difference in the local protonic environment in the precursor solution that in turn influences the photo-physical properties of the corresponding perovskite thin films.

5.3.4 Fabrication and analysis of PSCs

The photovoltaic performances of the PSCs employing α-$FAPbI_3$ and α-$CsFAPbI_3$ were probed in an FTO/c-TiO_2/m-TiO_2/SnO_2/Perovskite/Spiro-OMeTAD/Au device structure as illustrated in Figure 5.4 A. Expectedly,[19,20] the α-$CsFAPbI_3$ based PSCs exhibit a higher PCE of 19.2% as compared to 18.8% for α-$FAPbI_3$ based PSCs, and the steady-state efficiency of 19.14% (Figure 5.4 B and C) is measured for α-$CsFAPbI_3$.

To suppress the inhibition of ionic migration and a further improvement in the performance of PSCs, we adopted doping by ionic liquids; this will also reduce the ionic migration within the α-$CsFAPbI_3$ perovskite thin-film. We employed, the 1,3-bis(cyanomethyl)imidazolium bis(trifluoromethylsulfonyl)imide (IL)[21] as an additive into perovskite. The ionic liquid additivisation improved the crystallization of the perovskite layer and yielded an improvement in the thickness from 530 nm to 580 nm (Figure S5.2) because of the controlled crystallization process. The improved crystallization of perovskite film may attribute to the changing of surface tension within the precursor and the coordination between ionic liquid and PbI_2.[22,23]

Figure 5.4 D exhibits the *J-V* curves of PSCs based on various concentrations of IL doping. At the doping concentration of 0.7 mol%, the PCE of the PSCs improved to 20.55% (Table 5.2 and Figure 5.5), while under similar conditions the reference α-$CsFAPbI_3$-based PSCs measured 19.27% in the same batch. The steady-state efficiency of the devices was compared (Figure 5.4 E), and the PSC doped with IL displayed 20.38% PCE after 130 s of continuous illumination, further, we noted that the PCE is close to the value derived from the *J-V* curve, and under the similar condition the α-$CsFAPbI_3$ based PSCs measured a PCE of 19.13%. Furthermore, the integrated current density (J_{SC}) from the incident photon to current efficiency (IPCE) (Figure 5.4 F) over the spectral range from 350 to 900 nm to measure the veracity of the J_{SC} of the *J-V* curves. The integrated J_{SC} of PSCs based on references and doped with IL respectively achieved 22.86 and 22.81 mA cm^{-2} which is close to the short-circuit current density (J_{SC}) value from the *J-V* curves with a slight loss of 7%. We attribute these slight variations to the difference in the light source of *J-V* and IPCE used.

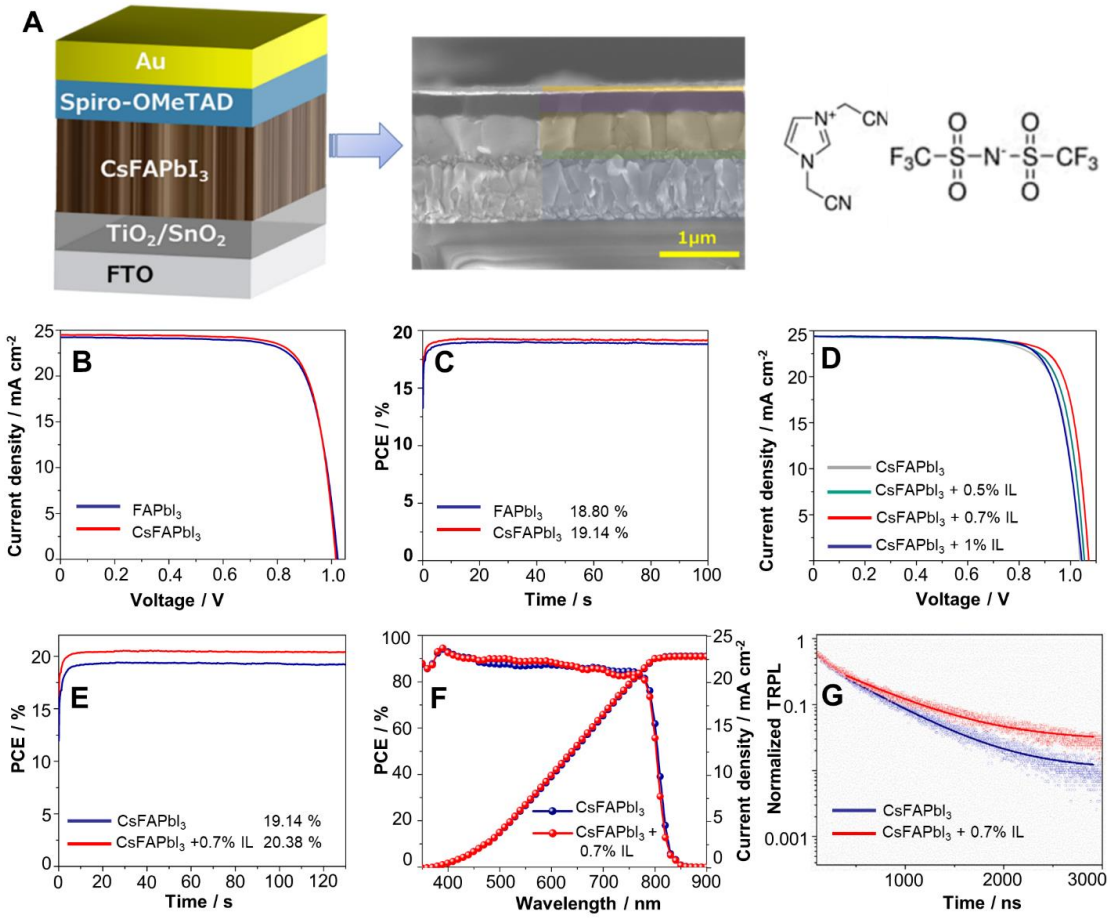

Figure 5. 4 Scheme and electro-optical analysis of perovskites and solar cells. (A) Schematic diagram and the corresponding cross-section image of α-$CsFAPbI_3$ based solar cells, the molecular structure of ionic liquids used, (B) *J-V* curves of devices based on α-$FAPbI_3$ and α-$CsFAPbI_3$, (C) the steady-state PCE of PSCs based on α-$FAPbI_3$ and α-$CsFAPbI_3$, (D) The champion *J-V* curves of α-$CsFAPbI_3$ based PSC doped with the various concentrations of IL, (E) the steady-state PCE of PSCs based on pristine α-$CsFAPbI_3$ and doped with 0.7 mol% IL, (F) IPCE of the devices based on α-$CsFAPbI_3$ (22.86 mA cm^{-2}) and doped with 0.7 mol% IL (22.81 mA cm^{-2}), (G) PL decay curve of pristine α-$CsFAPbI_3$ and 0.7 mol% IL doped α-$CsFAPbI_3$ perovskite film deposited on glass.

Table 5. 2 Photovoltaic parameters of the devices based on pristine $FAPbI_3$, $CsFAPbI_3$, and IL doped $CsFAPbI_3$ based solar cells.

Perovskites		***J*SC (mA cm^{-2})**	***V*OC (mV)**	**FF (%)**	**PCE (%)**
$FAPbI_3$	Max	24.22	1022	76.2	18.85
	Average	23.51±0.71	993±29	74.5±1.7	17.40±1.45
$CsFAPbI_3$	Max	24.38	1036	76.3	19.27

	Average	23.78±0.6	1011±25	74.4±1.9	17.90±1.37
CsFAPbI$_3$+IL 0.5 %	Max	24.36	1054	77.2	19.82
	Average	23.80±0.56	1004±50	75.2±2	18.00±1.82
CsFAPbI$_3$+ IL 0.7 %	Max	24.36	1072	78.7	20.55
	Average	23.43±0.93	1036±36	76.9±2.1	18.63±1.92
CsFAPbI$_3$+ IL 1 %	Max	24.40	1043	76.8	19.54
	Average	23.78±0.62	1015±28	75.7±1.1	18.16±1.38

Table 5. 3 Fitting parameters of *mono*-exponential decay function in TRPL measurements of CsFAPbI$_3$ perovskite in pristine form and with 0.7 mol% IL doping.

Film	**τ (ns)**
Glass/CsFAPbI$_3$	516.1
Glass/ CsFAPbI$_3$+ 0.7 %	614

We performed the Time-Resolved Photoluminescence (TRPL) measurements (Figure 5.4 G) of pristine and IL-doped α-CsFAPbI$_3$ on a structure of glass/perovskite to deduce the carrier lifetime of perovskite film, as well as the decay times. The data are fitted by a *mono*-exponential model at a long decay regime with τ components which indicated recombination.[24] On the additivisation of α-CsFAPbI$_3$ film with IL, the decay time (τ) of TRPL increased from 516.1 to 614 ns indicating the reduced recombination of photogenerated electrons and hole, which is attributed to the passivation of trap states by the ionic liquid.[21]

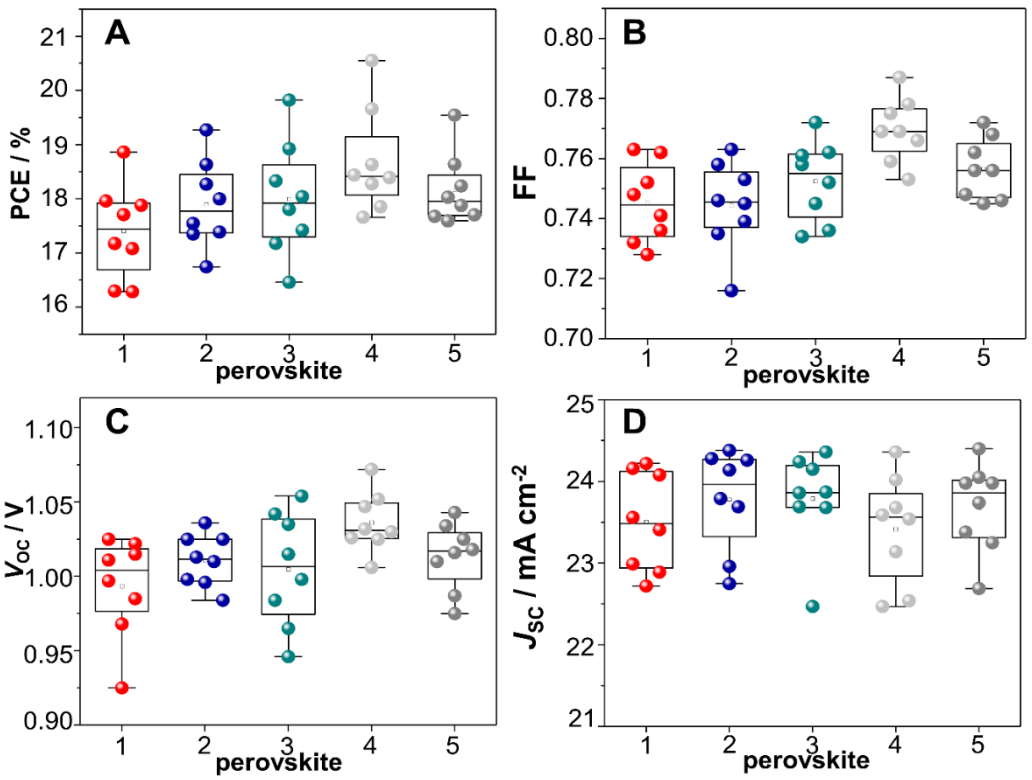

Figure 5. 5 Device parameters optimization, for (A) PCE, (B) FF, (C) V_{OC}, and (D) J_{SC} for perovskite with, 1- α-$FAPbI_3$; 2- α-$CsFAPbI_3$; 3- α-$CsFAPbI_3$ + 0.5% IL; 4- α-$CsFAPbI_3$ + 0.7% IL; 5- α-$CsFAPbI_3$ + 1% IL.

5.4 Conclusion

To conclude, here we employed transmission IR spectroscopy and demonstrated the suitability in allowing the tracking of local environment scenarios against the humidity and made quantification of ion migration to unravel the material´s intrinsic properties for device improvement. We noted the proton diffusion rate constants follow the order of $MAPbI_3$ > $FAPbI_3$ > $CsFAPbI_3$ and are lowest for $CsFAPbI_3$. The majority of techniques fall short to probe hydrogen species migration, our report reveals guidelines for deciphering the H^+ migration and diffusion coefficient to increase the photo-stability of perovskites. The incorporation of Cs not only pushes the performance but also significantly reduces the diffusion coefficient by five times in $FAPbI_3$. The development of such a protocol is an effective and rapid means to screen the viability of the material for perovskite solar cells technology and assess the fundamental limit of the materials to understand the local environment for reliability in a range of emerging semiconductors. We modelled the rate of H/D exchange employing first-order kinetics to elucidate

numerical parameters that can be directly correlated to probe the effectiveness of surface modification on environmental exposure.

5.5 Experimental Procedures

5.5.1 Chemical materials

All chemicals were purchased from Sigma Aldrich and were used as received without any further purification unless and otherwise stated.

5.5.2 Synthesis of $FAPbI_3$ powders

The δ-$FAPbI_3$ and α-$FAPbI_3$ powders were synthesized as explained in *section 4.5.1.1* in *Chapter 4*.

5.5.4 Synthesis of α-$CsFAPbI_3$ powder

Non-perovskite δ-$CsFAPbI_3$ was synthesized through a room temperature precipitation method, where, 10.7 mmol FAI and CsI (in a ratio of 9:1) were dissolved in 100 ml of acetonitrile (HPLC grade, Alfa Aesar) by stirring. 8.3 mmol of PbI_2 (99%) was added to the stirring solution and allowed the stirring to continue for 24 hours. The yellow powders were filtered and the residual components were removed by five times washing with acetonitrile solvent followed by a one-time wash with diethyl ether. The final product was dried under a continuous vacuum for another 24 hours and taken for α-$CsFAPbI_3$ synthesis.

5.5.5 Thin film and device fabrication

For the compact TiO_2 (C-TiO_2) layer, TAA solution in ethanol (0.2 mL of TAA in 6 mL of anhydrous ethanol) was sprayed at 450 °C and heated for 1 h. The mesoporous TiO_2 (m-TiO_2, 30-NRT) was diluted at ethanol with a ratio of 1:10 and coated on the C-TiO_2 substrate at a speed of 3000 rpm for 20 s with a ramp-up of 2000 rpm s^{-1} finally heating at 500 ℃ for 60 min. The $SnCl_4$ layer was dissolved in deionized water at a concentration of 12 μL/mL and spin-coating on the m-TiO_2 layer at a speed of 3000 rpm for 20 s with a ramp-up of 2000 rpm s^{-1} finally heating at 190 ℃ for 60 min, and then perovskite solutions were formulated by dissolving 1.4 M α-$FAPbI_3$ or α-$CsFAPbI_3$ powder in DMSO/DMF mixed solvent with a ratio of 1:8, 20 mg MACl was also added to the

perovskite solution. In the additivated perovskites, the ionic liquid was added in varying concentrations of IL into the perovskite precursors. All the perovskite solutions were filtered through a PTFE filter with a 450 nm pore size. The perovskite layers are fabricated by spin-coating at 1000 rpm for 10 s and 5000 rpm for 30 s, respectively. Then, 200 µL of chlorobenzene was dropped in 10 s at 5000 rpm. Perovskite films were annealed at 150 °C for 15 min. The HTM solution was prepared by dissolving 75 mg of Spiro-OMeTAD (Merck) with additives in 1 mL of chlorobenzene and film fabricated by spin-coating at 4000 rpm for 30 s. As additives, 18 µL of Li-bis(trifluoromethanesulfonyl) imide from the stock solution (520 mg in 1 mL of acetonitrile), 13 µL of FK209 [tris(2-(1*H*-pyrazol-1-yl)-4-*tert*-butylpyridine)-cobalt(III) tris(bis (trifluoromethylsulfonyl)imide) (375 mg in 1 mL of acetonitrile), and 30 µL of 4-*tert*-butylpyridine were added. Finally, the deposition of the 70 nm thick Au electrode by thermal evaporation on the Spiro-OMeTAD.

5.5.6 Characterizations Techniques

Instrumental details has been explained in detail in *section 2.4*.

5.6 Supporting Information

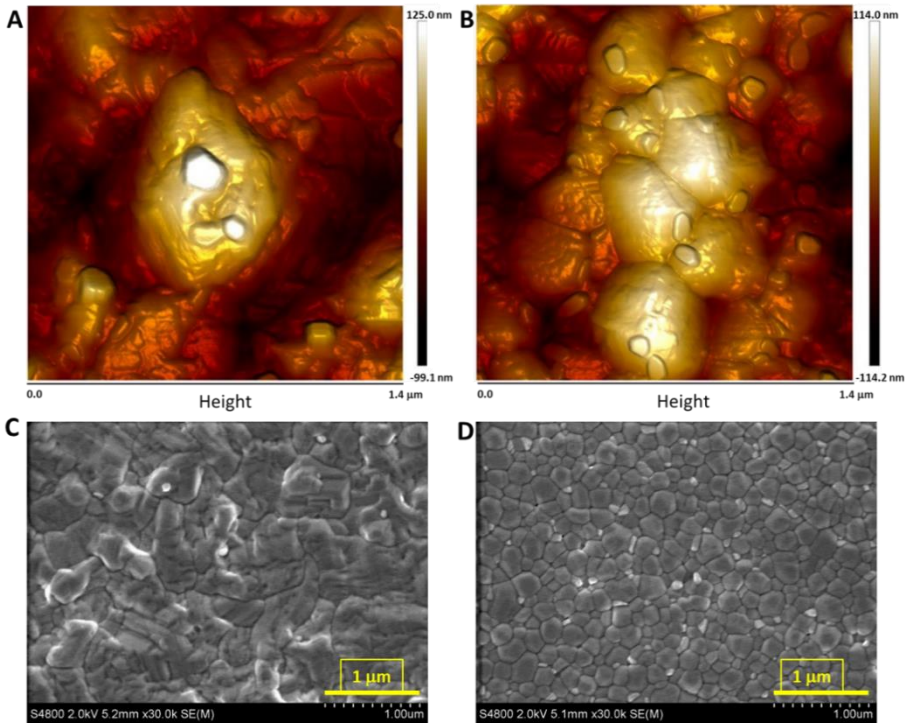

Figure S5. 1 (A, B) AFM image of (A) α-FAPI and (B) α-CsFAPI thin film acquired after IR experiments, and surface SEM (scale bar =1µm) images of (C) α-FAPI and (D) α-CsFAPI thin films.

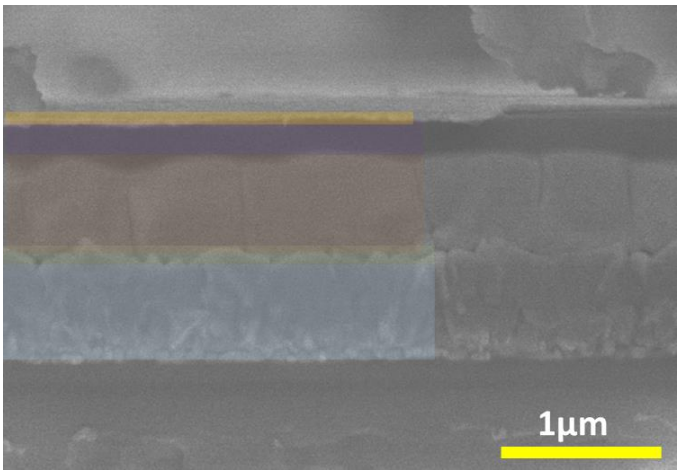

Figure S5. 2 Cross-sectional SEM image (scale bar = 1 µm) of a typical PSC with 0.7 mol% IL doped $CsFAPbI_3$.

5.7 References

(1) Boyd, C.C., Cheacharoen, R., Leijtens, T., and McGehee, M.D. 2018. Understanding Degradation Mechanisms and Improving Stability of Perovskite Photovoltaics. Chemical Reviews119, 3418–3451. https://doi.org/10.1021/acs.chemrev.8b00336.

(2) Holzhey, P., and Saliba, M. 2018. A full overview of international standards assessing the long-term stability of perovskite solar cells. Journal of Materials Chemistry A 6, 21794–21808. https://doi.org/10.1039/C8TA06950F.

(3) Haris, M.P.U., Kazim, S., Pegu, M., Deepa, M., and Ahmad, S. 2021. Substance and shadow of formamidinium lead triiodide based solar cells. Physical Chemistry Chemical Physics 23, 9049–9060. https://doi.org/10.1039/D1CP00552A.

(4) Zhang, D., Li, D., Hu, Y., Mei, A., and Han, H. 2022. Degradation pathways in perovskite solar cells and how to meet international standards. Communications Materials 3, 58. https://doi.org/10.1038/s43246-022-00281-z.

(5) Ho, K., Wei, M., Sargent, E.H., and Walker, G.C. 2021. Grain Transformation and Degradation Mechanism of Formamidinium and Cesium Lead Iodide Perovskite under Humidity and Light. ACS Energy Letters 6, 934–940. https://doi.org/10.1021/acsenergylett.0c02247.

(6) Walsh, A., and Stranks, S.D. 2018. Taking Control of Ion Transport in Halide Perovskite Solar Cells. ACS Energy Letters 3, 1983–1990. https://doi.org/10.1021/acsenergylett.8b00764.

(7) Yang, B., Brown, C.C., Huang, J., Collins, L., Sang, X., Unocic, R.R., Jesse, S., Kalinin, S.V., Belianinov, A., Jakowski, J., et al. 2017. Enhancing Ion Migration in Grain Boundaries of Hybrid Organic–Inorganic Perovskites by Chlorine. Advanced Functional Materials 27, 1700749. https://doi.org/10.1002/adfm.201700749.

(8) Harvey, S.P., Li, Z., Christians, J.A., Zhu, K., Luther, J.M., and Berry, J.J. 2018. Probing Perovskite Inhomogeneity beyond the Surface: TOF-SIMS Analysis of Halide Perovskite Photovoltaic Devices. ACS Applied Materials & Interfaces 10, 28541–28552. https://doi.org/10.1021/acsami.8b07937.

(9) Braun, A., and Chen, Q. 2017. Experimental neutron scattering evidence for proton polaron in hydrated metal oxide proton conductors. Nature Communications 8, 15830. https://doi.org/10.1038/ncomms15830.

(10) Sadhu, S., Buffeteau, T., Sandrez, S., Hirsch, L., and Bassani, D.M. 2020. Observing the Migration of Hydrogen Species in Hybrid Perovskite Materials through D/H Isotope Exchange. Journal of the American Chemical Society 142 (23), 10431–10437. https://doi.org/10.1021/jacs.0c02597.

(11) Ceratti, D.R., Zohar, A., Kozlov, R., Dong, H., Uraltsev, G., Girshevitz, O., Pinkas, I., Avram, L., Hodes, G., and Cahen, D. 2020. Eppur si Muove: Proton Diffusion in Halide Perovskite Single Crystals. Advanced Materials 32, 2002467. https://doi.org/10.1002/adma.202002467.

(12) Zhang, Y., Kim, S.-G., Lee, D.-K., and Park, N.-G. 2018. $CH_3NH_3PbI_3$ and $HC(NH_2)_2PbI_3$ Powders Synthesized from Low-Grade PbI_2: Single Precursor for High-Efficiency Perovskite Solar Cells. ChemSusChem 11, 1813–1823. https://doi.org/10.1002/cssc.201800610.

(13) Jeong, J., Kim, M., Seo, J., Lu, H., Ahlawat, P., Mishra, A., Yang, Y., Hope, M.A., Eickemeyer, F.T., Kim, M., et al. 2021. Pseudo-halide anion engineering for α-$FAPbI_3$ perovskite solar cells. Nature 592, 381–385. https://doi.org/10.1038/s41586-021-03406-5.

(14) Haris, M.P.U., Kazim, S., and Ahmad, S. 2022. Microstrain and Urbach Energy Relaxation in $FAPbI_3$-Based Solar Cells through Powder Engineering and Perfluoroalkyl Phosphate Ionic Liquid Additives. ACS Applied Materials & Interfaces 14 (21), 24546–24556. https://doi.org/10.1021/acsami.2c01960.

(15) Kucharska, E., Hanuza, J., Ciupa, A., Mączka, M., and Macalik, L. 2014. Vibrational properties and DFT calculations of formamidine-templated Co and Fe formates. Vibrational Spectroscopy 75, 45-50. https://doi.org/10.1016/j.vibspec.2014.09.001.

(16) Buffeteau, T., Hirsch, L., and Bassani, D.M. 2021. Comment on "Eppur si Muove: Proton Diffusion in Halide Perovskite Single Crystals": Eppur Non si Muove: A Critical Evaluation of Proton Diffusion in Halide Perovskite Single Crystals. Advanced Materials 33, 2007715. https://doi.org/10.1002/adma.202007715.

(17) Haris, M.P.U., Kazim, S., and Ahmad, S. 2021. Low-Temperature-Processed Perovskite Solar Cells Fabricated from Presynthesized $CsFAPbI_3$ Powder. ACS Applied Energy Materials 4, 2600–2606. https://doi.org/10.1021/acsaem.0c03160.

(18) Jung, M., Ji, S.-G., Kim, G., and Seok, S.I. 2019. Perovskite precursor solution chemistry: from fundamentals to photovoltaic applications. Chemical Society Reviews 48, 2011—2038. https://doi.org/10.1039/C8CS00656C.

(19) Lee, J.-W., Kim, D.-H., Kim, H.-S., Seo, S.-W., Cho, S.M., and Park, N.-G. 2015. Formamidinium and Cesium Hybridization for Photo- and Moisture-Stable Perovskite Solar Cell. Advanced Energy Materials 5 (20). https://doi.org/10.1002/aenm.201501310.

(20) Salado, M., Kazim, S., and Ahmad, S. 2018. The role of Cs^+ inclusion in formamidinium lead triiodide-based perovskite solar cell. Chemical Papers 72, 1645–1650. https://doi.org/10.1007/s11696-017-0373-7.

(21) Gao, X.-X., Ding, B., Kanda, H., Fei, Z., Luo, W., Zhang, Y., Shibayama, N., Züttel, A., Tirani, F.F., Scopelliti, R., et al. 2021. Engineering long-term stability into perovskite solar cells via application of a multi-functional TFSI-based ionic liquidCell Reports Physical Science 2 (7), 100475. https://doi.org/10.1016/j.xcrp.2021.100475.

(22) Wang, S., Li, Z., Zhang, Y., Liu, X., Han, J., Li, X., Liu, Z., Frank Liu, S., and Choy, W.C.H. 2019. Water-Soluble Triazolium Ionic-Liquid-Induced Surface Self-Assembly to Enhance the Stability and Efficiency of Perovskite Solar Cells. Advanced Functional Materials 29, 1900417. https://doi.org/10.1002/adfm.201900417.

(23) Wang, Y., Yang, Y., Li, N., Hu, M., Raga, S.R., Jiang, Y., Wang, C., Zhang, X., Lira-Cantu, M., Huang, F., et al. 2022. Ionic Liquid Stabilized Perovskite Solar Modules with Power Conversion Efficiency Exceeding 20%. Advanced Functional Materials 32, 2204396. https://doi.org/10.1002/adfm.202204396.

(24) Stolterfoht, M., Wolff, C.M., Márquez, J.A., Zhang, S., Hages, C.J., Rothhardt, D., Albrecht, S., Burn, P.L., Meredith, P., Unold, T., et al. 2018. Visualization and suppression of interfacial recombination for high-efficiency large-area pin perovskite solar cells. Nature Energy 3, 847–854. https://doi.org/10.1038/s41560-018-0219-8.

CHAPTER 6

6

LEAD-SULFUR INTERACTION INDUCED DAMP AND WATER STABILITY IN PURE FORAMAMIDINIUM LEAD IODIDE PEROVSKITE

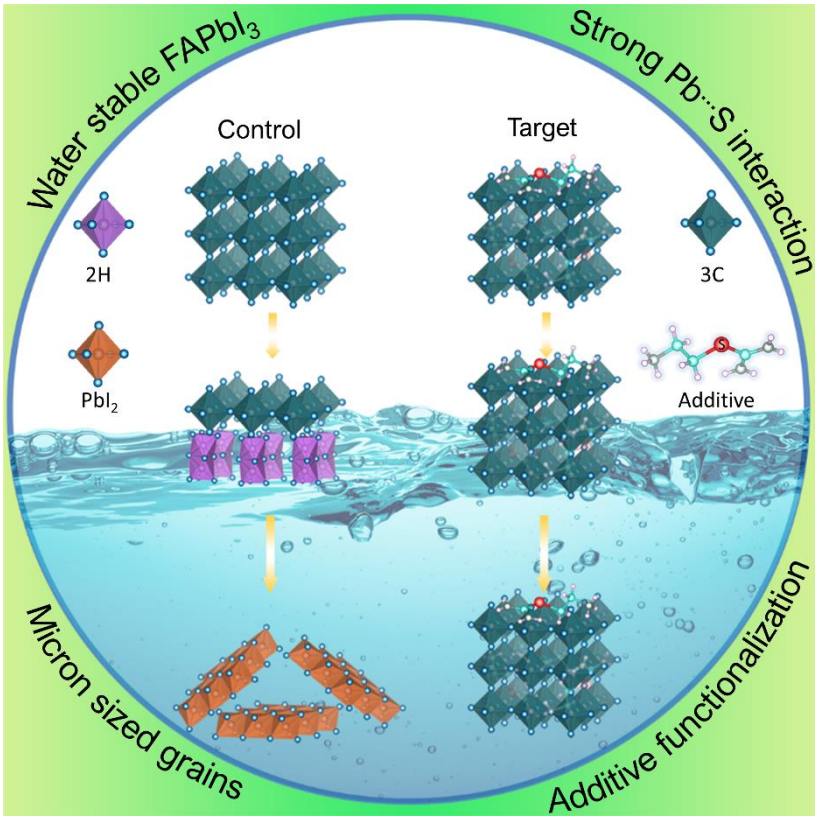

This chapter has been published in *Cell Reports Physical Science* entitled:

Lead-sulfur interaction induced damp and water stability in pure formamidinium lead triiodide

Muhammed. P. U. Haris, Eliseo Ruiz, Samrana Kazim, Shahzada Ahmad

M. P. U. Haris et al., Cell Reports Physical Science 4, 101516, August 16, 2023.

https://doi.org/10.1016/j.xcrp.2023.101516

6.1 Abstract

Research efforts in various multitudes have been demonstrated to stabilize the methylammonium (MA)-and bromide (Br)-free formamidinium lead triiodide (FAPI) perovskite thin films. Despite these commendable efforts, pure FAPI perovskite thin film is prone to critical phase transition issues due to its thermodynamically stable non-perovskite phase (2H). Here in this work, we propose a rational additivisation strategy to overcome this challenge. Our multifunctional ammonium salt containing sulfur hetero atom shifts the thermodynamic stability from the 2H phase to an intermediate phase closer to the cubic phase. Along with the high crystallinity, micron-sized grains with preferred (h00) facet orientation, stems Pb···S interaction to offer exceptional stability against high relative humidity, direct water incursion, and shelf life aging. Our findings through experimental and theoretical studies substantiate the role of Pb···S interaction in stabilizing the perovskite cubic phase and the stoichiometric distribution of elemental components.

6.2 Introduction

In recent years, tremendous efforts are being made to adapt the improved intrinsic stability of formamidinium lead triiodide (FAPI) against moisture and oxygen attacks and suppressed ion migration by employing hydrophobic long organic spacers or Lewis bases as additives. The incorporation of long-chain cations such as phenylethylammonium (PEA^+), 2-thiophenemethylammonium, n-butylammonium, etc., in the precursor solution, regulates the crystallization, phase transition, and ion migration kinetics.[1] In addition to acquiring a uniform surface with larger grains, the long-chain cations occupy the growing edge of 3D perovskites and stimulate their vertical growth to generate a (h00) orientation. The intrinsic hydrophobicity of long-chain cations is also exploited as a pathway to suppress the phase transition by preventing water incursion.[2] Lee et al demonstrated PEA^+ additive suppressed the phase transition of FAPI by preventing moisture incursion through grain boundaries.[3] The passivating effects of 2D cations on the grain boundaries further suppress the ion migration through the formation of PEA_2PbI_4 perovskite with a high energy barrier for ion diffusion. Contrarily, Lewis bases usually play the role of an electron donor and coordinate with the under-coordinated Pb atoms. Prior reports suggest that sulfur exhibits a stronger electron-donating property than

oxygen and nitrogen, and this triggered the successful employment of various sulfur-based non-volatile Lewis bases, such as thiocyanate (SCN^-), thioacetamide (TAA), thiourea, and thiophene derivatives.[4,5] Along with exceptionally larger grains, they showed improved stability against environmental stresses such as humidity, light, temperature, and their combinations. Although these strategies helped to slow down the degradation and phase transition, however, the core issue remains unanswered, i.e., the non-photovoltaic hexagonal (2H) phase remains the thermodynamically favourable phase for FAPI. Additionally, facet engineering investigations have shown that the (111) facet exhibits higher moisture stability than the (h00) facet, which is desirable for PV applications. Intense efforts are required to stabilize the (h00) facet-dominated FAPI surfaces.[6]

Here, to synergize the benefit of both Lewis base and 2D cation, we opted for a bifunctional organic ammonium salt, i.e., S-(2-Aminoethyl)isothiouronium iodide hydroiodide, as an additive and probed its influence on structural, photo-physical properties and phase-stability of FAPI. We identified an intermediate structure with the lowest formation energy than the well-established 2H phase, which is a thermodynamically favourable phase but on the other hand closer to the desirable cubic (3C) phase with our additive. Structure-photo-physical property correlation studies demonstrated exceptional stability against water infiltration, humidity, shelf life, and thermal stresses. Our modified film exhibited a (h00) dominated facet orientation with high stability.

6.3 Results and Discussions

6.3.1 Additive synthesis

S-(2-Aminoethyl)isothiouronium iodide hydroiodide (Isothio) salt depicted in Figure 6.1 A has been synthesized through a halogen exchange reaction (detailed in experimental procedure). The solution-based nuclear magnetic resonance spectroscopic (NMR) and X-ray photoelectron spectroscopic (XPS) analyses were undertaken to probe the Isothio structure. ^{1}H-NMR (Figure 6.1 B) and ^{13}C-NMR (Figure S6.1 A, supporting information, SI) certify the structure of synthesized Isothio additive. The XPS Br 3d core level spectra (Figure S6.1 B, SI) from Isothio crystals before and after the halogen exchange reaction

confirms the complete bromine-iodine exchange. Throughout this paper, all the XPS peaks were calibrated against the C 1s peak at 284.6 eV.

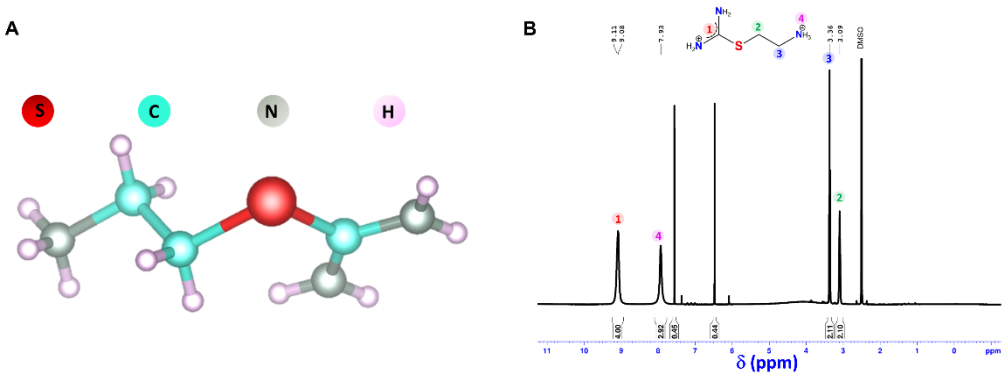

Figure 6. 1 (A) Structure and (B) solution H-NMR spectra of synthesized Isothio additive with labelled elements.

6.3.2 Perovskite thin film characterization

The synthesized Isothio salt was further introduced in perovskite precursor solution as an additive as detailed in experimental procedures. We chose Isothio salt to explore the inter-molecular interactions between two amino ends and sulfur heteroatom. To ensure uniform terminology throughout the chapter, we will refer to the control films as FAPI and the modified films as ISO. We first probed the photo-physical properties of solution-processed thin films. UV-Vis absorption and photoluminescence (PL) spectra (Figure 6.2 A) depict the enhanced absorption from the Isothio additive-based FAPI film termed as ISO film in the visible region, attributed to the higher crystallinity and increased film thickness noted from powder X-ray diffractograms (Figure 6.2 B) and scanning electron microscopy (SEM) cross-section images (Figure S6.2, SI) respectively. Thin film thickness increases from 330 nm to 470 nm with Isothio additivisation. Arguably, the ISO film displays a highly ordered (h00) facet orientation at the macroscopic level deduced by the intense peak at $2\theta = 14^{\circ}$ and 28°, whereas the FAPI film exhibited heterogeneous facet orientations. The reduced full width at half maximum (FWHM) and an induced small red shift of diffraction peaks due to the lattice contraction (Figure S6.3 A, SI) suggest the improved crystallinity and structural incorporation of Isothio additive in ISO films. Lattice contraction leads to reduced Pb-I bond lengths. Owing to the larger contribution of I 5p orbital to the valence band of FAPI, the lattice contraction can manipulate the valence band energy level and eventually results in PL redshifting (Figure

6.2A).[7] In this case, we attribute the small redshift in the PL emission to the lattice contraction of ISO film. The enlarged view of diffractograms at lower 2θ angles unravels the absence of 2D perovskite formation at the macroscopic level (Figure S6.3 B, SI) and the amount of Isothio additive in the precursor solution was optimized as 5 mol% for Pb content accordingly (Figure S6.4, SI). Moreover, FAPI film displayed a rough surface with a smaller grain size while the ISO film showed exceptionally large grain in several micrometer sizes with a much smoother surface under the SEM (Figure 6.2 C and D) and atomic force microscopy (AFM; Figure S6.5, SI) is in agreement with the reported Lewis base induced grain size enhancements.[4]

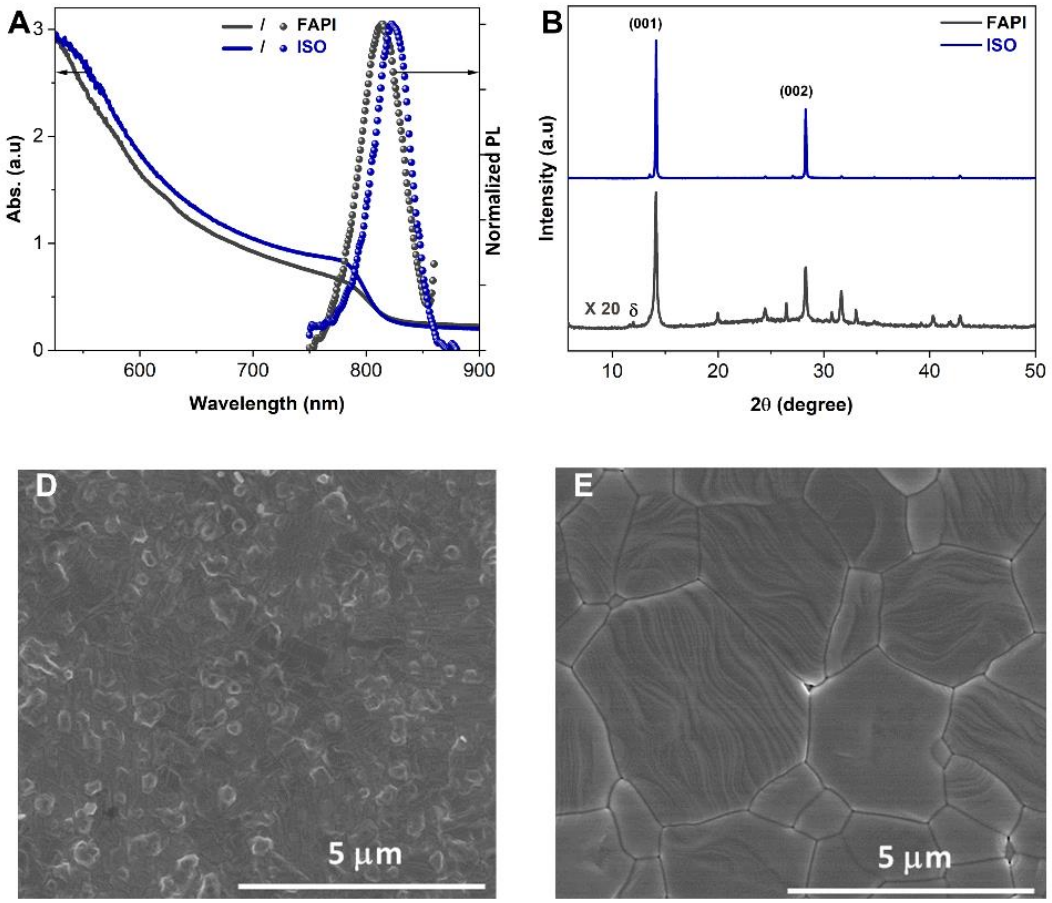

Figure 6. 2 (A) UV-Vis absorption and normalized PL spectra. (B) X-ray diffractograms, (C, D) surface SEM images of (C) FAPI and (D) ISO films with a scale bar of 5 µm.

We then investigated the FAPI and ISO perovskites by solid-state (ss) -NMR. ^{13}C and ^{1}H ss-NMR spectra were collected by scrapping the powders from the respective spin-coated thin films. The registered chemical shifts of all the 3 different C environments (Figure S6.6 A, SI) and the peak shift observed for corresponding ^{1}H-NMR spectra (Figure S6.6

B, SI) of Isothio additive in ISO perovskite confirms its substitutive nature and it is accordance with the peak shifting in diffractograms (Figure S6.3 A, SI).[8] The enlarged and deconvoluted view of the ^{13}C spectral area (Figure S6.6 C, SI) corresponding to FA cation indicates the Isothio additive resists the transition to the 2H phase. The FWHM of the 3C component of FAPI at 154.9 ppm was recorded as 0.78 ppm while that of ISO at 155.03 ppm showed a reduced FWHM of 0.68 ppm. The narrowing of ^{13}C resonance corroborates the improved crystallinity observed in ISO film.[9] The presence of Isothio in the perovskite film was re-affirmed by the S 2s core level XPS spectra (Figure S6.7, SI) and the intense shift of Pb $4f_{7/2}$ and $4f_{5/2}$ XPS peaks suggests strong intermolecular interaction between Pb and lone pairs of S atoms (Figure 6.3). It is evident from the deconvoluted Pb 4f peaks that the unfavorable under-coordinated metallic Pb component identified for FAPI thin film is eliminated upon additive treatment. Moreover, a significant Pb···S interacting component was identified with the ISO films.

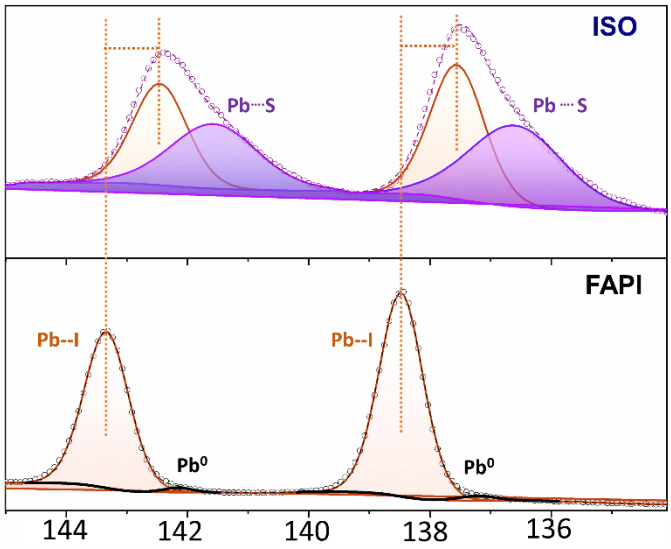

Figure 6. 3 Pb 4f core level PS spectra of FAPI and ISO films.

This Pb···S interaction supports the partial electron cloud migration from the lone pair of S atoms to the perovskite Pb atom.

The nanoscopic topology deduced from a high-resolution transmission emission microscope (HR-TEM) identified randomly oriented phases for FAPI (Figure S6.8 A- E, SI). Notorious edge dislocations and amorphous spots are noted across the surface (Figure S6.8 A-D, SI). Moreover, the interplanar spacing calculated from fast Fourier transformations (FFT) showed the presence of the 2H phase (δ-100) along with the 3C

phase (α-210) (Figure S6.8 E, SI). However, we observed an improved long-range ordered orientation along with a reduced amount of edge dislocation and amorphous spots for the ISO film (Figure S6.8 F, SI).[10] The long-range ordered structural distribution with mitigated edge dislocation and phase transition endorse our additive engineering. The structural, morphological, and optical characterization of thin films suggests enhanced crystallinity, macroscopic (h00) facet orientation, long-range ordered structural distribution, and high absorption over the entire visible range which is aligned with the reported Lewis base and 2D cation-based additive engineering.

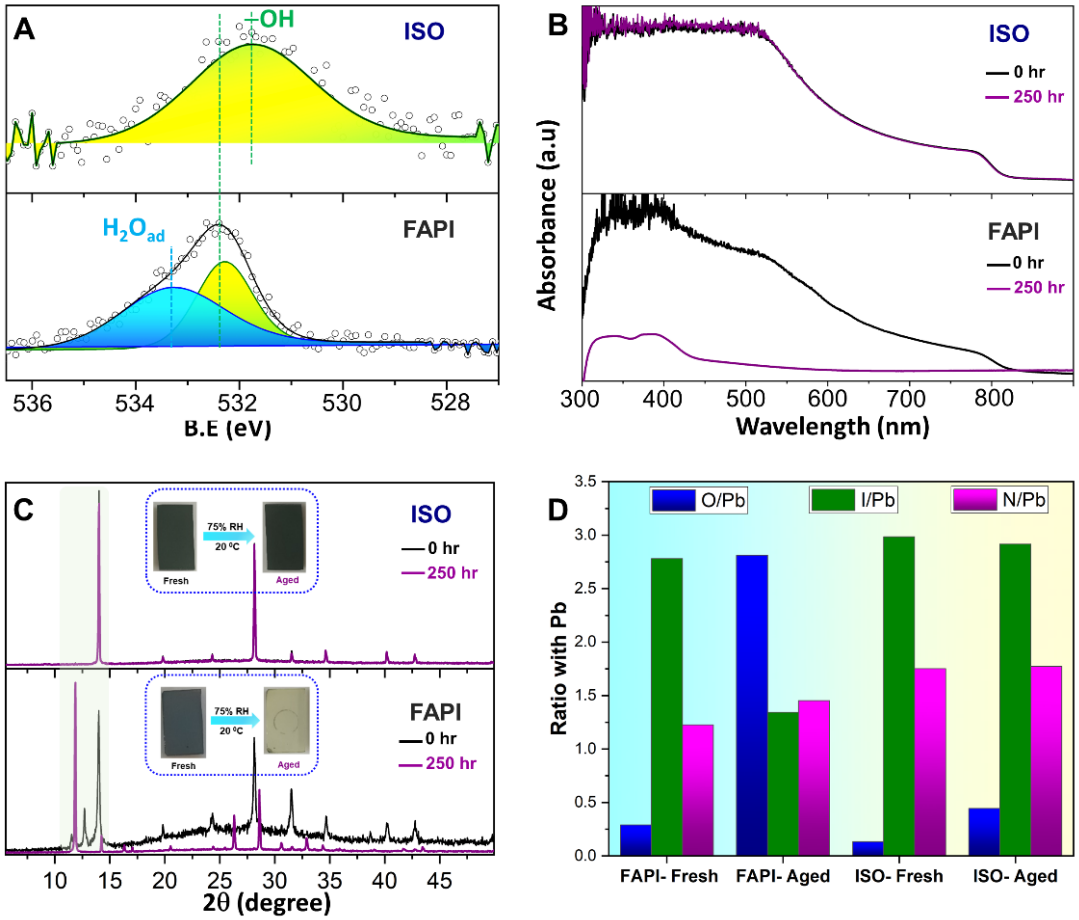

Figure 6. 4 (A) O 1s core level XPS spectra freshly prepared FAPI (bottom) and ISO (top) film films. Open circles and lines represent the recorded data and fitted lines, respectively. (B, C) (B) UV-Vis absorption spectra and (C) diffractograms and digital images (inset) of FAPI (bottom) and ISO (top) films before (black) and after (purple) the humidity attack. (D) histogram representing the XPS elemental composition before and after the humidity attack for FAPI and ISO films.

6.3.3 Perovskite stability against various stresses

To decipher how the additivisation addresses the notorious phase transition and stability concerns of FAPI is of paramount importance. The O 1s core level XPS spectrum (Figure 6.4 A) of the freshly prepared FAPI film deconvoluted into two components at binding energies of 532.2 and 533.2 eV, corresponding to the chemisorbed –OH and molecularly adsorbed H_2O_{ad} moieties respectively.[11] On the contrary, freshly prepared ISO film does not exhibit any H_2O_{ad} trace at the surface indicating high resistance towards the moisture at the perovskite-moisture interface. FAPI thin films with random facet orientation are highly sensitive to humidity and water infiltration where the water molecules interact with the surface Pb-I or FA-I terminal of (h00) facets and undergo a quick phase transition through a Pb-I bond elongation.[6] We monitored the Isothio-assisted phase stabilization by exposing the corresponding films to a controlled humidity atmosphere, water immersion, and shelf life storage experiments. Firstly, we exposed the films to a chamber with a controlled 75% relative humidity for 250 hours. The UV-Vis absorption, digital photograph (Figure 6.4 B), and diffractograms (Figure 6.4 C) of fresh and aged films depict the quick 3C-to-2H phase transition and additional PbI_2 formation for FAPI. Interestingly, ISO films showed no significant change either in absorption or in diffraction patterns that substantiates the high humidity stability. To understand the compositional changes upon moisture-induced degradation, we conducted XPS measurements on fresh and aged surfaces. It can be deduced (Figure 6.4 D), the O/Pb ratio showed a drastic 10 times increment, i.e. from 0.29 to 2.81, for the FAPI film, while the ISO-based film showed a comparatively 3 times increment, i.e. 0.14 to 0.44. Additionally, it is notable that the absence of H_2O_{ad} trace for both the fresh and aged ISO films (Figure S6.9 A, SI), suggesting the molecularly adsorbed H_2O_{ad} trace primarily drives the degradation than the chemisorbed –OH trace. We attribute the exceptional moisture stability of (h00) facet-oriented ISO film to the presence of strong Pb···S interaction that prevents the H_2O_{ad}. Along with the phase transition, surface compositional changes are also followed by humidity degradation. I/Pb and N/Pb ratios directly indicate the composition of the perovskite surface. Upon the humidity aging, FAPI film showed a drastic decrease in the I/Pb ratio (Figure 6.4 D) which is further supported by the highly intense peak of the Pb^o component in the deconvoluted Pb 4f XPS spectra of FAPI films (Figure S6.9 B, SI). The Pb 4f core level spectra of ISO films

(Figure S6.9 C, SI) eliminate the possibilities of PbI_2 formation and agree with the corresponding X-ray diffractograms.

To exploit the exceptional stability of ISO films against humidity exposure, we immersed FAPI and ISO thin films in deionized water and tracked the degradation via in-situ UV-Vis absorption spectroscopy. Expectedly, control FAPI has undergone very quick degradation[12] to the PbI_2 within the first 5 seconds (Figure 6.5 A) which was visible by the absorption peak around 525 nm. While the ISO film displayed the photoactive phase even after 10 minutes of water immersion and most interestingly both the PbI_2 and 2H phases were completely suppressed during the process (Figure 6.5 B), i.e., the water incursion was successfully restricted in ISO film. Though the 2H and PbI_2 phases remain suppressed during the process, the ISO film showed a gradual decrease in the absorption coefficient indicating a slow degradation. Nevertheless, on comparing with control FAPI, our modified ISO film demonstrates exceptional phase stability during the water immersion. The digital images collected (Figure 6.5 C and D) during the immersion of thin films substantiate the *in-situ* absorption studies.

Further, we tracked the shelf-life stability of thin films under ambient atmospheric conditions through diffractograms and digital photographs over a period of time, pointing towards the exceptional stability of ISO film. The macroscopic 2H phase emerged for control FAPI (2θ = 11.9, see Figure S6.10 A, SI) soon after the exposure to the atmospheric air and kept on diffusing throughout the film. The FAPI film fully converted to the 2H phase within 24 hours of atmospheric aging. While the developed ISO-based film stayed in the pure 3C phase at the macroscopic level for a longer time of 6 months of atmospheric aging. Continued aging changed the film from a visible black to a pale reddish colour (Figure S6.10 B, SI). Our combined results show that the developed Isothio additive engineering not only resists the phase transition but also stabilizes the composition or stoichiometry of 3C FAPI perovskite under high humidity, atmospheric air, and water attacks for an exceptionally long time.

6.3.4 Quantifying the crystallization kinetics

The unusual colour transition from black to pale red instead of black to yellow colour upon atmospheric aging inspired us to examine the crystallization kinetics. Though multiple intermediate polymorphs have been identified for FAPI,[13,14] 2H (yellow) stands as the thermodynamic stable phase. Here we tracked the crystallization kinetics of our

ISO perovskite film through optical, structural, and morphological studies. Firstly, spin-casted pristine FAPI (FAPI-RT) and ISO (ISO-RT) films are kept in an atmospheric environment without annealing.

Expectedly, the FAPI-RT film formed a yellow-coloured 2H phase at room temperature and continued in the same phase upon atmospheric exposure for a long time (Figure 6.6 A), in agreement with previous reports on FAPI degradation.[15] In the other case, ISO-RT film also forms a 2H phase soon after the spin coating, however, it initiates a dramatic colour change after 5 minutes and completely acquires pale red colour within the next 5 minutes (Figure 6.6 A). We exposed these films for a longer time in the air and noted FAPI-RT and ISO-RT films remained in the yellow and red colours respectively. The time-dependent ex-situ UV-Vis absorption spectra also support the observed coloration of ISO-RT film (Figure S6.11, SI). The X-ray diffractogram collected from ISO-RT suggests the presence of both 2H and 3C reflections with a slightly shifted to a high angle (Figure S6.12, SI).

This can be attributed to any of the following reasons, i) the formation of a thermodynamically stable intermediate phase between 2H and 3C, ii) the 2D perovskite formation with n>2, and iii) the formation of segregated regions of 2H (dominant) and 3C phase. To exclude the possibility of the formation of 2D perovskites (n>2) and thus induced coloration of the film, we used equimolar amount (to ammonium cations in Isothio additive) of phenylethyl ammonium iodide (PEA) and benzyl ammonium iodide (Benz) as additives. Room temperature (RT) processed films from PEA (PEA-RT) and Benz (Benz-RT) showed no change in the digital image, UV-Vis absorption, and XRD spectra for the FAPI-RT (Figure S6.13, SI). Such observation excludes the possibility of low-dimensional perovskite formation with n>2. We undertook the microscopic analysis to understand the uniformity of grains in FAPI-RT and ISO-RT films. We noted a uniform surface morphology of the 2H phase for FAPI-RT (Figure 6.6 B) whereas ISO-RT (Figure 6.6 C) displayed morphology similar to the 3C surface. This eliminates the third possibility of a segregated phase existence and endorses the possibility of a stable intermediate formation.

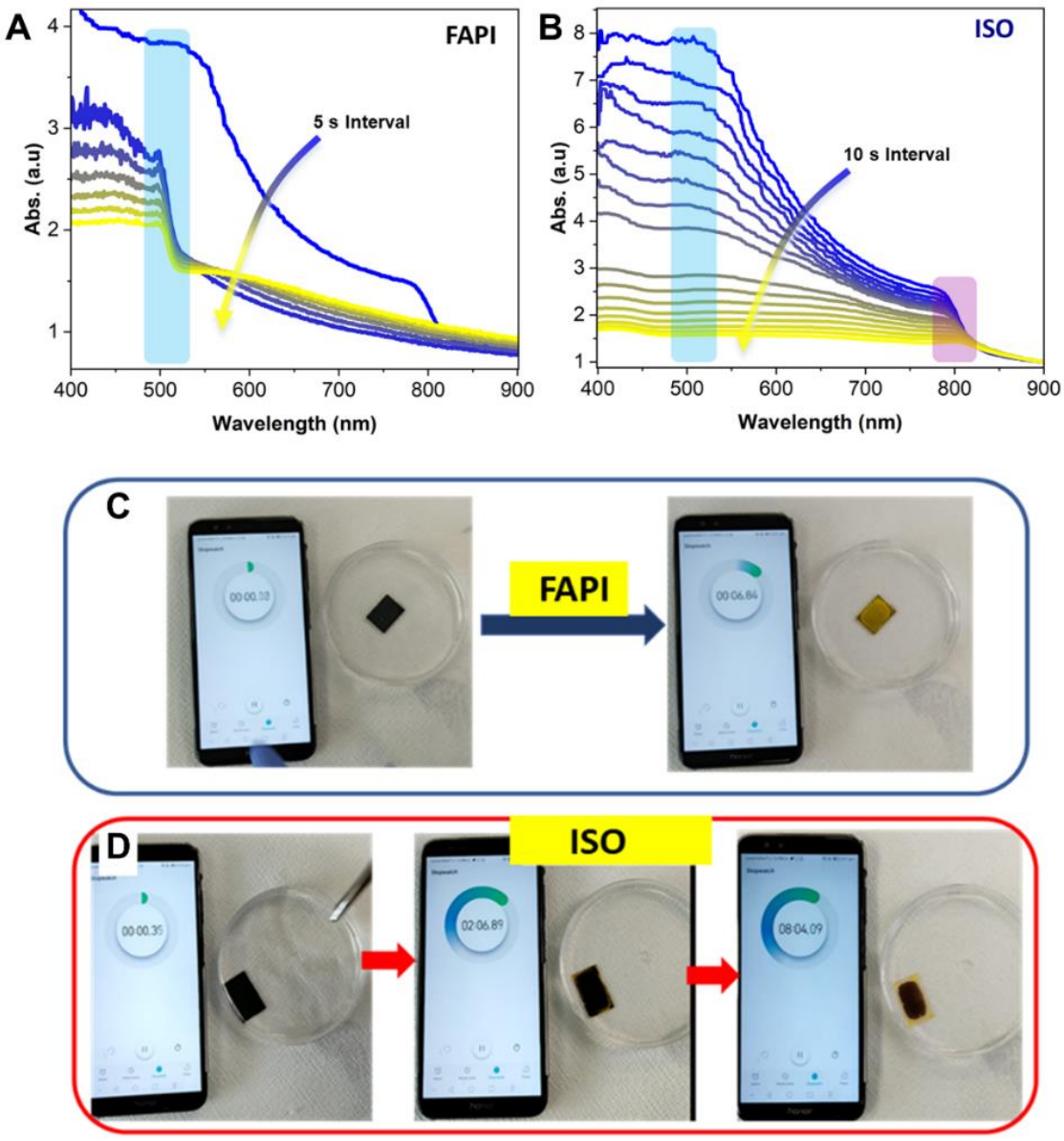

Figure 6. 5 (A,B) in-situ UV-Vis absorption spectra collected during the water immersion experiment for (A) FAPI and (B) ISO films at intervals of 5 s and 10 s, respectively. a.u. denotes arbitrary units. Digital images of (C) FAPI and (D) ISO films during the water immersion experiments.

The degraded (against atmospheric stress) FAPI and FAPI-RT films are known to show similar features in UV-Vis absorption and XRD analysis (Figure 6.6 D and S6.14 A, SI) since the 2H is the thermodynamic stable phase for FAPI. Similarly, on comparing the absorption and diffraction pattern of the degraded ISO and ISO-RT films, we noted both features to be precise (Figure 6.6 D and S6.14 B, SI), suggesting the formed intermediate phase as the thermodynamically stable phase. To unravel the origin of this stable intermediate formation, we compared the thin films from similar Lewis base additive

engineering. We opted thiourea to probe the role of Pb····S interaction in stabilizing the intermediate phase. The emergence of the absorption onset (Figure S6.15 A, SI) and a similar diffractogram (Figure S6.15 B, SI) in the thiourea additive and the absence of intermediate phase in 2D spacer additives (Figure S6.13, SI) substantiate our hypothesis that the Pb····S interaction drives the formation of the stable intermediate phase. Thiourea is reported to sit on the grain boundaries, in our case with the advantage of ammonium cations Isothio additive will incorporate into the structure and will stem strong Pb····S interaction. This in turn will stabilize the final 3C phase of FAPI against the notorious high humidity, water, and atmospheric air attacks.

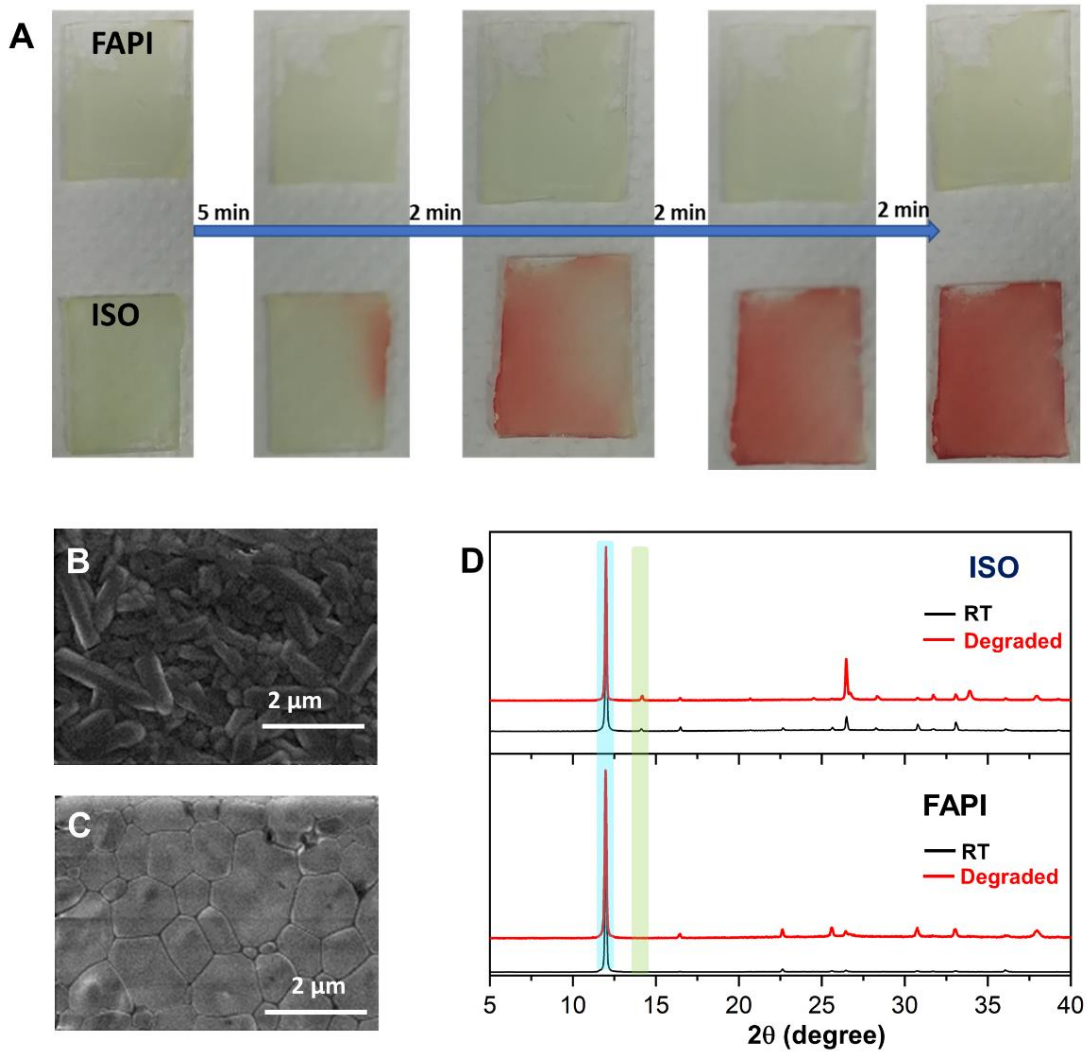

Figure 6. 6 (A) Digital images of FAPI-RT and ISO-RT films stored under an ambient atmosphere were collected over a given time interval. (B, C) surface SEM images of (B) FAPI-RT and (C) ISO-RT films indicate a uniform distribution of intermediate phase instead of segregated 2H and 3C phases in ISO film. (D) diffractograms of FAPI (bottom) and ISO (top) films, where the black lines and red lines represent the unannealed and degraded samples, respectively.

6.3.5 DFT calculations

To rationalize the additivisation protocol, it is important to know whether the Isothio additive structurally incorporates in the bulk or accumulates at the surface of perovskite thin film. For that, we performed periodic density functional theory (DFT) calculations (detailed in the Experimental and SI sections) and two different models have been adopted to study the inclusion of the Isothio dication in the FAPI structure. In Model-1 (Bulk substitution of two formamidinium cations by one Isothio dicationic molecule), for the 3C and 2H structures 2x2x3 and 2x1x3 supercells were used, respectively, containing the same number of atoms. Thus, in these unit cells, the isothio^{2+}/FA^{+} ratio is 1:10 (Figure 6.7 A and B). The energy difference per PbI_3 unit between both cases is only 1.4 kcal/mol favourable to the hexagonal system but shows an increase in the stability of the cubic phase in comparison to the pristine FAPI (3.0 kcal/mol of energy difference). Structural analysis reveals long Pb$\cdots$S contacts (below 5 Å) in the cubic structure with three contacts at 4.146, 4.153, and 4.765 Å while only one for the hexagonal phase at 4.254 Å. The percentage volume shows an increase due to the inclusion of the Isothio molecule substituting two FA^{+} cations. In the case of the cubic structure, it is only 1.2% while in the hexagonal structure; it requires a volume increase of 2.2%. This result shows that it is easier to accommodate the *isothio*$^{2+}$ molecule in the cubic structure than in the hexagonal one and consequently produces a relative stabilization of the cubic phase in agreement with the above-discussed experimental data.

In Model-2 (surface accumulation through iodide vacancy) a 2D system was generated and in the external layer, three FA^{+} cations and one iodide have been replaced by one Isothio molecule to preserve the neutrality (Figure 6.7 C and D). For the cubic structure a Pb$\cdots$S bond distance of 3.430 Å while in the hexagonal structure, sulfur is a bridging ligand with 3.355 Å. The comparison of the energy values with the equivalent FAPI slabs indicates a stabilization of the cubic structure for the interaction with the Isothio dication around 2.8 kcal/mol per PbI_3 unit. We have also evaluated the band structures for 3C cubic and 2H hexagonal phases in both models (Table S6.1; Figure S6.16 and S6.17, SI). The simulated data is in agreement with the experimental results (Figure S6.14, SI).

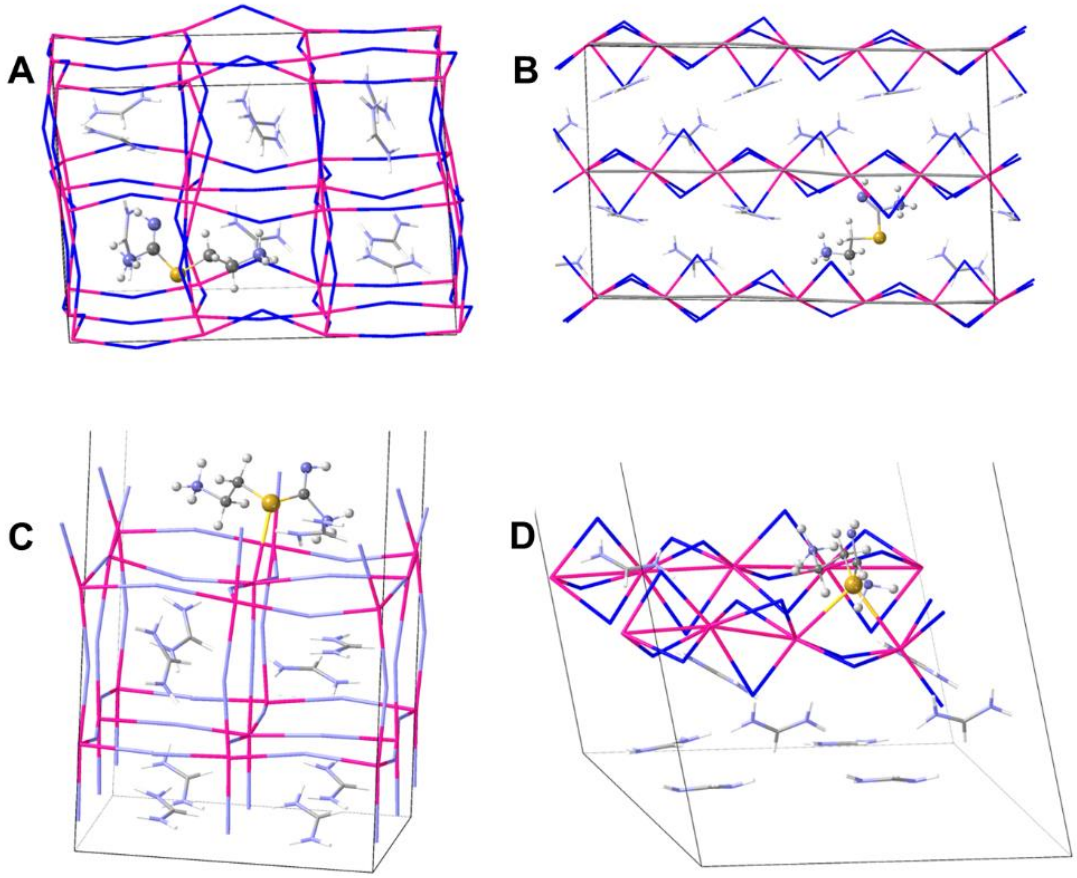

Figure 6. 7 DFT optimized structures with the Model-1 (substitution of two interstitial FA^+ cations by the $isothio^{2+}$ dication) of the supercells of the 3C cubic FAPI (A) and 2H phase (B); DFT optimized structures of the surface of the 3C cubic FAPI (C) and 2H phase (D) generating surface vacancies of one iodide and three FA^+ are replaced by the $Isothio^{2+}$ dication and the PbI_3 network was represented as sticks (Pb pink, I dark blue, C gray, N blue, and H white). The $Isothio^{2+}$ molecule is highlighted with a ball-and-stick representation.

The DFT calculation suggests the possible intercalation of Isothio additive in the bulk and as well as on the surface of the perovskite layer and for both cases results in an overstabilization of the cubic phase.

6.4 Conclusions

To summarize, we proposed a rational additivisation strategy with multifunctional ammonium salt containing sulfur hetero-atom to impart exceptional stability for FAPI film against humidity, water incursion, and shelf-life attacks. By employing a bifunctional diammonium cation with a sulfur heterostructure, we demonstrate that perovskite does

not acquire back the notorious 2H phase upon aging. The thermodynamically stable phase of our ISO film has been shifted from a 2H phase to an intermediate phase that is closer to the cubic 3C phase. Through various structural, photo-physical, and DFT studies, we showed that it is the Pb···S interaction, not the ammonium cation that drives the stabilization kinetics. By virtue of the S heterostructure, the optimized FAPI system showed exceptional stability against high humidity, water immersion, and shelf-life aging attacks. The developed hetero-atomic additivisation strategy can be further rationalized to achieve high intrinsic stability for FAPI thin films.

6.5 Experimental Section

6.5.1 Chemical materials

All chemicals were purchased from Sigma Aldrich and were used as received without any further purification unless otherwise stated.

6.5.2 Additive synthesis

S-(2-Aminoethyl)isothiouronium iodide hydroiodide (Isothio) salt has been synthesized through an inverse temperature crystallization from hydroiodic acid (57%, TCI chemicals). The precipitate was washed with diethyl ether (Acros organic) and recrystallized from absolute ethanol. The process of washing and recrystallization was repeated 5 times and the final product was dried overnight under a vacuum and 60 ^{o}C. The Isothio crystals were moved to the glove box until further use.

6.5.3 Perovskite thin film fabrication

1.4 M perovskite precursor solutions were formulated by dissolving 886.2 mg of pre-synthesized α-$FAPbI_3$ perovskite powder along with the 0-10 mol% (0 for FAPI and others for ISO films) of synthesized Isothio additive in a solvent mixture of DMF and DMSO in 8:1 volume/volume ratio. The α-$FAPbI_3$ perovskite powder was synthesized as explained in section *4.3.1.1*. The precursor solution was stirred overnight at 60 $^{\circ}$C to ensure complete solubility and then filtered via a 450 nm-sized PTFE filter before use. The perovskite layers are fabricated by spin-coating at 1000 rpm for 5 s and 5000 rpm for 20 s, respectively. Then, 100 µL of chlorobenzene was dropped in 15 s at 5000 rpm. Perovskite films were annealed at 150 $^{\circ}$C for 20 minutes.

6.5.4 Characterizations Techniques

Instrumental details has been explained in detail in *section 2.4*.

6.5.5 DFT calculations

The calculations were performed using the FHI-aims computer code[16] with the tight basis set and relativistic atomic ZORA corrections. Dispersion terms were added using the method proposed by Tkatchenko and Scheffler.[17] The calculated DFT energy values were obtained using the PBE[18] optimized structures. See a more detailed description of the calculations as well as additional results for the 3C (α-phase), 2H (δ-phase), TET (tetragonal β-phase), 4H, and 6H phases of the $FAPbI_3$ as Supporting Information.

6.6 Supporting Information

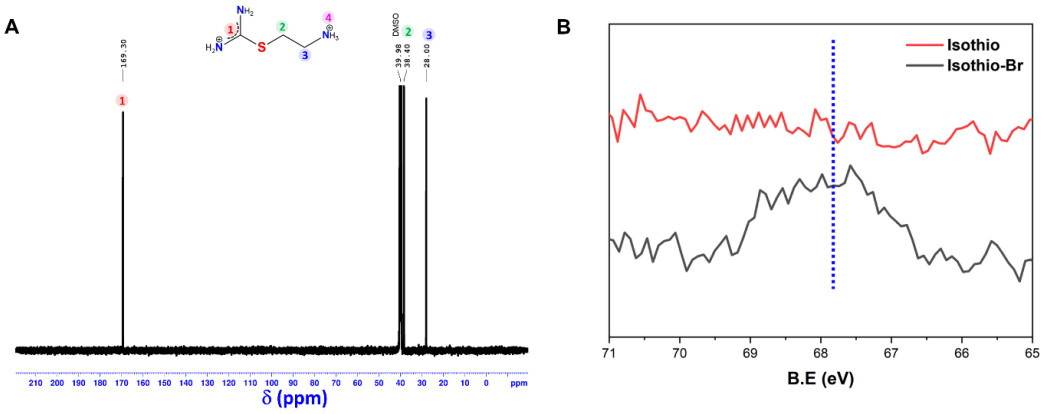

Figure S6. 1 Solution NMR and XPS spectra of Isothio additive. (A) ^{13}C-NMR spectra of synthesized Isothio additive, (B) Br 3d core level XPS spectra of the synthesized Isothio additive and parent Isothio-Br precursor.

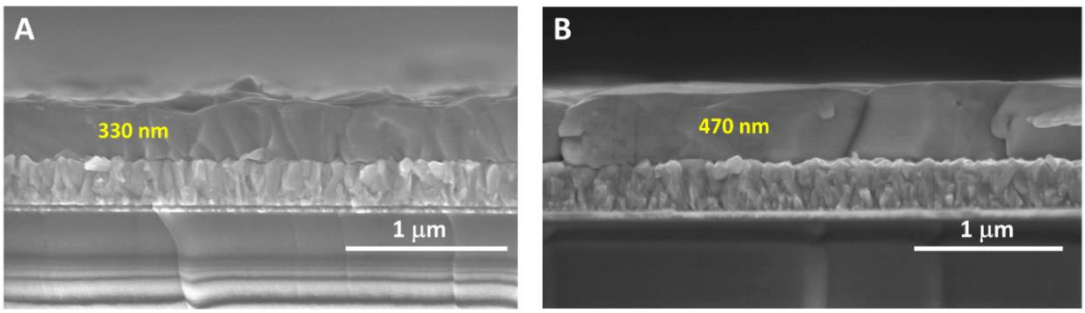

Figure S6. 2 Cross/sectional SEM analysis. (A, B) Cross/sectional SEM images of (A) FAPI and (B) ISO films with a scale bar of 1 μm.

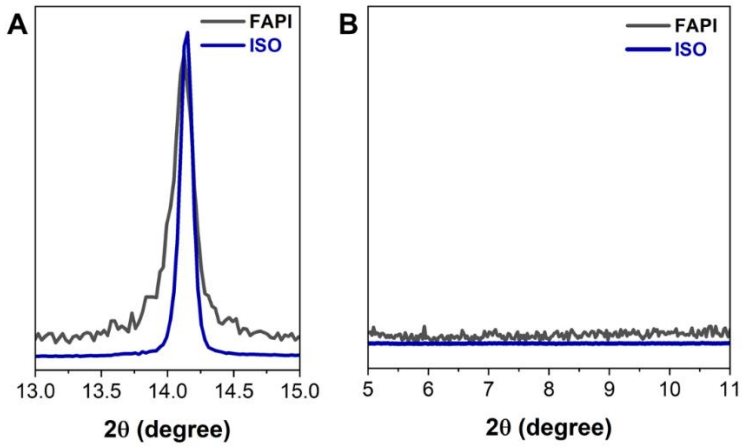

Figure S6. 3 Macroscopic examination of diffraction peaks. (A) FWHM of normalized PXRD peaks of FAPI and ISO films at 2θ=14°, and (B) enlarged view of diffractograms at lower 2θ angles.

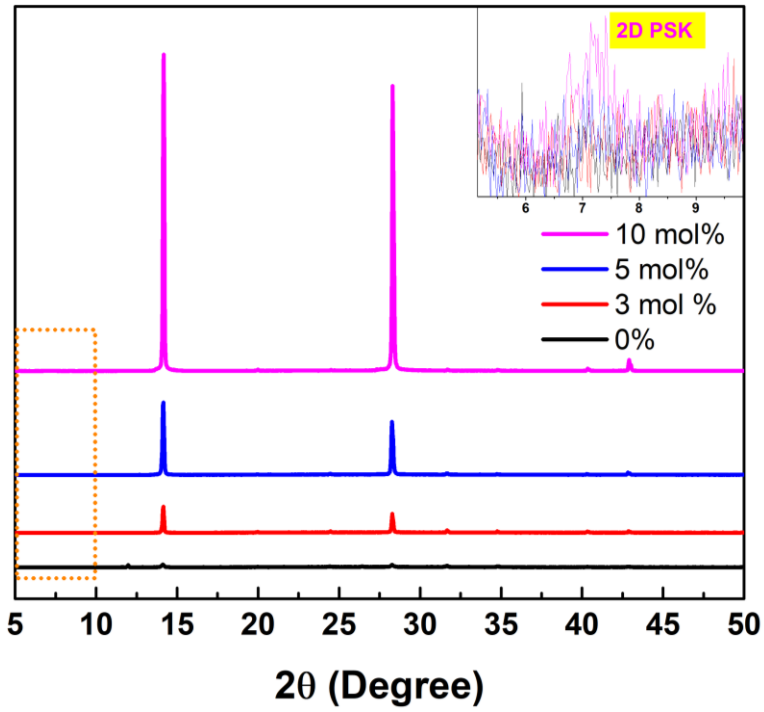

Figure S6. 4 Additive optimization. Diffractograms of ISO films with varying amounts of additive and the zoom-in view of the lower 2θ angles (in the inset).

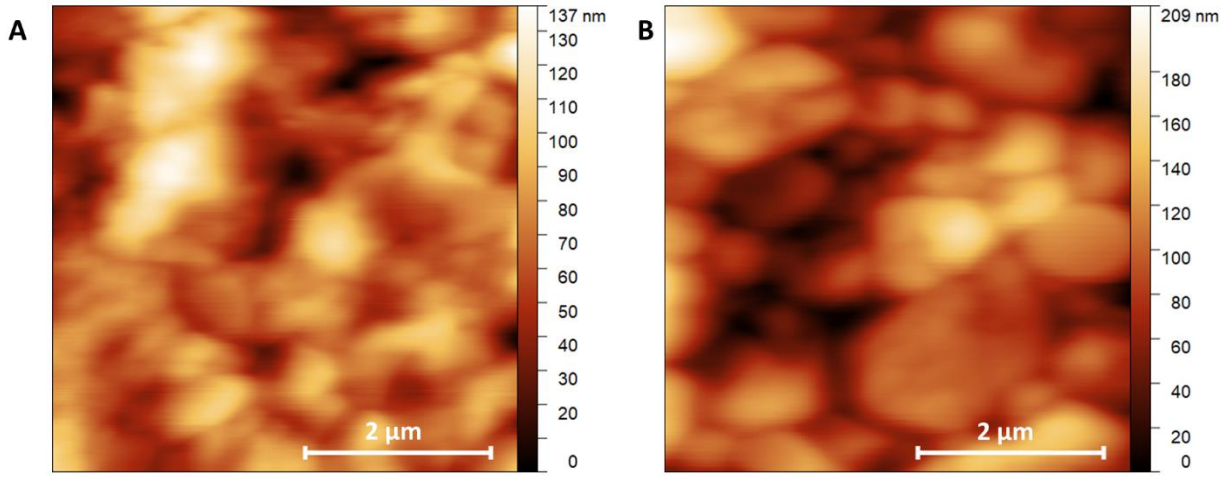

Figure S6. 5 AFM analysis. (A, B) topographic AFM images of (A) FAPI and (B) ISO thin films with a scale bar of 2 µm.

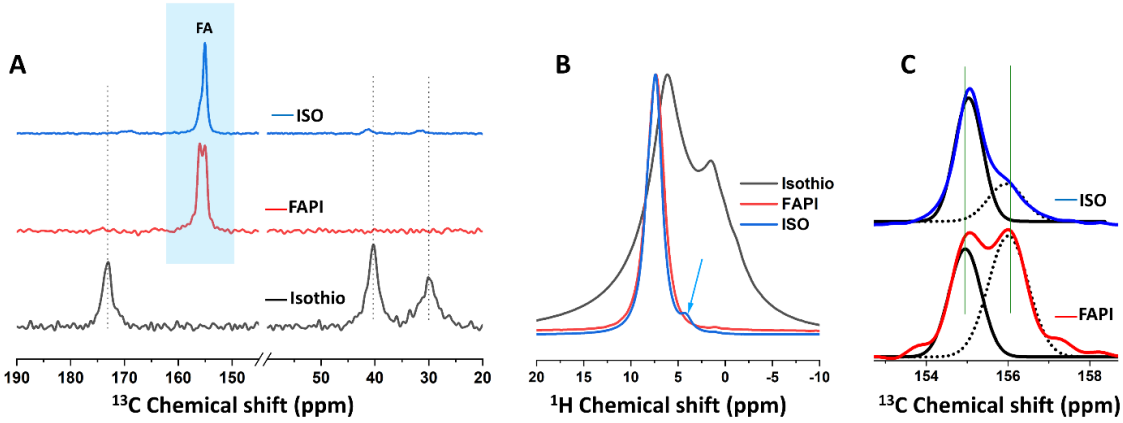

Figure S6. 6 Solid-state NMR analysis. (A) Solid-state ^{13}C NMR resonance reveals the incorporation of isothio additive into the FAPI structure and the (B) solid-state ^{1}H NMR corroborates the isothio inclusion in the FAPI system. (C) zoom-in view of FA resonance indicates the phase stabilization for ISO perovskite.

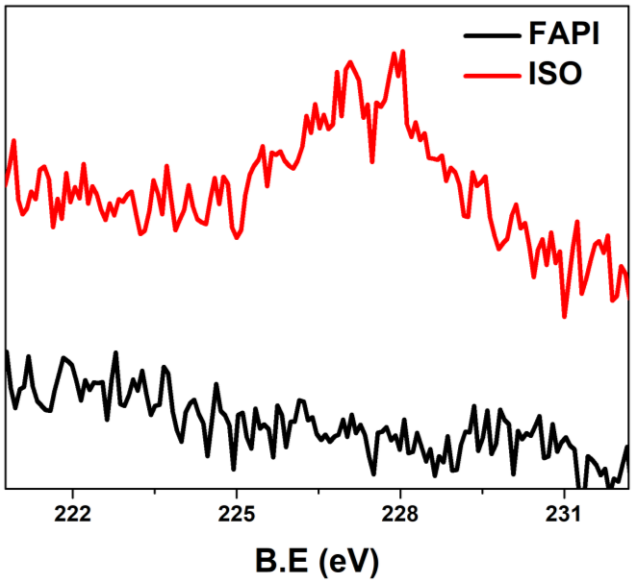

Figure S6. 7 XPS core spectra of thin films. XPS core level spectra of S 2s peak for FAPI and ISO films.

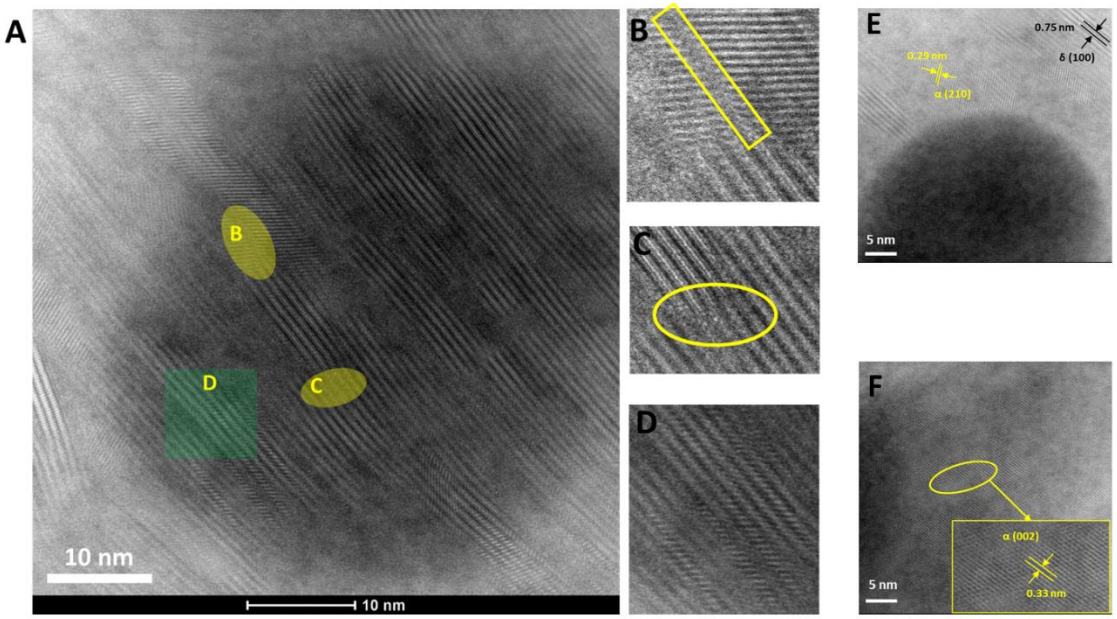

Figure S6. 8 HR-TEM morphology of FAPI Film. (A) Atomic resolution HAADF micrographs of FAPI thin film showing edge dislocations and 3C to 2H phase transitions (scale bar = 10 nm). The highlighted areas were zoomed in (B-D). (B, C) shows the edge dislocations present in (B) 3C and (C) 2H phases. (D) Shows the gradual transition from the 3C to the 2H phase. HRTEM images of (E) FAPI and (F) ISO thin film showing the interplanar spacing calculated from FFT with a scale bar of 5 nm.

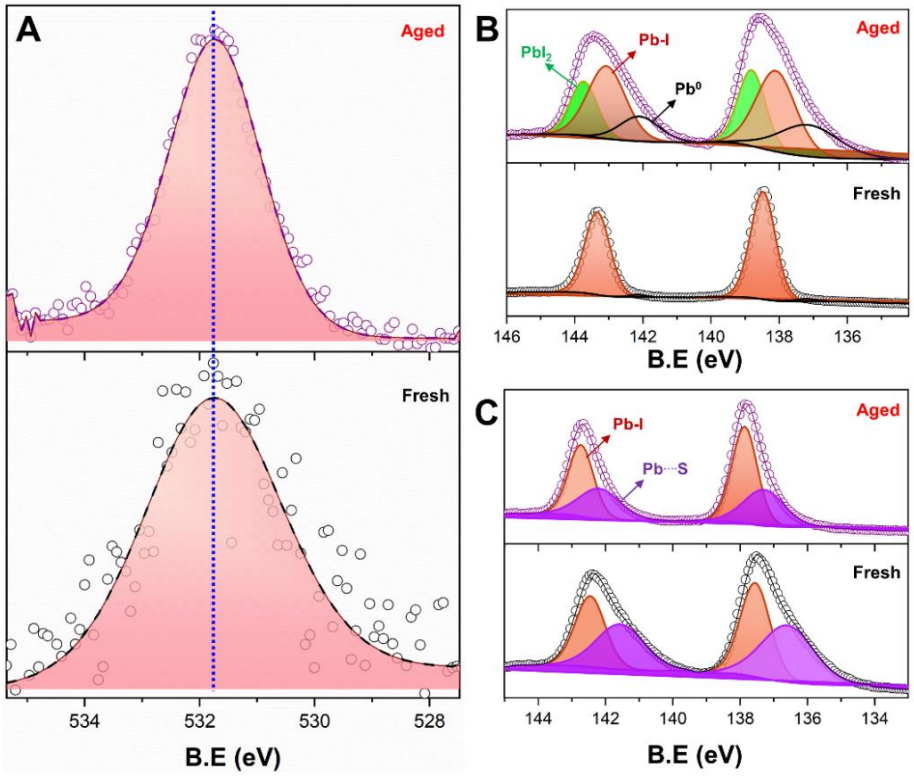

Figure S6. 9 XPS analysis of humidity-aged films. (A) O 1S core level spectra of ISO film before (bottom) and after (top) the humidity attack. (B, C) Pb 4f core level spectra of (B) FAPI and (C) ISO films before (bottom) and after (top) the humidity attack. Open circles and lines represent the recorded data and fitted lines, respectively.

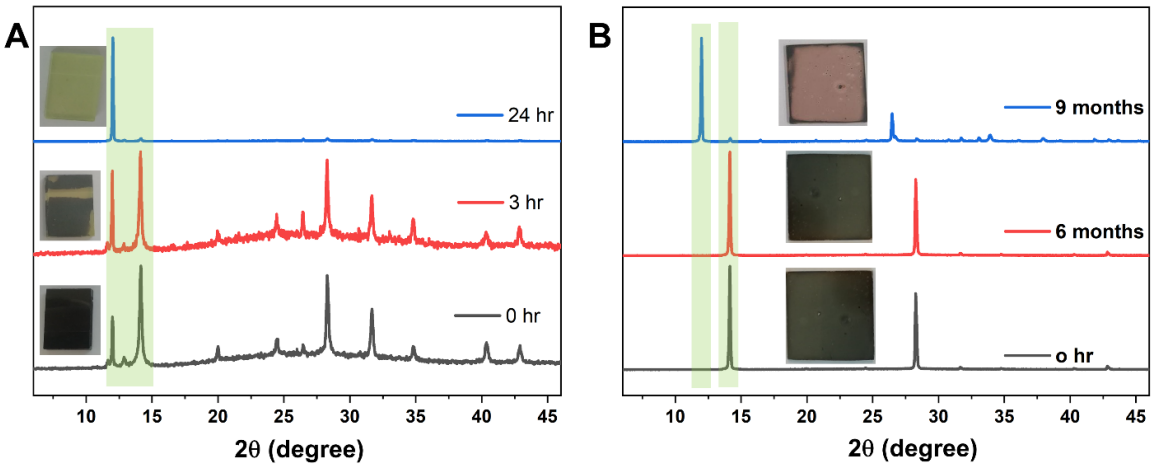

Figure S6. 10 Shelf-life aging of films. (A, B) X-ray Diffractograms and digital images of (A) FAPI and (B) ISO film when exposed to the atmospheric environment to assess the shelf-life stability.

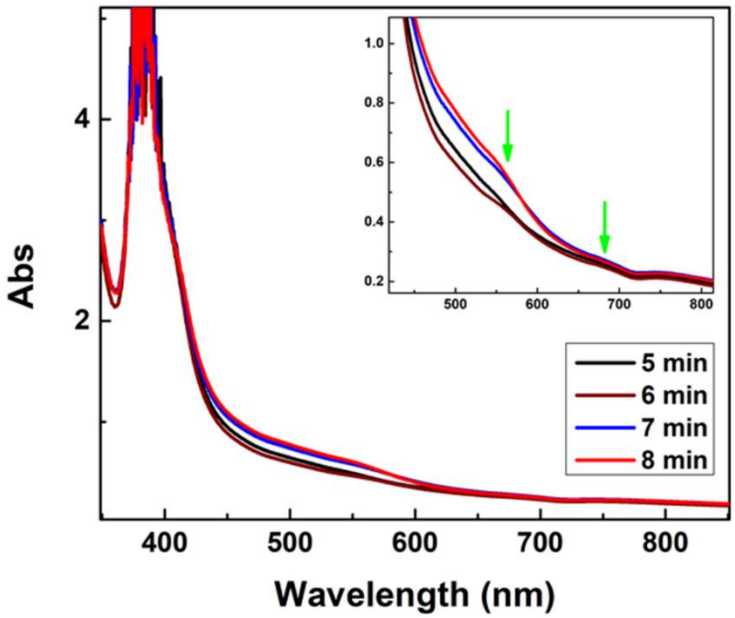

Figure S6. 11 Ex-situ tracking of coloration of ISO-RT films. Time-dependent ex-situ UV-Vis absorption spectra of ISO-RT film.

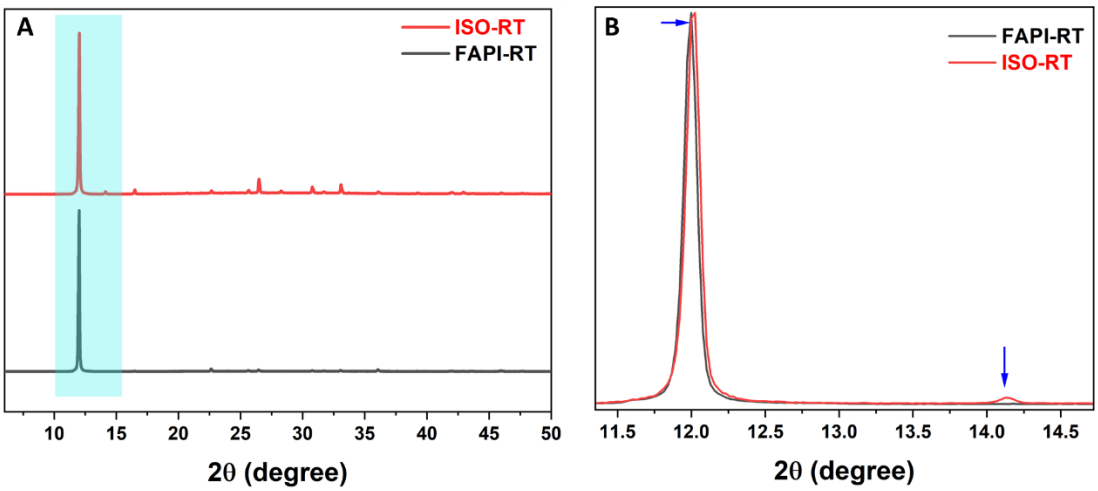

Figure S6. 12 Comparing unannealed thin films. (A) Diffractograms of room-temperature processed FAPI and ISO films. (B) zoom-in view of the selected area of 2θ = 11−15° indicating the 2H peak shift and the emergence of reflection corresponding to the 3C phase.

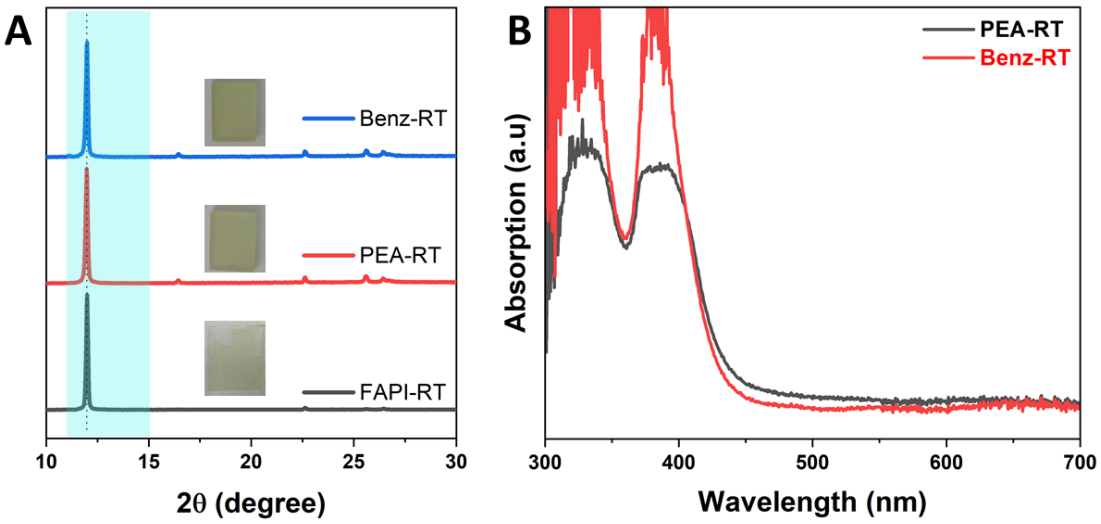

Figure S6. 13 Probing the 2D cationic effect in intermediate phase stabilization. (A) X-ray Diffractograms and digital images of room-temperature processed PEA-RT, Benz-RT, and FAPI-RT films. (B) UV-Vis absorption spectra of PEA-RT and Benz-RT films corroborate the absence of a stable intermediate phase.

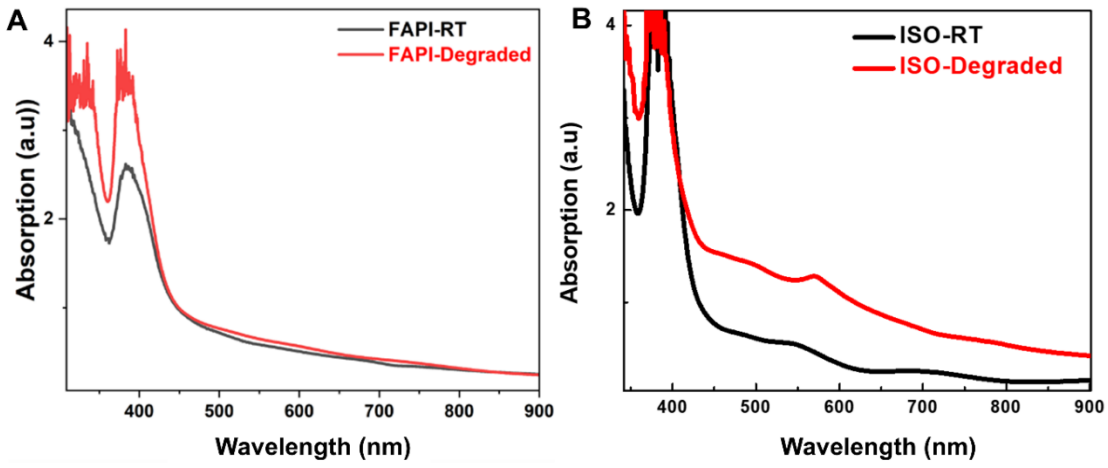

Figure S6. 14 Unannealed Vs degraded film. (A, B) diffractograms of (A) FAPI and (B) ISO films, where the black lines and red lines represent the unannealed and degraded samples, respectively.

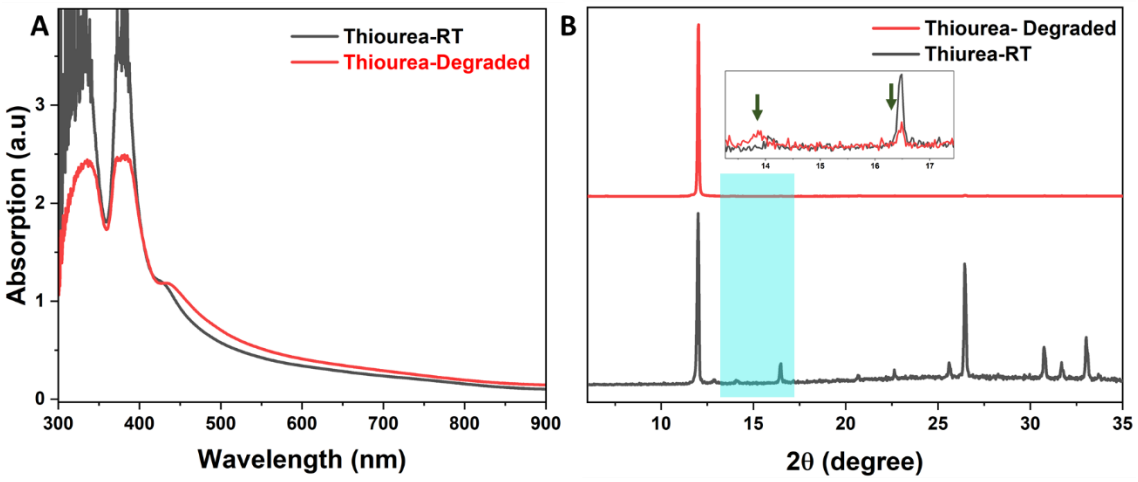

Figure S6. 15 Probing the role of the S atom in the stabilization of the intermediate phase. (A) UV-Vis absorption and (B) XRD patterns of Thiourea-RT and Thiourea-degraded films. The emerged absorption onset and presence of both 3C and 2H peaks supports our hypothesis of Pb···S hetero structure induced phase stabilization of FAPI.

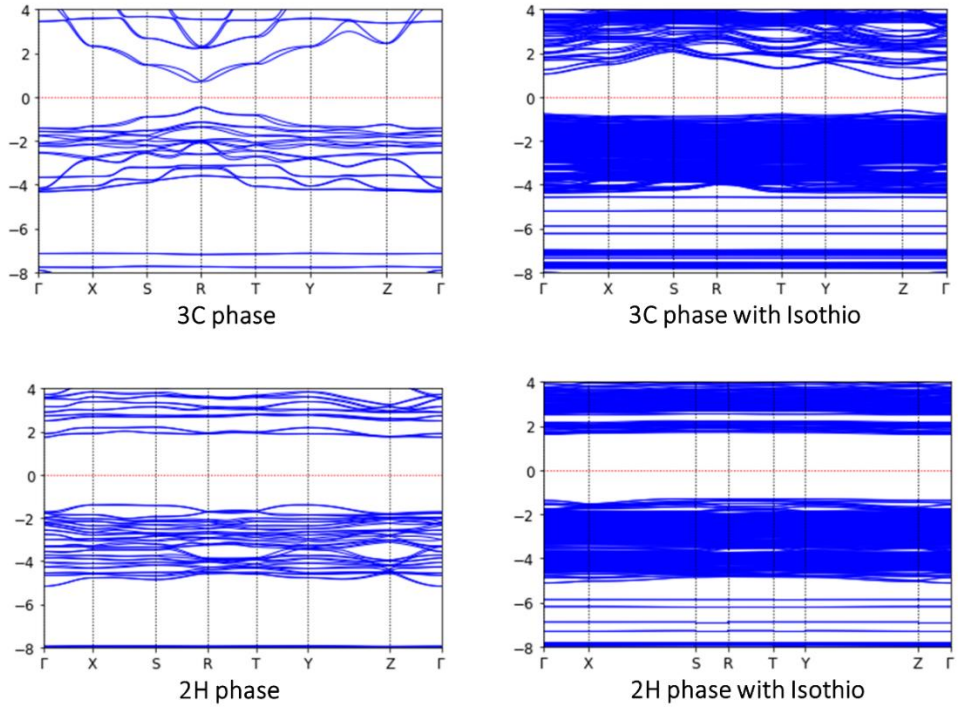

Figure S6. 16 Band structures of bulk substitution model. Band structures (energy in eV) including spin-orbit effects at HSE06 level by using PBE optimized structures for the systems with a bulk substitution of two FA^+ cations with the Isothio cation (Model-1, Figure 4 A and B).

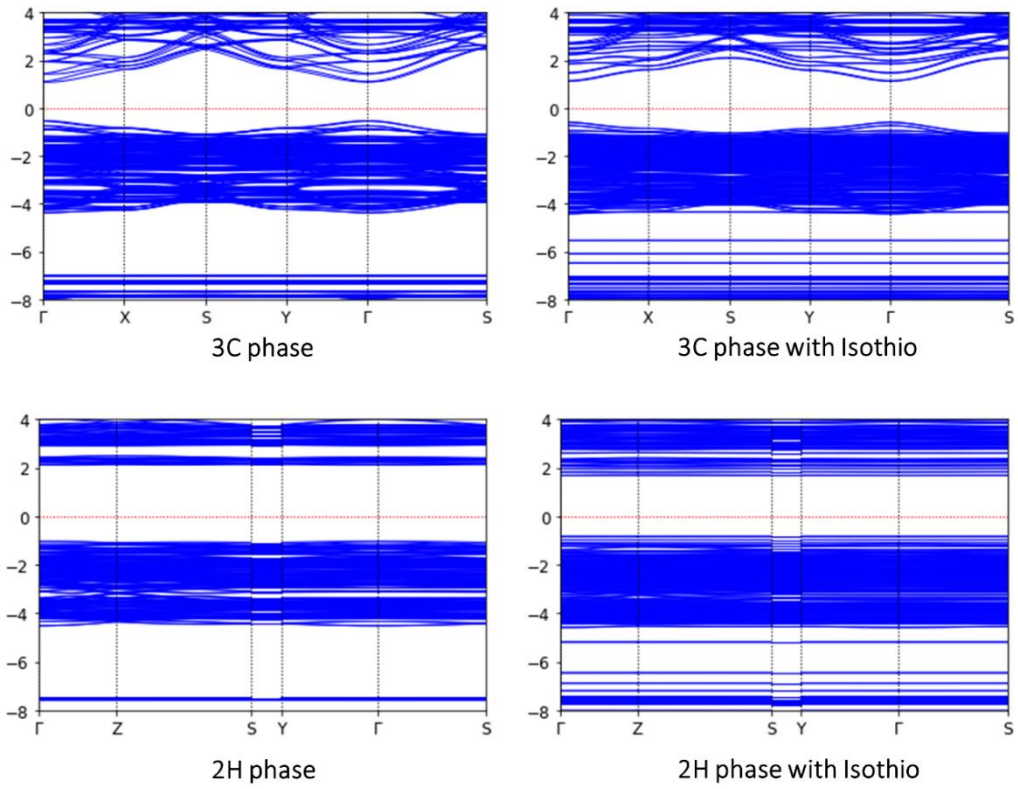

Figure S6. 17 Band structures of surface accumulation model. Band structures (energy in eV) including spin-orbit effects at the HSE06 level by using PBE optimized structures for the 2D systems with a substitution of three FA^+ cations and an iodide anion with the Isothio cation (Model-2, Figure 4 C and D).

Table S6. 1 DFT optimized structural parameters of different phases of $FAPbI_3$ using three different exchange-correlation functionals. The calculations were performed by using symmetry constraints (cell parameters and internal coordinates) except for the PBE* results without constraints (indicating average cell parameters). Calculated relative energies (in kcal/mol) per PbI_3 unit to compare the relative stability of the phases. Negative values indicate more stable structures.

	PBE	**PBE***	**HSE06**	**SCAN**	**Exp.**
3C					
a	6.407	6.382	6.388	6.300	6.3627 [19]
E_{rel}	0	0	0	0	
2H					
a, c	8.586, 8.132	8.709, 7.950	8.633, 8.128	8.720, 8.242	8.667, 7.908 [20]
E_{rel}	-1.9	-3.0	-1.1	-2.5	

TET					
a, c	9.058, 6.292	8.911, 6.400	8.9373, 6.300	8.911, 6.320	8.922, 6.326 [21]
E_{rel}	-1.5	-1.4	-1.6	-2.0	
4H					
a, c	8.744, 15.802	8.744, 15.860	8.733, 15.747	8.692, 15.743	8.814, 15.208 [13]*
E_{rel}	-2.2	-2.5	-1.8	-2.6	
6H					
a, c	8.724, 23.778	8.726, 23.372	8.7696, 23.471	8.772, 23.440	8.844, 22.452 [13]*
E_{rel}	-1.7	-1.1	-1.2	-2.6	

*$(MAPbBr_3)_{0.15}$ $(FAPbI_3)_{0.85}$

Note S6.1

DFT calculations

The calculations were performed using the FHI-aims computer code[16] with the *tight* basis set and relativistic atomic ZORA corrections. Dispersion terms were added using the method proposed by Tkatchenko and Scheffler.[17] The number of k-points was generated using a 4,4,4 partitioning scheme of the first Brillouin zone for the 3D systems, 3,3,2 for the supercells containing the Isothio molecule while 3,3,1 (or 1,3,3) was employed for the 2D structures. Table S1 lists the calculated values for the optimized structures for the 3C (α-phase), 2H (δ-phase), TET (tetragonal β-phase), 4H, and 6H phases for the $FAPbI_3$ compound using three different exchange-correlation functionals, a generalized gradient approximation (GGA) using the PBE functional,[22] a hybrid HSE06 functional[18] and a meta-GGA (SCAN functional).[23] The relative energy difference between these phases has been estimated showing in all cases that the cubic phase is the least stable. These calculations have been performed including constraints on the internal coordinates and the structural parameters to maintain the symmetry of the space group, moreover, the PBE* results correspond to an unconstrained optimization with the PBE functional. These unconstrained results show a good evolution of the relative energies for the phase transformation from 3C to 2H through the intermediate 4H and 6H structures.[13,24] Being

the 2H, 4H, and 6H phases -3.0, -2.5, and -1.1 kcal/mol per unit PbI_3 more stable than the cubic phase. Considering that in the inclusion models of the Isothio cations on the $FAPbI_3$, the symmetry will be broken, and these non-contraction values will be used as a reference. Thus, the results included in the main text have been obtained with the PBE functional using unconstrained optimization (PBE* in Table S1).

We have also calculated the band structures for both models. Band structures have been calculated by including spin-orbit coupling (SOC) effects[25] and the hybrid HSE06 functional was employed to provide accurate band gap value. The underestimation of the band gaps with the GGA functional is well known, thus, in Model-1, the 3C band gap at the PBE-SOC level is only 0.7 eV in comparison with the experimental value of around 1.4 eV. The inclusion of the Isothio cations in the 3C cubic system (Model-1) slightly increases the band gap (calculated HSE06 level, Figure S17), from 1.2 to 1.4 eV while the opposite behaviour is found for the 2H phase decreasing from 3.1 to 3.0 eV. On the other side, in band structures of the 2D models (Model-2, Figure S18), the inclusion of the Isothio dications in the 3C cubic system slightly increases the band gap, from 1.6 to 1.7 eV while the opposite behaviour is also found for the 2H phase decreasing from 3.1 to 2.5 eV.

6.7 References

(1) Sutanto, A. A., Szostak, R., Drigo, N., Queloz, V. I. E., Marchezi, P. E., Germino, J. C., Tolentino, H. C. N., Nazeeruddin, M. K., Nogueira, A. F., and Grancini, G. 2020. In Situ Analysis Reveals the Role of 2D Perovskite in Preventing Thermal-Induced Degradation in 2D/3D Perovskite Interfaces. Nano Letters 20, 3992–3998. https://doi.org/10.1021/acs.nanolett.0c01271

(2) Zhi, C., Li, Z., and Wei, B. 2021. Recent progress in stabilizing perovskite solar cells through two-dimensional modification. APL Materials 9, 070702. https://doi.org/10.1063/5.0056106

(4) Xu, C., Zhang, Z., Zhang, S., Si, H., Ma, S., Fan, W., Xiong, Z., Liao, Q., Sattar, A., Kang, Z., and Zhang, Y. 2021. Manipulation of Perovskite Crystallization Kinetics via Lewis Base Additives., Advanced Functional Materials 31, 2009425. https://doi.org/10.1002/adfm.202009425

(3) Lee, J. W., Dai, Z., Han, T. H., Choi, C., Chang, S. Y., Lee, S. J., De Marco, N., Zhao, H., Sun, P., Huang, Y., and Yang, Y. 2018. 2D perovskite stabilized phase-pure formamidinium perovskite solar cells. Nature Communications 9, 3021. https://doi.org/10.1038/s41467-018-05454-4

(5) Zhou, Y., Liu, C., Meng, F., Zhang, C., Wei, G., Gao, L., and Ma, T. 2021. Recent Progress in Perovskite Solar Cells Modified by Sulfur Compounds. Solar RRL. 5, 2000713. https://doi.org/10.1002/solr.202000713

(6) Ma, C., Grätzel, M., and Park, N. G. 2022. Facet Engineering for Stable, Efficient Perovskite Solar Cells. ACS Energy Letters 7, 3120–3128. https://doi.org/10.1021/acsenergylett.2c01623

(7) Ma, C., Eickemeyer, F. T., Lee, S.-H., Kang, D.-H., Kwon, S. J., Grätzel, M., and Park, N.-G. 2023. Unveiling facet-dependent degradation and facet engineering for stable perovskite solar cells. Science, 379, 173–178. https://doi.org/10.1126/science.adf3349

(8) Baikie, T., Barrow, N. S., Fang, Y., Keenan, P. J., Slater, P. R., Piltz, R. O., Gutmann, M., Mhaisalkar, S. G., and White, T. J. 2015. A combined single crystal neutron/X-ray diffraction and solid-state nuclear magnetic resonance study of the hybrid perovskites $CH_3NH_3PbX_3$ (X = I, Br and Cl). Journal of Materials Chemistry A 3, 9298–9307. https://doi.org/10.1039/c5ta01125f

(9) Doherty, T. a. S., Nagane, S., Kubicki, D. J., Jung, Y. K., Johnstone, D. N., Iqbal, A. N., Guo, D., Frohna, K., Danaie, M., Tennyson, E. M., et al. 2021. Stabilized tilted-octahedra halide perovskites inhibit local formation of performance-limiting phases. Science 374, 1598–1605. https://doi.org/10.1126/science.abl4890

(10) Rothmann, M. U., Kim, J. S., Borchert, J., Lohmann, K. B., O'Leary, C. M., Sheader, A. A., Clark, L., Snaith, H. J., Johnston, M. B., Nellist, P. D., et al. 2020. Atomic-scale microstructure of metal halide perovskite. Science 370(6516). https://doi.org/10.1126/science.abb5940

(11) Yamamoto, S., Bluhm, H., Andersson, K., Ketteler, G., Ogasawara, H., Salmeron, M., and Nilsson, A. 2008. In situx-ray photoelectron spectroscopy studies of water

on metals and oxides at ambient conditions. Journal of Physics: Condensed Matter 20, 184025. https://doi.org/10.1088/0953-8984/20/18/184025

(12) Chen, H., Wang, H., Xue, Y., Ge, Q., Du, Y., Yin, J., Yang, B., Yang, S., Liu, X., Cai, M., and Dai, S. 2022. Ultra-high moisture stability perovskite films, soaking in water over 360 min. Chemical Engineering Journal 450, 138028. https://doi.org/10.1016/j.cej.2022.138028

(13) Gratia, P., Zimmermann, I., Schouwink, P., Yum, J. H., Audinot, J. N., Sivula, K., Wirtz, T., and Nazeeruddin, M. K. 2017. The Many Faces of Mixed Ion Perovskites: Unraveling and Understanding the Crystallization Process. ACS Energy Letters 2, 2686–2693. https://doi.org/10.1021/acsenergylett.7b00981

(14) Tian, J., Cordes, D. B., Quarti, C., Beljonne, D., Slawin, A. M. Z., Zysman-Colman, E., and Morrison, F. D. 2019. Stable 6H Organic–Inorganic Hybrid Lead Perovskite and Competitive Formation of 6H and 3C Perovskite Structure with Mixed A Cations. ACS Applied Energy Materials 2, 5427–5437. https://doi.org/10.1021/acsaem.9b00419

(15) Cui, X., Jin, J., Tai, Q., and Yan, F. 2022. Recent Progress on the Phase Stabilization of $FAPbI_3$ for High-Performance Perovskite Solar Cells. Solar RRL 6, 2200497. https://doi.org/10.1002/solr.202200497

(16) Blum, V., Gehrke, R., Hanke, F., Havu, P., Havu, V., Ren, X., Reuter, K., and Scheffler, M. 2009. Ab initio molecular simulations with numeric atom-centered orbitals. Computer Physics Communications 180, 2175–2196. https://doi.org/10.1016/j.cpc.2009.06.022

(17) Tkatchenko, A., and Scheffler, M. 2009. Accurate Molecular Van Der Waals Interactions from Ground-State Electron Density and Free-Atom Reference Data. Physical Review Letters 102, 073005. https://doi.org/10.1103/physrevlett.102.073005

(18) Heyd, J., Scuseria, G. E., and Ernzerhof, M. 2003. Hybrid functionals based on a screened Coulomb potential. Journal of Chemical Physics 118, 8207–8215. https://doi.org/10.1063/1.1564060

(19) Weller, M.T., Weber, O.J., Frost, J.M. and Walsh, A. 2015. Cubic perovskite structure of black formamidinium lead iodide, α-$[HC(NH_2)_2]PbI_3$, at 298 K.

Journal of Physical Chemistry Letters6, 3209–3212. doi:10.1021/acs.jpclett.5b01432.

(20) Stoumpos, C. C., Malliakas, C. D., and Kanatzidis, M. G. 2013. Semiconducting Tin and Lead Iodide Perovskites with Organic Cations: Phase Transitions, High Mobilities, and Near-Infrared Photoluminescent Properties. Inorganic Chemistry 52, 15, 9019–9038. https://doi.org/10.1021/ic401215x.

(21) Weber, O. J., Ghosh, D., Gaines, S., Henry, P. F., Walker, A. B., Islam, M. S., and Weller, M. T. 2018. Phase Behavior and Polymorphism of Formamidinium Lead Iodide. Chemistry of Materials 30 (11), 3768-3778. https://doi.org/10.1021/acs.chemmater.8b00862.

(22) Perdew, J. P., Burke, K., and Ernzerhof, M. 1996. Generalized Gradient Approximation Made Simple. Physical Review Letters 77 (18), 3865-3868. https://doi.org/10.1103/PhysRevLett.77.3865.

(23) Sun, J., Ruzsinszky, A., and Perdew, J. P. 2015. Strongly Constrained and Appropriately Normed Semilocal Density Functional. Physical Review Letters 115 (3), 036402. https://doi.org/10.1103/PhysRevLett.115.036402.

(24) Nan, Z.-A., Chen, L., Liu, Q., Wang, S.-H., Chen, Z.-X., Kang, S.-Y., Ji, J.-B., Tan, Y.-Y., Hui, Y., Yan, J.-W., et al. 2021. Revealing phase evolution mechanism for stabilizing formamidinium-based lead halide perovskites by a key intermediate phase. Chem 7, 2513–2526. doi:10.1016/j.chempr.2021.07.011.

(25) Huhn, W. P. and Blum, V. 2017. One-hundred-three compound band-structure benchmark of post-self-consistent spin-orbit coupling treatments in density functional theoryPhysical Review Materials 1 , 033803. https://doi.org/10.1103/PhysRevMaterials.1.033803.

CHAPTER 7

7

SUMMARY AND OUTLOOK

7.1 Summary

In this thesis, we shed lights on both the fundamental and practical aspects of the current state-of-art single junction perovskite solar cell absorber material, i.e., MA-, Br-free $FAPbI_3$ perovskite. The fundamental aspect include understanding the crystallization mechanism, phase transition kinetics, and theoretical modelling along with the *in-depth* structural, optical and electrical characterizations. On the other side, practical aspect contains various process engineering and additivisation strategies to transfer the knowledge, acquired from fundamental investigations, towards realising a stable and efficient perovskite solar cell. In doing so, we tried to address the critical phase-instability issue of the $FAPbI_3$ absorber. Although the $FAPbI_3$ possess an advantageous lower-bandgap and higher Shockley-Queisser theoretical efficiency of upto 32.3%, their room-temperature polymorphism and existence of thermodynamically stable non-photoactive phase restrains them from the commercialisation. This dissertation describes fundamental knowledge correlating between the process condition especially the role of precursor material, doping and additives on solar light-to-electricity conversion and the intrinsic and extrinsic stability of both the absorber layer and devices. We anticipate this study extends solid proofs for various existing hypotheses in the community and opens new direction for the future research possibilities in the field.

Chapter 1 and 2 discuss the state of the art of hybrid perovskite solar cells starting with the material history, structure, optoelectronic properties, photovoltaic integration, pros and cons of previously employed hybrid perovskites, emergence and challenges with the hot $FAPbI_3$ perovskites while also including the fabrication and characterisation tools used in this thesis.

In *Chapter 3, 4* and *5* we demonstrate the universal applicability of our developed powder engineering strategies through ensuring the device performance enhancement along with

the reduced production cost. In *Chapter 3*, we developed a room-temperature processed *Cesium* amalgamated $FAPbI_3$ powder (δ-$Cs_{0.1}FA_{0.9}PbI_3$) and employed it as the precursor material instead of conventional precursors such as PbI_2. FAI and CsI. The Cs amalgamation reduced the processing temperature of perovskite absorber film from 150 ºC to 80 ºC. Moreover, we recorded enhanced efficiency from PSC fabricated from δ-$Cs_{0.1}FA_{0.9}PbI_3$ powder than that from the δ-$FAPbI_3$ powder. We ascribed the observed PCE of 17% with negligible hysteresis to the improved crystallinity observed from PXRD and SEM measurements, and higher light absorption visible from absorption measurements. Then, we performed thermal admittance spectroscopy at varying temperatures to reveal the shallow and deep defect density and trap energy distribution within the band gap of $CsFAPbI_3$ based PSCs fabricated at 80 ºC and 150 ºC, and substantiated the increment observed for the low-temperature processed PSC through trap density calculations. Further, we moved towards the synthesis of black α-$FAPbI_3$ powder via simple annealing of δ-$FAPbI_3$ powder and systematically compared the two powder methods with the conventional route in *Chapter 4*. On comparing the three precursor routes, we demonstrated that our powder engineering strategies improved the intrinsic phase stability of $FAPbI_3$ and the corresponding device performance. Through in-depth fundamental analyses, we identified it is the reduced microstrain values that directly contributed to the stabilization of powder based $FAPbI_3$ under shel-life aging. Then, we showed the reduced Urbach energy further improved the PCE by reducing the V_{OC} deficit. In search for cost-competitive fabrication of PSCs, we used low-purity (99%) PbI_2 in the powder engineering process, and then fabricated PSCs delivered slightly higher PCE compared to the conventional counterpart fabricated from high-purity PbI_2 precursor. Given the fact that the PSCs are expected to work under ambient atmosphere in real life scenario and the stability of each layer, especially the perovskite layer, against the humidity attack is of paramount interest. Although many reports elucidates the degradation pathways of perovskite layer, specifically $FAPbI_3$, the quantification of water uptake ability of perovskite layer is not well demonstrated. In *Chapter 5* we demonstrates the proton diffusion to analyse the indirect hydrogen migration using a home-modified transmission infrared spectroscopy, which allowed the direct monitoring of the deterioration of perovskite layer by moisture. We found the moisture/water blocking ability of perovskite layer is in the order of $Cs_{0.1}FA_{0.9}PbI_3$ > $FAPbI_3$ > $MAPbI_3$. Additionally, we quantified the water blocking ability of $Cs_{0.1}FA_{0.9}PbI_3$ as 5 times higher than that of $FAPbI_3$. However, we did not observed any significant change in the proton

diffusion rate for perovskite layer from our δ-$FAPbI_3$ and α-$FAPbI_3$ powders. From the microstrain and proton diffusion analyses, we believe that the microstrain values could regulates the intrinsic stability of $FAPbI_3$ layer but not the humidity attack at the $FAPbI_3$ surface.

Considering the fact that the humidity/water attack at the $FAPbI_3$ surface accelerates the unfavourable phase-transition from photoactive α-phase to photo-inactive δ-phase, we shortlisted various additivisation strategies as discussed in *Chapter 4, 5* and *6*. In search for the hydrophobic materials as additives, we opted non-volatile ionic liquids (ILs) as additives owing to their ultra-hydrophobic nature, high chemical and thermal stability, low-temperature processability and excellent electrochemical properties. *Chapter 4* demonstrates the use of two perfluoroalkyl phosphate-based ILs with ethyl (EMIFAP) and hexyl (HMIFAP) functionalized imidazolium cations as additives. From the XPS analysis, we observed that the emerged F-Pb semi-ionic interaction effectively stabilizes the under-coordinated Pb atoms at the $FAPbI_3$ surface. We also tracked the additivisation induced microstrain changes in the system. Through PXRD and depth-dependent XRD measurements, we found that the micrstrain values were drastically reduced from 1.95 $\times 10^{-4}$ to 1.87×10^{-4} and 1.67×10^{-4} for reference $FAPbI_3$, EMIFAP and HMIFAP films, respectively. This was further substantiated through the higher crystallinity observed from PXRD and SEM analyses. Then, we tracked the electronic disorder, Urbach energy, and identified a reduction from 13.22 to 12.98 and 12.47 meV for reference $FAPbI_3$, EMIFAP and HMIFAP films, respectively. With this understanding and knowledge in hand, we moved forward to fabricate corresponding PSCs and recorded PCE increment from 16.37 to 17.49 and 18.26% for reference $FAPbI_3$, EMIFAP and HMIFAP films, respectively. The hydrophobic nature of ILs seems to provide better stability for the PSCs against environmental stresses upon storage and operation conditions. In a similar way, we then employed 1,3-bis(cyanomethyl)imidazolium bis(trifluoromethylsulfonyl)imide (IL-TFSI), another IL moiety with TFSI group as anionic part, in $Cs_{0.1}FA_{0.9}PbI_3$ system as detailed in *Chapter 5*. Along with higher crystallinity, the achieved longer carrier lifetime due to passivation of trap states by the IL boosted the PCE from 19.27 to 20.55%.

Although the above-discussed powder methods, IL treatment and other reported strain engineering, facet modulation and long-chain ammonium or Lewis bases additive strategies helped to stabilize $FAPbI_3$, the core issue remained untouched. Despite these commendable efforts, the thermodynamic phase stability of $FAPbI_3$ system stayed with

the photo-inactive hexagonal phase (δ-Phase or 2H). To address this serious concern, we demonstrated a novel multifunctional additivisation route, where the rationally chosen S-*(2-Aminoethyl)isothiouronium iodide hydroiodide (Isothio)* molecule containing two ammonium ends along with a sulphur hetero atom used as additive. The choice of sulphur hetero atom was advocated by the prior literature findings stating the stronger electron-donating property of sulphur than oxygen and nitrogen. By employing a bifunctional diammonium cation with a sulfur heterostructure, we demonstrated that perovskite does not return to the notorious 2H phase upon aging. The thermodynamically stable phase of our modified $FAPbI_3$ film was shifted from a 2H phase to an intermediate phase closer to the cubic 3C phase. We attributed the credits to the emerged sulphur-Pb interaction and this was further substantiated by systematic structural, optical and morphological analyses. The synergic impacts from the diammlonium and sulphur atom delivered micron sized grains with higher crystallinity and preferred (h00) facet orientation at macroscopic level. Interestingly, our study demonstrated exceptional stability against high humidity environment, direct water immersion and shelf life aging experiments. The *Isothio* additivisation allowed the $FAPbI_3$ film to stay in its 3C phase for a longer time of 250 hours in a high humidity (75% RH) environment while the reference $FAPbI_3$ film undergone phase transition within couple of hours. Then, from real-time water incursion experiments, we decoded a different degradation pathway from our $FAPbI_3$ film, which helped to withstand the direct water incursion for a time up to 2 minutes whereas the reference film degraded within couple of seconds. Through in-depth XPS measurements, we identified that it is the surface-adsorbed water molecule, which accelerates the degradation of $FAPbI_3$ in the presence of water/humidity. The exceptional humidity stability of our film was substantiated by the complete suppression of surface-adsorbed water molecule even after 250-hour long exposure to high humidity. In comparison to the reference film, we witnessed a long-range ordered structural distribution with reduced edge dislocation and phase transition at nanoscopic level for our film from high-resolution transmission emission microscopic analysis.

In short, we believe that the knowledge accumulated in this thesis are important contributions towards stabilizing and upscaling the state-of-art single junction perovskite solar cells with $FAPbI_3$ as photo absorber. The elucidated fundamental understandings and practical approaches could be further extrapolated to the wide applications of hybrid organic-inorganic halide perovskites.

7.2 Future directions

Although, the perovskite technology has emerged as the first solution-processable technology to compete with the silicon solar cells through its rapid growth in PCE to over 26% within nearly 15 years, it still suffers from various challenges including material stability, lead toxicity, large area fabrication etc. Capitalising the current knowledge on material properties, crystallization and degradation kinetics, new strategies needs to be developed to ensure the material and device stability. We anticipate our works discussed in this thesis could be further extrapolated to address some of the existing concerns in the perovskite photovoltaic community. Firstly, our developed powder methodology could possibly find multiple applicability in the field. Despite the low-cost and higher efficiency achieved at the laboratory scale, the solution-processed PSCs are yet to fully convert to large-scale fabrication. Further, toxic solvents used in the precursor solution may find serious difficulties during their upscaling in industrial scale.[1,2] Reportedly; the vacuum deposition tool has emerged as one of the potential alternative. However, the conventional multi-source co-evaporation technique, where each precursor evaporated simultaneously, could face serious challenges regarding the control over the stoichiometric ratio and evaporation rate for individual precursors.[3,4] In this scenario; our pre-synthesized perovskite powder precursors could offer a solution. The possible development of single-source evaporation of perovskite layer could make the fabrication process much easier and reproducible at industrial scale. Their ease of bulk synthesis and stability during the long-time storage and transport may further reduce the production cost as well. Next, the knowledge acquired from this thesis, especially from the additive engineering strategy, could be utilized for screening potential additive moieties. The initial focus on the single-junction PSCs are seems to be shifting towards the tandem solar cells and modules in recent times. In this direction, many efforts are being put on silicon-perovskite and perovskite−perovskite tandem solar cells and modules.[5] An idea of additional perovskite layer on top of a perovskite-perovskite tandem cell has been evolved during last couple of years. The proposed architecture contains a top perovskite layer with a bandgap range of 1.9-2.3 eV, a middle perovskite layer with a bandgap range of 1.5-1.9 eV, and a bottom perovskite layer with a fixed bandgap of 1.22 eV. The newly emerged model aims to achieve higher output PCE of 37% in coming future. At this juncture, we anticipate the well stabilized $FAPbI_3$ perovskite layer with optical bandgap around 1.5 eV could be a

promising contributor to the triple-junction perovskite-perovskite-perovskite solar cells.[6,7]

7.3 References

(1) Leupold, N., Panzer, F., 2021. Recent advances and perspectives on powder-based halide perovskite film processing. Advanced Functional Materials 31, 2007350. doi:10.1002/adfm.202007350

(2) Ávila, J., Momblona, C., Boix, P.P., Sessolo, M., Bolink, H.J., 2017. Vapor-deposited perovskites: The route to high-performance solar cell production? Joule 1, 431–442. doi:10.1016/j.joule.2017.07.014

(3) Fan, P., Gu, D., Liang, G.-X., Luo, J.-T., Chen, J.-L., Zheng, Z.-H., Zhang, D.-P., 2016. High-performance perovskite $CH_3NH_3PbI_3$ thin films for solar cells prepared by single-source physical vapour deposition. Scientific Reports 6. doi:10.1038/srep29910

(4) Momblona, C., Gil-Escrig, L., Bandiello, E., Hutter, E.M., Sessolo, M., Lederer, K., Blochwitz-Nimoth, J., Bolink, H.J., 2016. Efficient vacuum deposited p-i-n and n-i-p perovskite solar cells employing doped charge transport layers. Energy & Environmental Science 9, 3456–3463. doi:10.1039/c6ee02100j

(5) Li, H., Zhang, W., 2020. Perovskite tandem solar cells: From fundamentals to commercial deployment. Chemical Reviews 120, 9835–9950. doi:10.1021/acs.chemrev.9b00780

(6) Hörantner, M.T., Leijtens, T., Ziffer, M.E., Eperon, G.E., Christoforo, M.G., McGehee, M.D., Snaith, H.J., 2017. The potential of multijunction perovskite solar cells. ACS Energy Letters 2, 2506–2513. doi:10.1021/acsenergylett.7b00647

(7) Wang, Z., Zeng, L., Zhu, T., Chen, H., Chen, B., Kubicki, D.J., Balvanz, A., Li, C., Maxwell, A., Ugur, E., dos Reis, R., Cheng, M., Yang, G., Subedi, B., Luo, D., Hu, J., Wang, J., Teale, S., Mahesh, S., Wang, S., Hu, S., Jung, E.D., Wei, M., Park, S.M., Grater, L., Aydin, E., Song, Z., Podraza, N.J., Lu, Z.-H., Huang, J., Dravid, V.P., De Wolf, S., Yan, Y., Grätzel, M., Kanatzidis, M.G., Sargent, E.H.,

2023. Suppressed phase segregation for triple-junction perovskite solar cells. Nature 618, 74–79. doi:10.1038/s41586-023-06006-7

APPENDICES

Appendix A: List of Publications

(1) **Haris, M.P.U.**, Kazim, S., Pegu, M., Deepa, M., Ahmad, S., 2021. Substance and shadow of formamidinium lead triiodide based solar cells. Physical Chemistry Chemical Physics 23, 9049–9060. doi:10.1039/d1cp00552a

(2) **Haris, M.P.U.**, Kazim, S., Ahmad, S., 2021. Low-temperature-processed perovskite solar cells fabricated from pre-synthesized $CsFAPbI_3$ powder. ACS Applied Energy Materials 4, 2600–2606. doi:10.1021/acsaem.0c03160

(3) **Haris, M.P.U.**, Kazim, S., Ahmad, S., 2022. Microstrain and Urbach energy relaxation in $FAPbI_3$-based solar cells through powder engineering and perfluoroalkyl phosphate ionic liquid additives. ACS Applied Materials & Interfaces 14, 24546–24556. doi:10.1021/acsami.2c01960

(4) **Haris, M.P.U.**, Xia, J., Kazim, S., Molenda, Z., Hirsch, L., Buffeteau, T., Bassani, D.M., Nazeeruddin, M.K., Ahmad, S., 2023. Probing proton diffusion as a guide to environmental stability in powder-engineered $FAPbI_3$ and $CsFAPbI_3$ Perovskites. Cell Reports Physical Science 4, 101304. doi:10.1016/j.xcrp.2023.101304

(5) **Haris, M.P.U.**, Ruiz, E., Kazim, S., Ahmad, 2023, Lead-sulfur interaction induced damp and water stability in pure formamidinium lead triiodide. Cell Reports Physical Science 4, 101516. doi:10.1016/j.xcrp.2023.101516.

(6) Assi, D.S., **Haris, M.P.U.**, Karthikeyan, V., Kazim, S., Ahmad, S., Roy, V.A., 2023. Low switching power neuromorphic perovskite devices with quick relearning functionality. Advanced Electronic Materials. doi:10.1002/aelm.202300285

(7) Klipfel, N., **Haris, M.P.U.**, Kazim, S., Sutanto, A.A., Shibayama, N., Kanda, H., Asiri, A.M., Momblona, C., Ahmad, S., Nazeeruddin, M.K., 2022. Structural and photophysical investigation of single-source evaporation of $CsFAPbI_3$ and $FAPbI_3$ perovskite thin films. Journal of Materials Chemistry C 10, 10075–10082. doi:10.1039/d2tc01164f

(8) Yildirim, M.O., Gok Yildirim, E.C., Eren, E., Huang, P., **Haris, M.P.U.**, Kazim, S., Vanschoren, J., Uygun Oksuz, A., Ahmad, S., 2022. Automated machine

learning approach in material discovery of hole selective layers for perovskite solar cells. Energy Technology 11, 2200980. doi:10.1002/ente.202200980

(9) Gok, E.C., Yildirim, M.O., **Haris, M.P.U.**, Eren, E., Pegu, M., Hemasiri, N.H., Huang, P., Kazim, S., Uygun Oksuz, A., Ahmad, S., 2021. Predicting perovskite bandgap and solar cell performance with Machine Learning. Solar RRL 6, 2100927. doi:10.1002/solr.202100927

(10) Pegu, M., **Haris, M.P.U.**, Kazim, S., Ahmad, S., 2020. Understanding and harnessing the potential of layered perovskite-based absorbers for solar cells. Emergent Materials 3, 751–778. doi:10.1007/s42247-020-00134-w

(11) Bakthavatsalam, R., **Haris, M.P.U.**, Shaikh, S.R., Lohar, A., Mohanty, A., Moghe, D., Sharma, S., Biswas, C., Raavi, S.S., Gonnade, R.G., Kundu, J., 2019. Ligand structure directed dimensionality reduction (2D →1D) in lead bromide perovskite. The Journal of Physical Chemistry C 124, 1888–1897. doi:10.1021/acs.jpcc.9b11033

(12) **Haris, M.P.U.**, Bakthavatsalam, R., Shaikh, S., Kore, B.P., Moghe, D., Gonnade, R.G., Sarma, D.D., Kabra, D., Kundu, J., 2018. Synthetic control on structure/dimensionality and photophysical properties of low dimensional organic lead bromide perovskite. Inorganic Chemistry 57, 13443–13452. doi:10.1021/acs.inorgchem.8b02042

(13) **Haris, M.P.U.**, Bakthavatsalam, R., Kundu, J., 2018. Colloidal Mn^{2+} Doped 2D (n =1) Lead Bromide Perovskites: Efficient Energy Transfer and Role of Anion in Doping Mechanism. ChemistrySelect 3, 6585–6595. doi:10.1002/slct.201801248